UNIVERSIDAD COMPLUTENSE DE MADRID
FACULTAD DE CIENCIAS QUÍMICAS

TESIS DOCTORAL

Micro y Nanopartículas de Polímeros Funcionales: de los Fundamentos a las Aplicaciones

Micro and Nanoparticles of Functional Polymers : From Fundamentals to Applications

MEMORIA PARA OPTAR AL GRADO DE DOCTOR

PRESENTADA POR

José Sena Fernández

DIRIGIDA POR

Aurora Nogales Ruiz
Tiberio Ezquerra Sanz

Madrid

UNIVERSIDAD COMPLUTENSE DE MADRID

FACULTAD DE CIENCIAS QUÍMICAS

TESIS DOCTORAL

MICRO Y NANOPARTÍCULAS DE POLÍMEROS FUNCIONALES: DE LOS FUNDAMENTOS A LAS APLICACIONES

MICRO AND NANOPARTICLES OF FUNCTIONAL POLYMERS: FROM FUNDAMENTALS TO APPLICATIONS

MEMORIA PARA OPTAR AL GRADO DE DOCTOR

PRESENTADA POR

JOSE SENA FERNÁNDEZ

DIRECTORES

AURORA NOGALES RUIZ

TIBERIO EZQUERRA SANZ

UNIVERSIDAD COMPLUTENSE DE MADRID

FACULTAD DE CIENCIAS QUÍMICAS

PROGRAMA DE DOCTORADO DE QUÍMICA AVANZADA

MICRO Y NANOPARTÍCULAS DE POLÍMEROS FUNCIONALES: DE LOS FUNDAMENTOS A LAS APLICACIONES

MICRO AND NANOPARTICLES OF FUNCTIONAL POLYMERS: FROM FUNDAMENTALS TO APPLICATIONS

JOSE SENA FERNÁNDEZ

Directores: AURORA NOGALES RUIZ

TIBERIO EZQUERRA SANZ

Septiembre, 2025

Agradecimientos

Después de cuatro años muy intensos, mi etapa predoctoral termina y ahora comienza un nuevo capítulo. Dicen que no hay que exprimir un buen discurso: vete pronto y déjalos riendo. Un buen consejo que intentaré tener en cuenta en estos agradecimientos.

Cuando pensé en hacer un doctorado, confieso que no era consciente de lo exigente que sería. Aun así, me prometí que me esforzaría en llevar a cabo esta tarea que resultaba la más dura y exigente que ninguna a la que me hubiera enfrentado, y que me hacía ilusión. Durante estos años he comprobado que hacer ciencia no siempre es fácil, y que a veces exige una profunda reflexión y perseverancia. Si bien el camino doctoral presenta sus desafíos, la búsqueda de los misterios científicos que merecen ser estudiados ha sido, sin duda, una parte gratificante de esta travesía.

Primero, gracias a todos, vuestra constancia y talento me han motivado a esforzarme cada día.

Agradezco profundamente al grupo SoftMatPol por la confianza depositada en mí, por transmitirme sus conocimientos y entusiasmo por la ciencia, especialmente a mis directores de tesis, Aurora y Tiberio, por su guía constante, paciencia y disponibilidad. Gracias también a Gonzalo (por nuestros momentos de "piti"), Mari Cruz, Jaime y Esther por sus charlas, consejos e inestimable ayuda. A quienes ya no están en el grupo, pero dejaron huella, como Alex, Óscar Toledano, Amelia o Juan Carlos, de los que me llevo también un buen recuerdo.

La vida científica es muchas veces como una fiesta, donde hay invitados entre los cuales algunos se van, otros se quedan y otros llegan. Esto me lleva a agradecer a quienes han pasado mucho tiempo conmigo. La vida en el despacho y laboratorio ha sido una experiencia enriquecedora, marcada por la camaradería y las valiosas amistades forjadas día a día. A mis compañeros de despacho, Iván (conocido cariñosamente como Juan), Alejandro y, especialmente, Patricia, con quien he compartido estos cuatro años completos y momentos muy especiales. Mi sincero agradecimiento por su apoyo y las incontables anécdotas.

Gracias al instituto en general, por estar lleno de personas generosas y maravillosas con las que he compartido grandes momentos y he aprendido mucho. En especial a Santiago Sánchez y Ana Crespo, Juanfran Vega, Viriginia y Andrés. Asimismo, quiero extender mi gratitud a todo el personal del instituto que hace posible nuestro día a día, como Angelita, Sole y el equipo de limpieza, cuyo trabajo y amabilidad siempre amenizaron las jornadas.

Agradecimientos

A lo largo de estos cuatro años, he tenido la oportunidad de irme de estancia y pasar unos meses con grandes científicos y personas. En particular, gracias a Nacho por darme la oportunidad de estar unos meses trabajando en su grupo, y también a las grandes personas que me acogieron y me hicieron sentir como en casa: Tim, Constantina, Ghazaleh, Huyen y Ale.

Finalmente, quiero agradecer y dedicar esta tesis a todos aquellos que me han hecho llegar hasta aquí y me han acompañado más allá del laboratorio. A mis padres y mi hermano, a mis abuelos y a toda mi familia. A todos mis amigos de siempre, especialmente a Raúl, por escucharme incansablemente hablar del trabajo y por su paciencia y comprensión durante los momentos de mayor exigencia de esta tesis, incluso en nuestros ratos de desconexión. A mis amigos científicos, que me llevé en la carrera y que muchos han compartido y vivido simultáneamente los retos de la experiencia de un doctorado, como Samu, Enrique o Aida, y a aquellos que no han hecho un doctorado, pero han estado ahí, como Miguel y Nacho. A Merce y Álvaro, mis antiguos tutores de TFG y amigos, que me han dado valiosos consejos. A José González Calbet, por aconsejarme y orientarme en este mundillo tan complejo. Esta Tesis es para todos vosotros.

A todos los que, de un modo u otro, habéis estado a mi lado durante esta etapa: gracias.

Finalmente, gracias a mí mismo por no rendirme y por haber llegado hasta aquí, y al deporte, que ha sido mi refugio y terapia para relajarme, desconectar y mantener el equilibrio y la claridad mental a lo largo de este camino.

Jose

List of scientific contributions

Papers

(1) Gutiérrez-Fernández, E.; Sena-Fernández, J.; Rebollar, E.; Ezquerra, T. A.; Hermoso-Pinilla, F. J.; Sanz, M.; Gálvez, O.; Nogales, A. Development of Polar Phases in Ferroelectric Poly(Vinylidene Fluoride) (PVDF) Nanoparticles. *Polymer* **2023**, *264*. https://doi.org/10.1016/j.polymer.2022.125540.

(2) Martínez-García, P.; Rebollar, E.; Nogales, A.; García-Gutiérrez, M. C.; Sena-Fernández, J.; Ezquerra, T. A. 3D Printing-Assisted Nanoimprint Lithography of Polymers. *Adv Eng Mater* **2023**, *25* (17). https://doi.org/10.1002/adem.202300344.

(3) Sena-Fernández, J.; Rebollar, E.; Hurtado-Mendoza, A.; Murdoch, T. J.; Vega, J. F.; Martín-Fabiani, I.; Ezquerra, T. A.; Nogales, A. Tuning Photophysical Properties of Semiconducting Polymer Nanoparticles for Improved Photocatalytic Activity. *Nanoscale* **2025**. https://doi.org/10.1039/d5nr01699a.

(4) **In preparation**: Santoro G., Toledano O., Horcajo H., Rebollar E, Ezquerra TA, Sena-Fernández J, Solano E., García-Gutiérrez MC. On the nature of fluorescence modification induced by deformation in regenerated silk fibroin.

(5) **In preparation**: Sena-Fernández J, Toledano O., Santoro G., Rebollar E, Gálvez O., Sanz M., Ezquerra TA, Nogales A. Development of ferroelectric phases in PVDF processed from solution.

Communication at Congress (oral/poster)

- Sena- Fernández, J.; Santoro, G.; Rebollar, E.; Ezquerra, T.A.; Nogales, A. "La Vida Secreta De Los Polímeros: Desde La Naturaleza Hasta La Tecnología." *XXI*

Introductory Course on Research in the Structure of Matter, Madrid, Spain. Oral contribution. **April 2025**.

- Sena- Fernández, J.; Rebollar, E.; Ezquerra, T.A.; Nogales, A. "The Ticking Of Time In Nanoparticle Preparation: How Aging Of P3HT Dissolutions Affects." *Nano Meets Soft V*, Madrid, Spain. Oral contribution. **December 2024**.
- Sena- Fernández, J.; Rebollar, E.; Ezquerra, T.A.; Nogales, A. "Degradación De Tintes Orgánicos A Través De Semiconductores Poliméricos Nanoestructurados." *VIII Simposio Anual en Química Avanzada*, Madrid, Spain. Oral contribution. **July 2024**.
- Sena- Fernández, J.; Rebollar, E.; Ezquerra, T.A.; Nogales, A. "Polímeros Semiconductores Nanoestructurados Para La Degradación De Contaminantes Orgánicos." *Congreso Nacional De Materiales (CNMAT) 2024*, Malaga, Spain. Oral contribution. **June 2024**.
- Sena- Fernández, J.; Santoro, G.; Rebollar, E.; Ezquerra, T.A.; Nogales, A. "PVDF: obtaining the electroactive phases." *II PhDay Campus Serrano CSIC*, Madrid, Spain. Poster contribution. **June 2024**.
- Sena- Fernández, J.; Rebollar, E.; Ezquerra, T.A.; Nogales, A. "Poly(3-Hexylthiophene) As A Degrading Agent For Organic Dyes." *POLY-CHAR 2024*, Madrid, Spain. Oral contribution. **May 2024**.
- Sena- Fernández, J.; Santoro, G.; Rebollar, E.; Ezquerra, T.A.; Nogales, A. "Polímeros: Más Allá De Los Plásticos." *XX Introductory Course on Research in the Structure of Matter*, Madrid, Spain. Oral contribution. **March 2024**.
- Sena- Fernández, J.; Santoro, G.; Rebollar, E.; Ezquerra, T.A.; Nogales, A. "PVDF: In Search Of Electroactive Phases." *Science Meeting (UNED-CSIC)*, Madrid, Spain. Oral contribution. **February 2024**.
- Sena- Fernández, J.; Rebollar, E.; Ezquerra, T.A.; Nogales, A. "P3ht As Photodegrading Agent." *I PhDay Campus Serrano CSIC,* Madrid, Spain. Poster contribution. **June 2023**.
- Sena- Fernández, J.; Rebollar, E.; Ezquerra, T.A.; Nogales, A. "Application Of P3HT And P3HT:PCBM Nanoparticles As Photodegrading Agents For Polluting Dyes." *Nano meets SOFT UNED-CSIC*, Las Rozas, Spain. Oral contribution. **December 2022**.
- Sena- Fernández, J.; Rebollar, E.; Ezquerra, T.A.; Nogales, A. "P3ht:Pcbm, The Most Efficient Organic Solar Cell Material... And More." *1.ª Jornada Jóvenes Investigadores*, Madrid, Spain. Oral contribution. **October 2022**.

Research stays

Martin-Fabiani Group, Loughborough University, Loughborough, United Kingdom. *February–May 2023 (3 months)*.

Supervisors: Dr. Ignacio Martin-Fabiani (Specialist in Material Science).

Project: Research stay for the characterisation of semiconducting polymers.

Focus: Advanced optical characterisation (FLIM) of semiconducting polymer nanoparticles.

Results: Results from this collaboration are integrated in Chapters 5 and 7.

Funded by: FPI-MCIN Contract (Ref. PRE2020-094362).

Table of contents

Resumen ..... **xiii**

Abstract ..... **xv**

List of symbols and abbreviations ..... **xvii**

1. Introduction **1**

1.1. The concept of molecular weight in polymers **4**

1.2. Polymer solubility **6**

1.2.1. Solubility parameters 8

1.2.2. Three-dimensional solubility parameters: Hansen solubility parameters 9

1.3. Crystallinity in polymers: Structure, thermodynamics and solution crystallisation **10**

1.3.1. Thermal transitions in semicrystalline polymers 11

1.3.2. Chain organisation and morphological features 13

1.3.3. Crystallisation from solution 14

1.4. Semiconducting polymers **15**

1.4.1. Conjugated bonds in semiconducting polymers 16

1.4.2. Optical properties 18

1.4.2.1. **Exciton formation and J-H aggregates** **18**

1.4.3. Poly(3-hexylthiophene) (P3HT) 20

1.5. Ferroelectric polymers **24**

1.5.1. Ferroelectricity 25

1.5.2. Poly(vinylidene fluoride) (PVDF) 26

1.5.2.1. Polymorphism and electroactive phase formation in PVDF 27

1.5.2.2. Formation of electroactive phases 29

1.6. Preparation of nanoparticles **30**

1.7. Applications of functional polymers **31**

1.7.1. Photocatalysis with P3HT nanoparticles 32

1.8. Main objectives and outline of the thesis **34**

1.9. Bibliography **36**

2. Materials, methods and techniques **50**

2.1. Materials **51**

2.1.1. Polymers 51

2.1.1.1. Poly(3-hexyltiophene) (P3HT) 51

2.1.1.2. Poly(vinylidene fluoride) (PVDF) 53

2.1.2. Non-polymeric materials 53

2.1.2.1. Sodium Dodecyl Sulphate (SDS) 53

2.1.2.2. Methylene Blue (MB) 54

2.1.3. Solvents 56

2.2. Preparation of nanoparticles **57**

2.2.1. Nanoparticles prepared by dialysis 58

2.2.1.1. Preparation of nanoparticles by dialysis 58

2.2.2. Flash nanoprecipitation 60

2.2.2.1. Nanoparticles prepared by the flash method 62

2.2.2.2. Fash by microfluidic 63

2.2.3. Miniemulsion 65
2.2.3.1. Nanoparticles prepared by miniemulsion method 66
2.3. Deposition techniques 67
2.3.1. Spin coating 67
2.3.2. Drop casting 69
2.4. Experimental techniques 71
2.4.1. Wide Angle X-ray Scattering (WAXS) 71
2.4.2. Atomic Force Microscopy (AFM) 79
2.4.3. Dynamic Light Scattering (DLS) 84
2.4.4. Optical techniques 93
2.4.4.1. Ultraviolet-Visible Spectroscopy 94
2.4.4.2. Fluorescence spectroscopy 98
2.4.4.3. Fluorescence Lifetime Imaging Microscopy (FLIM) 101
2.4.5. Infrared Spectroscopy (FTIR) 103
2.4.6. Liquid chromatography coupled with mass spectrometry (LC-MS) 105
2.5. Photodegradation test 106
2.6. Bibliography 107

3. Flash nanoprecipitation of P3HT nanoparticles: Tuning morphology, crystallinity, and optical properties via concentration, solvent ratio, and aging effects 114
3.1. Effect of the P3HT solution concentration on the properties of flash nanoparticles 116
3.1.1. Effects of solution concentration on the crystalline structure of the P3HT nanoparticles prepared by flash 122
3.1.2. Optical properties of the P3HT nanoparticles prepared by flash: absorption and emission 127
3.2. Effect of the THF/water ratio (R) on the morphology and characteristics of the nanoparticles 136
3.2.1. Effects of R on the size, morphology and aggregation 137
3.2.2. Effects of R on the crystalline structure of the P3HT nanoparticles prepared by flash 139
3.2.3. Optical properties of P3HT nanoparticles: absorption and emission 141
3.3. Effect of aging on the morphology and characteristics of the nanoparticles 142
3.3.1. Effect of the P3HT solution aging on the optical properties 143
3.3.2. Effect of the P3HT solution aging on the morphology and characteristics of the nanoparticles 146
3.3.3. Crystalline structure of aged P3HT nanoparticles 152
3.3.4. Optical properties of aged P3HT nanoparticles: absorption and emission 155
3.4. Conclusions 159
3.5. Bibliography 160

4. Physical properties of P3HT nanoparticles prepared by miniemulsion 167
4.1. Effect of sonication on the size, morphology and aggregation of the nanoparticles 169
4.2. Crystalline structure of the P3HT nanoparticles prepared by miniemulsion 174

4.3. Optical properties of P3HT nanoparticles at different sonication levels: absorption and emission 178
4.4. Conclusions 184
4.5. Bibliography 184

5. Comparative preparation of P3HT nanoparticles: flash versus miniemulsion and effects on structural, optical and FLIM properties 189
5.1. Effects of the solvent on P3HT solutions 190
5.2. Comparison of the size and aggregation of the nanoparticles depending on the preparation method 193
5.3. Changes in crystalline structure in nanoparticles: GIWAXS 195
5.4. Changes in optical properties in nanoparticles: absorption and emission 197
5.5. Fluorescence lifetime of the nanoparticle suspensions 199
5.6. Conclusions 203
5.7. Bibliography 203

6. Development of polar phases in PVDF deposits and NPs 207
6.1. Evaluation of solvent properties for PVDF crystallisation 208
6.2. Solvent effects on the morphology and crystallisation of free-standing PVDF deposits 211
6.2.1. Impact of solvent properties on the developed crystalline phases of PVDF deposits 212
6.2.2. Influence of solvent on the chain conformation in PVDF deposits: A quantitative FTIR spectroscopic study 216
6.2.3. Influence of solvent properties on the crystalline phase formation of PVDF: role of the boiling point, solubility and polarity 219
6.3. Preparation and characterisation of PVDF NPs: Effect of dialysis and flash techniques on morphology, size, and phase formation 223
6.3.1. Investigation of solvent effects on PVDF NP by flash nanoprecipitation 224
6.3.1.1. Morphological and size characterisation of PVDF NPs prepared by flash nanoprecipitation 224
6.3.1.2. Solvent-induced variations in the crystalline structure of PVDF NPs prepared by flash: 226
6.3.1.3. Modulation of PVDF crystalline phases by solvent: FTIR study 228
6.3.1.4. Influence of solvent properties on crystalline phases of PVDF NPs prepared by flash nanoprecipitation 230
6.3.2. The influence of solvent on PVDF NPs prepared by dialysis 232
6.3.2.1. Dialysis NPs prepared at room temperature 232
6.3.2.1.1. Influence of solvent on the size, morphology, and nucleation mechanisms of PVDF NPs 232
6.3.2.1.2. Solvent-Dependent crystalline phase composition in dialysis prepared PVDF NPs 234
6.3.2.1.3. Influence of solvent on PVDF crystalline phase composition: FTIR Study 236
6.3.2.1.4. The role of solvent and antisolvent miscibility and solvent polarity on the crystalline phase formation of dialysis prepared PVDF NPs 238

6.3.2.2. Tuning electroactive phase formation in PVDF NPs via binary solvent mixtures of DMA and acetone 241
6.3.2.2.1. Influence of binary solvent mixtures on the crystallisation and phase formation of PVDF NPs 241
6.3.2.2.2. Tuning PVDF crystalline phases with solvent mixtures: An FTIR spectroscopic investigation 243
6.3.2.2.3. Solvent mixtures and their impact on PVDF crystalline phase composition: A comparative WAXS and FTIR study 244
6.3.2.3. Impact of dialysis bath temperature on crystalline structure of PVDF NPs processed from DMA 245
6.3.2.3.1. Effect of bath temperature on PVDF phase formation and crystallinity 246
6.3.2.3.2. Investigation of temperature effects on PVDF crystalline phases: An FTIR perspective 247
6.3.2.3.3. Influence of dialysis bath temperature on electroactive phase formation in PVDF NPs: A GIWAXS and FTIR Study 248
6.3.3. Comparative analysis of flash microfluidic and dialysis for PVDF NPs formation 250
6.3.3.1. The effect of solvent on PVDF NP morphology 250
6.3.3.2. Comparative study of PVDF NPs crystallinity and electroactive phase formation 251
6.4. A comparative analysis of solvent influence on crystallinity and crystalline phases of PVDF deposits and dialysis-prepared NPs 254
6.5. Conclusions 256
6.6. Bibliography 257

7. Photodegradation of methylene blue mediated by P3HT nanoparticles prepared by flash and miniemulsion: A comparative study and analysis of degradation products 262
7.1. Photolysis of methylene blue in the absence of photocatalyst: A control 264
7.2. Evaluation of the intrinsic photostability of P3HT nanoparticles under irradiation 269
7.3. Photocatalytic activity of P3HT flash nanoparticles prepared from fresh and aged solutions in the degradation of methylene blue 271
7.4. The influence of sonication intensity on the photocatalytic efficiency of P3HT nanoparticles prepared by miniemulsion 277
7.5. Comparative photocatalytic performance of methylene blue: Nanoparticles prepared by flash vs prepared by miniemulsion 282
7.6. Adsorption of methylene blue onto P3HT nanoparticles in dark conditions 285
7.7. LC-MS characterisation of methylene blue photodegradation: Demethylation and mineralisation pathways 286
7.8. Conclusions 289
7.9. Bibliography 290

Conclusions 296

Resumen

Micro y Nanopartículas de Polímeros Funcionales: De los Fundamentos a las Aplicaciones.

Esta Tesis Doctoral se centra en el estudio exhaustivo, fabricación y desarrollo de nanoestructuras tridimensionales (nanopartículas, NPs) de polímeros funcionales. En particular, se investigan dos sistemas representativos: el poli(3-hexiltiofeno) (P3HT) y el poli(fluoruro de vinilideno) (PVDF), utilizando métodos de preparación a partir de disolución. El objetivo principal ha sido comprender cómo las propiedades fundamentales de estos polímeros pueden verse modificadas a través de la nanoestructuración y el control de las condiciones de preparación, con especial interés en su morfología y comportamiento estructural, y, en el caso del P3HT, también en sus propiedades ópticas y actividad fotoinducida. Las nanoestructuras obtenidas presentan no solo un gran potencial para mejorar el rendimiento en dispositivos electrónicos y optoelectrónicos, sino que también se postulan como candidatas idóneas para explorar procesos fotoinducidos, como la fotodegradación, gracias a su morfología y elevada actividad superficial.

Para P3HT se desarrollaron y optimizaron métodos de dispersión post-polimerización, incluyendo la **nanoprecipitación flash** y la **miniemulsión**. A través de un enfoque multidisciplinar empleando técnicas avanzadas de caracterización como microscopía de fuerzas atómicas, dispersión dinámica de luz, difracción de rayos X, espectroscopía Ultravioleta-Visible, espectroscopia de fluorescencia, o estudios de tiempos de vida de fluorescencia, se logró **establecer la correlación entre las condiciones de preparación y las propiedades estructurales y ópticas de las NPs**. Esto permitió establecer cómo las variables del procedimiento de preparación influyen en las propiedades finales de las NPs.

Asimismo, una parte relevante del trabajo se centra en el **estudio de las fases cristalinas polares (β y γ) del PVDF en forma de depósitos preparados por "drop casting" y NPs preparadas por diálisis y por nanoprecipitación flash a través de la microfluídica**. Se prepararon estos sistemas mediante la elección adecuada del disolvente. Los sistemas resultantes fueron estudiados mediante microscopía de fuerzas atómicas, espectroscopía Infrarroja por Transformada de Fourier y difracción de rayos X, lo que permitió determinar las condiciones para maximizar la contribución de las fases polares. Este control resulta clave en el diseño de materiales funcionales con propiedades ferroeléctricas optimizadas.

Finalmente, se investigó la eficiencia fotocatalítica de las NPs de P3HT seleccionadas y se evaluó la degradación de colorantes orgánicos modelo como el azul de metileno bajo irradiación ultravioleta-visible. Se encontró una relación directa entre las propiedades estructurales y ópticas de las NPs y su capacidad para degradar contaminantes. Los resultados resaltan el papel fundamental de la nanoestructura en la eficiencia fotocatalítica, proporcionando conocimiento clave para el diseño de fotocatalizadores poliméricos más efectivos.

En resumen, esta Tesis Doctoral subraya la importancia del control de la nanoescala y de las condiciones de preparación como herramientas clave para optimizar el rendimiento funcional de materiales poliméricos. Los resultados obtenidos avanzan significativamente en la comprensión de las relaciones estructura-propiedad en polímeros nanoestructurados, y ofrecen una base sólida para el diseño y la optimización de materiales con funcionalidades específicas, en aplicaciones clave como la electrónica, la optoelectrónica o la fotocatálisis. Además, abre nuevas posibilidades para el desarrollo de materiales poliméricos avanzados orientados a la sostenibilidad y a aplicaciones emergentes en tecnologías limpias. Estos hallazgos también sientan las bases para futuros desarrollos en entornos sostenibles.

Abstract

Micro and Nanoparticles of Functional Polymers: From Fundamentals to Applications

The present thesis focuses on the comprehensive study, fabrication and development of three-dimensional nanostructures (nanoparticles, NPs) of functional polymers. In particular, two representative systems are investigated: poly(3-hexylthiophene) (P3HT) and poly(vinylidene fluoride) (PVDF), using solution-based preparation methods. The principal objective of this study has been to understand how the fundamental properties of these polymers can be modified through nanostructuring and the control of preparation conditions. The study focuses particularly on their morphology and structural behaviour, and, in the case of P3HT, also on their optical properties and photoinduced activity. The nanostructures obtained not only present great potential for enhancing the performance of electronic and optoelectronic devices. In addition, they have been proposed as suitable candidates for the exploration of photoinduced processes, such as photodegradation, on account of their morphology and high surface activity.

For P3HT, post-polymerisation dispersion methods were developed and optimised, including **flash nanoprecipitation** and **miniemulsion**. A multidisciplinary approach was employed, utilising advanced characterisation techniques such as atomic force microscopy, dynamic light scattering, X-ray diffraction, ultraviolet–visible spectroscopy, fluorescence spectroscopy and fluorescence lifetime imaging microscopy. **A correlation was established between the preparation conditions and the structural and optical properties of the NPs**. This facilitated the determination of the influence of the variables of the preparation procedure on the final properties of the NPs.

Furthermore, a significant proportion of the research is dedicated to the **investigation of the polar crystalline phases (β and γ) of PVDF in the form of deposits prepared by "drop casting" and NPs prepared by dialysis and by flash nanoprecipitation through microfluidics**. These systems were prepared by an appropriate choice of solvent. The resulting systems were analysed using a range of analytical techniques, including Atomic Force Microscopy, Fourier Transform Infrared Spectroscopy, and X-Ray diffraction. The application of these methodologies enabled the determination of the optimal conditions for

maximising the contribution of polar phases. This control is key in the design of functional materials with optimised ferroelectric properties.

Finally, the photocatalytic efficiency of the selected P3HT NPs was investigated, and the degradation of model organic dyes such as methylene blue under ultraviolet-visible irradiation was evaluated. A direct relationship was found between the structural and optical properties of the NPs and their ability to degrade pollutants. The results of the study highlight the fundamental role of nanostructure in photocatalytic efficiency, providing key knowledge for the design of more effective polymeric photocatalysts.

In summary, this Thesis underscores the pivotal role of nanoscale control and preparation conditions in enhancing the functional performance of polymeric materials. The results obtained significantly advance the understanding of structure-property relationships of nanostructured polymers and provide a solid foundation for the design and optimisation of materials with specific functionalities, in key applications such as electronics, optoelectronics or photocatalysis. Moreover, it creates new opportunities for the advancement of innovative polymeric materials with a focus on sustainability and the development of new applications in the field of clean technologies. These findings also establish the foundation for future advancements in sustainable environments.

List of symbols and abbreviations

α	Absorption coefficient
α_f	Exit angle
α_i	Incidence angle
β	Full width at half maximum of the diffraction peaks
δ	Solubility parameter
δ	Charge difference
δ_d	Dispersion forces
δ_h	Hydrogen bonding
δ_p	Polar interactions
ε	Permittivity of the solvent
ε_0	Permittivity of free space
ε_r	Dielectric constant
$\varepsilon(\lambda)$	Extinction/Absorption coefficient
Φ	Out-of-plane angle
χ	Electronegativity of the monomer
χ	Azimuthal angle
χ_{EA}	Electroactive phase obtained by X Ray scattering
χ_α	α phase obtained by X Ray scattering
Φ_{EA}	Electroactive phase obtained by FTIR
Φ_α	α phase obtained by FTIR
ΔG_m	Gibbs free energy of mixing

ΔH_m	Enthalpy of mixing
ΔS_m	Entropy of mixing
ΔU	Energy required for vaporisation
$\sum G$	Sum of the molar attraction constants
λ	Wavelength
η	Viscosity
μ	Dipole moment
μ	Cumulants
μm	Micrometer
π	Pi molecular orbital
ρ	Density
σ	Sigma molecular orbital
τ	Time
τ_i	Lifetimes
Γ	Mean decay of the translational diffusion coefficient
•OH	Hydroxyl radical
$O_2^{\bullet -}$	Superoxide anion radicals
2θ	Diffraction angle between the incident vector and the scattered vector
1D	One dimension
2D	Two dimensions
3D	Three dimensions
ai	Pre-exponential coefficients
a_i	Amplitude

a, b, c	Unit cell dimensions
A	Absorbance
A	Proportional constant
A_i	Intensity fraction of species with a particle diameter
A_α, A_β, A_γ	Area of the phase obtained by X-ray scattering
AFM	Atomic force microscopy
ATR	Attenuated Total Reflectance
b	System optics and detector alignment
B	Baseline
$BaTiO_3$	Mixed oxide of barium and titanium
BM	Bending magnets
c, c_0, c_{MB}	Concentration
CB	Conduction band
CH_3	Methane
$CHCl_3$	Chloroform
CO_2	Carbon dioxide
Cr_2O_3	Chromium (III) oxide
d	Interplanar distance between diffracting planes
d	Distance between charges
d_c	Thicknesses of the crystalline lamellae
d_a	Thicknesses of the amorphous lamellae
D	Debyes
D	Diffusion coefficient
D_h	Hydrodynamic diameter
D_n	Number size average

DLS	Dynamic Light Scattering
DMA	N,N-Dimethylacetamide
DMSO	Dimethyl sulfoxide
e^-	Electrons
E	Energy
E_{CB}	Conduction band edge
E_d	Cohesive energy of the dispersion interactions
E^e	Energy of the free electrons on the hydrogen scale
E_g	Band gap energy
E_h	Cohesive energy of the hydrogen bond interactions
E_p	Cohesive energy of the polar interactions
E_{VB}	Valence band edge
EG	Ethylene glycol
EtOH	Ethanol
eV	Electronvolts
F_{att}	Attractive force
F_{repr}	Repulsive force
F_{ext}	External force
FA	Formic acid
$FeCl_3$	Iron (III) chloride
FeRAM	Ferroelectric Random Access Memory
FLIM	Fluorescence Lifetime Imaging Microscopy
FTIR	Fourier Transform infrared spectroscopy
FWHM	Full width at half maximum
$g^{(1)}(\tau)$	First-order correlation function

$g^{(2)}(\tau)$	Second-order correlation function
G	Gauché
GIWAXS	Grazing-Incidence Wide-Angle X-ray Scattering
h^+	Holes
hν	Photon energy
HOMO	Highest Occupied Molecular Orbital
I	Intensity
I_0	Intensity of the incident light
ID	Insertion devices
IR	Infrared
IRF	Instrument response function
J_0	Exciton coupling
k_0	Constant kinetic of zero order
k_{app}	Constant kinetic of one order
K	Scherrer shape factor or Scherrer constant
K_{840}, K_{763}	Absorption constant in FTIR
k_B	Boltzmann's constant
H^+	Proton
H_2O	Water
HH	Head-to-head coupling
HT	Head-to-tail coupling
l	Optical path length
L_p	Long period of the crystalline and amorphous lamellae
LUMO	Lowest Unoccupied Molecular Orbital
M_0	Molecular weight

M_n	Number Average Molecular Weight
M_w	Weight Average Molecular Weight
MB	Methylene Blue
MetOH	Methanol
MEK	Methyl Ethyl Ketone
mV	Milivolts
n	Exponent characterising electronic transition nature
NH_4^+	Ammonium
NO_3^-	Nitrate
NP	Nanoparticle
NPs	Nanoparticles
N.S.	Non-sonicated
OFETs	Organic Field-Effect Transistor
OLEDs	Organic Light-Emitting Diode
OPVs	Organic Photovoltaics
OSCs	Organic Solar Cell
P3HT	Poly(3-hexylthiophene-2,5-diyl)
PC	Polypropylene Carbonate
PDI	Polydispersity index of the molecular weight
PMMA	Poly(methyl methacrylate)
POMA	Poly(o-methyloxyaniline)
PVDF	Poly(vinylidene fluoride)
q	Scattering vector
q_y	Scattering vector parallel to the surface
q_z	Scattering vector perpendicular to the surface

Q	Polydispersity index of the nanoparticles obtained by DLS
R	Solvent-antisolvent ratio
R_0	Interaction radius or solubility radius
R_a	Distance between two compounds in the 3D sphere
RF	Radio frequency
rad/s^2	Radians per second squared
ROS	Reactive Oxygen Species
rpm	Revolutions per minute
RR	Regioregularity
SEM	Scanning Electron Microscopy
SDS	Sodium Dodecyl Sulphate
SO_4^{2-}	Sulphate
STM	Scanning Tunnelling Microscope
t	Time
$t_{1/2}$	Half-life
T	Trans
T	Temperature
T_b	Boiling Temperature
T_c	Crystallisation Temperature
T_g	Glass transition Temperature
T_m	Melting Temperature
THF	Tetrahydrofuran
TCSPC	Time-Correlated Single Photon Counting
TT	Tail-to-tail coupling
UV	Ultraviolet

UV-Vis	Ultraviolet-Visible
V^{o}	Molar volume of the liquid
VB	Valence band
Vis	Visible
WAXS	Wide-Angle X-ray Scattering
XRD	X-ray diffraction
ZnO	Zinc oxide

Chapter 1

Introduction

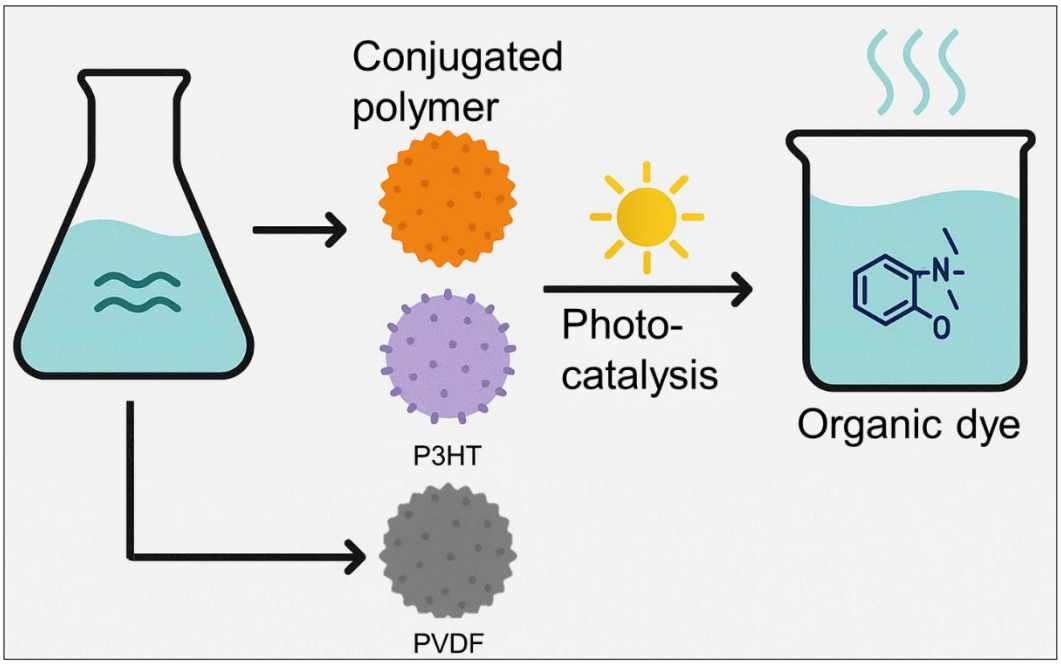

Graphical abstract representing the main idea of Chapter 1

Universidad Complutense de Madrid

Jose Sena Fernández

Micro and Nanoparticles of Functional Polymers: From Fundamentals to Applications

In the face of escalating global challenges, ranging from environmental pollution to resource depletion and the imperative for sustainable development, there is an urgent need to develop sustainable materials and technologies that are both effective and environmentally benign. The accelerated process of industrialisation, in conjunction with the increasing human population, has resulted in a significant release of pollutants into vital ecosystems, particularly water sources. Among these pollutants, organic dyes, which are extensively utilised in various industrial sectors, including textiles, paper, and cosmetics, constitute a notable example of persistent contaminants[1,2]. It is noteworthy that a considerable number of these compounds, including methylene blue (MB) and rhodamine B, are not only toxic but also carcinogenic, and have been demonstrated to cause substantial aesthetic, ecological and physiological damage[2–4]. Their complex chemical structures render them highly resistant to conventional degradation methods, and traditional water treatment often falls short in eliminating these pollutants or converting them into equally harmful intermediates[2]. The necessity for alternative remediation strategies is highlighted, emphasising the critical need for advanced, efficient, and environmentally benign water purification and waste treatment technologies. In parallel with this environmental crisis, the global shift towards sustainability and circular economy principles profoundly transforms materials science and engineering. There is an increasing demand for materials that are not only high-performing but also process-friendly, cost-effective, and environmentally benign in their manufacturing and application phases. Conventional fabrication methods frequently rely on the use of hazardous organic solvents, which contribute to environmental issues and health risks[5]. Consequently, the development of aqueous-based nanoparticle dispersions and processing techniques has enabled the elimination of hazardous solvents[6–8] while utilising high surface-to-volume ratios to enhance and sustain photocatalytic performance under sunlight[7–10].

The utilisation of functional polymers as a solution to these multifaceted challenges is of particular significance, as they offer a nexus of materials science and environmental sustainability[11–13]. Specifically, conjugated semiconducting polymers and ferroelectric polymers are notable for their remarkable and versatile properties.

Among these, semiconducting polymers, such as poly(3-hexylthiophene) (P3HT), with their unique delocalised π-electron systems, offer strong, tunable visible-light absorption with adjustable bandgaps and charge generation capabilities. This makes them ideal for a wide array of optoelectronic applications[14–16], including the highly relevant field of photocatalysis, allowing for efficient photogeneration of reactive species and degradation of dyes in aqueous environments. P3HT is a flexible material offering clear advantages over

traditional inorganic photocatalysts (which are often brittle and costly), and its solution processability, particularly in water-based systems, contributes to its sustainability.

Furthermore, ferroelectric polymers such as poly(vinylidene fluoride) (PVDF) offer reversible polarisation and multifunctionality, combining chemical and mechanical robustness with electroactive properties, offering piezoelectric, pyroelectric and ferroelectric responses[17]. Its inherent polarisation makes it invaluable in sensors, actuators, and energy devices, and crucially, it can enhance photocatalytic performance[18–22].The polar phases of the PVDF are responsible for the generation of internal electric fields, which in turn facilitate the efficient separation of charges. These characteristics could make PVDF an ideal partner for semiconducting polymers in the development of hybrid materials with improved photocatalytic performance.

This thesis builds upon these innovations by addressing the urgent need for advanced, sustainable materials for environmental remediation. This is achieved by developing water-based dispersions of semiconducting (P3HT) and ferroelectric (PVDF) nanoparticles (NPs) and establishing detailed structure–property–performance relationships as outlined in Figure 1.1. The present study focuses on the following specific aspects:

- The eco-friendly preparation of P3HT and PVDF nanoparticle methods (e.g., flash nanoprecipitation, miniemulsion, and dialysis)[6–8].
- The investigation of the interplay between nanostructure, intrinsic properties, and enhanced functional performance in these polymer systems.
- The development of scalable, high-efficiency treatments for challenging organic dye pollutants in water, utilising advanced polymer materials under visible light, in accordance with green-chemistry principles.

The present Chapter thus introduces the fundamental principles of polymers, along with their key characteristics and their application in the field of photocatalytic technology, which is necessary to comprehend the content of the work.

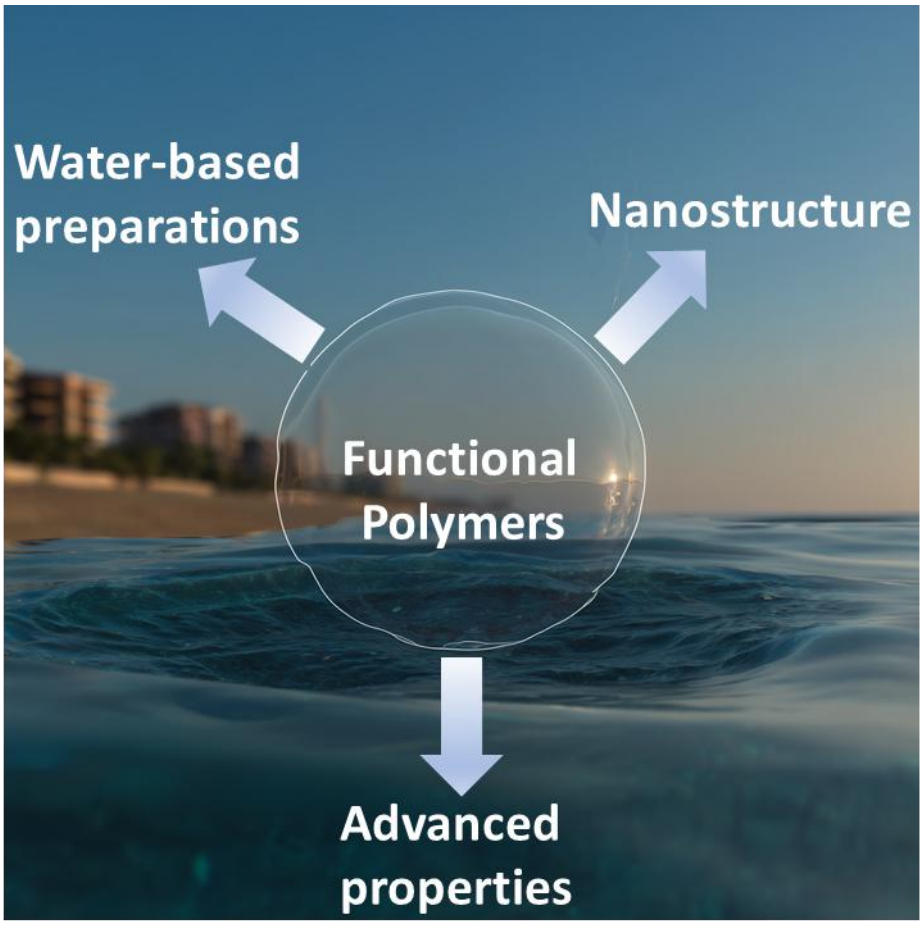

Figure 1.1. Schematic overview of the main research topics addressed in this thesis.

1.1. The concept of molecular weight in polymers

The significance of organic materials in modern life is due to their inherent properties, such as low weight, flexibility, ease of manipulation, cost-effectiveness, and lower processing temperatures compared to inorganic materials or metals[23]. Among these materials, polymers are of particular significance and are currently the most widely used class of materials, accounting for over 50% of all manufactured materials in terms of volume[23,24]. The term "polymer" is derived from the prefix "*poly-*", which means "many", and the suffix "*-mer",* which denotes "unit". Thus, polymers are large macromolecules composed of simple repeating subunits (mers), which are linked by covalent bonds. Typically, polymers are synthesised by organic polymerisation reaction mechanisms, such as addition or condensation[24–27]. The process of addition polymerisation is characterised by the successive addition of precursor units or monomers to an expanding polymer chain, with no loss of

atoms[27]. In contrast, condensation polymerisation involves the reaction of functional groups on monomers, resulting in the elimination of a small molecule, such as water or methanol[27]. These distinct mechanisms have been demonstrated to significantly impact the final polymer structure and properties.

The properties of a polymer depend fundamentally on its chemical structure and molecular weight. The type and strength of the bonds involved, especially carbon-based ones, the nature of functional groups, and the resulting intermolecular interactions (e.g., Van der Waals, dipole-dipole, or hydrogen bonding), all contribute to key features like chain rigidity, crystallinity, and solubility[24,28–32]. For instance, fluorinated polymers such as poly(vinylidene fluoride) (PVDF) exhibit low intermolecular interaction due to the high electronegativity of fluorine and short bond distances, which affects their tendency to crystallise in certain phases[28–31,33].

However, it should be noted that a polymer is not necessarily composed of monomers or individual molecules of the same composition, molecular weight, or molecular structure[24,34]. The capacity of diverse polymer synthesis processes to yield narrow or broad molecular weight distributions varies significantly. A range of synthesis processes gives rise to divergent molecular weight distributions. Consequently, the characteristics of polymers can be described in various ways. The description of these distributions employs the use of averages, including the number-average molecular weight (M_n) and the weight-average molecular weight (M_w)[24,34]. The former assigns equal weight to all chains, while the latter is more sensitive to longer chains[24,34]. Consequently, these averages are pivotal in characterising the breadth or spread of the molecular weight distribution, which, in turn, is indicative of the uniformity of chain lengths within a polymer sample. This breadth is quantitatively expressed by the polydispersity index (PDI), defined as the ratio of M_w to M_n.[35] A PDI value close to 1.0 indicates a narrow distribution, while higher values denote a broader range of chain lengths[24,34]. Figure 1.2 provides a schematic representation of the molecular weight distribution, alongside the M_n and M_w.

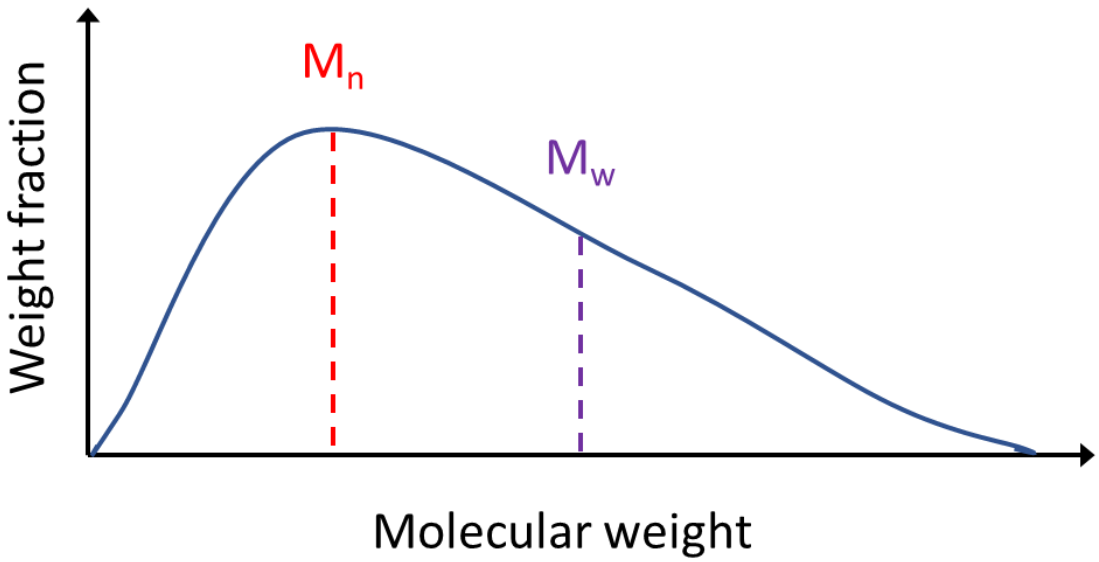

Figure 1.2. Plot of the molecular weight distribution of a polymer. The integrity of a polymer can be examined by looking at its molecular weight distribution. For a monodisperse polymer, these four values would be the same. However, since a polymer consists of chains of different sizes, $M_n \leq M_w$.

1.2. Polymer solubility

Polymer solubility in a given solvent plays a crucial role in processing polymer materials from solution. In contrast to the dissolution of small molecules, which typically involves a rapid and homogeneous mixing at the molecular level, polymer dissolution is a multistep process due to their significantly larger size and entanglement. The following steps are typically involved:

1. The initial contact between the polymer and the solvent: The solvent molecules begin to interact with the polymer surface.
2. The diffusion of solvent molecules into the polymer matrix (swelling): The solvent molecules penetrate the bulk polymer, causing it to swell and decreasing the polymer-polymer interactions. At this stage, the polymer transitions into a swollen, gel-like state, but the chains remain largely entangled within the original matrix.
3. The outward diffusion of polymer chains into the solvent (unentanglement and solvation): As the process of swelling progresses, individual polymer chains begin to disentangle from the swollen matrix and diffuse outwards into the

surrounding solvent. Concurrently, these disentangled chains become fully solvated by the solvent molecules, adopting their characteristic coiled conformations in solution.

This series of steps constitutes the basis of the dissolution process and is inherently linked to the change in energy during mixing.

From a thermodynamic perspective, the process of dissolution is governed by the Gibbs free energy of mixing (ΔG_m), which must be negative for dissolution to occur spontaneously[36,37]. This phenomenon is expressed by the fundamental thermodynamic equation:

$$\Delta G_m = \Delta H_m - T\Delta S_m \qquad \text{Eq. 1.1.}$$

In this equation, ΔH_m denotes the enthalpy of mixing, *T* is the absolute temperature, and ΔS_m is the entropy of mixing. In polymer solutions, the entropy term is generally positive due to the increased disorder that occurs when polymer chains and solvent molecules combine[36,38]. This means that the determining factor for dissolution is the ΔH_m. The existence of favourable interactions between the polymer and the solvent leads to dissolution, with a negative change in ΔH_m being a prerequisite for this process. This negative enthalpy is typically observed when the intermolecular attractive forces between polymer and solvent molecules (e.g., hydrogen bonding, dipole-dipole, or strong dispersion forces) are stronger or more numerous than the average of the polymer-polymer and solvent-solvent interactions. Conversely, if the interactions are predominantly weak dispersion forces, dissolution may critically depend on entropic contributions ($T\Delta S_m$) as enthalpic gains are minimal.

The general principle of solubility, which states that like dissolves like, is a fundamental concept in this field. This suggests that polymer and solvent molecules with high similarity in chemical and structural properties are likely to mix efficiently without significant repulsive interactions[36,39]. Conversely, significant differences often result in phase separation. This is of particular relevance in polymer systems, where partial or total miscibility can depend on crystallinity, molecular weight, and interaction forces[36]. For instance, in the context of high molecular weight polymers, the entropy term is often less pronounced due to the minimal variation in conditions during the mixing process[40].

1.2.1. Solubility parameters

The solubility parameter (δ) is widely utilised in the quantitative estimation of the degree of miscibility between a polymer and a solvent. This parameter, initially defined by Hildebrand[41], can be expressed as the square root of the cohesive energy density, which quantifies the strength of intermolecular forces within a substance[38]:

$$\delta = \left(\frac{\Delta U}{V^o}\right)^{1/2} \qquad \text{Eq. 1.2.}$$

The quantity of energy required for the process of vaporisation is denoted by ΔU, whilst the molar volume of the liquid is indicated by V^o.[42] As polymers do not vaporise, the determination of δ is indirect, frequently achieved through the measurement of polymer swelling or viscosity changes in solvents[43]. Alternatively, estimation of δ can be achieved by summing the molar attraction constants (∑G) of each functional group in the polymer:

$$\delta = \frac{\rho \sum G}{M_0} \qquad \text{Eq. 1.3.}$$

where ρ is the density of the polymer (or solvent)[43]. In general, the dissolution of a polymer in a liquid is most effective when the respective solubility parameter values of the polymer and liquid are closely matched[42]. The proximity of the δ values indicates favourable polymer-solvent interactions and predicts the potential for dissolution or the likelihood of precipitation upon the addition of a second liquid to a solution.

1.2.2. Three-dimensional solubility parameters: Hansen Solubility Parameters

The limitations of a single solubility parameter do not provide a sufficient foundation for reliable predictions. Consequently, more sophisticated models have been developed. Initially, Burrell[44,45] classified solvents based on their hydrogen bonding ability and overall solubility parameters, labelling them as poor, moderate, or strong solvents. Subsequent refinements by researchers such as Crowley et al.[46] (including dipole moment) introduced greater complexity. However, the approach by Blanks and Prausnitz[47] further improved the predictive power of solubility models by demonstrating that the total cohesive energy of polar solvents could be more accurately described by separating it into distinct polar and non-polar contributions.

Nevertheless, a significant advancement in the field of characterising polymer-solvent interactions was marked by the introduction of the Hansen solubility parameters (HSP)[48], which subdivide the total solubility parameter into three distinct components:

$$E = E_d + E_p + E_h \qquad \text{Eq. 1.4.}$$

The total cohesive energy (E) or the square of the total solubility parameter (δ^2) can thus be expressed as:

$$\delta^2 = \delta_d^2 + \delta_p^2 + \delta_h^2 \qquad \text{Eq. 1.5.}$$

In this theoretical model, δ_d is representative of dispersion forces (non-polar or London interactions), δ_p is indicative of polar interactions (permanent dipole interactions), and δ_h is associated with hydrogen bonding[38]. For example, the incorporation of polar functional groups such as -OH, -COOH or -NH_2 into the polymer backbone increases the contribution of the δ_p and δ_h components of the Hansen parameter, thereby enhancing solubility in polar solvents such as water or alcohols.

The three parameters thus delineate a three-dimensional solubility space[37,38,49]. The distance (R_a) between a solvent and a polymer in this space is given by:

$$R_a = \sqrt{4 \times \left(\delta_{d_1} - \delta_{d_2}\right)^2 + \left(\delta_{p_1} - \delta_{p_2}\right)^2 + \left(\delta_{h_1} - \delta_{h_2}\right)^2} \qquad \text{Eq. 1.6.}$$

In this space, each solvent is represented by a point, and the solubility of a polymer can be visualised as a solubility sphere[37,38,49]. The centre of this sphere corresponds to the HSPs of the polymer, and its radius, R_0 (often referred to as the interaction radius or solubility radius), quantifies the solubility range of the polymer. Solvents that fall within this sphere ($R_a < R_0$) are considered good solvents for a given polymer, while those outside this sphere are considered to be poor solvents or non-solvents[37,38,49]. This three-dimensional approach provides a more nuanced, comprehensive and accurate framework for predicting polymer solubility than the Hildebrand parameter by considering the specific nature of intermolecular forces, especially for polar systems.

It is important to acknowledge that while these theoretical models offer valuable predictive capabilities, none are universally valid for all polymer-solvent systems due to the inherent complexity of macromolecular interactions, and empirical verification remains essential.

1.3. Crystallinity in polymers: Structure, thermodynamics and solution crystallisation

Polymers, as long-chain macromolecules, inherently exhibit a high degree of conformational disorder. In contrast to small molecules, whose crystals are characterised by highly ordered, well-defined periodic atomic lattices, polymer systems generally exhibit only partial order, existing as a complex mixture of crystalline and amorphous regions[50–53]. The semi-crystalline character of the polymer is of crucial importance, since the crystalline domains significantly enhance certain physical properties, which are particularly relevant for the functional performance of polymers such as PVDF and P3HT.

In amorphous solutions or molten states, polymers characteristically adopt a random coil conformation. The capacity of a polymer to crystallise is determined by a combination of intrinsic and extrinsic factors. Intrinsically, chain rigidity, symmetry, tacticity, and the presence of side groups govern the tendency of the polymer to adopt stable, ordered structures[54,55]. Although high tacticity and regular linear chains generally favour crystallisation, even polymers with branching, or less regular structures, such as P3HT, are capable of efficient crystallisation when other factors promote ordering[55]. The significant internal flexibility of polymer chains, arising from rotation around covalent bonds, leads to a vast number of conformations[56,57]. Additionally, restricted rotational states can result in energetically stable, ordered structures, including helical conformations as observed in PVDF, where stereoisomerism can dictate chain packing and specific crystalline forms. Molecular weight is also a significant factor, with longer chains introducing topological entanglements that impede orderly packing[55–58]. Finally, extrinsic factors such as processing conditions (e.g. cooling rate, solvent environment) significantly influence the degree and nature of the crystalline morphology formed[54,55,59].

1.3.1. Thermal transitions in semicrystalline polymers

The physical properties of semicrystalline polymers are profoundly influenced by temperature, as their inherent conformational flexibility governs their microstructural order. As shown in Figure 1.3, the thermal behaviour of semi-crystalline polymers is governed by three key temperatures: the glass transition temperature (T_g), the melting temperature (T_m), and the crystallisation temperature (T_c)[24]. In addition to these thermal transitions, the degree of crystallinity plays a pivotal role in determining the resulting mechanical, thermal, and barrier properties, as variations in the degree of crystallinity can markedly alter polymer performance even at identical T_g and T_m values. Below the T_g, polymers are characterised by rigidity and a glassy state[24]. Between the T_g and the T_m, they exhibit a flexible, rubbery, liquid-like phase defined as the viscoelastic state[24]. Above T_m, the crystalline domains melt, and the polymer transforms into a viscous liquid[60]. The term T_c is defined as the temperature at which crystallisation occurs upon cooling from the melt or during annealing[24,60], making the control of these transitions crucial for tailoring chain mobility and ordering.

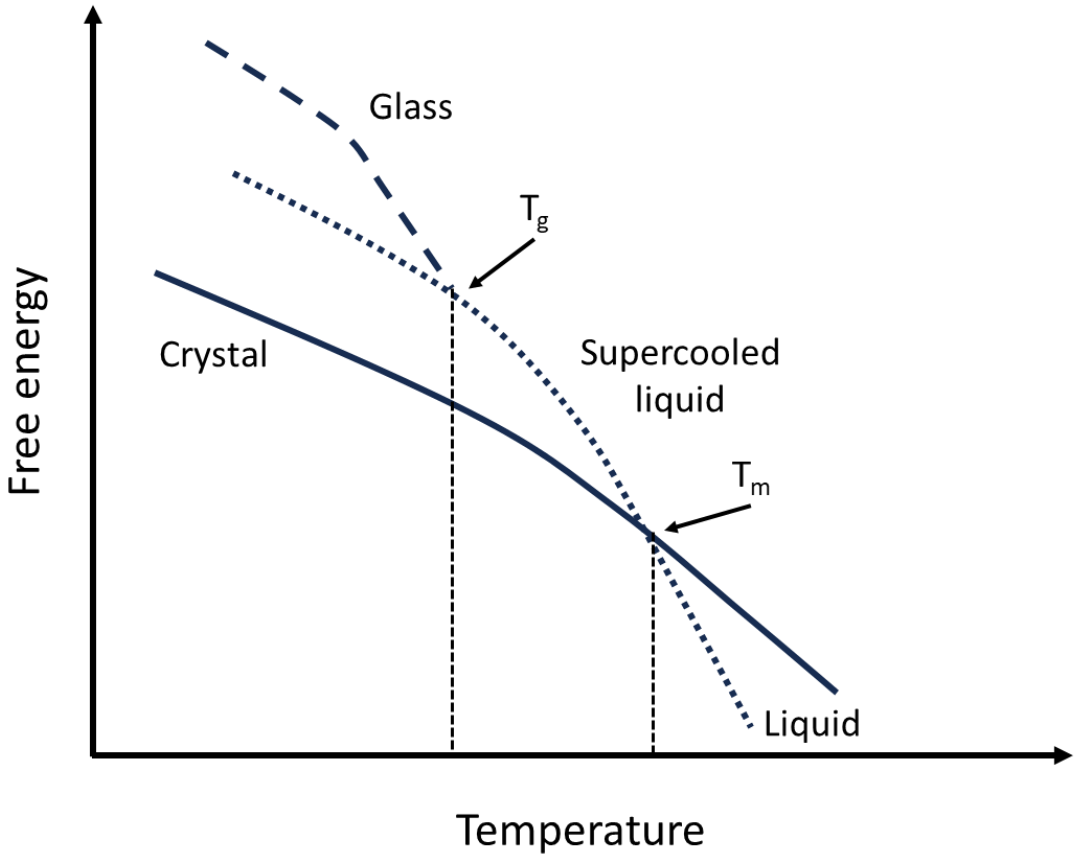

Figure 1.3. Free energy of different material states as a function of temperature. The curve illustrates typical cooling profiles for a crystalline solid (solid line), a supercooled liquid (dotted line) and an amorphous glass (dashed line). The melting temperature (T_m) marks the first-order phase transition from liquid to crystalline solid and is characterised by a discontinuity in free energy. In contrast, the glass transition temperature (T_g) marks a second-order transition from a supercooled liquid to a glass. During this transition, the system falls out of equilibrium, and the free energy decreases more gradually. Figure taken from the reference [61].

It is noteworthy that certain semicrystalline polymers manifest additional thermal transitions, particularly polymorphic transitions. They appear in some crystalline polymers, which present different crystalline phases that give rise to different temperatures and physical properties. The stability of polymorphs is governed by their free energy, with the phase exhibiting the lowest free energy being the most stable[62]. The formation of the various phases is determined by thermodynamic factors, which represent stability, and kinetic factors. These transitions between polymorphs (via crystal–crystal transitions or recrystallisation) are governed by both thermodynamic and kinetic factors[63].

1.3.2. Chain organisation and morphological features

In the early studies on polymer crystal structure using X-ray diffraction, a dual nature was revealed, encompassing both crystalline and amorphous regions. This finding led to the formulation of the micellar model, later revised in 1957[64,65], which proposed that polymer crystals are formed by very thin terraces or lamellae, typically 10-20 nm thick, where molecules crystallise perpendicularly to the lamellar surface, often forming U-shaped loops (see Figure 1.4)[55]. This finding led to the concept of molecular folding, given that lamellar dimensions are smaller than typical polymer chain lengths[55]. The exact nature of this folding has been debated, but the currently accepted model incorporates a highly ordered crystalline core, an interfacial region where chains enter and exit the crystallite, and an interzonal or amorphous region of disordered chains[66]. The resulting crystals are typically oriented perpendicularly to the chain folding direction[66].

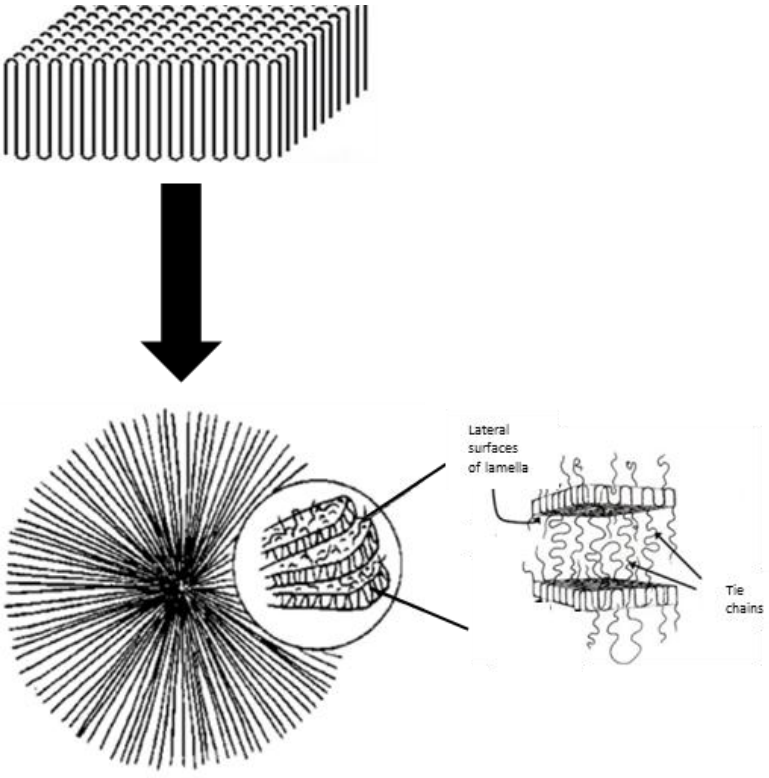

Figure 1.4. Structural motifs at different scales in a semicrystalline polymer. This figure illustrates the hierarchical morphological organisation of a polymer crystallising from the melt, spanning the mesoscopic and microscopic scales. The key structural elements depicted are lamellar crystals and the arrangement of individual polymer chains. Image modified from references [67,68].

The organisation within individual crystallites is further elucidated by the concept of the unit cell[69], defined by its symmetry and crystallographic parameters: three axes (*a, b, c*) and three angles (α, β, γ)[69]. Crystallographic planes within the unit cell are denoted in terms of Miller indices (*h,k,l*)[69].

Generally, a chain may also connect two different lamellae, thereby forming a tie chain[70]. These connected lamellae are of particular significance in semiconducting polymers like P3HT, where charge transport occurs across crystalline domains[70]. The properties of a semicrystalline polymer are largely determined by its degree of crystallinity, the size and distribution of crystallites, and the morphology of the overall system[57]. Crystallites typically range in size from 10 to 100 nanometres, though some have been observed to extend to millimetres.

1.3.3. Crystallisation from solution

Solution crystallisation offers a distinct advantage over melt crystallisation by providing a high degree of control over the crystalline morphology, microstructure, and crystal quality, often leading to highly crystalline and well-defined morphologies with a reduced dependence on molecular weight compared to melt crystallisation[55,60]. In this process, the role of the solvent, the polymer concentration, and the degree of supersaturation become of paramount importance. In contrast to the process of melt crystallisation, where the mobility of chains is dictated by temperature and viscosity, solution crystallisation occurs because of the supersaturation of a polymer solution. In solution, polymer chains are isolated and exist in a disordered arrangement, leading to a non-uniform distribution of polymer segments[55]. Through solvent evaporation, temperature or pressure change, or antisolvent addition, these chains, or parts of them, can undergo ordering, adopting favoured rotational or oriented states that lead to regular, ordered crystalline structures[55].

The crystallisation process is governed by the nucleation stage, which is characterised by an induction period for the formation of stable nuclei[54,55,60,71]. It is during this stage that favourable chain orientations emerge as a result of free energy fluctuations, leading to the formation of stable nuclei once a critical size is achieved[54,55,59,60]. The process of nucleation is followed by crystal growth, where a rapid primary crystallisation stage, which is then followed

by a slower secondary crystallisation as pseudo-equilibrium is reached[54,55,59,60]. The crystallite size is principally governed by the crystallisation temperature, with parameters such as solute concentration, solvent properties, and, to a lesser extent, molecular weight, exerting an influence on the crystal growth rate[56,58].

In a supersaturated solution, polymer chains spontaneously organise into nuclei that, besides crystallising in lamellae, also crystallise in other morphologies such as spherulites or fibrillar crystals, depending on the crystallisation kinetics and solvent properties[55,60,66,72]. The nucleation process can be categorised as either homogeneous, where nucleation occurs uniformly in the solution, or heterogeneous, where nucleation is induced by impurities, interfaces, or additives acting as nucleating agents[55,60]. The degree of supersaturation is a determining factor in the nucleation rate; a high supersaturation (with diluent content exceeding about 70%) has been observed to result in rapid nucleation, though this may yield smaller or metastable crystals[55]. In such concentrated solutions, polymer segments exhibit a more random distribution. While moderate supersaturation (e.g., in dilute solutions where polymer molecules are isolated) increases the nucleation energy barrier, it allows for slower, more ordered growth[55].

Moreover, solvent selectivity is a fundamental aspect of solution crystallisation. The promotion of dissolution by good solvents can be accompanied by a hindrance to nucleation, while swelling solvents that favour chain-chain interactions can promote early-stage aggregation and nucleation[55,60]. It is also imperative to consider the parameters of temperature, polymer concentration, and solution viscosity[60,72]. It has been demonstrated that slow evaporation or controlled cooling often leads to larger and more crystalline domains, while fast evaporation may trap disordered chains in metastable conformations[55]. Thus, solution crystallisation not only allows great control over crystalline morphology but also yields larger, more ordered domains with fewer defects, translating into enhanced optoelectronic performance.

1.4. Semiconducting polymers

The field of organic semiconductors, which has been subject to active investigation for several decades, holds the potential to revolutionise various technologies at the intersection of polymer chemistry and device physics[73]. Despite the prevalence of inorganic materials in

numerous electronic devices, soft materials, most notably conjugated polymers, exhibit distinctive advantages[73]. These include lightness, cost-effectiveness, ease of processing and flexibility, making them highly attractive for optoelectronic and electronic applications[74–76].

Conjugated polymers have experienced significant advancements since the synthesis of the first semiconducting polymers. This breakthrough was pioneered by Alan Heeger, Alan MacDiarmid, and Hideki Shirakawa[77], who, in 1977, demonstrated semiconducting behaviour by synthesising doped polyacetylene. This discovery earned them the Nobel Prize in Chemistry in 2000. This pioneering work establishes the foundation for subsequent breakthroughs that have propelled these materials into applications ranging from organic light-emitting diodes (OLEDs) and organic solar cells (OSCs) to advanced biomedical technologies and beyond[78–88]. Almost forty years after the first complete organic electronic device (an OLED) was reported, a profound understanding of conjugated polymer physics now underpins their integration into key flexible and emerging technologies. Nevertheless, substantial development is still required to fully establish and enhance the presence of semiconducting polymers in the global market[78,79].

Given that the electrical and optical behaviour of conjugated polymers arises from the same delocalised π-electron system, this section explores their interrelated properties, dividing the discussion into electrical and optical phenomena for clarity.

1.4.1. Conjugated bonds in semiconducting polymers

The semiconducting nature of conjugated polymers, crucial for their functional applications, stems from their unique molecular structure and charge transport mechanisms. Unlike conventional insulating polymers that consist exclusively of strong, localised σ bonds (from sp^3-hybridised carbons)[53], conjugated polymers possess a backbone chain characterised by alternating localised single (σ) and delocalised double (π) or triple bonds (see Figure 1.5 (a))[78]. For example, polyacetylene, P3HT, and polypyrrole, illustrated in Figure 1.5 (b)), exhibit such conjugated structures. The delocalised π electrons in the conjugated system result in a continuum of energy states, characterised by a band structure that facilitates electron mobility along the molecular backbone[89]. The band structure is defined by the highest occupied molecular orbital (HOMO) and the lowest unoccupied molecular orbital (LUMO), separated by an energy barrier known as the band gap (E_g)[90,91].

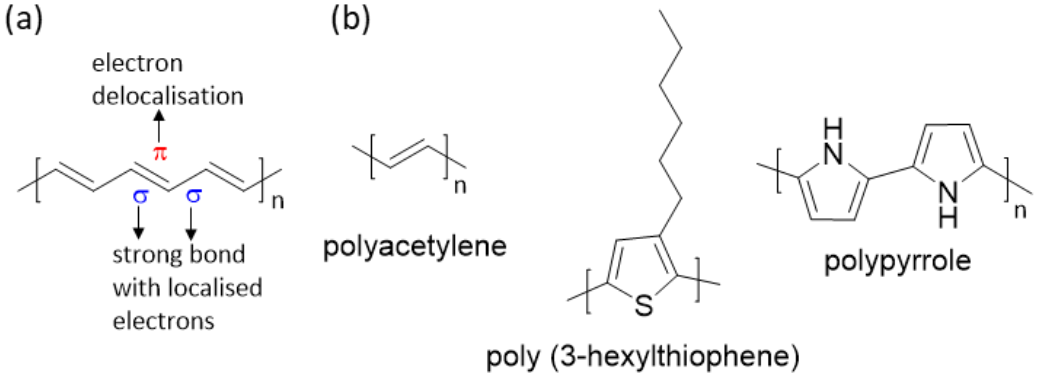

Figure 1.5. (a) The molecular structure of polyacetylene, showing alternating single (σ) and double (π) bonds along the backbone characteristic of conjugated polymers. **(b)** Examples of conjugated polymers include polyacetylene, poly(3-hexylthiophene) (P3HT) and polypyrrole.

In the case of semiconducting polymers, this E_g is typically smaller (0.5-3 eV) than in insulators[92]. This allows for charge mobility through the delocalisation of π electrons and facilitates transitions between HOMO and LUMO states upon excitation. The band gap in conjugated polymers often corresponds to the visible or infrared range due to extended conjugation, making them optically active and relevant for various applications[79].

Beyond the existence of appropriate band gaps, charge carrier mobility is also dependent on the morphology, and the ordering and packing of the polymer chains, specifically the orientation of the conjugated backbone, the degree of π–π stacking, and the presence of structural defects[89,93], which are critical for interchain charge transport and device performance[78]. For instance, studies on regioregular P3HT have consistently demonstrated that interchain π−π stacking (specifically face-to-face stacking) is imperative for macroscopic charge transport in polymer films[94,95]. It is also important to note that high mobilities can occur even in materials with complex microstructures, suggesting that bulk crystallinity is not always the only determining factor. Well-connected aggregates with short-range order often suffice for effective charge transport[70].

1.4.2. Optical properties

As mentioned above, conjugated polymers exhibit pronounced absorption in the ultraviolet-visible (UV-Vis) range, often extending into the near-IR regions, with typical E_g values ranging from 0.5 to 3 eV (corresponding to approximately 400 nm or greater)[79,92]. This strong absorption capacity is responsible for the highly relevant variety of applications, particularly those involving light interactions[74–76]. To enhance the performance of such devices, it is vital to minimise non-radiative recombination and exciton quenching. The extended π-conjugation not only enables efficient light absorption but also governs the exciton dynamics, which are critical for the optical behaviour of these materials,[78,89] as discussed in the following section.

Efficient photoexcitation and exciton generation are critical for applications in photocatalysis, such as those studied in this thesis. Furthermore, molecular packing and aggregation affect how these excitons behave and how the material interacts with light[7,8,9]. These optical phenomena are deeply influenced by the polymer microstructure and are crucial for understanding the performance of conjugated polymer nanoparticles (NPs) in aqueous environments[7,8], where they are used as photocatalysts.

1.4.2.1. Exciton formation and J-H aggregates

The optical properties of conjugated polymers are governed not only by their chemical structure but also by their solid-state organisation. Kasha's pioneering exciton theory established the theoretical framework for understanding the formation of excitons, defined as bound electron-hole pairs, within conjugated systems[96–98]. In the process of absorption, a photon with energy equal to or greater than the band gap is absorbed, exciting an electron from the HOMO level to the LUMO[89]. This process forms electrostatically bound electron-hole pairs, or excitons. In polymer aggregates, the exciton can travel both within the same molecule (intra-chain) and between adjacent molecules (inter-chain).

For efficient charge transport, these excitons must overcome their electrostatic attraction and dissociate into free charge carriers. This process, frequently referred to as "photodoping" in the context of p-type materials, results in the generation of free electrons and holes that can be transported through the material[75,78].

The spatial arrangement of polymer chains gives rise to different types of exciton aggregation, which in turn impacts the absorption and photoluminescence spectra. Spano and colleagues[99–104] built upon Kasha's exciton theory, extending it to the domain of conjugated polymers. This theoretical development elucidates the role of molecular packing in dictating excitonic coupling and spectral features, consequently resulting in distinct optical properties that are dependent on the aggregation state and excitonic coupling[99–104]. Two predominant aggregation types have been commonly observed:

- J-Aggregates: Characterised by an extended, head-to-tail alignment of polymer chains (see Figure 1.6), which results in strong intrachain coupling[99–104]. These aggregates typically exhibit a red-shifted absorption band compared to isolated chains[99–104].
- H-Aggregates: Where chains stack side-by-side or face to face configuration (see Figure 1.6), leading to strong interchain coupling. H-aggregates generally exhibit a blue-shifted absorption band[99–104].

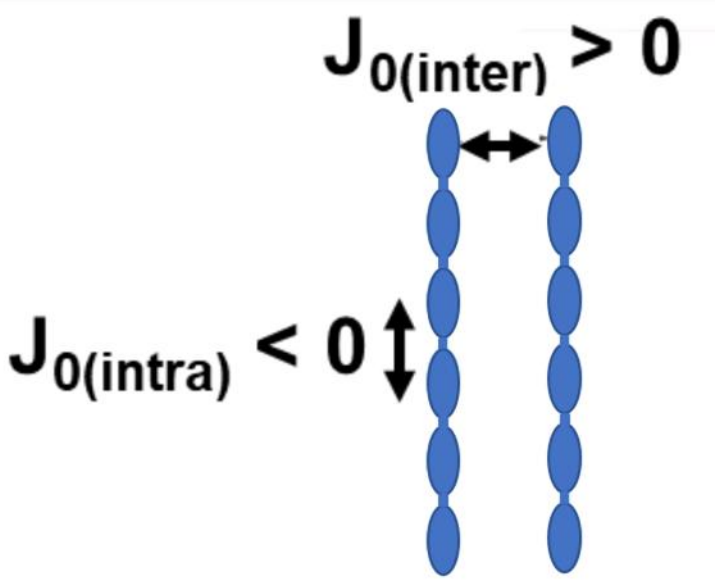

Figure 1.6. Schematic illustration of molecular arrangements in HJ-aggregates. This figure specifically depicts HJ-aggregates, where J-aggregates are represented by the vertical orientation ($J_{o(\text{intra})}$) indicating excitonic coupling between consecutive repeat units (head to tail). In contrast, H-aggregates are shown as the horizontal aggregates ($J_{o(\text{inter})}$), denoting the excitonic coupling between neighbouring chains (face to face). Figure modified from reference [102].

In real polymeric systems, both types of aggregates have been observed to coexist. Tuning the polymer structure or processing conditions can modulate the ratio of J- to H-aggregates and, by extension, their optical properties[99–104]. Recent research has moved beyond static descriptions of aggregation, focusing instead on the dynamic evolution of excitonic states following photoexcitation[10,105]. In this thesis, these aggregation states are especially relevant in the context of P3HT NPs, resulting in distinct morphologies and aggregation states, influencing both light absorption and photocatalytic behaviour.

1.4.3. Poly(3-hexyltiophene) (P3HT)

Of the many materials that have been studied so far, polythiophenes are the best known as p-type polymers[106]. The first successful synthesis of this homopolymer was in 1982 through oxidative polymerisation of 3-hexylthiophene with $FeCl_3$[12]. Early polythiophenes faced challenges with insolubility[107], but the addition of alkyl side chains significantly improved their solubility and processability[106], facilitating their widespread study. The model polythiophene is poly(3-hexyltiophene) or poly(3-hexylthiophene-2,5-diyl) (P3HT), shown in Figure 1.7 (a), chosen for its favourable optical and electrical properties, ease of synthesis and processing, and its ability to self-assemble into ordered structures[106].

This conjugated polymer is characterised by having a backbone with alternating single and double bonds in which the π-electrons are delocalised along the main chain, facilitating electronic delocalisation, which is central to its optoelectronic behaviour[15,108]. The configuration of the alkyl side chain concerning the main chain axes determines the form of P3HT, which can be divided into three distinct regioisomers (Figure 1.7 (b)): head-to-head (HH) coupling, head-to-tail (HT) coupling and tail-to-tail (TT) coupling[109,110]. The polymer can exhibit varying degrees of regioregularity following the combination of the four types of couplings: HT-HT, HT-HH, TT-HT and TT-HH[109,110]. The term "regioregular P3HT" (RR-P3HT) is used to describe a polymer in which the main chain is formed solely by HT-HT couplings. In contrast, regiorandom or irregular P3HT, with a mixture of couplings. RR-P3HT leads to planarity and extended π-conjugation, crucial for self-assembly and high charge mobility.

One of the characteristics of P3HT that renders it a cornerstone polymer is its semi-crystalline nature at room temperature, resulting from the incompatibility between the conjugated polythiophene backbone and the alkyl side chains. Its relative environmental stability, particularly its photostability, and strong absorption in the UV-Vis range are also noteworthy[106,111–113]. Furthermore, its excellent high charge carrier mobility, in particular holes, makes it a suitable candidate for applications such as photocatalysis.

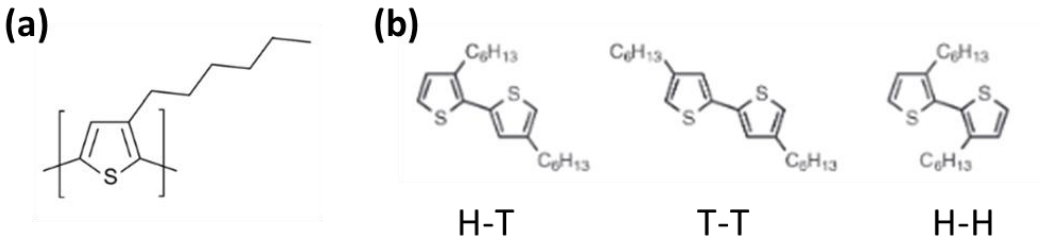

Figure 1.7. (a) The chemical structure of P3HT and **(b)** the regioselective isomers. Figure **(b)** taken from [109].

The greatest hole mobility is in the direction of the molecular backbone chain (intrachain electronic delocalisation)[112], making the conductivity of P3HT highly anisotropic[114]. An intermediate value of hole mobility is found in the π–π stacking direction. The mobility of the holes is significantly reduced along the lamellar stack because the charge carriers have to pass through the σ-bonded carbons of the alkyl side chains, which act as insulating barriers[70,95]. This high intrachain mobility enhances charge separation while aggregation-induced anisotropy presents both challenges and opportunities in device design.

P3HT has a relatively small GAP, between 1.9-2.1 eV, it effectively absorbs visible light, with a conduction band (LUMO) between -3.5 and -2.7 eV and with a high energy valence band (HOMO) between -4.9 and -5.2 eV (Figure 1.8)[115,116]. Notably, the energy levels of this polymer can be tuned.

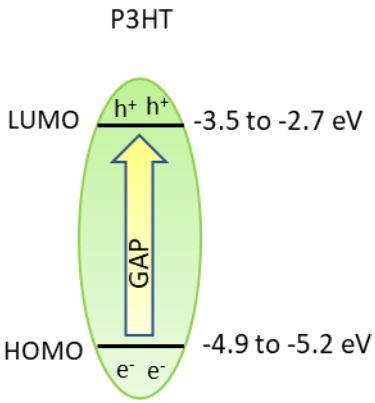

Figure 1.8. Schematic diagram of the electronic structure of P3HT, illustrating the HOMO, LUMO, and the resulting energy gap (E_g).

The main function of the chains is to allow solution processability and to influence the supramolecular organisation of the conjugated chains. Therefore, P3HT can coexist in two phases in solution since it is a solvatochromic polymer, a first phase of dissolved P3HT and a second in the form of microcrystalline aggregates[117]. Owing to the chemical incompatibility of the aliphatic side chains and the conjugated backbones, P3HT is assembled in layers or lamellae of π–π stacked backbones separated by the side chain layers. As shown in Figure 1.9, the crystalline region of P3HT crystallises thermodynamically favourably with a monoclinic unit cell with planar and packed all-trans molecules with alkyl side chains extended in the perpendicular direction of the thiophene rings due to π–π interactions [117,118]. Its optical features and aggregation state highly sensitive to solvent polarity and concentration.

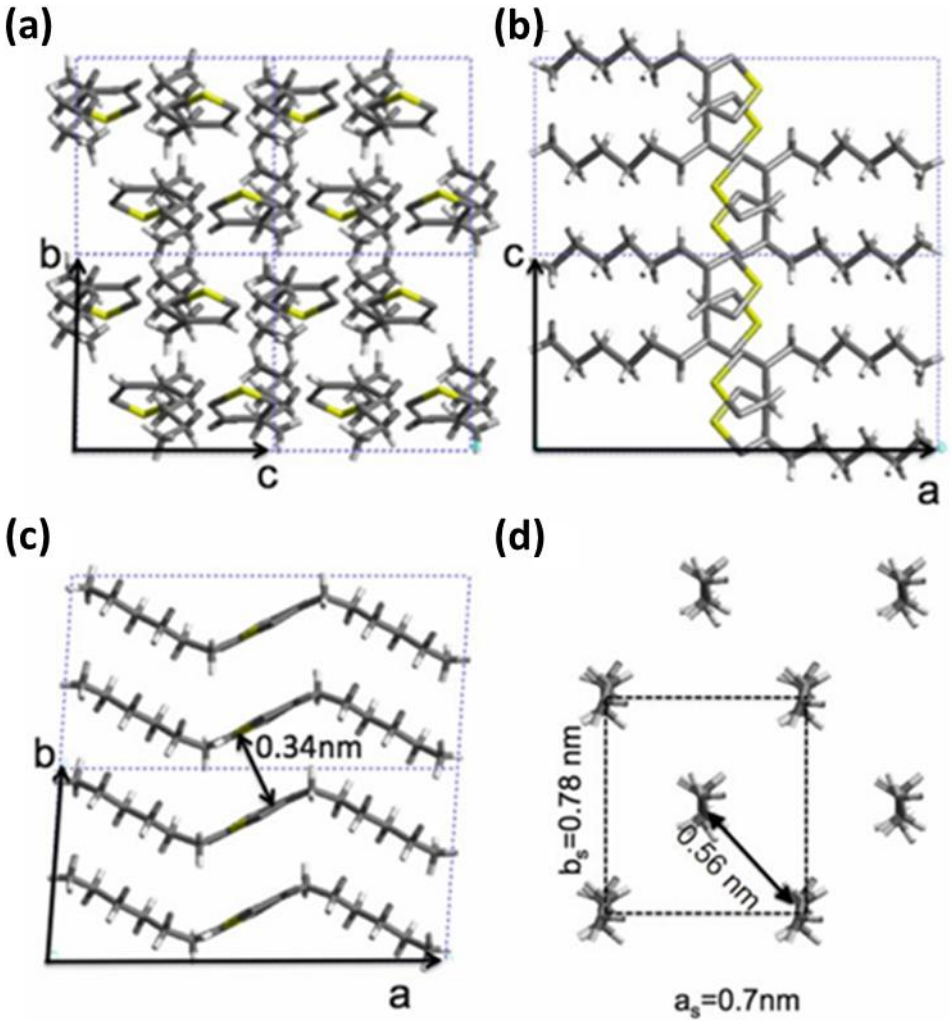

Figure 1.9. (**(a)-(c)**) Representation of the crystalline arrangement of P3HT along the principal *a*, *b*, and *c* directions of the monoclinic unit cell, illustrating backbone orientation and π–π stacking. **(d)** Monoclinic unit cell of P3HT, illustrating the organisation of the n-hexyl side chains within the crystalline framework. Adapted from [119].

RR-P3HT forms hierarchical nanostructures, including: (i) a π-π stacking distance of approximately 0.34 nm between adjacent RR-P3HT sheets; (ii) a backbone-to-backbone distance of 1.5 nm separated by alkyl side chains; and (iii) semi-crystalline sheets exhibiting a periodicity of ~28 nm, which form larger aggregates[120]. Furthermore, the amorphous regions of P3HT are composed of disordered end chains and tethered segments, which disrupt the crystalline order and contribute to the overall structural complexity, which can influence the electronic properties of the material (Figure 1.10)[113]. The degree of crystallinity and chain orientation in these structures can be controlled through processing conditions, such as solvent choice, temperature, and deposition technique[117].

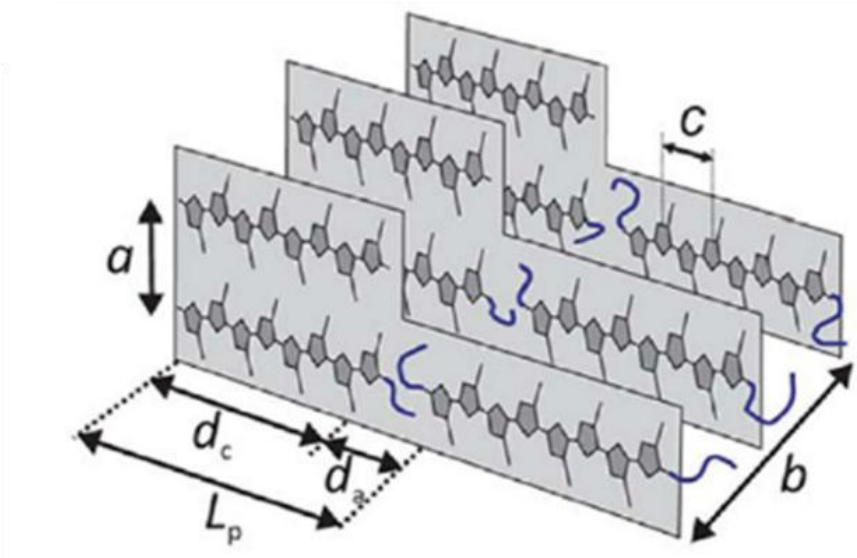

Figure 1.10. Schematic diagram illustrating the semi-crystalline architecture of regioregular P3HT. The unit cell dimensions *a*, *b* and *c* are indicated. d_c and d_a represent the thicknesses of the crystalline and amorphous lamellae, respectively. Their sum (L_p) defines the long period. Reprinted from the reference [121].

Despite the numerous advantages exhibited by P3HT, the polymer is also characterised by certain limitations and challenges that are the subject of ongoing research. A primary concern for the long-term application of this material pertains to its vulnerability to degradation, particularly photochemical and thermal degradation, a process that is exacerbated by the presence of oxygen and moisture[122–125]. On the other hand, the efficiency of P3HT-based devices depends largely on their morphology, molecular weight, and degree of crystallisation. It is limited by electron mobility and its tendency to aggregate, requiring careful processing techniques to ensure optimum performance. However, research continues to improve its properties through doping, copolymer synthesis, molecular structure modification, and new processing techniques.

1.5. Ferroelectric polymers

In addition to semiconducting polymers, another important class of functional polymers, ferroelectric materials, has emerged as a critical material due to their unique polarisation behaviour, with applications in electronic and electromechanical devices. Among the

ferroelectric polymers, poly(vinylidene fluoride) (PVDF) stands out due to its unique combination of processability, ferroelectricity, and chemical stability. This section introduces the concept of ferroelectricity in polymers and focuses on the structural characteristics of PVDF.

1.5.1. Ferrolectricity

A ferroelectric material is characterised by its ability to exhibit a spontaneous polarisation that can be reoriented by an external electric field, and which persists even after the field is removed (known as remanent polarisation)[126,127]. The direction of these electric dipoles can be reversed, or "flip-flopped", by applying an external electric field in the opposite direction. This process gives rise to characteristic hysteresis loops[128].

In order to comprehend these macroscopic electrical behaviours, it is necessary to investigate their microscopic origins, which are derived from the molecular design strategies employed to introduce permanent dipoles. In polymers, ferroelectricity emerges not from a rigid crystal lattice but from the cooperative alignment of molecular dipoles in semi-crystalline domains. In polymers, ferroelectricity does not arise from a rigid crystal lattice, but from the cooperative alignment of molecular dipoles in semicrystalline regions, especially in highly ordered phases such as the β-phase of PVDF[129]. Furthermore, the microscopic origin of ferroelectricity in polymers is primarily attributed to the presence of polar bonds and electric dipoles, typically generated by incorporating heteroatoms into the polymer backbone or side groups[129,130]. The generation of electric dipoles in these heteroatoms is attributable to differences in electronegativity. In particular, the incorporation of highly electronegative atoms, such as fluorine, in the PVDF, has been shown to commonly result in the creation of strong and stable local dipole moments[129]. These dipoles not only enhance the ferroelectric response but also improve the planarity of the polymer backbone due to strong intra- or inter-chain interactions and conformational rigidity, thereby promoting effective aggregation and crystallinity[130,131].

Moreover, ferroelectric polymers frequently exhibit piezoelectricity, a phenomenon in which these polymers undergo mechanical stress in response to an electric field, or conversely, generate an electric field in response to mechanical stress[91]. This phenomenon is a direct consequence of the change in dipole orientation and alignment in response to

external stimuli[19,20]. The piezoelectric behaviour exhibited by ferroelectric polymers is attributable to their non-centrosymmetric molecular structure, which facilitates dipolar reorientation in response to mechanical deformation or electrical excitation[17,132,133]. For instance, in PVDF, the β-phase is crucial for enabling the bidirectional electromechanical response[17,20]. Consequently, ferroelectric polymers have been identified as a potential solution for a variety of technological applications due to their reversible dipole behaviour and mechanical response. These properties are vital in the development of sensors, actuators, non-volatile memories (e.g., FeRAM), mechanical transducers, and energy-harvesting systems, especially where flexibility and lightweight materials are required, and more recently, in photocatalysis[21,22,132–135]. While the present thesis does not offer a direct characterisation of the piezoelectric or ferroelectric response of PVDF, it does direct attention towards the maximisation of electroactive crystalline phases, which are understood to manifest such behaviour. This phase-engineering approach provides the structural basis for future integration into functional devices.

1.5.2. Poly(vinylidene fluoride) (PVDF)

Poly(vinylidene fluoride) (PVDF) is a semi-crystalline polymer widely recognised for its exceptional properties, including high chemical resistance, thermal stability, excellent mechanical strength, flexibility, and durability[129]. Its molecular structure is composed of repetitive units of vinylidene fluoride or 1,1-difluoroethane (-CH_2-CF_2-), generates a strong electrical dipole due to the presence of alternating CH_2 y CF_2, particularly because of the low polarizability and strong electronegativity of fluorine as well as the small Van der Waals radius and robust C–F bonds (Figure 1.11)[135–137].

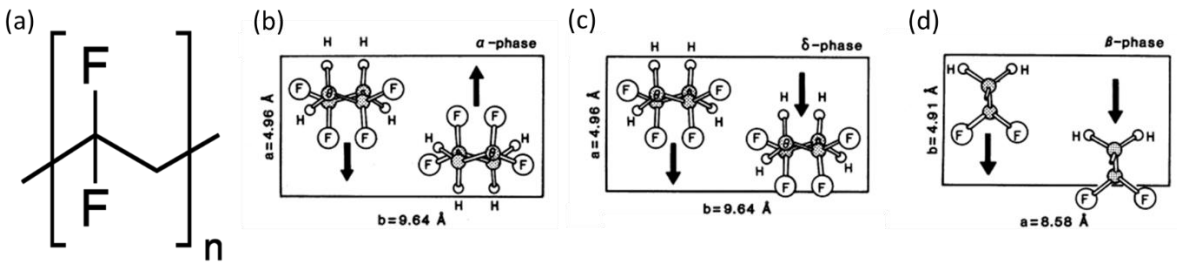

Figure 1.11. (a) Molecular structure of poly(vinylidene fluoride) (PVDF). **(b)** Crystalline configurations of PVDF in the α-phase (left), β-phase (centre) and γ-

phase (right), shown as projections of their respective unit cells onto the a-b plane. The arrows represent dipole moment orientation, which is perpendicular to the polymer chains and varies depending on phase symmetry and molecular conformation. The image in **(b)** is adapted from reference [129].

PVDF exhibits a T_g between -35℃ and -45℃ and a T_m between 167℃ and 190℃ depending on molecular weight and thermal history[17,135]. Its notable thermal stability, attributed to the strong C-F bond, allows PVDF to operate over a wide temperature range while maintaining its mechanical and electrical properties, crucial for demanding applications. In addition, this polymer is highly resistant to solvents, acids, bases, and UV radiation, making it highly suitable for corrosive environments, exterior coatings, and protective films. An outstanding property of PVDF is its piezoelectric, pyroelectric and ferroelectric behaviour, which allows it to generate an electrical current in response to mechanical stimuli or temperature changes[17].

1.5.2.1. Polymorphism and electroactive phase formation in PVDF

PVDF is typically 50-60% crystalline, comprising a mixture of ordered and disordered phases, and exhibits the ability to crystallise into five distinct polymorphic phases: α, β, γ, δ and ε[19,129,130,135,138–140]. Each phase has different electrical and mechanical properties that depend on the crystallisation conditions, such as heat treatments, mechanical stretching or chemical additives[128–130,141]. Due to the electronegativity of fluorine, which induces partially negatively charged zones near the fluorine atoms and positively charged zones in the hydrogen regions, there is a strong dipole moment perpendicular to the chain and parallel to the C-F bond[140]. The dipole moment per monomer is determined by the intrinsic properties of the repeating unit[140] and the overall chain conformation; during crystallisation, the additive effect of aligned dipoles within the unit cell gives rise to macroscopic ferroelectricity[19,129,130,135,136,138–140]. Only phases where the polymer chains are packed with parallel dipoles (e.g. β, γ and δ) possess a net dipole moment and thus exhibit ferroelectricity. Polar phases are characterised by a trans conformation and display piezoelectric, pyroelectric and ferroelectric properties[142], which depend on the fraction of electroactive phase, degree

of crystallinity, chain alignment and dipole moment. If they are antiparallel chain dipoles, as in α and ε, the moment disappears[138].

- α: It is the most thermodynamically stable phase and is characterised by the twist trans-gauché (*TGTG′*) conformational sequence[140]. This phase adopts a monoclinic crystal structure (Figure 1.11 (b)). The α phase is apolar and paraelectric since its dipole moments, with a magnitude of 1.3 Debye per monomer, are oriented in opposite directions and cancel each other out[129,140]. This configuration provides improved dielectric constant, mechanical properties and thermal stability, making it a robust material for various applications requiring stability and strength.
- β: It is particularly important because of its pronounced piezoelectric and ferroelectric properties[129,130,139,143,144]. This phase is characterised by an all-trans (*TTTT*) planar zigzag molecular conformation, with fluorine atoms aligned on the same side of the chain, resulting in a significant dipole moment of 2.1 Debye per monomer[139,140]. Its orthorhombic crystal structure and more extended chains contribute to a high degree of molecular order, unidirectional polarisation and electroactive behaviour (Figure 1.11 (b))[139]. While obtaining a high proportion of the pure β-phase can be challenging, various methods have been developed to enhance its formation. Notably, the dipole moment of the monomer increases by 50% as the chains transition into the crystalline state.
- γ: Exhibiting a conformational sequence T_3GT_3G' and can crystallise in either an orthorhombic or monoclinic structure with the same *a* and *b* axes but with a doubled *c* axis compared to α (Figure 1.11 (b))[140]. This phase is dipolar and electroactive, although it has a lower piezoelectricity than the other phases[145,146]. It is obtained by annealing the α phase or by crystallisation at high temperatures[140,147].
- δ and ε: These two phases are less common. The δ phase is characterised by being orthorhombic (*TG′TG*), and is a polar phase of α, formed by reorientation of the polymer chains, leading to an inversion of the dipolar component every two chains[136]. The ε phase has a T_3GT_3G' conformation and is characterised by being non-polar[140].

1.5.2.2. Formation of electroactive phases

Numerous strategies have been developed to encourage the development of electroactive phases, with a particular emphasis on the β-phase, through direct or indirect methods. Direct methods for the synthesis of the β-phase of PVDF include the blending of PVDF with small amounts of other polymers, such as poly(methyl methacrylate) (PMMA) or poly(o-methyloxyaniline) (POMA), thermal annealing, rapid quenching, and crystallisation under controlled conditions[138–141,143,144]. The use of additives such as ionic salts, zinc oxide (ZnO) NPs, or carbon nanotubes act as nucleating agents and also facilitate β-phase formation, although the effectiveness of these additives is highly dependent on concentration and dispersion[148]. Indirect methods involve the mechanical transformation of α-phase PVDF into β-phase through uniaxial stretching, compression, the application of electric fields, or solvent casting[138–140,144].

Among all these approaches, solvent-induced crystallisation has gained increasing attention due to its simplicity and effectiveness, especially for nanostructured PVDF. The role of solvent polarity in determining the crystalline phase of PVDF is critical. Polar solvents (e.g., dimethylacetamide (DMA), dimethyl sulfoxide (DMSO)) interact preferentially with the fluorine atoms in PVDF, thereby favouring the formation of electroactive phases (particularly the β and γ phases) through dipole-dipole interactions and hydrogen bonding that stabilise trans chain conformations[149–151]. Other studies have demonstrated that polar solvents with high dipole moments enhance electroactive phase crystallisation, especially at lower temperatures[142,150]. The use of binary or controlled solvent systems can further enhance phase inversion and improve electroactivity[150]. Additionally, the incorporation of additives such as mixed oxide of barium and titanium ($BaTiO_3$) facilitates the formation of the *TTTT* conformation through specific interactions with the polymer chains[139,148]. Therefore, these phenomena are particularly relevant at the nanoscale, where confinement effects and rapid solvent evaporation significantly affect the final crystal morphology. In PVDF NPs, this interaction can lead to enhanced formation of electroactive phases even in the absence of mechanical or electrical post-treatment. However, the precise mechanisms governing the interaction between the dipole of the solvent and β-phase of the PVDF structure remain an area of ongoing research, and uncontrolled processing conditions (including temperature, humidity, or polarisation field) can lead to structural defects or morphological instabilities.

Current research focuses on modifying the inherent properties of PVDF and developing new processing methods for innovative applications.

1.6. Preparation of nanoparticles

In the preceding decade, there has been a marked increase in the level of interest in the study of polymers in their nanostructured forms. This phenomenon can be attributed to the unique properties that emerge at the nanoscale, offering highly effective areas and other advantageous characteristics compared to the same polymer in bulk form[152,153]. Nanostructuring facilitates a more profound comprehension of the correlation between material nanostructure and its macroscopic properties[154,155], frequently resulting in considerably enhanced efficiencies, which is a prerequisite for the advancement of sophisticated electronic devices.

Furthermore, the precise control over nanostructure morphology can be achieved through various fabrication methods, notably self-assembly concepts[156]. Self-assembly offers distinct advantages over atomic manipulation due to less demanding fabrication steps, although much remains to be fully understood regarding its mechanisms.

In the field of polymer nanostructures, polymer NPs represent a particularly versatile and extensively studied morphology, offering numerous advantages. The primary advantages of this material are attributable to two key factors: firstly, confinement effects and, secondly, the large surface-to-volume ratio[152,157]. These factors can exert a significant influence on the thermal, mechanical, optical and electrical properties of the material.

Polymer NPs[158] are generally defined as colloidal systems with diameters ranging from 5 to 1000 nm, although the majority are found between 100 and 500 nm[159]. The categorisation of these entities typically falls into two classifications: nanospheres, defined as solid matrix particles, and nanocapsules, characterised as core-shell vesicles[159]. The fabrication of these entities can be accomplished through the utilisation of a singular polymer or a combination of multiple polymers, encompassing donor-acceptor blends and core-shell arrangements[6,158,160].

The morphology, size, and structure of polymer NPs can be precisely adjusted by controlling their preparation conditions, such as solvent polarity, polymer concentration, and

temperature[7,135,161,162]. This tunability is crucial, as the geometry of the nanostructure exerts a significant influence on various properties, including the geometric confinement of the electronic structure, catalytic activity, and optical properties. Furthermore, NPs facilitate the investigation of fundamental physical properties under 3D confinement, thereby providing insights into the intrinsic relationship between nanostructure and macroscopic behaviour[163,164].

In semicrystalline polymers such as P3HT and PVDF, NPs have been observed to exhibit smaller crystallites and increased grain boundaries, which have been shown to favour certain properties[165,166]. For example, this has been shown to favour certain properties; for instance, in photovoltaic devices[167], smaller crystallites and increased interfacial area in P3HT NPs reduce exciton diffusion lengths, enhancing charge separation. Similarly, in PVDF, controlled crystal size and grain boundaries can influence dipole alignment and domain switching dynamics, leading to an improved ferroelectric response in memory applications[168,169]. Furthermore, it has been demonstrated that chain orientation and crystallinity can be profoundly affected by nanoscale confinement, as this enhances charge transfer and produces smaller crystallites. For instance, for conjugated polymers such as P3HT, conductivity is highly anisotropic and sensitive to chain alignment[11,170]. Consequently, the nanoscale confinement facilitates precise calibration of these characteristics, thereby exerting a direct influence on the performance of the material.

Polymer NPs can be prepared in two principal approaches: polymerisation of monomers in a dispersed phase (in-situ polymerisation), or the reprocessing of previously synthesised polymers (post-polymerisation methods)[158,171,172]. In this thesis, the latter approach is employed, utilising solvent-based methods such as dialysis, flash nanoprecipitation and miniemulsion[158,163,173]. These methodologies offer advantages, including precise control over morphology, scalability and environmental compatibility, and have been successfully applied to polymers such as polystyrene, poly(ethyl methacrylate), P3HT and PVDF[6,163,164,170,173–175].

1.7. Applications of functional polymers

Functional polymers such as P3HT and PVDF have attracted significant attention across various scientific and technological fields due to their unique properties.

P3HT is a cornerstone material in organic electronics and optoelectronics. It exhibits properties that make it highly attractive for applications in organic electronics, including organic photovoltaics (OPVs), organic field-effect transistors (OFETs), OLEDs and photodetectors[15,16,108,176–180]. Additionally, its photophysical behaviour has enabled its exploration in photocatalysis and environmental remediation.

On the other hand, PVDF is used extensively in sensors, actuators, energy harvesting devices, and membranes for separation technologies[19,20,135,181–183]. The ability to tailor its crystalline phases through processing conditions opens up further potential in nanoelectronics and ferroelectric memory[18,19,135]. Moreover, the enhancement of electroactive phases such as β-PVDF has drawn significant interest for dielectric applications, including capacitive energy storage, where high dielectric constants can be achieved through phase engineering[184]. While the present work does not address functional dielectric testing, the structural optimisation reported herein provides a solid basis for future exploitation in such applications.

1.7.1. Photocatalysis with P3HT nanoparticles

The chemical decomposition of materials induced by light, or photodegradation, is a process increasingly harnessed through photocatalysis for environmental remediation. The potential of certain semiconducting polymers like P3HT to function as photocatalysts for the degradation of organic pollutants, including dyes such as MB, has attracted considerable attention. The process is fundamentally dependent on the capacity of the polymer to absorb light and generate excited states capable of initiating redox reactions.

This photodegradation process is shown in Figure 1.12. When the conjugated polymer, in this case P3HT, is irradiated, it absorbs light, leading to the formation of an exciton[88,103,185]. The efficiency of exciton formation and dissociation is significantly influenced by the molar extinction coefficient[88]. Following its formation, the exciton diffuses to the boundary of the absorbing material[88]. This migration is in direct competition with exciton recombination[88,185], the primary block for photocatalytic efficiency. The fate of the exciton is governed by various de-excitation processes. Kasha's rule stipulates that light absorption generates excited states, which subsequently rapidly deactivate to the lowest excited state (S_1 for singlets or T_1 for triplets) via non-radiative processes, such as intersystem crossing[96–98,103]. From these low-energy excited states, the exciton can either recombine or dissociate at the interface[88].

Recombination, which returns the system to its ground state by releasing energy as heat or light, can occur via geminate processes[186], where the electron–hole pair recombines before full separation, or via trap-assisted[187] pathways involving defects or impurities that capture one carrier before eventual recombination. Both routes reduce the population of free carriers available for photocatalytic activity.

If the exciton successfully reaches the surface of the NP and encounters other molecules (e.g., pollutant molecules or an acceptor), it can dissociate into free electrons and holes[88,185]. These free charge carriers subsequently participate in redox reactions, often generating highly reactive oxygen species (ROS) such as hydroxyl radicals (•OH) and superoxide anions ($O_2^{\bullet -}$), which degrade the contaminant molecules[188–191].

Consequently, the overall efficiency and yield of the photocatalytic process are intimately linked to the exciton diffusion length, recombination dynamics, and effective charge separation[186,187,192]. Minimising recombination losses requires morphologies that favour rapid exciton migration to interfaces and reduced trap densities, thereby prolonging carrier lifetimes[192,193]. Thus, efficient control of the nanoscale morphology of the polymer is crucial to maximise exciton dissociation and, ultimately, photocatalytic activity.

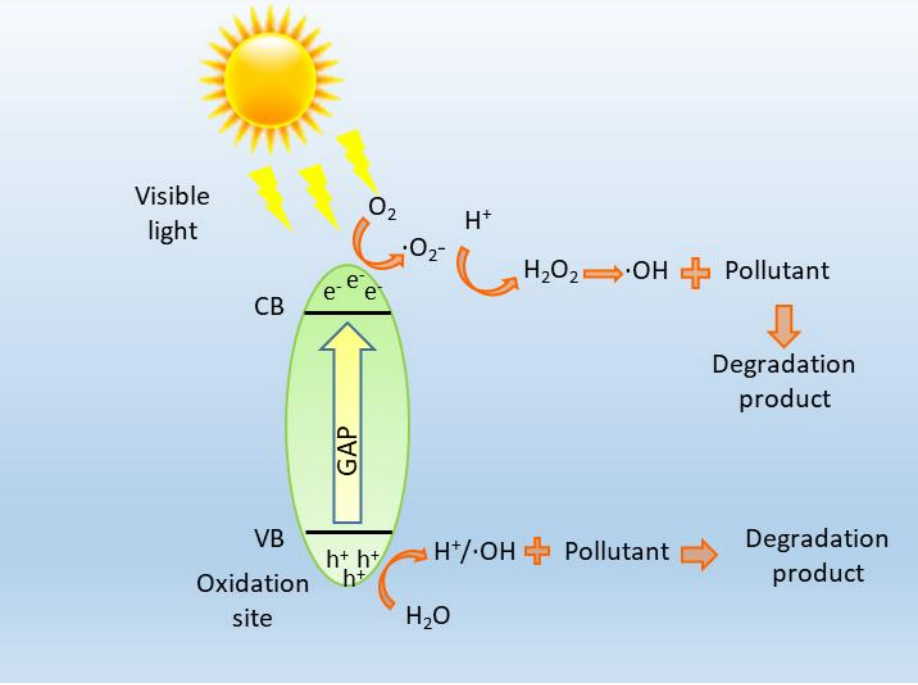

Figure 1.12. Schematic representation of the photodegradation process of a pollutant when using a semiconductor such as P3HT.

1.8. Main objectives and outline of the thesis

The overarching objective of this Doctoral Thesis is the preparation and characterisation of three-dimensional nanostructured polymer systems, specifically in the form of NPs, and the systematic study of their physical properties resulting from nanoscale confinement. The present study focuses on two functional polymers: P3HT, as a semiconducting polymer, and PVDF, as a ferroelectric polymer. This work aims to establish a fundamental understanding of how preparation methodologies and resulting nanoscale morphology dictate the structure-property relationships of these materials, with particular emphasis on crystallinity, morphology, and functional properties. Furthermore, the influence of processing conditions on the performance of these nanomaterials, particularly in areas like photocatalysis and ferroelectric response, is of particular interest.

To achieve this main objective, the present Thesis is structured into eight principal chapters:

- Chapter 2 provides a comprehensive overview of the experimental methodologies employed in this thesis. The text provides a comprehensive description of the materials employed, the NP preparation methods (including dialysis, flash nanoprecipitation, and miniemulsion), and the deposition strategies for NPs and deposit fabrication. It also includes a detailed account of the structural, morphological, and optical characterisation techniques utilised for the prepared systems, such as Atomic Force Microscopy (AFM), Dynamic Light Scattering (DLS), X-ray scattering, UV-Vis spectroscopy, fluorescence spectroscopy, time-resolved fluorescence microscopy (FLIM) and Fourier Transform Infrared spectroscopy (FTIR), along with the analysis methods, tools for data interpretation, and specifics of the photodegradation experiment.
- Chapter 3 presents a systematic study on the preparation and characterisation of P3HT NPs by the flash nanoprecipitation method. The influence of various key parameters such as polymer concentration, solvent/antisolvent ratio (R), and solution aging on the resulting NP morphology, structure, and optical properties is thoroughly evaluated. The study highlights the impact of processing parameters on nanoscale features and allows the identification of optimised P3HT NPs suitable for diverse applications, including photocatalysis.
- Chapter 4 is focused on the preparation of P3HT NPs by miniemulsion. The investigation focuses on the effect of sonication intensity (ultrasonic bath vs.

sonication probe at varying amplitudes) on the final physical properties, including NP size, morphology, crystallinity, and optical properties. The results are then compared with samples prepared without sonication in order to elucidate the critical role of this particular processing step. This will further guide the selection of optimal NPs for photocatalytic applications.

- Chapter 5 provides a comparative analysis of the P3HT NPs prepared by both flash nanoprecipitation (Chapter 3) and miniemulsion (Chapter 4). The study systematically examines the intrinsic differences between the two preparation methodologies, comparing the physicochemical properties of the precursor solutions and, more importantly, the resulting NP characteristics. Furthermore, FLIM is employed to gain further insight into the exciton dynamics and charge separation pathways. This chapter aims to identify the underlying causes and correlations of observed differences and to provide a more in-depth analysis of the physical processes that govern NP formation by each method.
- Chapter 6 addresses the preparation and phase control of water-dispersed PVDF NPs and deposits. This study focuses on the optimisation and maximisation of the ferroelectric β- and γ-phases through the manipulation of the solvent. The preparation of NPs is achieved through the utilisation of dialysis and flash microfluidics techniques, whereas the formation of deposits is obtained by means of solvent casting. The resulting structures are characterised by AFM, X-ray scattering, and FTIR to quantify the phase composition and assess the decisive role of the solvent in determining phase formation under different processing conditions. This chapter aims to provide insights into the control of ferroelectricity at the nanoscale.
- Chapter 7 provides a direct investigation of the photocatalytic activity of the prepared P3HT NPs under visible light irradiation, with a specific focus on MB degradation. This chapter explores how the distinct preparation conditions from Chapter 3 (e.g., aging effect for flash NPs) and Chapter 4 (e.g., sonication for miniemulsion NPs) influence the physical properties of the NPs and, consequently, their photocatalytic performance. The efficiency of the process will be evaluated by monitoring the decrease in MB concentration via UV-Vis spectroscopy and calculating kinetic constants. This will establish the link between nanoscale structure and photocatalytic functionality.

- Finally, conclusions synthesise the key findings from the experimental chapters, highlighting the most relevant structure–property relationships identified throughout the Thesis. The broader implications of this research for advanced applications (e.g., electronics, optoelectronics, environmental remediation) are discussed, and future research directions are outlined.

1.9. Bibliography

(1) Kumari, H.; Sonia; Suman; Ranga, R.; Chahal, S.; Devi, S.; Sharma, S.; Kumar, S.; Kumar, P.; Kumar, S.; Kumar, A.; Parmar, R. A Review on Photocatalysis Used For Wastewater Treatment: Dye Degradation. *Water Air Soil Pollut* **2023**, *234* (6). https://doi.org/10.1007/s11270-023-06359-9.

(2) Kolya, H.; Kang, C. W. Toxicity of Metal Oxides, Dyes, and Dissolved Organic Matter in Water: Implications for the Environment and Human Health. *Toxics* **2024**, *12* (2). https://doi.org/10.3390/toxics12020111.

(3) Khan, I.; Saeed, K.; Zekker, I.; Zhang, B.; Hendi, A. H.; Ahmad, A.; Ahmad, S.; Zada, N.; Ahmad, H.; Shah, L. A.; Shah, T.; Khan, I. Review on Methylene Blue: Its Properties, Uses, Toxicity and Photodegradation. *Water* **2022**, *14* (2). https://doi.org/10.3390/w14020242.

(4) Ismail, M.; Akhtar, K.; Khan, M. I.; Kamal, T.; Khan, M. A.; M. Asiri, A.; Seo, J.; Khan, S. B. Pollution, Toxicity and Carcinogenicity of Organic Dyes and Their Catalytic Bio-Remediation. *Curr Pharm Des* **2019**, *25* (34), 3645–3663. https://doi.org/10.2174/1381612825666191021142026.

(5) Welton, T. Solvents and Sustainable Chemistry. *Proceedings of the Royal Society A: Mathematical, Physical and Engineering Sciences* **2015**, *471* (2183), 26. https://doi.org/10.1098/rspa.2015.0502.

(6) Landfester, K.; Montenegro, R.; Scherf, U.; Güntner, R.; Asawapirom, U.; Patil, S.; Neher, D.; Kietzke, T. Semiconducting Polymer Nanospheres in Aqueous Dispersion Prepared by a Miniemulsion Process. *Advanced Materials* **2002**, *14* (9), 651–655. https://doi.org/10.1002/1521-4095(20020503)14:9<651::AID-ADMA651>3.0.CO;2-V.

(7) Nagarjuna, G.; Baghgar, M.; Labastide, J. A.; Algaier, D. D.; Barnes, M. D.; Venkataraman, D. Tuning Aggregation of Poly(3-Hexylthiophene) within Nanoparticles. *ACS Nano* **2012**, *6* (12), 10750–10758. https://doi.org/10.1021/nn305207b.

(8) Gutiérrez-Fernández, E.; Ezquerra, T. A.; Rebollar, E.; Cui, J.; Marina, S.; Martín, J.; Nogales, A. Photophysical and Structural Modulation of Poly(3-Hexylthiophene) Nanoparticles via Surfactant-Polymer Interaction. *Polymer* **2021**, *218*. https://doi.org/10.1016/j.polymer.2021.123515.

(9) Brus, L. E. Electron-Electron and Electron-Hole Interactions in Small Semiconductor Crystallites: The Size Dependence of the Lowest Excited Electronic State. *J Chem Phys* **1984**, *80* (9), 4403–4409. https://doi.org/10.1063/1.447218.

(10) Ghosh, S.; Chakraborty, S.; Ghosh, A.; Marjit, K.; Ghosh, G.; Patra, A. Ultrafast Relaxation Dynamics of Conjugated Polymer Nanoparticles by Tuning Their Interchain Interactions. *J Phys Chem C* **2022**, *126* (42), 18177–18187. https://doi.org/10.1021/acs.jpcc.2c06093.

(11) Heeger, A. J. Semiconducting Polymers: The Third Generation. *Chem Soc Rev* **2010**, *39* (7), 2354–2371. https://doi.org/10.1039/b914956m.

(12) Guo, X.; Facchetti, A. The Journey of Conducting Polymers from Discovery to Application. *Nat Mater* **2020**, *19* (9), 922–928. https://doi.org/10.1038/s41563-020-0778-5.

(13) Ding, L.; Yu, Z. Di; Wang, X. Y.; Yao, Z. F.; Lu, Y.; Yang, C. Y.; Wang, J. Y.; Pei, J. Polymer Semiconductors: Synthesis, Processing, and Applications. *Chem Rev* **2023**, *123* (12), 7421–7497. https://doi.org/10.1021/acs.chemrev.2c00696.

(14) Li, G.; Shrotriya, V.; Huang, J.; Yao, Y.; Moriarty, T.; Emery, K.; Yang, Y. High-Efficiency Solution Processable Polymer Photovoltaic Cells by Self-Organization of Polymer Blends. *Nat Mater* **2005**, *4* (11), 864–868. https://doi.org/10.1038/nmat1500.

(15) Brabec, C. J.; Heeney, M.; Mc Culloch, I.; Nelson, J. Influence of Blend Microstructure on Bulk Heterojunction Organic Photovoltaic Performance. *Chem Soc Rev* **2011**, *40* (3), 1185–1199. https://doi.org/10.1039/c0cs00045k.

(16) Ulum, S.; Holmes, N.; Darwis, D.; Burke, K.; David Kilcoyne, A. L.; Zhou, X.; Belcher, W.; Dastoor, P. Determining the Structural Motif of P3HT:PCBM Nanoparticulate Organic Photovoltaic Devices. *Solar Energy Materials and Solar Cells* **2013**, *110*, 43–48. https://doi.org/10.1016/j.solmat.2012.11.015.

(17) Sessler, G. M. Piezoelectricity in Polyvinylidenefluoride. *Journal of the Acoustical Society of America* **1981**, *70* (6), 1596–1608. https://doi.org/10.1121/1.387225.

(18) Naber, R. C. G.; Asadi, K.; Blom, P. W. M.; De Leeuw, D. M.; De Boer, B. Organic Nonvolatile Memory Devices Based on Ferroelectricity. *Advanced Materials* **2010**, *22* (9), 933–945. https://doi.org/10.1002/adma.200900759.

(19) Bauer, S.; Bauer, F. Piezoelectric Polymers and Their Applications. In *Piezoelectricity: Evolution and Future of a Technology*; Heywang, W., Lubitz, K., Wersing, W., Eds.; Springer: Berlin, 2008; Vol. 114, pp 157–177.

(20) Qi, F. X.; Xu, L.; He, Y.; Yan, H.; Liu, H. PVDF-Based Flexible Piezoelectric Tactile Sensors: Review. *Crystal Research and Technology* **2023**, *58* (10). https://doi.org/10.1002/crat.202300119.

(21) Nthunya, L. N.; Gutierrez, L.; Lapeire, L.; Verbeken, K.; Zaouri, N.; Nxumalo, E. N.; Mamba, B. B.; Verliefde, A. R.; Mhlanga, S. D. Fouling-Resistant PVDF Nanofibre Membranes for the Desalination of Brackish Water in Membrane Distillation. *Sep Purif Technol* **2019**, *228*. https://doi.org/10.1016/j.seppur.2019.115793.

(22) Kundu, S.; Karak, N. Polymeric Photocatalytic Membrane: An Emerging Solution for Environmental Remediation. *Chemical Engineering Journal* **2022**, *438*. https://doi.org/10.1016/j.cej.2022.135575.

(23) Chanda, M.; Roy, S. K. *Industrial Polymers, Specialty Polymers, and Their Applications*, 1st ed.; Taylor & Francis: Boca Raton, 2008. https://doi.org/10.1201/9781420080599.

(24) Strobl, G. *The Physics of Polymers: Concepts for Understanding Their Structures and Behavior*; Springer: Berlin, 2007. https://doi.org/10.1007/978-3-540-68411-4.

(25) Gompper, G.; Schick, M. *Soft Matter: Polymer Melts and Mixtures*, 1st ed.; John Wiley & Sons: New Jersey, 2006.

(26) Braun, D.; Cherdron, H.; Rehahn, M.; Ritter, H.; Voit, B. *Polymer Synthesis: Theory and Practice: Fundamentals, Methods, Experiments*; Springer: Wiesbaden, 2012. https://doi.org/10.1007/978-3-642-28980-4.

(27) Odian, G. *Principles of Polymerization*, 4th ed.; John Wiley & Sons: New Jersey, 2004. https://doi.org/10.1002/047147875X.

(28) Chang, R.; Overby, J. *General Chemistry: The Essential Concepts*, 6th ed.; McGraw-Hill: New York, 2010.

(29) Atkins, P.; de Paula, J. *Physical Chemistry*, 9th ed.; Oxford University Press: Oxford, 2009.

(30) Haynes, W. M. *Handbook of Chemistry and Physics*, 97th ed.; Taylor & Francis: New York, 2016.

(31) Lide, D. R. *CRC Handbook of Chemistry and Physics*, 88th ed.; Taylor & Francis: New York, 2007.

(32) Mark, J. E. *Physical Properties of Polymers Handbook*, 2nd ed.; Springer: New York, 2006.

(33) Tro, N. J. *Chemistry: A Molecular Approach*, 5th ed.; Pearson: London, 2019.

(34) Gedde, U. W. *Polymer Physics*, 1st ed.; Springer: Dordrecht, 1999. https://doi.org/10.1007/978-94-011-0543-9.

(35) Sperling, L. H. *Introduction to Physical Polymer Science*, 4th ed.; John Wiley & Sons: New York, 2005. https://doi.org/10.1002/0471757128.

(36) Prausnitz J. M.; Lichtenthaler, R. N.; de Azevedo, E. G. *Molecular Thermodynamics of Fluid-Phase Equilibria*, 3rd ed.; Pearson: London, 1998.

(37) Hildebrand, J. H.; Scott, R. L. *The Solubility of Nonelectrolytes*, 3rd ed.; Reinhold Publishing Corporation: New York, 1950; Vol. 55.

(38) Barton, A. F. M. . *Handbook of Solubility Parameters and Other Cohesion Parameters*; Taylor & Francis: Boca Raton, 1997.

(39) Rubinstein, M.; Colby, R. H. *Polymer Physics*; Oxford University Press: Oxford, 2003. https://doi.org/10.1093/oso/9780198520597.001.0001.

(40) Higgins, J. S.; Lipson, J. E. G.; White, R. P. A Simple Approach to Polymer Mixture Miscibility. *Philosophical Transactions of the Royal Society A: Mathematical, Physical and Engineering Sciences* **2010**, *368* (1914), 1009–1025. https://doi.org/10.1098/rsta.2009.0215.

(41) Hildebrand, J. H. The Entropy of Solution of Molecules of Different Size. *J Chem Phys* **1947**, *15* (5), 225–228. https://doi.org/10.1063/1.1746484.

(42) Ethier, J.; Antoniuk, E. R.; Brettmann, B. Predicting Polymer Solubility from Phase Diagrams to Compatibility: A Perspective on Challenges and Opportunities. *Soft Matter*. Royal Society of Chemistry July 8, 2024, pp 5652–5669. https://doi.org/10.1039/d4sm00590b.

(43) Small, P. A. Some Factors Affecting the Solubility of Polymers. *Journal of Applied Chemistry* **1953**, *3* (2), 71–80. https://doi.org/10.1002/jctb.5010030205.

(44) Burrell H. Solubility Parameters. *Interchemistry Review* **1955**.

(45) Burrell, H. Trends in Solvent Science and Technology. *Advances in Chemistry Series* **1973**, No. 124, 10.

(46) Crowley, J. D.; Teague, G. S.; Lowe, J. W. A Three Dimensional Approach to Solubility. *Journal of Paint Technology* **1966**, *38* (496).

(47) Blanks, R. F.; Prausnitz, J. M. Thermodynamics of Polymer Solubility in Polar and Nonpolar Systems. *Industrial & Engineering Chemistry Fundamentals* **1964**, *3* (1). https://doi.org/10.1021/i160009a001.

(48) Hansen, C. M. The Universality of the Solubility Parameter. *Industrial & Engineering Chemistry Product Research and Development* **1969**, *8* (1), 2–11.

(49) Hansen, C. M. *Hansen Solubility Parameters*, 2nd ed.; Taylor and Francis: Boca Raton, 2007.

(50) Chanda, Manas. *Introduction to Polymer Science and Chemistry : A Problem-Solving Approach*, 2nd ed.; Taylor & Francis: Boca Raton, 2013. https://doi.org/https://doi.org/10.1201/b14577.

(51) Fitch, R. M. *Polymer Colloids: A Comprehensive Introduction*, 1st ed.; Academic Press: New York, 1997.

(52) Nogales, A.; Ezquerra, T. A.; Denchev, Z.; Šics, I.; Baltá Calleja, F. J.; Hsiao, B. S. Molecular Dynamics and Microstructure Development during Cold Crystallization in Poly(Ether-Ether-Ketone) as Revealed by Real Time Dielectric and x-Ray Methods. *J Chem Phys* **2001**, *115* (8), 3804–3813. https://doi.org/10.1063/1.1388627.

(53) *Handbook of Conducting Polymers*, 3th ed.; Skotheim, T. A., Reynolds, J., Eds.; Taylor & Francis: Boca Raton, 2007; Vol. 2.

(54) Avrami, M. Kinetics of Phase Change. I: General Theory. *J Chem Phys* **1939**, *7* (12), 1103–1112. https://doi.org/10.1063/1.1750380.

(55) Wunderlich, B. *Macromolecular Physics*; Academic Press: New York, 1976; Vol. 2. https://doi.org/10.1016/B978-0-12-765601-4.X5001-X.

(56) Ergoz, E.; Fatou, J. G.; Mandelkern, L. Molecular Weight Dependence of the Crystallization Kinetics of Linear Polyethylene. I. Experimental Results. *Macromolecules* **1972**, *5* (2), 147–157. https://doi.org/10.1021/MA60026A011.

(57) Voight-Martin, I. G.; Mandelkern, L. Quantitative Electron-Microscopic Study of a Linear Polyethylene Fraction Cystallized at Different Temperatures. *Journal of Polymer Science: Part A-Polymer Physics* **1981**, *19* (11), 1769–1790. https://doi.org/10.1002/pol.1981.180191109.

(58) Larbi, F. B.; Hert, M.; Grenier, M.-F.; Rault, J. Assessment of Long Branches in Free Radical Polyethylene: Correlation between the Melt and Solid States. *Macromolecules* **1985**, *18* (2), 164–170. https://doi.org/10.1021/ma00144a009.

(59) Avrami, M. Granulation, Phase Change, and Microstructure Kinetics of Phase Change. III. *J Chem Phys* **1941**, *9* (2), 177–184. https://doi.org/10.1063/1.1750872.

(60) Yamamoto, T. Computer Modeling of Polymer Crystallization - Toward Computer-Assisted Materials' Design. *Polymer* **2009**, *50* (9), 1975–1985. https://doi.org/10.1016/j.polymer.2009.02.038.

(61) Hancock, B. C.; Shamblin, S. L. Molecular Mobility of Amorphous Pharmaceuticals Determined Using Differential Scanning Calorimetry. *Thermochim Acta* **2001**, *380*, 95–107. https://doi.org/10.1016/S0040-6031(01)00663-3.

(62) Bernstein, J. *Polymorphism in Molecular Crystals*, 2nd ed.; International Union of Crystallography: Oxford, 2007. https://doi.org/10.1093/acprof:oso/9780199236565.001.0001.

(63) Danusso, F. Macromolecular Polymorphism and Stereoregular Synthetic Polymers. *Polymer* **1967**, *8*, 281–320. https://doi.org/10.1016/0032-3861(67)90031-6.

(64) Till, P. H. The Growth of Single Crystals of Linear Polyethylene. *Journal of Polymer Science Part B-Polymer Physics* **1957**, *24* (106), 301–306. https://doi.org/10.1002/pol.1957.1202410616.

(65) Keller, A. A Note on Single Crystals in Polymers - Evidence for a Folded Chain Configuration. *Philosophical Magazine* **1957**, *2* (21). https://doi.org/10.1080/14786435708242746.

(66) Mandelkern, L. Relation Between Properties and Molecular Morphology of Semicrystalline Polymers. *Faraday Discuss Chem Soc* **1979**, *68*, 310–319. https://doi.org/10.1039/DC9796800310.

(67) Unversity of Cambridge. *Spherulites and optical properties*. https://www.doitpoms.ac.uk/tlplib/polymers/spherulites.php (accessed 2025-06-17).

(68) Hu, W. *Polymer Physics*, 1st ed.; Springer Vienna: Vienna, 2013. https://doi.org/10.1007/978-3-7091-0670-9.

(69) Callister Jr, W. D.; Rethwisch, D. G. *Materials Science and Engineering An Introduction*, 10th ed.; Wiley: London, 2018.

(70) Noriega, R.; Rivnay, J.; Vandewal, K.; Koch, F. P. V.; Stingelin, N.; Smith, P.; Toney, M. F.; Salleo, A. A General Relationship between Disorder, Aggregation and Charge Transport in Conjugated Polymers. *Nat Mater* **2013**, *12* (11), 1038–1044. https://doi.org/10.1038/nmat3722.

(71) Avrami, M. Kinetics of Phase Change. II Transformation-Time Relations for Random Distribution of Nuclei. *J Chem Phys* **1940**, *8* (2), 212–224. https://doi.org/10.1063/1.1750631.

(72) Park, W. I.; Kim, D. H.; Jung, J.; Hong, S. W.; Lin, Z.; Byun, M. Spatially Ordered Poly(3-Hexylthiophene) Fibril Nanostructures via Controlled Evaporative Self-Assembly. *Adv Mater Technol* **2019**, *4* (1). https://doi.org/10.1002/admt.201800554.

(73) Lu, H.; Chang, C. H.; Wu, B. R.; Wu, N. C.; Liang, J. Z.; Dai, C. A.; Yang, A. C. M. Reaching Nearly 100% Quantum Efficiencies in Thin Solid Films of Semiconducting Polymers via Molecular Confinements under Large Segmental Stresses. *ACS Nano* **2022**, *16* (5), 8273–8282. https://doi.org/10.1021/acsnano.2c02083.

(74) Yu, D.; Ding, S.; Li, J.; Mi, W.; Tian, Y.; Hu, W. Molecular Spinterface in F4TCNQ-Doped Polymer Spin Valves. *J Mater Chem C Mater* **2022**, *10* (7), 2608–2615. https://doi.org/10.1039/d1tc04259a.

(75) Tsokkou, D.; Cavassin, P.; Rebetez, G.; Banerji, N. Bipolarons Rule the Short-Range Terahertz Conductivity in Electrochemically Doped P3HT. *Mater Horiz* **2022**, *9* (1), 482–491. https://doi.org/10.1039/d1mh01343b.

(76) Cho, J.; Yoon, S.; Min Sim, K.; Jin Jeong, Y.; Eon Park, C.; Kwon, S. K.; Kim, Y. H.; Chung, D. S. Universal Selection Rule for Surfactants Used in Miniemulsion Processes for Eco-Friendly and High Performance Polymer Semiconductors. *Energy Environ Sci* **2017**, *10* (11), 2324–2333. https://doi.org/10.1039/c7ee01943b.

(77) Shirakawa, H.; Louis, E. J.; Macdiarmid, A. G.; Chiang, C. H.; Heegerr, A. J. Synthesis of Electrically Conducting Organic Polymers : Halogen Derivatives of Polyacetylene, (CH)X. *Journal of the Chemical Society-Chemical Communications* **1977**, *16*, 578–580. https://doi.org/10.1039/c39770000578.

(78) Facchetti, A. π-Conjugated Polymers for Organic Electronics and Photovoltaic Cell Applications. *Chemistry of Materials* **2011**, *23* (3), 733–758. https://doi.org/10.1021/cm102419z.

(79) Sirringhaus, H. 25th Anniversary Article: Organic Field-Effect Transistors: The Path beyond Amorphous Silicon. *Advanced Materials* **2014**, *26* (9), 1319–1335. https://doi.org/10.1002/adma.201304346.

(80) Norman, J. W.; Sun, S. S. A Potential Dual-Functional Thermoelectric and Electroelectric Polymer Composite. *Mater Lett* **2022**, *308*. https://doi.org/10.1016/j.matlet.2021.131263.

(81) Cai, Y.; Wei, Z.; Song, C.; Tang, C.; Han, W.; Dong, X. Optical Nano-Agents in the Second near-Infrared Window for Biomedical Applications. *Chem Soc Rev* **2019**, *48* (1), 22–37. https://doi.org/10.1039/c8cs00494c.

(82) Burroughes, J. H.; Bradley, D. D. C.; Brown, A. R.; Marks, R. N.; Mackay, K.; Friend, R. H.; Burn, P. L.; Holmes, A. B. Light-Emitting Diodes Based on Conjugated Polymers. *Nature* **1990**, *347* (6293), 539–541.

(83) Samuel, I. D. W.; Turnbull, G. A. Polymer Lasers: Recent Advances. *Materials Today* **2004**, *7* (9), 28–35.

(84) Tessler, N.; Denton, G. J.; Friend, R. H. Lasing from Conjugated-Polymer Microcavities. *Nature* **1996**, *382* (6593), 695–697.

(85) Hide, F.; Diaz-Garcia, M. A.; Schwartz, B. J.; Andersson, M. R.; Pei, Q.; Heeger, A. J. Semiconducting Polymers: A New Class of Solid-State Laser Materials. *Science (1979)* **1996**, *273* (5283), 1833–1836.

(86) Tyler McQuade, D.; Pullen, A. E.; Swager, T. M. Conjugated Polymer-Based Chemical Sensors. *Chem Rev* **2000**, *100* (7), 2537–2574. https://doi.org/10.1021/cr9801014.

(87) Liu, Y.; Bhattarai, P.; Dai, Z.; Chen, X. Photothermal Therapy and Photoacoustic Imaging: Via Nanotheranostics in Fighting Cancer. *Chem Soc Rev* **2019**, *48* (7), 2053–2108. https://doi.org/10.1039/c8cs00618k.

(88) Günes, S.; Neugebauer, H.; Sariciftci, N. S. Conjugated Polymer-Based Organic Solar Cells. *Chem Rev* **2007**, *107* (4), 1324–1338. https://doi.org/10.1021/cr050149z.

(89) Babel, A.; Zhu, Y.; Cheng, K. F.; Chen, W. C.; Jenekhe, S. A. High Electron Mobility and Ambipolar Charge Transport in Binary Blends of Donor and Acceptor Conjugated Polymers. *Adv Funct Mater* **2007**, *17* (14), 2542–2549. https://doi.org/10.1002/adfm.200600312.

(90) Chenming, H. *Modern Semiconductor Devices for Integrated Circuits*, 1st ed.; Prentice Hall, Ed.; Pearson: London, 2009.

(91) Kittel, C. *Introduction to Solid State Physics*, 8th ed.; John Wiley & Sons Inc: New Calcedonia, 2005.

(92) Le, T.-H.; Yoon, H. Fundamentals of Conjugated Polymer Nanostructures. In *Conjugated Polymer Nanostructures for Energy Conversion and Storage Applications*; Ghosh, S., Ed.; Wiley: Weinheim, 2021. https://doi.org/10.1002/9783527820115.ch1.

(93) Fulay, P.; Lee, J.-K. *Electronic, Magnetic, and Optical Materials*, 2nd ed.; Taylor & Francis: Boca Raton, 2016. https://doi.org/10.1201/9781315371870.

(94) Salleo, A. Charge Transport in Polymeric Transistors. *Materials Today* **2007**, *10* (3), 38–45. https://doi.org/10.1016/S1369-7021(07)70018-4.

(95) Sirringhaus, H.; Brown, P. J.; Friend, R. H.; Nielsen, M. M.; Bechgaard, K.; Langeveld-Voss, B. M. W.; Spiering, A. J. H.; Janssen, R. A. J.; Meijer, E. W.; Herwig, P.; De Leeuw, D. M. Two-Dimensional Charge Transport in Self-Organized, High-Mobility Conjugated Polymers. *Nature* **1999**, *401*, 4.

(96) Kasha, M. Relation Between Exciton Bands and Conduction Bands in Molecular Lamellar Systems. *Rev Mod Phys* **1959**, *31* (1), 162–169. https://doi.org/10.1103/RevModPhys.31.162.

(97) Kasha, M. Energy Transfer Mechanisms and the Molecular Exciton Model for Molecular Aggregates. *Radiat Res* **1963**, *20* (1), 55–71. https://doi.org/10.2307/3571331.

(98) Kasha, M.; Rawls, H. R.; Ashraf El-Bayoumi, M. The Exciton Model in Molecular Spectroscopy. *Pure and Applied Chemistry* **1965**, *11*, 371–392.

(99) Spano, F. C. The Spectral Signatures of Frenkel Polarons in H- And J-Aggregates. *Acc Chem Res* **2010**, *43* (3), 429–439. https://doi.org/10.1021/ar900233v.

(100) Yamagata, H.; Spano, F. C. Interplay between Intrachain and Interchain Interactions in Semiconducting Polymer Assemblies: The HJ-Aggregate Model. *J Chem Phys* **2012**, *136* (18). https://doi.org/10.1063/1.4705272.

(101) Manas, E. S.; Spano, F. C. Absorption and Spontaneous Emission in Aggregates of Conjugated Polymers. *J Chem Phys* **1998**, *109* (18), 8087–8101. https://doi.org/10.1063/1.477457.

(102) Spano, F. C.; Silva, C. H- and J-Aggregate Behavior in Polymeric Semiconductors. *Annu Rev Phys Chem* **2014**, *65*, 477–500. https://doi.org/10.1146/annurev-physchem-040513-103639.

(103) Clark, J.; Silva, C.; Friend, R. H.; Spano, F. C. Role of Intermolecular Coupling in the Photophysics of Disordered Organic Semiconductors: Aggregate Emission in Regioregular Polythiophene. *Phys Rev Lett* **2007**, *98* (20). https://doi.org/10.1103/PhysRevLett.98.206406.

(104) Clark, J.; Chang, J. F.; Spano, F. C.; Friend, R. H.; Silva, C. Determining Exciton Bandwidth and Film Microstructure in Polythiophene Films Using Linear Absorption Spectroscopy. *Appl Phys Lett* **2009**, *94* (16). https://doi.org/10.1063/1.3110904.

(105) Mosconi, E.; Salvatori, P.; Saba, M. I.; Mattoni, A.; Bellani, S.; Bruni, F.; Santiago Gonzalez, B.; Antognazza, M. R.; Brovelli, S.; Lanzani, G.; Li, H.; Brédas, J. L.; De Angelis, F. Surface Polarization Drives Photoinduced Charge Separation at the P3HT/Water Interface. *ACS Energy Lett* **2016**, *1* (2), 454–463. https://doi.org/10.1021/acsenergylett.6b00197.

(106) Fichou, D. *Handbook of Oligo- and Polythiophenes*; Wiley-VCH: Verlag, 1998. https://doi.org/10.1002/9783527611713.

(107) Yamamoto, T.; Sanechika, K.; Yamamoto, A. Preparation and Characterization of Poly(Thienylene)s. *Bull Chem Soc Jpn* **1983**, *56* (5), 1497–1502. https://doi.org/10.1246/bcsj.56.1497.

(108) Zhu, M.; He, B.; Zhang, K.; Hussain, S.; Li, T. Recent Progress of Poly(3-Hexylthiophene)-Based Materials for Thermoelectric Applications. *Mater Chem Front* **2024**, *8* (13), 2454–2492. https://doi.org/10.1039/d4qm00213j.

(109) Pappenfus, T. M.; Hermanson, D. L.; Kohl, S. G.; Melby, J. H.; Thoma, L. M.; Carpenter, N. E.; Da Silva Filho, D. A.; Bredas, J. L. Regiochemistry of Poly(3-Hexylthiophene): Synthesis and Investigation of a Conducting Polymer. *J Chem Educ* **2010**, *87* (5), 522–525. https://doi.org/10.1021/ed800144p.

(110) Chen, T.-A.; Wu, X.; Rieke, R. D. Regiocontrolled Synthesis of Poly(3-Alkylthiophenes) Mediated by Rieke Zinc: Their Characterization and Solid-State Properties. *J Am Chem Soc* **1995**, *117* (1), 233–244. https://doi.org/10.1021/ja00106a027.

(111) Howard, I. A.; Laquai, F. Optical Probes of Charge Generation and Recombination in Bulk Heterojunction Organic Solar Cells. *Macromol Chem Phys* **2010**, *211* (19), 2063–2070. https://doi.org/10.1002/macp.201000353.

(112) Coropceanu, V.; Cornil, J.; da Silva Filho, D. A.; Olivier, Y.; Silbey, R.; Brédas, J. L. Charge Transport in Organic Semiconductors. *Chem Rev* **2007**, *107* (4), 926–952. https://doi.org/10.1021/cr050140x.

(113) Brinkmann, M.; Wittmann, J. C. Orientation of Regioregular Poly(3-Hexylthiophene) by Directional Solidification: A Simple Method to Reveal the Semicrystalline Structure of a Conjugated Polymer. *Advanced Materials* **2006**, *18* (7), 860–863. https://doi.org/10.1002/adma.200501838.

(114) O'Connor, B.; Kline, R. J.; Conrad, B. R.; Richter, L. J.; Gundlach, D.; Toney, M. F.; DeLongchamp, D. M. Anisotropic Structure and Charge Transport in Highly Strain-Aligned Regioregular Poly(3-Hexylthiophene). *Adv Funct Mater* **2011**, *21* (19), 3697–3705. https://doi.org/10.1002/adfm.201100904.

(115) Zhu, H.; Gong, L.; Li, Z. Construction and Mechanism of a Novel Z-Scheme Photocatalyst α-Fe2O3/P3HT with O-Ti-O for Organic Pollutant Degradation under Visible Light. *Appl Surf Sci* **2020**, *505*. https://doi.org/10.1016/j.apsusc.2019.144639.

(116) Floresyona, D.; Goubard, F.; Aubert, P. H.; Lampre, I.; Mathurin, J.; Dazzi, A.; Ghosh, S.; Beaunier, P.; Brisset, F.; Remita, S.; Ramos, L.; Remita, H. Highly Active Poly(3-Hexylthiophene) Nanostructures for Photocatalysis under Solar Light. *Appl Catal B* **2017**, *209*, 23–32. https://doi.org/10.1016/j.apcatb.2017.02.069.

(117) Chen, J. H.; Li, J. Y.; Chen, L. C.; Su, C. I. Morphology and Microstructure of Aggregates and Gelation Behaviour of Poly (3-Hexylthiophene) in Xylene Solution. In *Applied Mechanics and Materials*; 2014; Vol. 479–480, pp 115–120. https://doi.org/10.4028/www.scientific.net/AMM.479-480.115.

(118) Brinkmann, M.; Rannou, P. Effect of Molecular Weight on the Structure and Morphology of Oriented Thin Films of Regioregular Poly(3-Hexylthiophene) Grown by Directional Epitaxial Solidification. *Adv Funct Mater* **2007**, *17* (1), 101–108. https://doi.org/10.1002/adfm.200600673.

(119) Kayunkid, N.; Uttiya, S.; Brinkmann, M. Structural Model of Regioregular Poly(3-Hexylthiophene) Obtained by Electron Diffraction Analysis. *Macromolecules* **2010**, *43* (11), 4961–4967. https://doi.org/10.1021/ma100551m.

(120) Prosa, T. J.; Winokur, M. J.; Moulton, J.; Smith, P.; Heegert, A. J. X-Ray Structural Studies of Poly(3-Alkylthiophenes): An Example of an Inverse Comb. *Macromolecules* **1992**, *25*, 4364–4372. https://doi.org/10.1021/ma00043a019.

(121) Müller-Buschbaum, P. The Active Layer Morphology of Organic Solar Cells Probed with Grazing Incidence Scattering Techniques. *Advanced Materials* **2014**, *26* (46), 7692–7709. https://doi.org/10.1002/adma.201304187.

(122) Cao, H.; He, W.; Mao, Y.; Lin, X.; Ishikawa, K.; Dickerson, J. H.; Hess, W. P. Recent Progress in Degradation and Stabilization of Organic Solar Cells. *J Power Sources* **2014**, *264*, 168–183. https://doi.org/10.1016/j.jpowsour.2014.04.080.

(123) Grossiord, N.; Kroon, J. M.; Andriessen, R.; Blom, P. W. M. Degradation Mechanisms in Organic Photovoltaic Devices. *Org Electron* **2012**, *13* (3), 432–456. https://doi.org/10.1016/j.orgel.2011.11.027.

(124) Jørgensen, M.; Norrman, K.; Krebs, F. C. Stability/Degradation of Polymer Solar Cells. *Solar Energy Materials and Solar Cells* **2008**, *92* (7), 686–714. https://doi.org/10.1016/j.solmat.2008.01.005.

(125) Mateker, W. R.; McGehee, M. D. Progress in Understanding Degradation Mechanisms and Improving Stability in Organic Photovoltaics. *Advanced Materials* **2017**, *29* (10). https://doi.org/10.1002/adma.201603940.

(126) Dawber, M.; Rabe, K. M.; Scott, J. F. Physics of Thin-Film Ferroelectric Oxides. *Rev Mod Phys* **2005**, *77*, 1083–30. https://doi.org/10.1103/RevModPhys.77.1083.

(127) Furukawa, T. Structure and Functional Properties of Ferroelectric Polymers. *Adv Colloid Interface Sci* **1997**, *71* (2), 183–208. https://doi.org/10.1016/S0001-8686(97)90017-8.

(128) Furukawa, T.; Date, M.; Fukada, E. Hysteresis Phenomena in Polyvinylidene Fluoride under High Electric Field. *J Appl Phys* **1980**, *51* (2), 1135–1141. https://doi.org/10.1063/1.327723.

(129) Lovinger, A. J. Ferroelectric Polymers. *Science (1979)* **1983**, *220* (4602), 1115–1121. https://doi.org/10.1126/science.220.4602.1115.

(130) Nalwa, H. S. *Ferroelectric Polymers: Chemistry, Physics and Applications*, 1st ed.; Taylor & Francis: Boca Raton, 1995. https://doi.org/10.1201/9781482295450.

(131) Cessac, G. L.; Curro, J. G. Raman Scattering in Uniaxially Oriented Samples of Planar Zigzag Poly(Vinylidiene Fluoride). *Journal of Polymer Science Part B-Polymer Physics* **1974**, *12* (4), 695–702. https://doi.org/10.1002/pol.1974.180120406.

(132) Vijayakanth, T.; Liptrot, D. J.; Gazit, E.; Boomishankar, R.; Bowen, C. R. Recent Advances in Organic and Organic–Inorganic Hybrid Materials for Piezoelectric Mechanical Energy Harvesting. *Adv Funct Mater* **2022**, *32* (17). https://doi.org/10.1002/adfm.202109492.

(133) Liang, Z.; Yan, C. F.; Rtimi, S.; Bandara, J. Piezoelectric Materials for Catalytic/Photocatalytic Removal of Pollutants: Recent Advances and Outlook. *Appl Catal B* **2019**, *241*, 256–269. https://doi.org/10.1016/j.apcatb.2018.09.028.

(134) Scott, J. F. Applications of Modern Ferroelectrics. *Science (1979)* **2007**, *315* (5814), 954–959. https://doi.org/10.1126/science.1129564.

(135) Martins, P.; Lopes, A. C.; Lanceros-Mendez, S. Electroactive Phases of Poly(Vinylidene Fluoride): Determination, Processing and Applications. *Prog Polym Sci* **2014**, *39* (4), 683–706. https://doi.org/10.1016/j.progpolymsci.2013.07.006.

(136) Li, M.; Wondergem, H. J.; Spijkman, M. J.; Asadi, K.; Katsouras, I.; Blom, P. W. M.; De Leeuw, D. M. Revisiting the δ-Phase of Poly(Vinylidene Fluoride) for Solution-Processed Ferroelectric Thin Films. *Nat Mater* **2013**, *12* (5), 433–438. https://doi.org/10.1038/nmat3577.

(137) Tocci, E.; Rizzuto, C.; Macedonio, F.; Drioli, E. Effect of Green Solvents in the Production of PVDF-Specific Polymorphs. *Ind Eng Chem Res* **2020**, *59* (12), 5267–5275. https://doi.org/10.1021/acs.iecr.9b06701.

(138) Sencadas, V.; Gregorio, R.; Lanceros-Méndez, S. α to β Phase Transformation and Microestructural Changes of PVDF Films Induced by Uniaxial Stretch. *Journal of Macromolecular Science, Part B: Physics* **2009**, *48* (3), 514–525. https://doi.org/10.1080/00222340902837527.

(139) Ruan, L.; Yao, X.; Chang, Y.; Zhou, L.; Qin, G.; Zhang, X. Properties and Applications of the β Phase Poly(Vinylidene Fluoride). *Polymers* **2018**, *10* (3), 1–27. https://doi.org/10.3390/polym10030228.

(140) Martins, P.; Lopes, A. C.; Lanceros-Mendez, S. Electroactive Phases of Poly(Vinylidene Fluoride): Determination, Processing and Applications. *Prog Polym Sci* **2014**, pp 683–706. https://doi.org/10.1016/j.progpolymsci.2013.07.006.

(141) Roopa, T. S.; Murthy, H. N. N.; Bandgar, K.; Harish, D. V. N.; Angadi, G. Improving Beta Phase of Spin Coated PVDF Thin Films by Doping with Silver Nanoparticles. *Ferroelectrics* **2023**, *613* (1), 194–201. https://doi.org/10.1080/00150193.2023.2215513.

(142) Li, X.; Wang, Y.; He, T.; Hu, Q.; Yang, Y. Preparation of PVDF Flexible Piezoelectric Film with High β-Phase Content by Matching Solvent Dipole Moment and Crystallization Temperature. *Journal of Materials Science: Materials in Electronics* **2019**, *30* (22), 20174–20180. https://doi.org/10.1007/s10854-019-02400-y.

(143) Oflaz, K.; Özaytekin, İ.; Sadasivuni, K. K. Enhancing the Piezoelectric Performance of Composite PVDF Flexible Films through Optimizing β Phase Content, Investigating Additive Effects, Step-Wise Polarization, and Thermal Pressing Time for Energy Harvesting Applications. *J Appl Polym Sci* **2024**, *141* (25). https://doi.org/10.1002/app.55530.

(144) Zhang, X.; Xia, W.; Liu, J.; Zhao, M.; Li, M.; Xing, J. PVDF-Based and Its Copolymer-Based Piezoelectric Composites: Preparation Methods and Applications. *J Electron Mater* **2022**, *51* (10), 5528–5549. https://doi.org/10.1007/s11664-022-09825-y.

(145) Kaeopisan, A.; Thanachayanon, C.; Wattanasarn, H. Tunable α-γ-Phase of Polyvinylidene Fluoride to Enhance Piezoelectric Coefficient. *Journal of Polymer Research* **2022**, *29* (6). https://doi.org/10.1007/s10965-022-03087-2.

(146) Biswas, A.; Henkel, K.; Schmeißer, D.; Mandal, D. Comparison of the Thermal Stability of the α, β and γ Phases in Poly(Vinylidene Fluoride) Based on in Situ Thermal Fourier Transform Infrared Spectroscopy. *Phase Transitions* **2017**, *90* (12), 1205–1213. https://doi.org/10.1080/01411594.2017.1337902.

(147) Satapathy, S.; Pawar, S.; Gupta, P. K.; Varma, B. R. Effect of Annealing on Phase Transition in Poly(Vinylidene Fluoride) Films Prepared Using Polar Solvent. *Bulletin of Materials Science* **2011**, *34* (4), 727–733. https://doi.org/10.1007/s12034-011-0187-0.

(148) Zhang, M.; Liu, C.; Li, B.; Shen, Y.; Wang, H.; Ji, K.; Mao, X.; Wei, L.; Sun, R.; Zhou, F. Electrospun PVDF-Based Piezoelectric Nanofibers: Materials, Structures, and Applications. *Nanoscale Adv* **2023**, *5* (4), 1043–1059. https://doi.org/10.1039/d2na00773h.

(149) Tao, M.; Liu, F.; Ma, B.; Xue, L. Effect of Solvent Power on PVDF Membrane Polymorphism during Phase Inversion. *Desalination* **2013**, *316*, 137–145. https://doi.org/10.1016/j.desal.2013.02.005.

(150) Wang, T.; Wang, Y.; Dang, F.; Liu, M.; Sun, S.; Jin, K.; Cheng, P. Optimizing Solvent Dipole Moment Enables PVDF to Improve Piezoelectric Performance. *Nanotechnology* **2024**, *35* (7). https://doi.org/10.1088/1361-6528/ad0907.

(151) Ma, W.; Zhang, J.; Chen, S.; Wang, X. Crystalline Phase Formation of Poly(Vinylidene Fluoride) from Tetrahydrofuran/N,N-Dimethylformamide Mixed Solutions. *Journal of Macromolecular Science, Part B: Physics* **2008**, *47* (3), 434–449. https://doi.org/10.1080/00222340801954811.

(152) Liz-Marzán, L. M.; Kamat, P. V. *Nanoscale Materials*; Kluwer Academic Publishers: Boston, 2003.

(153) Zhang, C.; Guo, Y.; Priestley, R. D. Glass Transition Temperature of Polymer Nanoparticles under Soft and Hard Confinement. *Macromolecules* **2011**, *44* (10), 4001–4006. https://doi.org/10.1021/ma1026862.

(154) Martín, J.; Nogales, A.; Martín-González, M. The Smectic-Isotropic Transition of P3HT Determines the Formation of Nanowires or Nanotubes into Porous Templates. *Macromolecules* **2013**, *46* (4), 1477–1483. https://doi.org/10.1021/ma302516e.

(155) García-Gutiérrez, M. C.; Linares, A.; Martín-Fabiani, I.; Hernández, J. J.; Soccio, M.; Rueda, D. R.; Ezquerra, T. A.; Reynolds, M. Understanding Crystallization Features of P(VDF-TrFE) Copolymers under Confinement to Optimize Ferroelectricity in Nanostructures. *Nanoscale* **2013**, *5* (13), 6006–6012. https://doi.org/10.1039/c3nr00516j.

(156) Gunkel, I. Directing Block Copolymer Self-Assembly on Patterned Substrates. *Small*. Wiley-VCH Verlag, November 15, 2018. https://doi.org/10.1002/smll.201802872.

(157) Alcoutlabi, M.; McKenna, G. B. Effects of Confinement on Material Behaviour at the Nanometre Size Scale. *Journal of Physics: Condensed Matter*. April 20, 2005. https://doi.org/10.1088/0953-8984/17/15/R01.

(158) Rao, J. P.; Geckeler, K. E. Polymer Nanoparticles: Preparation Techniques and Size-Control Parameters. *Prog Polym Sci* **2011**, *36* (7), 887–913. https://doi.org/10.1016/j.progpolymsci.2011.01.001.

(159) Lu, X. Y.; Wu, D. C.; Li, Z. J.; Chen, G. Q. Polymer Nanoparticles. In *Progress in Molecular Biology and Translational Science*; Villaverde, A., Ed.; Elsevier: San Diego, 2011; Vol. 104, pp 299–323. https://doi.org/10.1016/B978-0-12-416020-0.00007-3.

(160) Kietzke, T.; Neher, D.; Landfester, K.; Montenegro, R.; Güntner, R.; Scherf, U. Novel Approaches to Polymer Blends Based on Polymer Nanoparticles. *Nat Mater* **2003**, *2* (6), 408–412. https://doi.org/10.1038/nmat889.

(161) Millstone, J. E.; Kavulak, D. F. J.; Woo, C. H.; Holcombe, T. W.; Westling, E. J.; Briseno, A. L.; Toney, M. F.; Fréchet, J. M. J. Synthesis, Properties, and Electronic Applications of Size-Controlled Poly(3-Hexylthiophene) Nanoparticles. *Langmuir* **2010**, *26* (16), 13056–13061. https://doi.org/10.1021/la1022938.

(162) Satapathi, S.; Gill, H. S.; Li, L.; Samuelson, L.; Kumar, J.; Mosurkal, R. Synthesis of Nanoparticles of P3HT and PCBM for Optimizing Morphology in Polymeric Solar Cells. *Appl Surf Sci* **2014**, *323*, 13–18. https://doi.org/10.1016/j.apsusc.2014.07.175.

(163) Martínez-Tong, D. E.; Soccio, M.; Sanz, A.; García, C.; Ezquerra, T. A.; Nogales, A. Chain Arrangement and Glass Transition Temperature Variations in Polymer Nanoparticles under 3D-Confinement. *Macromolecules* **2013**, *46* (11), 4698–4705. https://doi.org/10.1021/ma400379a.

(164) Martínez-Tong, D. E.; Cui, J.; Soccio, M.; García, C.; Ezquerra, T. A.; Nogales, A. Does the Glass Transition of Polymers Change upon 3D Confinement? *Macromol Chem Phys* **2014**, *215* (17), 1620–1624. https://doi.org/10.1002/macp.201400244.

(165) Labastide, J. A.; Baghgar, M.; Dujovne, I.; Venkatraman, B. H.; Ramsdell, D. C.; Venkataraman, D.; Barnes, M. D. Time- and Polarization-Resolved Photoluminescence of Individual Semicrystalline

Polythiophene (P3HT) Nanoparticles. *Journal of Physical Chemistry Letters* **2011**, *2* (17), 2089–2093. https://doi.org/10.1021/jz200958x.

(166) Martínez-Tong, D. E.; Soccio, M.; Sanz, A.; García, C.; Ezquerra, T. A.; Nogales, A. Ferroelectricity and Molecular Dynamics of Poly(Vinylidenefluoride-Trifluoroethylene) Nanoparticles. *Polymer* **2015**, *56*, 428–434. https://doi.org/10.1016/j.polymer.2014.11.040.

(167) Gehan, T. S.; Bag, M.; Renna, L. A.; Shen, X.; Algaier, D. D.; Lahti, P. M.; Russell, T. P.; Venkataraman, D. Multiscale Active Layer Morphologies for Organic Photovoltaics through Self-Assembly of Nanospheres. *Nano Lett* **2014**, *14* (9), 5238–5243. https://doi.org/10.1021/nl502209s.

(168) Hu, Z.; Tian, M.; Nysten, B.; Jonas, A. M. Regular Arrays of Highly Ordered Ferroelectric Polymer Nanostructures for Non-Volatile Low-Voltage Memories. *Nat Mater* **2009**, *8* (1), 62–67. https://doi.org/10.1038/nmat2339.

(169) Horiuchi, S.; Tokura, Y. Organic Ferroelectrics. *Nat Mater* **2008**, *7* (5), 357. https://doi.org/10.1038/nmat2137.

(170) Dimitriev, O. P. Effect of Confinement on Photophysical Properties of P3HT Chains in PMMA Matrix. *Nanoscale Res Lett* **2017**, *12*. https://doi.org/10.1186/s11671-017-2270-y.

(171) Zhang, C.; Guo, Y.; Priestley, R. D. Confined Glassy Properties of Polymer Nanoparticles. *Journal of Polymer Science, Part B-Polymer Physics* **2013**, *51* (7), 574–586. https://doi.org/10.1002/polb.23268.

(172) Pecher, J.; Mecking, S. Nanoparticles of Conjugated Polymers. *Chem Rev* **2010**, *110* (10), 6260–6279. https://doi.org/10.1021/cr100132y.

(173) Zhang, C.; Pansare, V. J.; Prud'Homme, R. K.; Priestley, R. D. Flash Nanoprecipitation of Polystyrene Nanoparticles. *Soft Matter* **2012**, *8* (1), 86–93. https://doi.org/10.1039/c1sm06182h.

(174) Beer, P.; Reichstein, P. M.; Schötz, K.; Raithel, D.; Thelakkat, M.; Köhler, J.; Panzer, F.; Hildner, R. Disorder in P3HT Nanoparticles Probed by Optical Spectroscopy on P3HT- b-PEG Micelles. *J Phys Chem A* **2021**, *125* (47), 10165–10173. https://doi.org/10.1021/acs.jpca.1c08377.

(175) Gutiérrez-Fernández, E.; Sena-Fernández, J.; Rebollar, E.; Ezquerra, T. A.; Hermoso-Pinilla, F. J.; Sanz, M.; Gálvez, O.; Nogales, A. Development of Polar Phases in Ferroelectric Poly(Vinylidene Fluoride) (PVDF) Nanoparticles. *Polymer* **2023**, *264*. https://doi.org/10.1016/j.polymer.2022.125540.

(176) Sirringhaus, H. Device Physics of Solution-Processed Organic Field-Effect Transistors. *Advanced Materials* **2005**, *17* (20), 2411–2425. https://doi.org/10.1002/adma.200501152.

(177) Holmes, N. P.; Ulum, S.; Sista, P.; Burke, K. B.; Wilson, M. G.; Stefan, M. C.; Zhou, X.; Dastoor, P. C.; Belcher, W. J. The Effect of Polymer Molecular Weight on P3HT:PCBM Nanoparticulate Organic Photovoltaic Device Performance. *Solar Energy Materials and Solar Cells* **2014**, *128*, 369–377. https://doi.org/10.1016/j.solmat.2014.05.046.

(178) Holmes, N. P.; Ulum, S.; Sista, P.; Burke, K. B.; Wilson, M. G.; Stefan, M. C.; Zhou, X.; Dastoor, P. C.; Belcher, W. J. The Effect of Polymer Molecular Weight on P3HT:PCBM Nanoparticulate Organic Photovoltaic Device Performance. *Solar Energy Materials and Solar Cells* **2014**, *128*, 369–377. https://doi.org/10.1016/j.solmat.2014.05.046.

(179) Kim, H.; So, W. W.; Moon, S. J. The Importance of Post-Annealing Process in the Device Performance of Poly(3-Hexylthiophene): Methanofullerene Polymer Solar Cell. *Solar Energy Materials and Solar Cells* **2007**, *91* (7), 581–587. https://doi.org/10.1016/j.solmat.2006.11.010.

(180) Tsoi, W. C.; Spencer, S. J.; Yang, L.; Ballantyne, A. M.; Nicholson, P. G.; Turnbull, A.; Shard, A. G.; Murphy, C. E.; Bradley, D. D. C.; Nelson, J.; Kim, J. S. Effect of Crystallization on the Electronic Energy Levels and Thin Film Morphology of P3HT:PCBM Blends. *Macromolecules* **2011**, *44* (8), 2944–2952. https://doi.org/10.1021/ma102841e.

(181) Yao, P.; Zhu, B.; Zhai, H.; Liao, X.; Zhu, Y.; Xu, W.; Cheng, Q.; Jayyosi, C.; Li, Z.; Zhu, J.; Myers, K. M.; Chen, X.; Yang, Y. PVDF/Palygorskite Nanowire Composite Electrolyte for 4 v Rechargeable Lithium Batteries with High Energy Density. *Nano Lett* **2018**, *18* (10), 6113–6120. https://doi.org/10.1021/acs.nanolett.8b01421.

(182) Singh, B.; Padha, B.; Verma, S.; Satapathi, S.; Gupta, V.; Arya, S. Recent Advances, Challenges, and Prospects of Piezoelectric Materials for Self-Charging Supercapacitor. *J Energy Storage* **2022**, *47*. https://doi.org/10.1016/j.est.2021.103547.

(183) Chang, C.; Tran, V. H.; Wang, J.; Fuh, Y. K.; Lin, L. Direct-Write Piezoelectric Polymeric Nanogenerator with High Energy Conversion Efficiency. *Nano Lett* **2010**, *10* (2), 726–731. https://doi.org/10.1021/nl9040719.

(184) Drakopoulos, S. X.; Wu, J.; Maguire, S. M.; Srinivasan, S.; Randazzo, K.; Davidson, E. C.; Priestley, R. D. Polymer Nanocomposites: Interfacial Properties and Capacitive Energy Storage. *Prog Polym Sci* **2024**, 156. https://doi.org/10.1016/j.progpolymsci.2024.101870.

(185) Zhu, Y.; Dan, Y. Photocatalytic Activity of Poly(3-Hexylthiophene)/Titanium Dioxide Composites for Degrading Methyl Orange. *Solar Energy Materials and Solar Cells* **2010**, *94* (10), 1658–1664. https://doi.org/10.1016/j.solmat.2010.05.025.

(186) Set, Y. T.; Heinemann, M. D.; Birgersson, E.; Luther, J. On the Origin of the Quadrant I Semicircle in Intensity-Modulated Photocurrent Spectra of P3HT:PCBM Bulk Heterojunction Solar Cells: Evidence of Degradation-Related Trap-Assisted Recombination. *J Phys Chem C* **2013**, *117* (16), 7993–8000. https://doi.org/10.1021/jp310841v.

(187) Pal, S. K.; Kesti, T.; Maiti, M.; Zhang, F.; Inganäs, O.; Hellström, S.; Andersson, M. R.; Oswald, F.; Langa, F.; Österman, T.; Pascher, T.; Yartsev, A.; Sundström, V. Geminate Charge Recombination in Polymer/Fullerene Bulk Heterojunction Films and Implications for Solar Cell Function. *J Am Chem Soc* **2010**, *132* (35), 12440–12451. https://doi.org/10.1021/ja104786x.

(188) Criado-Gonzalez, M.; Marzuoli, C.; Bondi, L.; Gutierrez-Fernandez, E.; Tullii, G.; Lagonegro, P.; Sanz, O.; Cramer, T.; Antognazza, M. R.; Mecerreyes, D. Porous Semiconducting Polymer Nanoparticles as Intracellular Biophotonic Mediators to Modulate the Reactive Oxygen Species Balance. *Nano Lett* **2024**, *24* (24), 7244–7251. https://doi.org/10.1021/acs.nanolett.4c01195.

(189) Zangoli, M.; Cantelli, A.; Candini, A.; Lewinska, A.; Fardella, F.; Tino, A.; Tommasini, G.; Wnuk, M.; Moschetta, M.; Perotto, S.; Lucarini, M.; Tortiglione, C.; Lanzani, G.; Di Maria, F. Photoreactivity of Thiophene-Based Core@Shell Nanoparticles: The Effect of Photoinduced Charge Separation on In Vivo ROS Production. *J Phys Chem C* **2023**, *127* (9), 4672–4683. https://doi.org/10.1021/acs.jpcc.2c06986.

(190) Watanabe, T.; Kitamura, A.; Kojima, E.; Nakayama, C.; Hashimoto, K.; Fujishima, A. Photocatalytic Activity of TIO2 Thin-Film Under Room Light. In *Photocatalytic Purification and Treatment of Water and Air*; Ollis, D., Alekabi, H., Eds.; Elsevier Science: Amsterdam, 1993; Vol. 3, pp 747–751.

(191) Yan, H.; Deng, Y.; Shen, M.; Ye, Y. X.; Zhu, F.; Yang, X.; Ouyang, G. Regulation the Reactive Oxygen Species on Conjugated Polymers for Highly Efficient Photocatalysis. *Appl Catal B* **2022**, *314*. https://doi.org/10.1016/j.apcatb.2022.121488.

(192) Brnovic, A.; Hunt, L. A.; Tian, H.; Hammarström, L. Revising Exciton Diffusion Lengths in Polymer Dot Photocatalysts. *Physical Chemistry Chemical Physics* **2024**, *27* (2), 1083–1088. https://doi.org/10.1039/d4cp04108a.

(193) Tamai, Y.; Ohkita, H.; Benten, H.; Ito, S. Exciton Diffusion in Conjugated Polymers: From Fundamental Understanding to Improvement in Photovoltaic Conversion Efficiency. *Journal of Physical Chemistry Letters* **2015**, *6* (17), 3417–3428. https://doi.org/10.1021/acs.jpclett.5b01147.

Chapter 2

Materials, methods and techniques

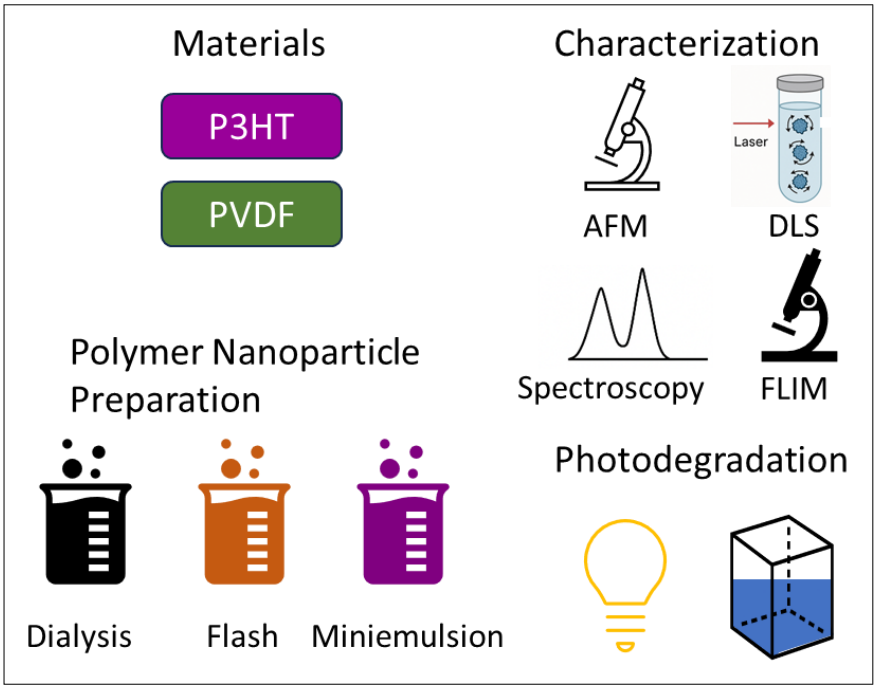

Graphical abstract representing the main idea of Chapter 2

Universidad Complutense de Madrid

Jose Sena Fernández

Micro and Nanoparticles of Functional Polymers: From Fundamentals to Applications

This chapter contains all the information related to the experimental details employed in this study. The chapter is structured into four sections:

-Section 2.1 is dedicated to a detailed description of the materials used in the study.

-In Section 2.2 the methods used for the preparation of polymer nanoparticles are described, outlining the procedures and conditions.

-Section 2.3 describes the techniques employed for the deposition of NPs and film fabrication.

-Section 2.4 describes the experimental techniques used to characterise the physical and structural properties of the prepared systems. This section also explains the analysis methods and the tools used to obtain and interpret the experimental data.

-Finally, Section 2.5 describes the setup of the photodegradation process.

2.1. Materials

In this thesis, two different polymers have been studied: poly(3-hexylthiophene-2,5-diyl), in brief referred to as poly(3-hexylthiophene) (P3HT), and poly(1,1-difluoroethane-1,2-diyl), or poly(1,1-difluoroethylene), referred to as polyvinylidene fluoride (PVDF)[1,2]. For the preparation of polymer nanoparticles, sodium dodecyl sulphate (SDS) was used as a surfactant in particular cases. Methylene blue is used in this thesis as a model water contaminant. Finally, the solvents used in the preparation and deposition processes are detailed, with the relevant properties of each solvent specified, such as purity, boiling point and miscibility in water.

2.1.1. Polymers

2.1.1.1. Poly(3-hexyltiophene) (P3HT)

In this study, P3HT was utilised as an organic semiconductor material, with its chemical structure illustrated in Figure 2.1. The repeating thiophene units are functionalised with hexyl side chains, enhancing solubility in organic solvents and facilitating the processing of P3HT in solution.

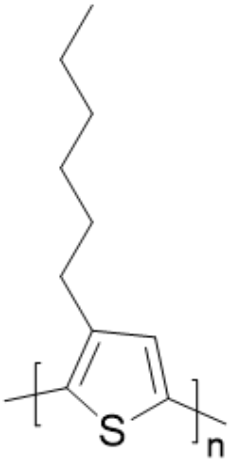

Figure 2.1. The chemical structure of P3HT.

In the present study, regioregular (RR) P3HT supplied by Ossila Ltd. (Sheffield, UK) was used. Two batches of P3HT with similar molecular weights (batches M102 and M1011) were employed. This polymer is commercially available under the tradename Lisicon® SP001. The key physicochemical characteristics of the polymer batches are summarised in Table 2.1.

Table 2.1. Molecular weights of the P3HT samples investigated.

Polymer (batch)	M_w (g/mol)	PDI	Regioregularity
P3HT (M102)	65200	2.2	95.7%
P3HT (M1011)	60150	2.1	97.6%

P3HT was utilised to prepare nanoparticles (NPs). The solvent chosen, the concentration, and processing conditions were optimised to achieve controlled nanoparticle (NP) size and stability.

2.1.1.2. Poly(vinylidene fluoride) (PVDF)

The chemical structure of PVDF is shown in Figure 2.2. The PVDF used in this thesis was procured from Sigma-Aldrich.

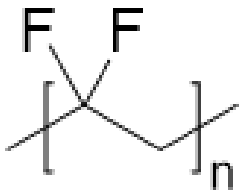

Figure 2.2. Chemical structure of PVDF.

PVDF was dissolved for the preparation of both deposits and NP dispersions to explore its electroactive phases and their potential applications.

Table 2.2. Molecular weight and characteristic temperatures of the PVDF samples used in this study.

Polymer	M_w (g/mol)	Glass temperature (°C)	Melting temperature (°C)
PVDF	534000	-38	171

2.1.2. Non-polymeric materials

2.1.2.1. Sodium Dodecyl Sulphate (SDS)

Sodium dodecyl sulphate (SDS), also known as sodium lauryl sulphate, is an anionic surfactant with many applications in scientific, industrial and commercial fields. As shown in Figure 2.3, its chemical formula is $C_{12}H_{25}OSO_3^-Na^+$, consisting of a 12-carbon hydrophobic alkyl chain (dodecyl tail) linked to a hydrophilic sulphate head group. SDS is typically found as a white solid or crystalline powder. The molecular structure of SDS is characterised by an amphiphilic nature, which allows it to reduce surface tension, form micelles, and stabilise emulsions effectively[3–6].

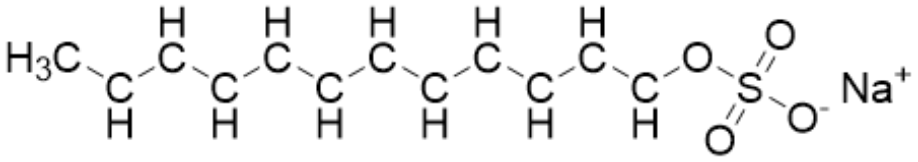

Figure 2.3. Chemical structure of SDS.

In the present study, SDS (Sigma-Aldrich, ACS reagent grade, St. Louis, MO, USA) was used as a surfactant in some of the NPs preparations.

2.1.2.2. Methylene Blue (MB)

Methylthioninium chloride, $(C_{16}H_{18}ClN_3S)$[7], commonly known as methylene blue (MB), is a heterocyclic aromatic organic compound that appears as a dark green crystalline powder with a bronze sheen. When dissolved in water, it acquires an intense blue colour. Its molecular formula is Figure 2.4.

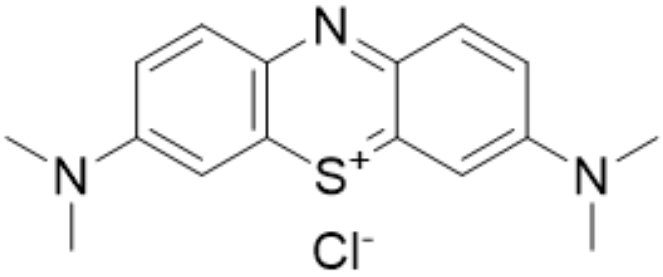

Figure 2.4. Chemical structure of MB.

The MB used in this was supplied by Merck (purity ≥82%, M_w = 319.85 g/mol, powder).

The UV-Vis spectrum of a 15 mg/L water solution of MB is presented in Figure 2.5. The intense absorption around 665 nm is responsible for the blue colouration of the solution, and this will be used to monitor the efficiency of the photocatalysis processes, as described later.

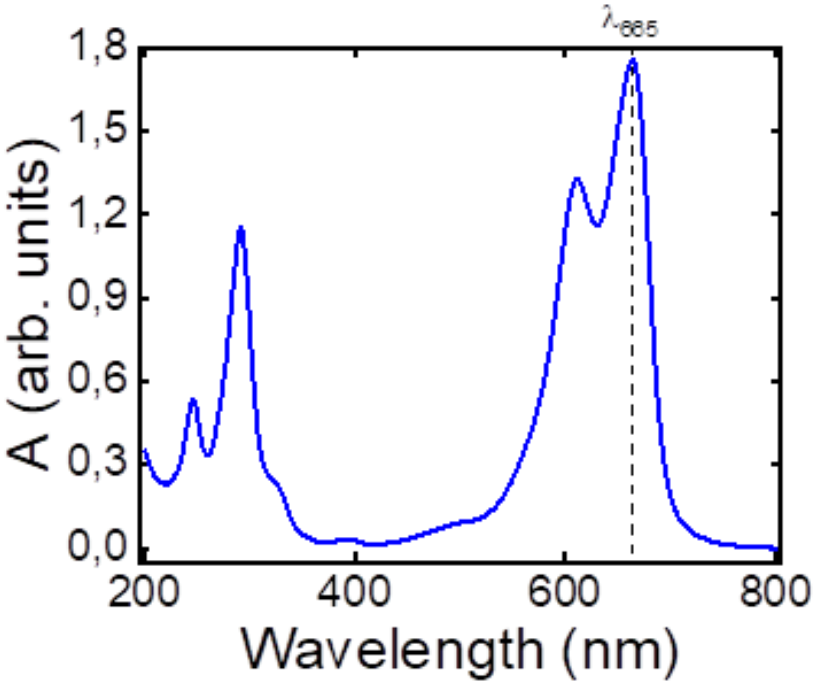

Figure 2.5. UV-Vis spectra of MB. The reference wavelength at which the concentration is obtained is 665 nm (marked with a dotted line).

From the preparation of different concentrations of MB solution, a calibration line was obtained through linear regression in order to determine the molar extinction coefficient (see Figure 2.6) according to equation 2.19.

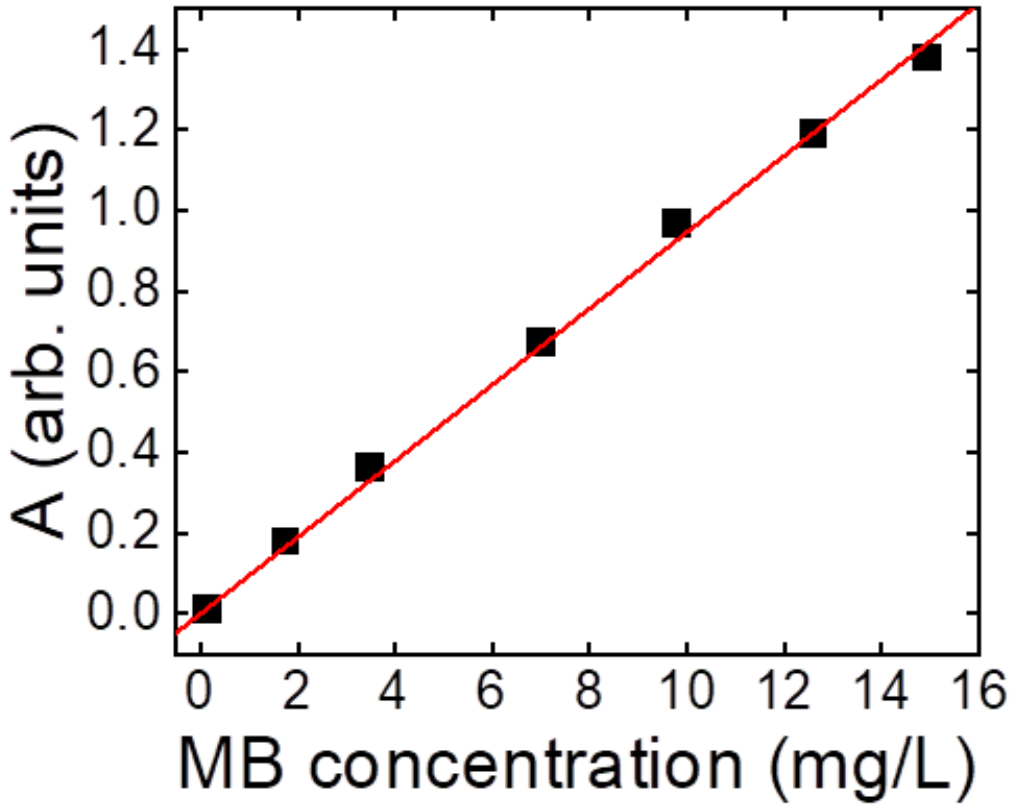

Figure 2.6. Regression line between the absorbance and the concentration of MB, which allows the molar absorptivity to be calculated.

The result of the slope calculation is the value of the molar extinction coefficient, which is found to be 0.190 $mg^{-1} \cdot L \cdot m^{-1}$.

2.1.3. Solvents

Given the diversity of materials employed, the processing techniques utilised, and the aims of this thesis, a considerable number of organic solvents have been utilised, as summarised in Table 2.3 alongside their most significant properties. Furthermore, throughout this thesis, Milli-Q water has been employed.

Table 2.3 Solvents used in this work.

Solvent	Abbreviation	Supplier	Purity (%)	Boiling Point (ºC)	Water miscibility	Material dissolved
Trichloromethane (Chloroform)	$CHCl_3$	Quimipur	≥99.0	62 (<H_2O)	No	P3HT
Oxolane (Tetrahydrofuran)	THF	Alfa Aesar	99.0	66 (<H_2O)	Yes	P3HT PVDF
Dimethyl sulfoxide	DMSO	Merck	≥99.7	189 (>H_2O)	Yes	PVDF
N, N-dimethylacetamide	DMA	Sigma Aldrich	≥99.0	165 (>H_2O)	Yes	PVDF
Propylene carbonate	PC	Thermo Scientific	≥99.5	242 (>H_2O)	Yes	PVDF
Methyl ethyl ketone	MEK	Sigma Aldrich	≥99	80 (<H_2O)	Yes	PVDF
Ethylene glycol	EG	ITW reagents	99	197 (>H_2O)	Yes	PVDF
Formic Acid	FA	Sigma Aldrich	≥96	101 (≈H_2O)	Yes	PVDF
Methanol	MetOH	Sigma Aldrich	≥99.9	66 (<H_2O)	Yes	PVDF
Ethanol	EtOH	Emsure	-	78 (<H_2O)	Yes	PVDF
Acetone	Acetone	Sigma Aldrich	≥96	56 (<H_2O)	Yes	PVDF

2.2. Preparation of nanoparticles

A variety of techniques can be used to prepare polymer NPs, including salting-out[8], dialysis[8,9], flash nanoprecipitation[10,11], miniemulsion[8,12], or surfactant-free emulsion[8]. This section describes in detail the three methods used in this Thesis to nanostructure the materials studied. All three methods are based on the exchange of a good solvent for a poor solvent (antisolvent or non-solvent). In this context, the term "antisolvent" is employed in instances where the solvent is water miscible, whereas "non-solvent" is used in cases where it is immiscible. In all cases, the antisolvent will be water.

2.2.1. Nanoparticles prepared by dialysis

In the process of NP preparation, dialysis involves placing a polymer solution inside a membrane with pores of defined size to retain the NPs to be formed, while allowing the organic solvent to pass through[8,13]. This process necessitates the immersion of the membrane in a substantial volume of antisolvent, typically deionized water, which functions as a "drag solvent".[8,13–16] The diffusion process creates a gradient that displaces the solvent inside the membrane by the antisolvent, so that aggregation occurs in the form of NPs. The NPs are retained within the membrane[8,17].

The characteristics of the different elements in the dialysis process define the final product of this process:

- Membrane pore size: it defines the size of the aggregates or molecules that will be retained in the inner part of the volume enclosed by the membrane.
- Volume ratio between the solution and the dialysis solvent: A larger volume of the dialysis medium allows more effective removal of solvent or impurities by facilitating the diffusion of solutes out of the bag.
- Dialysis time: Dialysis may take several hours or even days to complete, depending on the concentration and type of components to be removed.

In this thesis, dialysis was used in the preparation of two different types of NPs. In the case of the miniemulsion method for preparing NPs, which will be described later, dialysis was used as a final step to remove the excess of surfactant. The other type of NPs was prepared using dialysis in a single step. In both cases, the dialysis membrane, stored in a saline solution in a refrigerator[18]. The dialysis membrane employed was a Visking DTV manufactured by Medicell Int Ltd., London, UK, with a cutoff range of 12000-14000 $g \cdot mol^{-1}$. It is delivered in the form of a tube with a diameter of 25.5 mm. Prior to utilisation, the membrane is subjected to a thorough cleaning process involving rinsing with distilled water and the solvent utilised during preparation.

2.2.1.1. Preparation of nanoparticles by dialysis

The dialysis method for the preparation of polymer NPs is outlined in Figure 2.7 and consists of the following steps:

1. Washing membrane: The membrane, which has previously been stored in a saline solution, is then washed in the organic solvent that has been utilised for the dissolution of the polymer.
2. Preparation of polymer solution: A solution of the polymer is prepared at a fixed concentration in the corresponding water-miscible organic solvent (Table 2.4).

Table 2.4 Polymer prepared by dialysis, concentration and solvent used.

Polymer	Concentration (g/L)	Solvent
PVDF	2	THF
		DMSO
		DMA
		PC
		MEK
		EG
		FA
		MetOH
		EtOH
		Acetone

3. Sample preparation: A magnetic clamp closes one end of the membrane. The solution is then poured on a dialysis membrane, and the other end of the membrane is sealed by another clamp, taking care not to leave any air space in the membrane.
4. Immersion in dialysis solvent: The dialysis membrane is immersed in a large volume of deionised water, which acts as the dialysis medium, and stirred at low speed.
5. Diffusion: As the system is stirred, the organic solvent diffuses into the dialysis medium through the membrane. This displacement causes a continuous aggregation of the polymer due to decreased solubility until a homogeneous colloid of the polymer in water is retained in the volume enclosed by the membrane. A low concentration of polymer solution is required. This ensures that the polymer chains are dispersed and can be separated into nanodomains.

6. Change of the dialysis medium: Depending on the preparation, the dialysis medium is changed periodically to improve efficiency, maintain a concentration gradient, overcome chemical equilibrium, and accelerate the process.
7. Termination: After a certain time, the membrane containing the NPs is removed from the bath, and the dispersion is obtained.

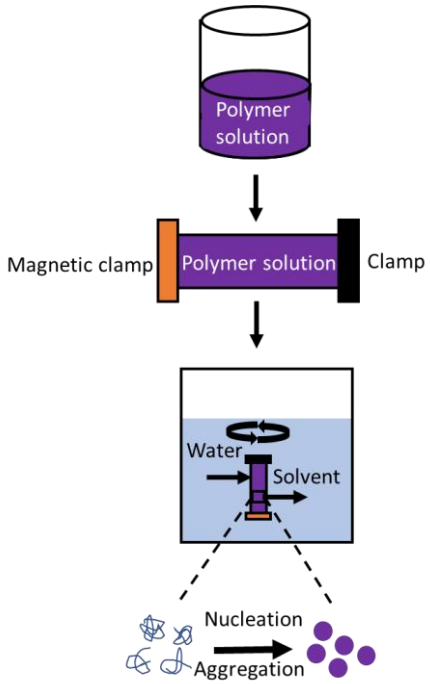

Figure 2.7. Schematic representation of the dialysis process used to prepare polymer NPs.

2.2.2. Flash nanoprecipitation

Flash nanoprecipitation, also referred to as reprecipitation or the solvent displacement method, is a highly versatile, efficient, effective and straightforward technique for preparing NPs, particularly polymer NPs[19,20]. The basis of flash nanoprecipitation underlies the phenomenon of supersaturation and controlled nucleation. The process involves mixing the water-miscible organic solvent (with a lower boiling point than the antisolvent) in which the polymer is dissolved with an excess of the antisolvent phase (most commonly water) under turbulent flow (Figure 2.8)[8,21,22]. The fast diffusion of the solvent into the antisolvent, induced by the rapid mixing and the reduction of the solubility of the polymer, results in local supersaturation of the polymer[8,22]. This phenomenon, similar to dialysis, causes the

hydrophobic interactions between the polymer chains, which normally ensure their effective dispersion in solution, to be disrupted by a significant change in the quality of the medium, resulting in almost instantaneous collapse and aggregation of the polymer chains due to the low solubility of the polymer in the antisolvent[8]. The rapid mixing process generates many nuclei, which generally favours the formation of small-sized, narrowly distributed NPs (Figure 2.8)[8,21–23]. During the mixing process, a competitive kinetic process exists between nucleation and nuclei growth[8]. The final size and distribution of the NPs are thus dependent on various factors, including the mixing rate, the volume ratio and nature of solvent and antisolvent, the type of polymer, temperature, and polymer concentration[8,21,22]. For instance, sufficiently intense mixing ensures that the size of the NPs depends only on the composition of the streams and not on the flow rate, causing precipitation nuclei to form instantaneously and ensuring uniform nanoparticle formation[8,22,23]. Additionally, the process may result in the formation of NP aggregates. To obtain small particles, it is essential to adjust the preparation conditions to maximise nucleation, which is strongly influenced by supersaturation, while maintaining a low growth rate to ensure the formation of uniform, well-defined particles[24]. Achieving this balance is imperative to ensure uniform particle size, control particle morphology and avoid excessive aggregation[8].

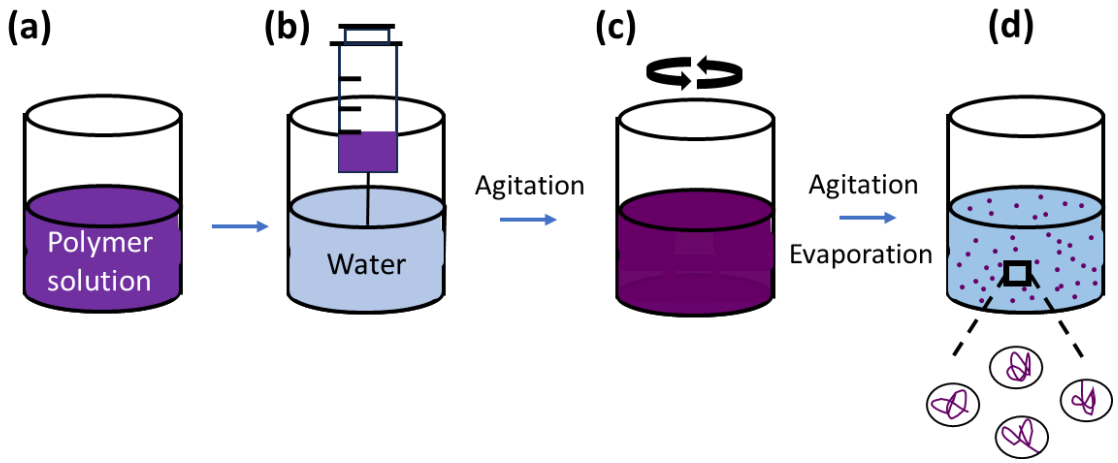

Figure 2.8. Schematic illustration of the steps involved in preparing functional polymer nanoparticles from water-based inks through flash nanoprecipitation.

The process is relatively simple and fast to implement[8,23], and the rapid formation of NPs minimises solvent exposure time, which can be essential for some organic solvents[11,21,22]. However, it is important to note that achieving precise control over size and distribution can

be challenging if all parameters are not meticulously regulated, which can affect reproducibility.

2.2.2.1. Nanoparticles prepared by the flash method

The steps that have been followed in this thesis to prepare polymer NPs are outlined below:

1. Dissolution of the polymer: The polymer is dissolved in a good water-miscible organic solvent with a lower boiling point at a certain concentration.
2. Mixing with the aqueous phase: The polymer solution is rapidly injected into the aqueous phase with vigorous stirring, immediately reducing solubility. Due to the rapid decrease in solubility, NPs form during this step, with nucleation occurring almost instantaneously and the formation of small particles. As the process continues, these particles grow to the desired nanometre size.
3. Evaporation of the organic solvent: Finally, the water-mixed organic solvent is removed by evaporation.
4. Sonication of the samples: A final ultrasonication step can be included to break some NPs aggregates.

In this study, two distinct methodologies were employed for the preparation of the NPs. The first method involved the injection of the solution into water via a syringe, as illustrated in Table 2.5, for the preparation of P3HT NPs. The second method involved using a microfluidic set-up to prepare PVDF NPs, as detailed in Table 2.6.

Table 2.5 Summary of flash P3HT NPs preparation conditions.

Material	Concentration (g/L)	Solvent/Antisolvent volume ratio (R)	Solvent
P3HT	1	1/4	THF/H_2O
		1/6	
		1/8	
	3	1/4	
		1/6	

		1/8	
	5	1/4	
		1/6	
		1/8	

Furthermore, NPs were prepared from a 3 g/L solution with a volume ratio of 1/6, aging the solution for 24, 72, and 168 hours.

2.2.2.2. Flash by microfluidic

A method derived from flash nanoprecipitation is known as flash microfluidics. The fundamental principle of flash microfluidics is similar to that of flash, but with one key difference: the mixing of the solvent and non-solvent is performed through microfluidic devices. These devices enable precise control of the rate of addition and mixing in the channels, facilitating the preparation of more reproducible NPs (see Figure 2.9)[24,25]. The process is analogous to that depicted in Figure 2.9 (a). The polymer solution is introduced into a syringe while the non-solvent is introduced into another syringe. At a controlled speed, the two liquids converge at a point, resulting in the displacement of the solvent by the antisolvent.

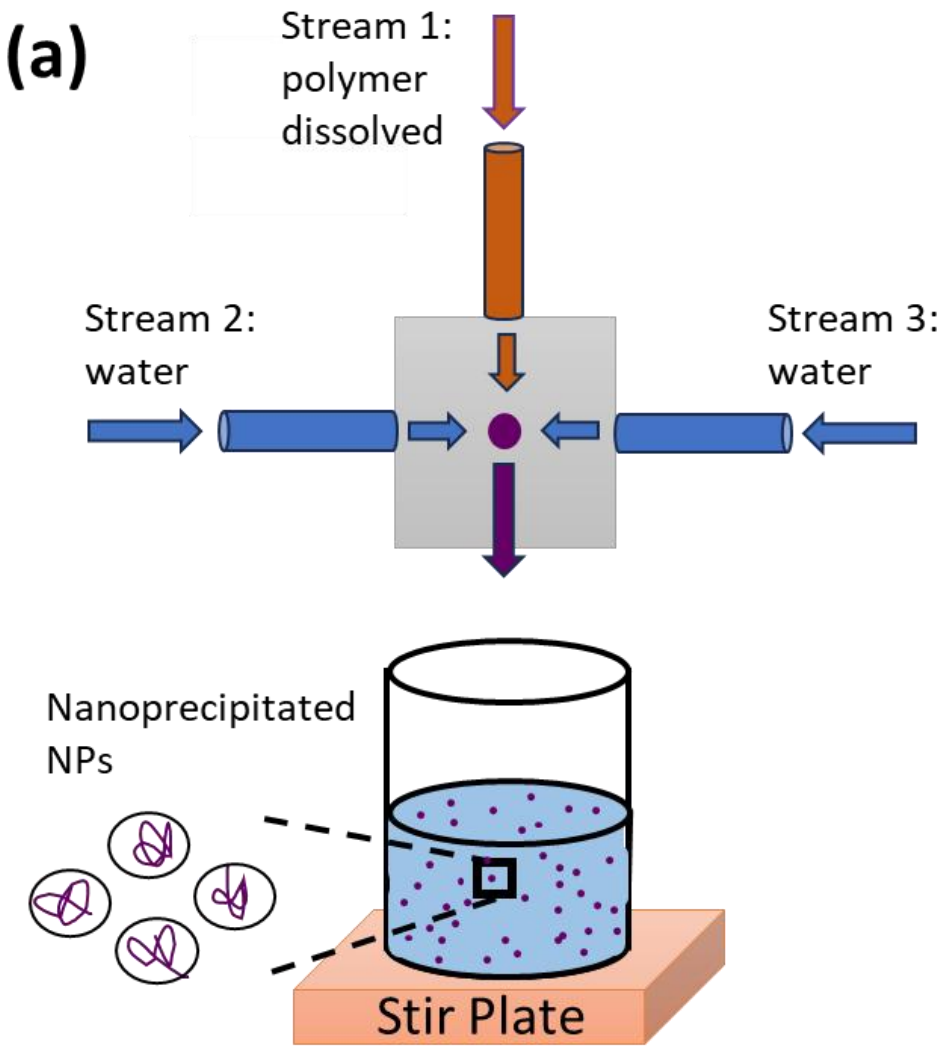
(a)
Stream 1:
polymer
dissolved
Stream 2:
water
Stream 3:
water
Nanoprecipitated
NPs
Stir Plate

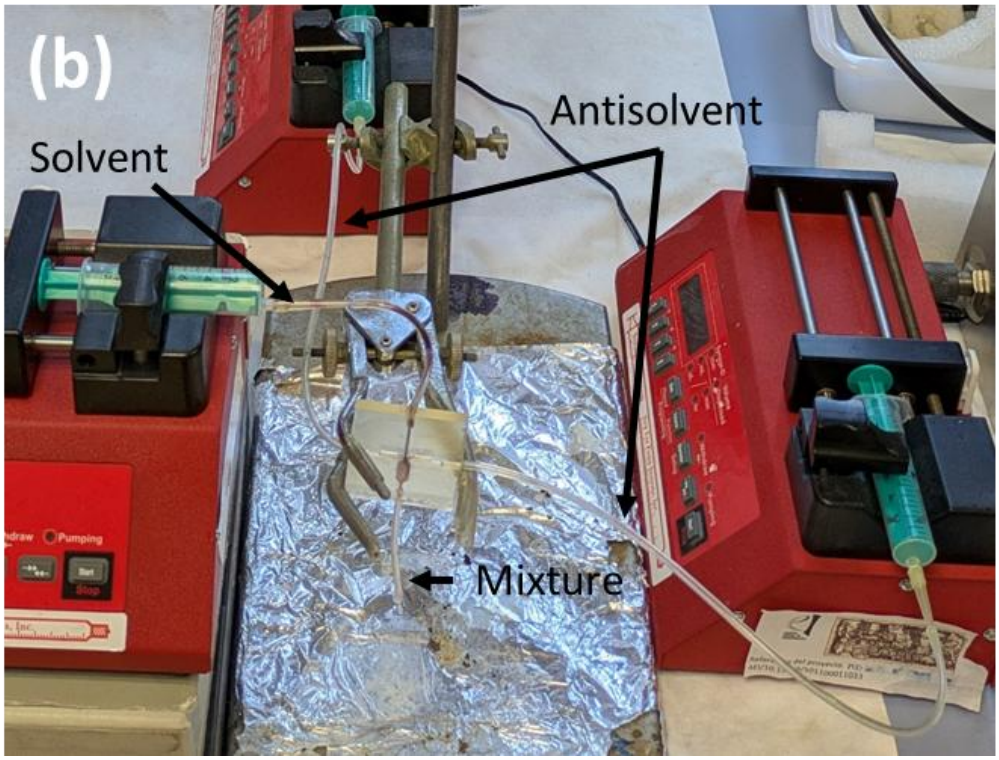
(b)
Solvent
Antisolvent
Mixture

Figure 2.9. (a) Schematic setup of the Flash Nanoprecipitation mixing process by microfluidic aimed to generate NPs. **(b)** Experimental scheme showing three microfluidic devices, one for the solvent and two for the antisolvent. The channels converge on a chip where the mixture is produced and falls into a vial.

In this thesis, three one-channel microfluidic devices of the Model 300 type (New Era Pump Systems, NY, USA) were utilised; one channel was utilised for the dissolved polymer and two for the antisolvent (water) (Figure 2.9 (b)). Consequently, the exchange of one for the other is favoured. The injection syringes employed were 10 mL (Ecoject), thereby limiting the rates to between $1.4x10^{-4}$ mL/min and 6.2 mL/min. In the present study, a flow rate of 4 mL/min was employed. The syringes were connected via 1.6 mm internal diameter silicon tubes to the chip, which was prepared by 3D printing from resin by the group of Prof. Juan Rodriguez-Hernandez. The chip has channels of 1 mm where fluid mixing occurs. The mixture was then poured into a vial containing a magnet that stirred the mixture, and the organic solvent was subsequently evaporated. Detailed information regarding these preparations can be found in Table 2.6.

Table 2.6 Preparation conditions of NPs by Flash microfluidics.

Polymer	Concentration (g/L)	Solvent	Speed (mL/min)	Volume ratio
PVDF	2	THF	4	1/2
		MEK		
		EtOH		
		MetOH		
		Acetone		

2.2.3. Miniemulsion

The miniemulsion preparation method is a process that produces colloidal-type particles. The miniemulsion protocol consists of mixing a polymer solution with a surfactant solution in a medium that has the characteristics of being immiscible with the polymer solvent and acts as a non-solvent for the polymer[26–28]. The presence of a surfactant stabilises polymer solution droplets, which, once the solvent is evaporated, become NPs. In general, the

surfactant is dissolved in water, which acts as the non-solvent medium, while the solvent used for the polymer has a boiling point lower than that of water[29–31].

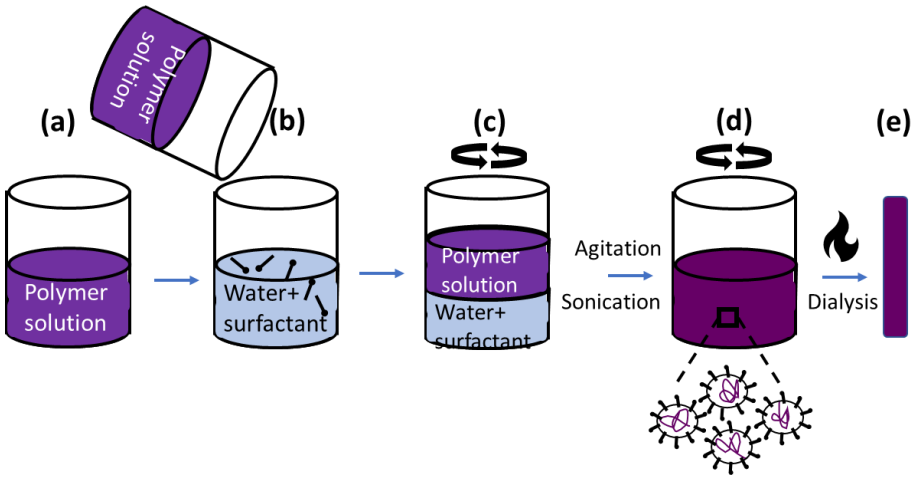

Figure 2.10. Schematic representation of the miniemulsion process: **(a)** dissolution of the polymer, **(b)** mixing of the solution and the surfactant in water, **(c)** pre-emulsification, **(d)** emulsification and **(e)** obtaining NPs.

2.2.3.1. Nanoparticles prepared by miniemulsion method

The miniemulsion preparation method is outlined in Figure 2.10 and consists of the following steps:

1. The polymer is dissolved in the organic solvent.
2. Subsequently, the polymer solution and the surfactant aqueous solution are mixed. In the present case, the surfactant used is SDS. The conditions for preparation are reported in Table 2.7. In this way, an emulsion is formed, and polymer solution droplets remain dispersed in water without coalescing throughout the process[26,27,32–34].
3. Afterwards, the emulsion undergoes a process of stirring and sonication. The emulsion is vigorously stirred and sonicated with an ultrasonic bath or with an ultrasonic probe so that the combined action of stirring and surface tension force causes the dispersed particles to take on a spherical shape, forming the miniemulsion[35,36]. In the absence of stirring, the polymer droplets would begin to coalesce[32,33,36].

4. The next stage of the process is the evaporation of the organic solvent. The ultrasonicated mixture is heated to a temperature below its water boiling point, where the organic solvent can be evaporated. In this way, the droplets are transformed into solid polymer particles.
5. Finally, the water suspension is dialysed against water to remove the excess of SDS[13,21].

Table 2.7 Miniemulsion preparation conditions for NPs.

Polymer	Sonication	Concentration (g/L)	Solvent	% wt SDS	Volume ratio (solution/SDS)
P3HT	Without	3	$CHCl_3$	1	1
	Bath				
	Probe (10% amplitude)				
	Probe (25% amplitude)				
	Probe (35% amplitude)				

In this investigation, P3HT NPs were prepared through miniemulsion, with detailed descriptions of the preparations provided in Table 2.7. The sonication process was conducted in an ultrasonic bath with a power of 150 watts. Model 3000513 (JP Selecta, Spain) and an ultrasonication probe: The Sonopuls HD 2070.2 (BANDELIN electronic, Germany) was utilised, attached by a microprobe type MS-72, which possesses a total amplitude of 282 μm and an admissible amplitude setting ranging from 10% to 50%.

2.3. Deposition techniques

2.3.1. Spin coating

The spin coating technique, or spin casting, is one of the most widely used methods for the uniform deposition of a wide variety of materials, including NPs[9,37–39], on flat solid

substrates due to its simplicity, speed, reproducibility and ability to cover surfaces and produce homogeneous layers over large areas uniformly[40,41].

In the "static" spin coating process (see Figure 2.11), which is the one used in this thesis, a small volume of the solution or suspension is first deposited onto a substrate that is initially stationary. The substrate is then allowed to rotate at a given acceleration, thereby enabling the uniform distribution of the solution[40]. The rotation speed, or spin speed, is increased until high speeds are reached, causing the solution to spread over the entire surface of the substrate and the excess liquid to be expelled towards the edges[40]. The resulting centrifugal force and the frictional forces of the fluid distribute the material evenly over the substrate surface[42,43]. The rotation continues at a high speed for a given time to allow the solvent to evaporate and the deposit to form[42,43].

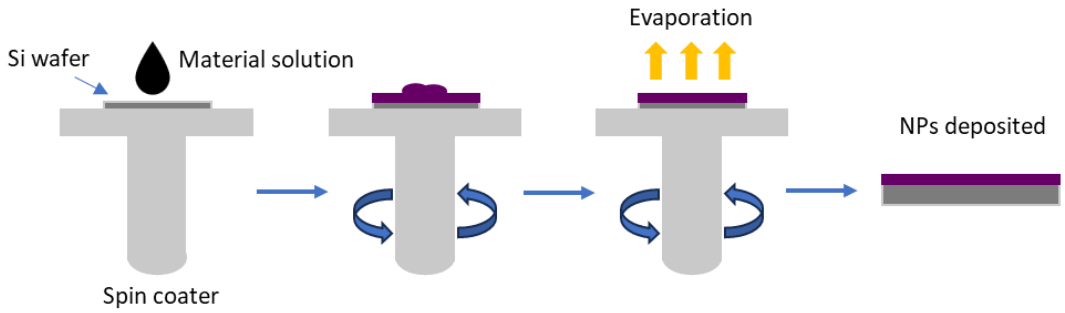

Figure 2.11. Schematic of the spin coating process for the deposition of NPs.

The thickness and uniformity of the final film and the density of the deposited NPs depend on several parameters, such as:

- Spin speed[42–44]: Higher speeds generally result in the deposition of less material[41].
- Spin Time[42]: Controls drying and material distribution[41,43].
- Solution concentration[40,42–44]: More concentrated solutions will result in greater deposition[40,42].
- Solvent properties: Viscosity[42] and solvent evaporation rate have a significant effect on the deposition[44].
- Substrate surface[44]: The properties of the substrate surface influence the interactions between the system and the substrate[40].

This technique is optimal for flat substrates, as the centrifugal force may not allow uniform coverage on surfaces with complex geometries.

In the present thesis, the spin-coater employed was the Laurell Technologies Model WS-650HZB-23NPPB/ED3. Arsenic-doped silicon substrates with a thickness of 525 μm and a resistivity of <0.005 Ohm/cm (<100>, Neyco, Vannes, France) measuring approximately 2 cm x 2 cm are cut and immersed in a selection of solvents, including ethanol, acetone, water and isopropanol. Each substrate is then subjected to ultrasonication for five minutes in each solvent. Following this, the substrates are dried using nitrogen gas. The dispersions are then ultrasonicated for 5 minutes and stirred before deposition in order to obtain a uniform mixture. The final step involves executing the spin coating process, as previously outlined. The study of how different parameters affect the deposition of NPs and the optimal values was carried out in previous research in the group. The deposition of approximately 0.1 mL (it should be noted that the deposited volume depends on the dimensions of the substrate) is performed either by spin coating at 1200 revolutions per minute (rpm) for 2 minutes (acceleration of 1.05 radians per second squared (rad/s^2)) under ambient conditions. The characterisation of NPs deposited by spin coating is carried out using various techniques, such as Atomic Force Microscopy (AFM).

2.3.2. Drop casting

Drop casting is a simple, effective, and versatile technique widely used to deposit nanoparticles or other materials onto solid substrates or to prepare self-supporting films, known as "free-standing films".[45] The process involves depositing a small volume of a solution or suspension of the material onto a substrate and allowing the solvent to evaporate, either exposed to air-dry at room temperature or gently heated in a vacuum. As the liquid evaporates, the NPs aggregate, or the film-forming material is distributed over the substrate surface[46] (Figure 2.12).

The process can be described in several steps:

1. Solution preparation: A solution or suspension containing the NPs in a suitable dispersion medium is prepared. The choice of medium significantly influences the deposition process, affecting factors such as uniformity, drying time, and

residual medium content due to its properties such as volatility, viscosity, surface tension, and affinity with the substrate.

2. Drop deposition: A drop (typically a few microlitres (μL)) is carefully deposited onto the clean substrate (in this case, silicon). The volume of the droplet can significantly influence the material deposited.
3. Solvent evaporation: The solvent evaporation rate plays a crucial role in determining the morphology and uniformity of the material deposited, as well as avoiding film defects. In the case of free-standing films, a film remains that is held together by physical or chemical interactions[45,47]. The film is then carefully separated from the substrate, resulting in a free-standing film[47–52]. Free-standing films typically have a controlled thickness, typically ranging from nanometres to micrometres.

Figure 2.12. Deposition method using drop casting.

In the present cases, P3HT and PVDF NPs were deposited under ambient conditions onto similar wafers to those described above for the case of spin coating (conductive heavily doped n-type silicon wafers with a thickness of 525 nm, with both sides polished, from Neyco, France). The wafers and dispersions were treated under the same conditions as spin coating.

Free-standing films or deposits of PVDF were prepared by drop casting. PVDF solutions from different solvents. For this purpose, circular glass substrates with edges have been utilised to contain the solution within the substrate. A volume of 700 μL was added for each film. The evaporation process was carried out in air at room temperature, except for cases where the solvent was too viscous or had an elevated boiling point. In these cases, the films are obtained in a vacuum oven at a temperature not higher than 35°C.

The characterisation of NPs deposited by drop casting was performed using a variety of advanced techniques, including Atomic Force Microscopy (AFM) and X-ray diffraction

(XRD), and the characterisation of films or deposits obtained is conducted using various advanced techniques, including XRD and Fourier Transform Infrared spectroscopy (FTIR).

2.4. Experimental techniques

2.4.1. Wide Angle X-ray Scattering (WAXS)

X-ray diffraction (XRD) is a fundamental analytical characterisation technique that has been utilised for over a century to investigate the crystalline structure of materials at the atomic and molecular level[53–56]. When X-rays, with wavelengths comparable to interatomic distances (typically 10^{-11}-10^{-8} m), interact with a crystalline sample, they are scattered by the electrons of the atoms within the crystal lattice[53–56]. The constructive interference of these scattered waves occurs when the Bragg condition is satisfied through the specular reflection in the crystal planes. This gives rise to a characteristic diffraction pattern that reveals details about the periodicity and atomic arrangement of the material[53,56]. Bragg's Law (Equation 2.1) describes this phenomenon, which establishes the relationship between the wavelength (λ) of the incident X-ray, the diffraction angle between the incident vector and the crystal plane (θ) and the interplanar distance between diffracting planes (d) (Figure 2.13).

$$n\lambda = 2d \sin\theta \qquad \text{Eq. 2.1.}$$

In Equation 2.1, n is an integer representing the diffraction order, and the term $2d\sin\theta$ is defined as the difference in path length between X-rays scattered from adjacent planes[54,55]. Constructive interference (and thus observable diffraction) occurs when this path difference is an integer multiple of the X-ray wavelength.

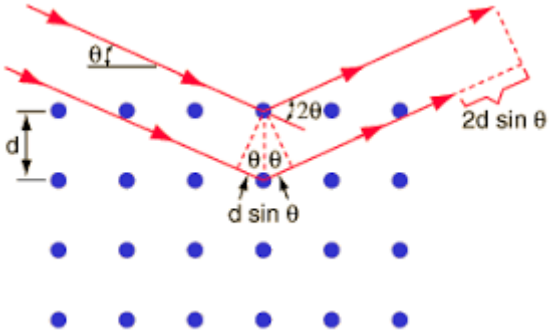

Figure 2.13. The equivalence of Bragg's Law for the special case of the 2D square lattice.

Additionally, the scattering vector or wave vector transfer (q) is defined as the difference between the incident wave vector and the scattered vector[53,57].

$$q = \frac{4\pi}{\lambda}\sin(\theta) \qquad \text{Eq. 2.2.}$$

Here θ is again the Bragg angle (half of the total scattering angle 2θ) between the incident and scattered beams. It is also important to note that the magnitude of the scattering vector is inversely proportional to the interplanar distance, thereby providing a direct link between the diffraction pattern in reciprocal space and the real-space structure:

$$q = \frac{2\pi}{d} \qquad \text{Eq. 2.3.}$$

XRD experiments have been boosted by the development of synchrotron radiation sources (Figure 2.14), which provide high-intensity, collimated, and wavelength-tunable X-ray beams. X-ray scattering experiments using synchrotron sources allow the study of time-dependent experiments, like crystallisation in real-time, or the study of samples with low scattering power, like the case of polymer thin films. Synchrotron radiation is generated when high-energy electrons are accelerated along a curved trajectory (Figure 2.14). As magnetic fields deflect the electrons, they lose energy, which is continuously emitted in the form of highly collimated X-ray radiation. This radiation is characterised by its brilliance (many orders of magnitude higher than conventional X-ray sources), its polarisation (linear, elliptical or

circular), and its continuous electromagnetic radiation (ranging from infrared to hard X-rays), emitted tangentially to their orbit[58,59]. Dedicated beamlines for given experiments are constructed as tangential extensions from the synchrotron storage ring (Figure 2.14) to make use of this radiation.

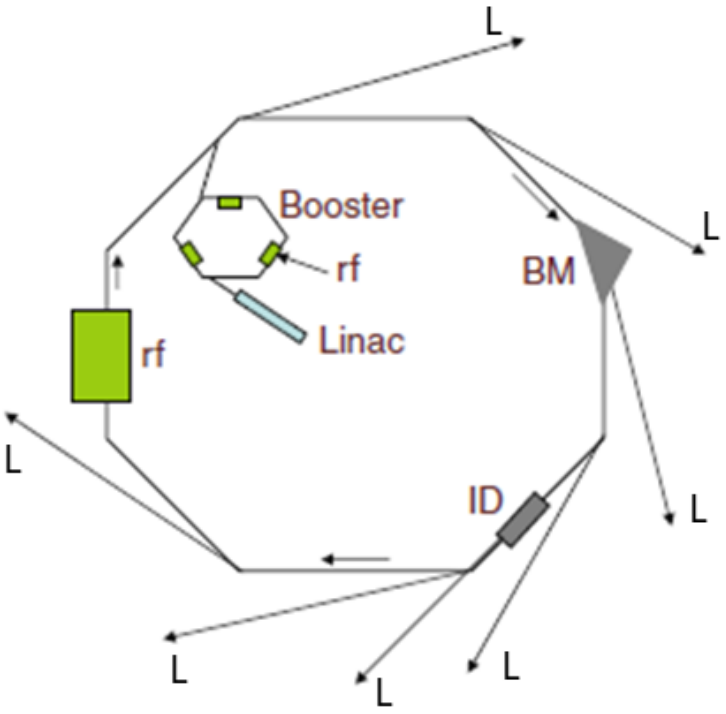

Figure 2.14. A schematic of a standard synchrotron radiation facility. The closed circuit represents the storage ring (typical diameter around 300 m). The injection-accelerating system (Linac + Booster) is located outside the storage ring, a polygon with bending magnets at its vertices. Bunches of charged particles (electrons or positrons) circulate in a storage ring. The bending magnets (BM), positioned at the ring's vertices, deflect the electron trajectories, thereby producing synchrotron radiation that escapes forward. Insertion devices (ID) are strategically placed in the straight sectors to generate specific synchrotron light. The radiofrequency cavity (RF) of the storage ring is also indicated, along with the focusing magnets in an insertion device, which forces the particles to execute small oscillations, producing intense beams of radiation. This radiation subsequently traverses a series of optical components, including a monochromator and a focusing device, to ensure the delivery of a beam of radiation with the requisite properties to the sample. Figure adapted from the book [59].

Wide-Angle X-ray Scattering (WAXS) (Figure 2.15) was performed at a synchrotron source. This thesis employs two geometries: transmission WAXS (Figure 2.15 (a)) used for bulk samples (powders, thick films or capillaries) and grazing incidence wide-angle X-ray scattering (GIWAXS) (Figure 2.15 (b)), which is particularly suitable for thin films or deposited materials onto solid substrates.

In transmission WAXS (Figure 2.15 (a)), the beam reaches the sample perpendicularly to the sample surface, and the scattered intensity is collected after being transmitted through the sample. In GIWAXS (Figure 2.15 (b)), the incident X-ray beam reaches the sample surface with a certain small incidence angle, α_i, relative to the surface, typically less than the critical angle for total external reflection of the substrate. This allows for enhanced surface sensitivity and reduces the contribution of the scatter from the substrate. The scattering vector can be decomposed into components parallel (q_y) and perpendicular (q_z) to the surface, providing information about the in-plane (structural ordering perpendicular to the substrate) and out-of-plane (structural ordering parallel to the substrate) structural correlations, respectively[59]. Both WAXS and GIWAXS are generally used to identify or determine the crystalline structure of the material or materials of the sample.

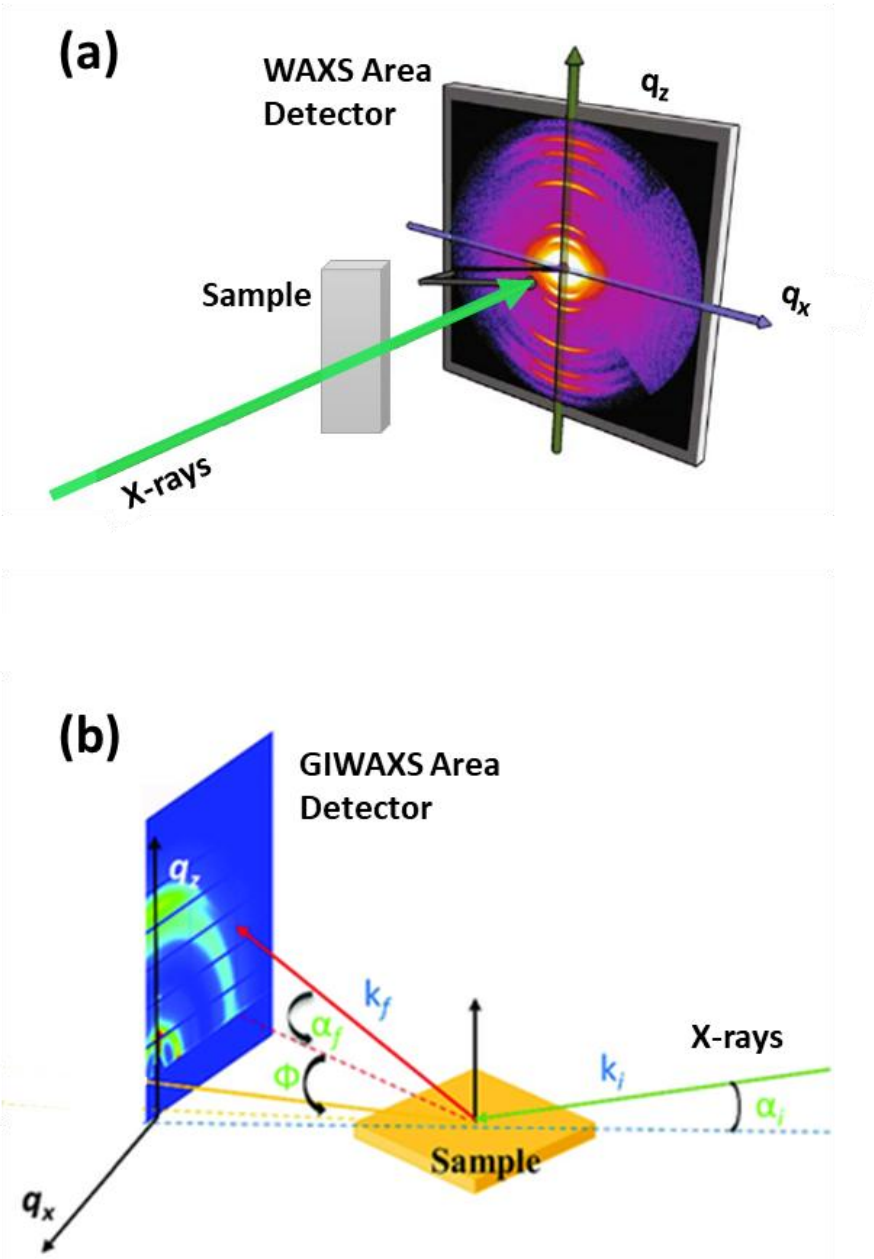

Figure 2.15. Schematics of X-ray scattering geometry. **(a)** WAXS scattering geometry, where the sample intercepts the incident X-ray beam, and the scattering is detected with a 2D detector. **(b)** GIWAXS scattering geometry where the sample is tilted at a small angle of incidence α_i with respect to the incident X-ray beam. The scattering is recorded using a 2D detector as a function of the exit angle α_f and the out-of-plane angle Φ. In both schemes, the specular and direct beams are blocked by a beam stop (represented by the grey arm) to avoid detector oversaturation. The colour code represents the scattered intensity in the 2D detector. Figure (a) adapted from [59] and (b) from [60].

In particular, WAXS and GIWAXS are valuable tools for characterising the crystalline structure of polymers. As mentioned in Chapter 1, unlike fully crystalline materials, the

presence of crystalline domains in a semicrystalline polymer coexists with amorphous regions. In such cases, XRD can be used to determine the crystal structure, degree of crystallinity and the average size of the ordered domains within the polymer matrix, among other parameters. In the context of fully crystalline systems, the coherence length, which is commonly estimated from the inverse of the width at half height of the Bragg peaks, corresponds to the particle size. However, in semicrystalline systems, the crystal size, or more accurately, the coherence length, is smaller than the particle size due to the amorphous content[61,62]. This reduction in coherence length is manifested as a broadening of the diffraction peaks. The broadening increases with increasing diffraction angle, which is related to the presence of lattice imperfections and finite domain sizes[61,62]. Consequently, the coherence length serves as a valuable metric for evaluating the quality and crystalline order of a material[62]. It can be estimated from the broadening of the diffraction peaks using the Scherrer equation (Eq. 2.4)[53,63]:

$$D = \frac{K \cdot \lambda}{\beta \cos(\theta)} \qquad \text{Eq. 2.4.}$$

where D is the crystallite size (typically in nanometres), K is the Scherrer shape factor or Scherrer constant (generally between 0.89 and 1; 0.9 for approximate sphericity)[61], λ is the wavelength of the X-ray used in the experiment (in nanometres), β is the full width at half maximum (FWHM) of the diffraction peak (in radians)[63].

In this work, WASX and GIWASX experiments were performed at the BL11 NCD-SWEET beamline of ALBA Synchrotron. ALBA is a third-generation synchrotron. The incident monochromatic X-ray beam energy was set to 12.4 keV, equivalent to 0.103 nm, utilising a Si (1 1 1) channel-cut monochromator, with a beam size of 30 μm × 120 μm (vertical × horizontal). In the context of grazing incidence experiments, the sample was initially positioned horizontally with its surface parallel to the X-ray beam at a height that intercepted half of the beam intensity. Subsequently, the sample was tilted to achieve an incidence angle between the sample surface and the beam. The exposition time was optimised to maximise the number of counts while avoiding saturation of the detector, typically set to 5 seconds for each incident angle. The incidence angle, α_i, for the X-rays was set between 0.1-0.4°. The critical angle of silicon is 0.1°, and for angles larger than 0.4°, the scattering mainly arises from the substrate itself. WAXS and GIWAXS intensities were

recorded on a LX255-HS area detector from Rayonix®, which consists of a pixel array of 5760 × 1920 pixels (vertical × horizontal) with a pixel size of 44 × 44 μm^2. The data are expressed as a function of q, calibrated using Cr_2O_3 as the standard sample. This calibration yielded a sample-to-detector distance that was found to vary slightly depending on the beamtime (measurements have been made at four different beamtime campaigns), within a range from 0.113 to 0.211 m. 2D GIWAXS patterns were corrected from background scattering, azimuthally integrated, i.e., the intensity counts are summed over all azimuthal angles, and analysed using the pyFAI package[64]. The azimuthal integration of the 2D images between the angles $\chi = 0^o$ and $\chi \approx 90^o$ resulted in 1D (Figure 2.18) scattering patterns, which are presented in this thesis after background subtraction and analysis by the Origin program.

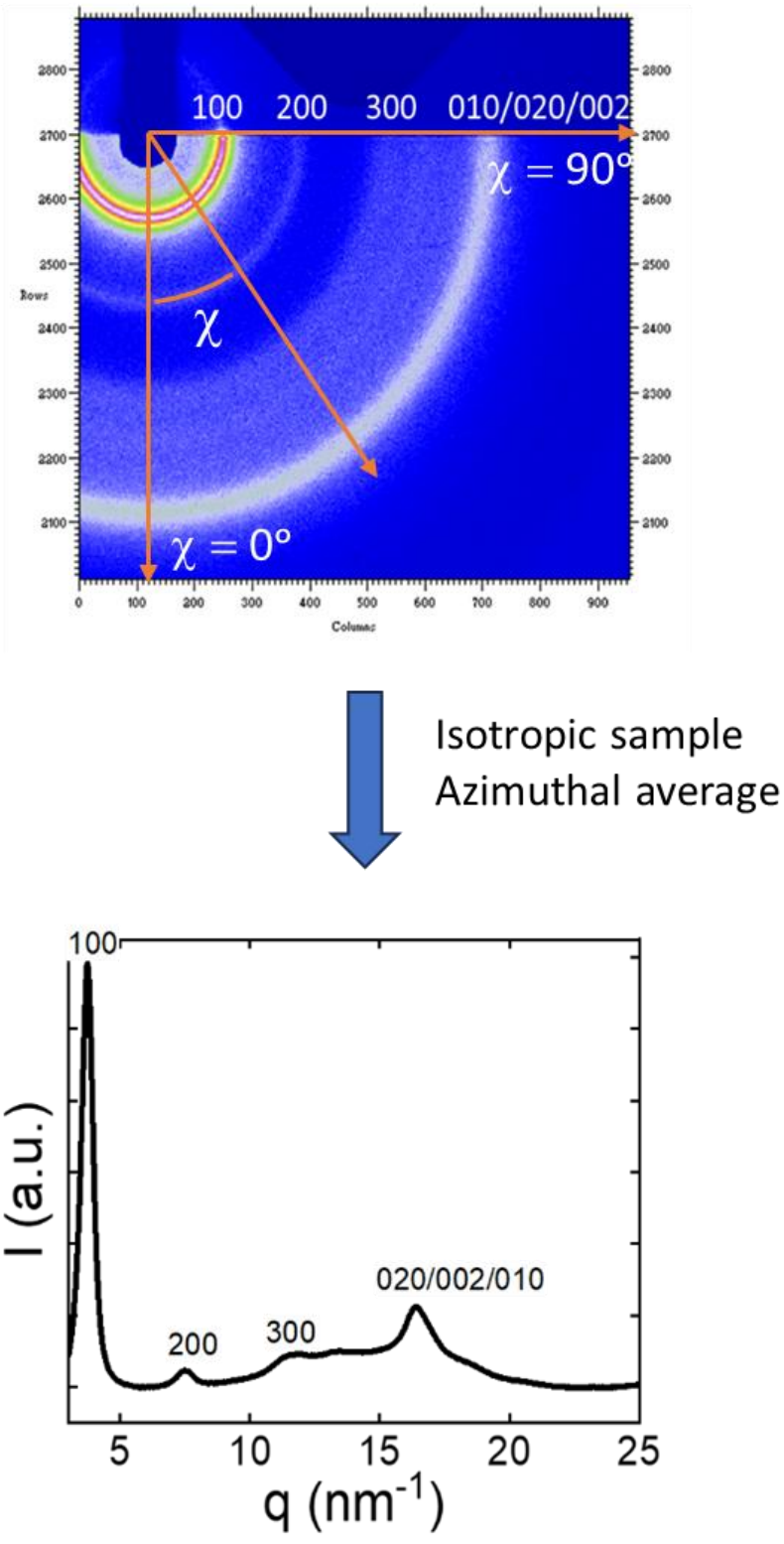

Figure 2.16. X-ray diffractogram of a P3HT sample showing the defined maxima corresponding to an isotropic sample. For isotropic samples, the scattering can be azimuthally integrated to produce a plot of integrated scattered intensity versus wave vector transfer.

X-ray studies on NPs in this work were performed in GIWAXS geometry. For these experiments, NPs were deposited from aqueous dispersions onto silicon wafers by drop casting and allowed to dry for several days under ambient conditions or gently heated in a vacuum. WAXS in transmission geometry was performed to study the structure of free-standing PVDF films or deposits.

2.4.2. Atomic Force Microscopy (AFM)

The development of Atomic Force Microscopy (AFM) can be traced back to the invention of the Scanning Tunnelling Microscope (STM) in 1982 by Gerd Binnig and Heinrich Rohrer at IBM Zurich Research Laboratories[65]. Building on the principles of STM, the AFM was later developed by Binnig, Quate, and Gerber in 1986 at Stanford University in collaboration with IBM San Jose Research Laboratory[66]. It allows high-resolution imaging of the surface of materials at the nanometre scale, revealing the topography and surface properties of materials in various environments (vacuum, atmosphere, and liquid)[67–69]. AFM relies on the mechanical interaction of an extremely thin probe, called a cantilever[67,70]. This cantilever contains an ultra-small mass nanometric tip typically composed of silicon or nitride silicon[67,70], which, as it approaches the surface, is affected by interaction forces, including van der Waals, electrostatic, and contact forces (Figure 2.17). These forces can cause a deflection at the cantilever. This deflection is then used to generate a topographic image of the surface[66,67,70]. While the AFM was originally developed to measure topographic images, it can also provide information about physical processes at the nanoscale. For instance, appropriate analysis of the interaction between the tip and the sample may provide information about mechanical properties[71], dielectric interactions[72], ferroelectric response[73,74], and electrical conductivity[75,76], among others[70].

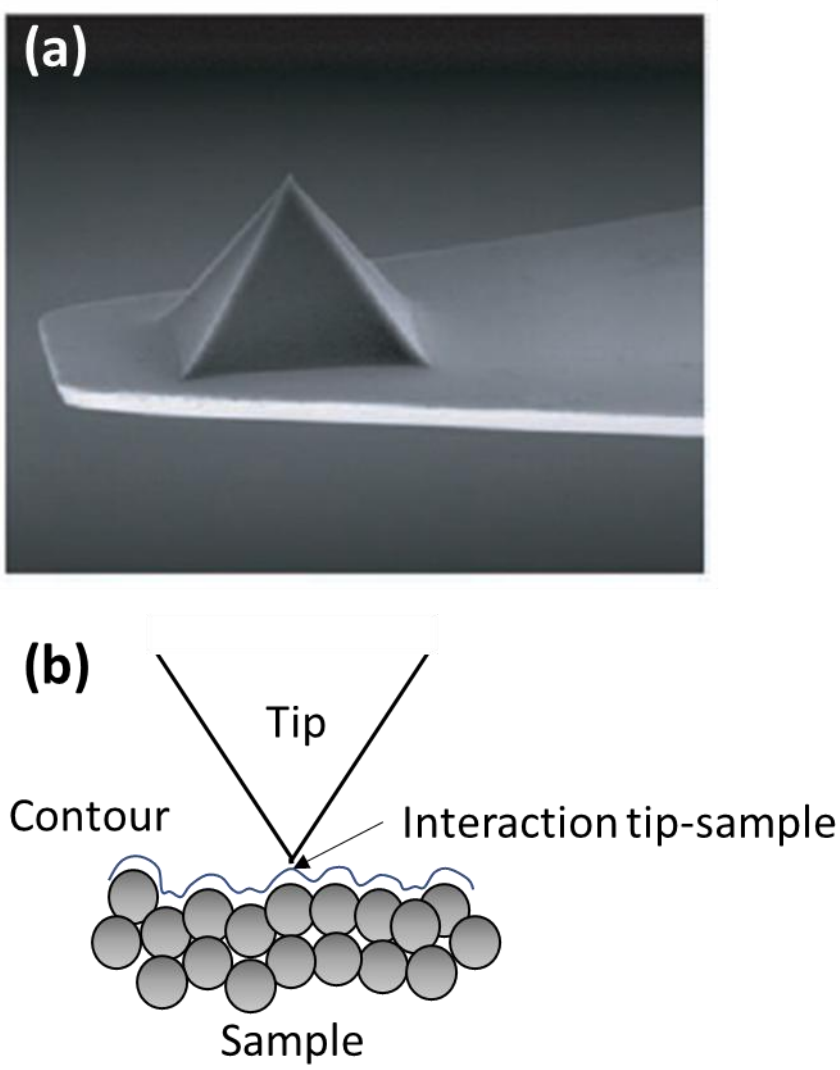

Figure 2.17 (a) Scanning electron microscope images of the tip of a rectangular cantilever of a silicon nitride contact mode AFM probe. Images courtesy of NanoWorld AG (http://nanoworld.com)[70] and **(b)** Schematic diagram of sample-tip interaction. The tip follows a contour to maintain a constant force between the tip and the sample (AFM, sample and tip are either insulating or conducting). The tip apex determines the resolution.

The basic operation of an AFM is composed of three fundamental steps:

1. Tip-sample interaction: This process involves the repetitive movement of the tip along the surface of the sample. The tip of the cantilever approaches the sample and experiences forces that are dependent on the distance between the tip and the surface[67,70]. These forces can attract or repel the tip, generating a deflection that is subsequently detected with great precision[66,67,70].

2. Deflection detection: A laser beam is focused on the back of the cantilever (Figure 2.18). This beam is reflected by a photodiode detector[70]. The deflection of the cantilever results in a change in the position of the laser on the detector. Monitoring the laser position allows for the reconstruction of the topography of the sample[70].

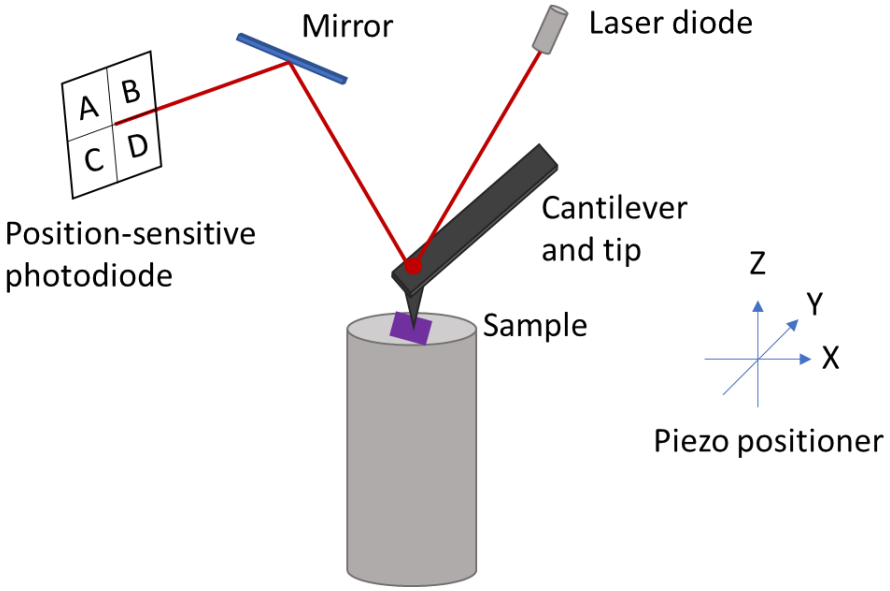

Figure 2.18. Schematic diagram of how the AFM works. Normal and torsional movements of the cantilever measure normal and lateral forces acting on the tip. A light beam is reflected from the back of the cantilever. Angular deflections of the laser beam are measured with a position-sensitive detector (4-quadrant photodiode). The signal on the z-axis is proportional to the normal force, and the signal on the y-axis is proportional to the torsional force. Figure from reference[77].

3. Image generation: This is achieved through the utilisation of controlled scanning in the XY plane and continuous adjustment in the Z axis. This process enables the generation of a 3D image of the surface topography of the sample[66]. The procedure can be performed in different modes, such as contact and tapping modes, each of which is appropriate for distinct types of materials and surface features[66,70].
    - Contact mode: This mode constitutes the classical model. In this mode, the tip maintains consistent contact with the surface at a fixed deflection setpoint. This ensures a constant force between the tip and the sample (Figure 2.19). As topographic features are identified, the system generates feedback and moves the sample with respect to the tip to maintain the deflection constant.

The topographic profile can then be generated by recording the distance between the motion of the sample with respect to the tip[77]. This configuration is optimal for hard materials that can withstand pressure from the tip[67,70]. For soft materials, in contact mode, drag effects may be exerted over the surface sample, a phenomenon attributable to the higher mechanical modulus of the tip in comparison to that of the soft matter sample.

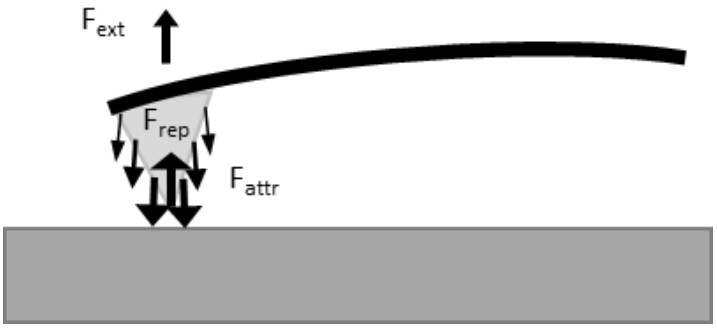

Figure 2.19. Equilibrium of forces in contact mode. The long-range attractive forces F_{attr} between tip and sample are balanced by the short-range repulsive force F_{repr} at the contact and the external force F_{ext} exerted by the cantilever bending. The bend is chosen to minimise the resulting force, but not to prevent a jump out of contact.

- Non-contact mode: The tip remains close to the surface without touching it, detecting long-range interaction forces. This mode is suitable for softer or more fragile materials[67,70].
- Tapping mode or intermittent contact mode (Figure 2.20): The tip oscillates at a specified frequency (generally around $3x10^5$ Hz), known as the resonant frequency, close to the sample surface. In this mode, the tip makes intermittent and brief contacts with the surface, enabling a controlled scanning of the surface[66,67,70]. As the tip approaches the surface, the interaction force between the tip and the sample dampens the vibration, causing a change in the oscillation amplitude[66,67,70]. When the tip encounters a topographic accident within the sample surface, such as a hole or a mountain, the distance between the tip and the sample will be altered, also affecting the frequency and the amplitude of the cantilever oscillation. A

feedback system is employed to adjust the height of the cantilever, maintaining the amplitude setpoint of vibration at a constant level. When the tip approaches the surface too closely, the repulsive force will be amplified, leading to an increase in oscillation frequency. Conversely, an increase in the attractive force experienced by the tip will decrease the oscillation frequency. The information obtained from this process is then utilised to generate a topographical image of the surface, line by line[66,70], minimising damage in soft samples. In this thesis, tapping mode is employed for the following reasons[77]:

- Less damage to the sample: The absence of constant contact with the surface, which is not the case in other modes of operation. This results in minimised wear and deformation of soft or sensitive samples.
- Better resolution: The tapping mode has been shown to provide enhanced resolution due to its high vibration frequency, which allows for the acquisition of images with higher lateral and vertical resolution. Additionally, it facilitates better differentiation of topographical features on surfaces with minimal height variation.
- Minimisation of image artefacts: The tapping mode has been demonstrated to minimise image artefacts that can distort contact mode images[66,67,78,79].

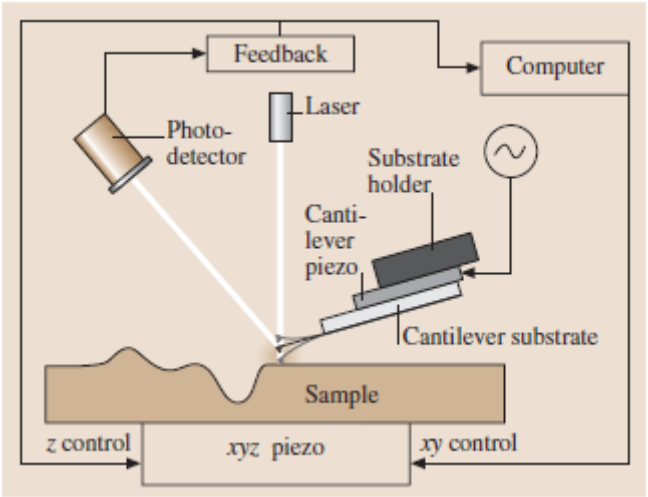

Figure 2.20. Schematic of tapping mode used to measure surface roughness. Figure taken from [67].

The technique is particularly useful for non-conducting nanoparticles, where techniques such as scanning electron microscopy (SEM) can have limitations[70].

In this thesis, we have employed a Multimode 8 AFM, equipped with a Nanoscope V software (Bruker, Karlsruhe, Germany) in tapping mode under ambient conditions. Tapping images were collected using gold-coated silicon probes (Tap300GB-G probes by BudgetSensors, Sofia, Bulgaria) (resonant frequencies = 300 kHz, k = 40 N/m). The scan rates ranged from 0.50 to 1.00 Hz. The measurements were performed with 512 scan lines. Different regions of the samples were scanned to ensure the representativeness of the morphology and size of the observed features. NPs were deposited by drop-casting and spin-coating on silicon wafers doped with arsenic (Neyco, Vannes, France), utilising the abovementioned conditions.

2.4.3. Dynamic Light Scattering (DLS)

The technique known as Dynamic Light Scattering (DLS) is used to determine the size and distribution of objects at the submicrometric range in a suspension through the speeds at which they move, rotate, and change conformationally[80,81].

A laser illuminates the liquid sample, and light is scattered by the objects suspended in the liquid. The fundamental components of the DLS technique are illustrated in Figure 2.21, which includes the laser beam, the colloidal suspension and the detector that receives the scattered light. The working principle of DLS is relatively simple. The objects in the liquid sample scatter the incident light (either dissolved macromolecules or suspended particles). The total scattered intensity measured by the detector is the result of the superposition of the scattered waves by each individual particle. The magnitude of this total scattered intensity varies as a function of time. The time dependency of the scattered intensity is analysed by a correlator, providing information on particle dynamics, particle diameter and particle distribution in the medium[81,82].

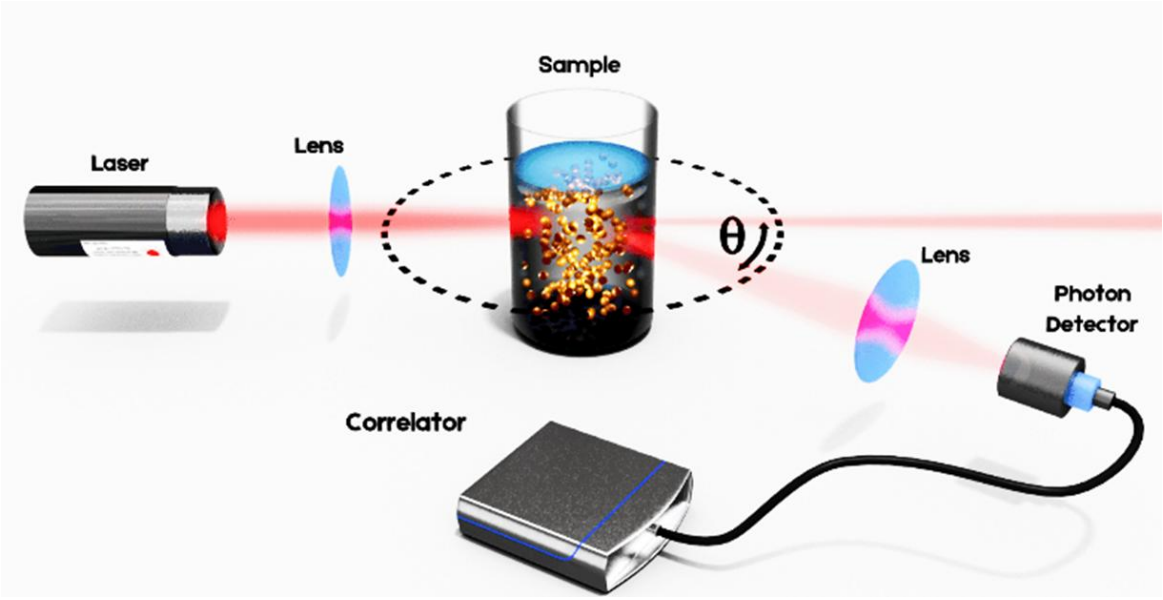

Figure 2.21. A schematic representation of the experimental setup for the light-scattering experiment. Adapted figure from the LS Instruments website [83].

If the particles move quickly, the intensity fluctuations exhibit high frequencies; if they move slowly, the fluctuations show smaller frequencies (Figure 2.22)[84]. The information obtained from the fluctuations through the digital correlator is used to obtain a mathematical function known as the scattered light intensity's time correlation function (Figure 2.22)[82].

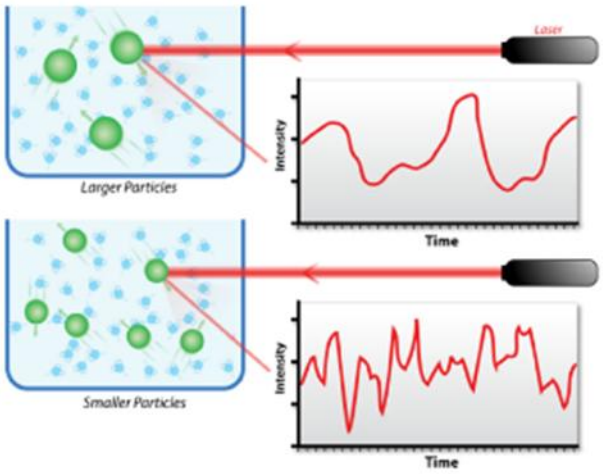

Figure 2.22. The hypothetical fluctuation of the scattering intensity of two distinct particle sizes: top for large particles and bottom for small particles[84].

To quantify the intensity correlations in time, the second-order correlation function $g^{(2)}(\tau)$ is used (Figure 2.23). Qualitatively, the autocorrelation function is a measure of how similar the intensity function is to itself when shifted by time τ. As the value of τ increases, the similarity of the intensity at the time (t+τ) disappears. $g^{(2)}(\tau)$ function is defined as follows[85]:

$$g^{(2)}(\tau) = \langle I(t) \cdot I(t+\tau) \rangle \qquad \text{Eq. 2.5.}$$

and it describes the correlations of the scattered intensity (*I*) measured at two different times, t and t+τ.

An intensity fluctuating rapidly with time would translate into a rapidly decaying correlation function (Figure 2.23). The characteristic time of this decay is directly proportional to the diffusion coefficient of the particles (D), which in turn is related to its hydrodynamic diameter of the particles (D_h)[86–89].

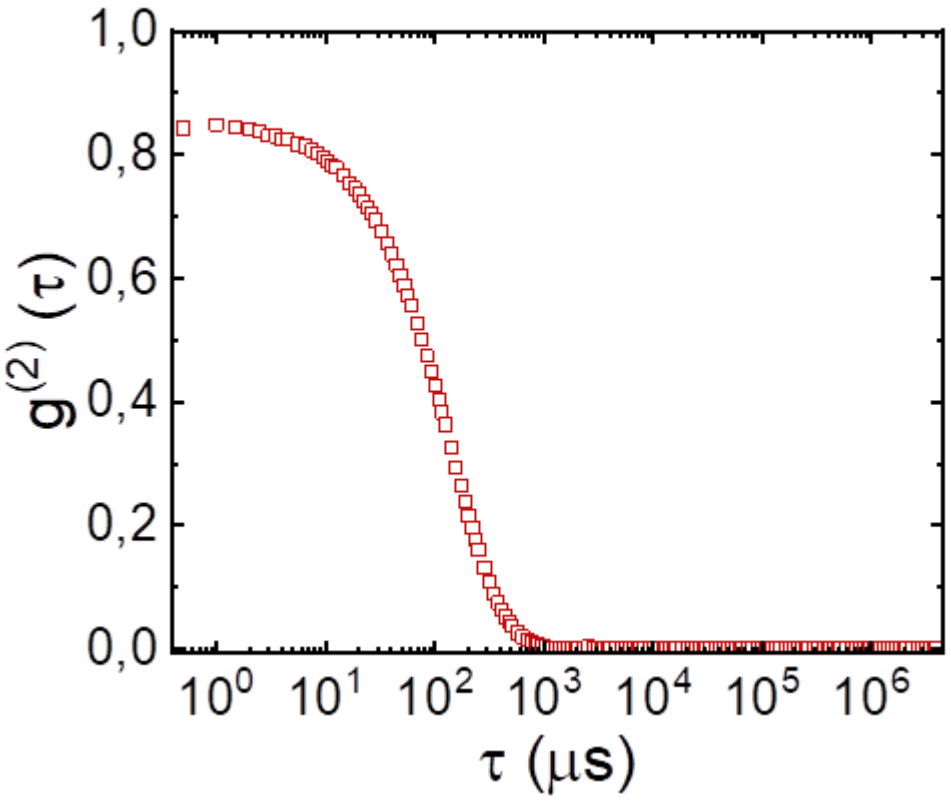

Figure 2.23. Example of a correlation function ($g^{(2)}(\tau)$) for a P3HT sample.

Similarly, a dispersed field correlation function (Figure 2.24) can be defined as:

$$g^{(1)}(\tau) = \langle E(t) \cdot E^*(t+\tau) \rangle / \langle E(t) \rangle^2 \qquad \text{Eq. 2.6.}$$

$g^{(2)}(\tau)$ and $g^{(1)}(\tau)$ are related by the Siegert relationship[84]:

$$g^{(2)}(\tau) = B + b\,[g^{(1)}(\tau)]^2 \qquad \text{Eq. 2.7.}$$

In equation 2.7, baseline *B,* which should take a value of around 1, and the *b* is related to the system optics and detector alignment[84].

Depending on whether the sample is monodisperse or not, two approaches can be followed to obtain the correlation function's size distribution and mean diameter: cumulant analysis for one population and multiple exponential fits (for more populations).

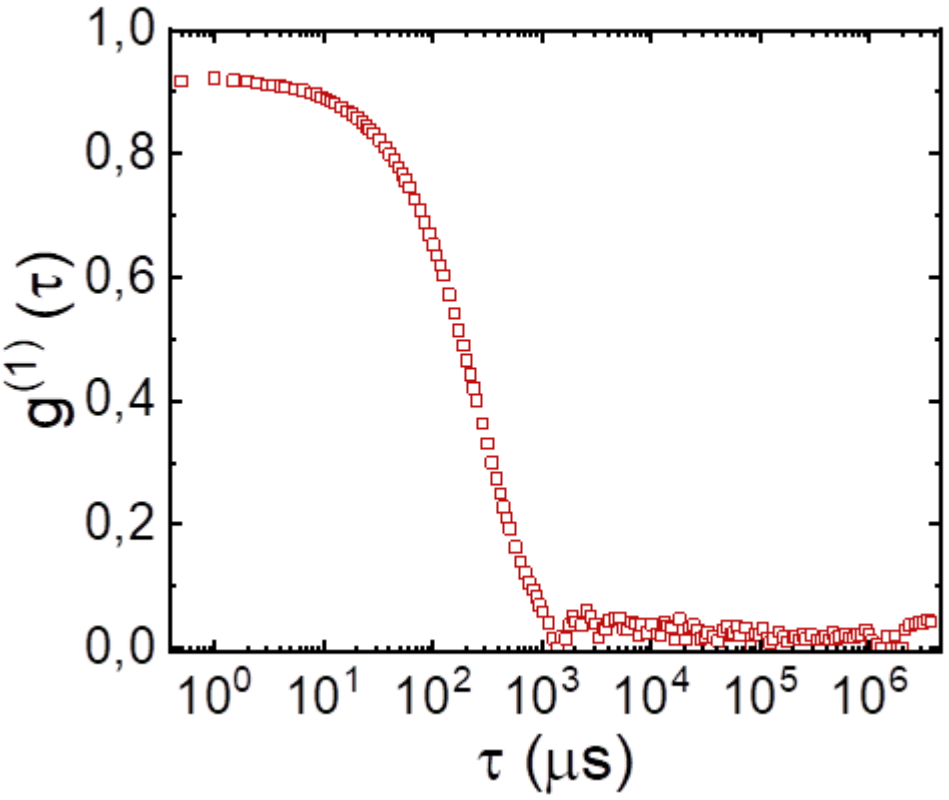

Figure 2.24. Example of a correlation function ($g^{(1)}(\tau)$) obtained through $g^{(2)}(\tau)$ for a P3HT sample.

In the case of cumulant analysis[80–82,86], particle diameter information is extracted by decomposing the correlation function into its statistical moments. In this way, the decay section is adjusted (Figure 2.25). The first-order correlation function, $g^{(1)}(\tau)$, is expanded as the exponential of a series of Taylor, as follows:

$$g^{(1)}(\tau) = \exp\left(-\Gamma\tau + \frac{\mu_2}{2!}\tau^2 - \frac{\mu_3}{3!}\tau^3 + \ldots\right) \qquad \text{Eq. 2.8.}$$

Typically, a third-degree polynomial is fitted. Γ is the mean decay value related to the translational diffusion coefficient by Eq. 2.9, defined as the product of the translational diffusion coefficient by the squared scattering vector[80,82], μ_2, and μ_3 are the cumulants describing the deviation of the distribution from a monodisperse distribution (polydispersity)[87–89]. μ_2, and μ_3 only depend on the particle size distribution and not on

experimental parameters such as delay time. Specifically, μ_2 is related to the variance and the width of the size distribution, while μ_3 is related to the skewness of the distribution[86–89].

$$\Gamma = Dq^2 \qquad \text{Eq. 2.9.}$$

From these values, a polydispersity (Q) can be defined as[80,82,86]:

$$Q = \mu_2 \Gamma^2 = \mu_2/\mu_1^2 \qquad \text{Eq. 2.10.}$$

This approach is highly accurate when working with small and monodisperse particles, as the diffusion dynamics of these particles produce a simple decay in the correlation function. However, in multiple population systems or with larger particles, the scattering behaviour is more complex because anisotropic scattering is observed (i.e., the intensity of the scattered light depends on the scattering angle). This results in the correlation function deviating from a single exponential decay, instead following a combination of multiple exponentials. Consequently, the accuracy and precision of the cumulant method for describing such systems are diminished.

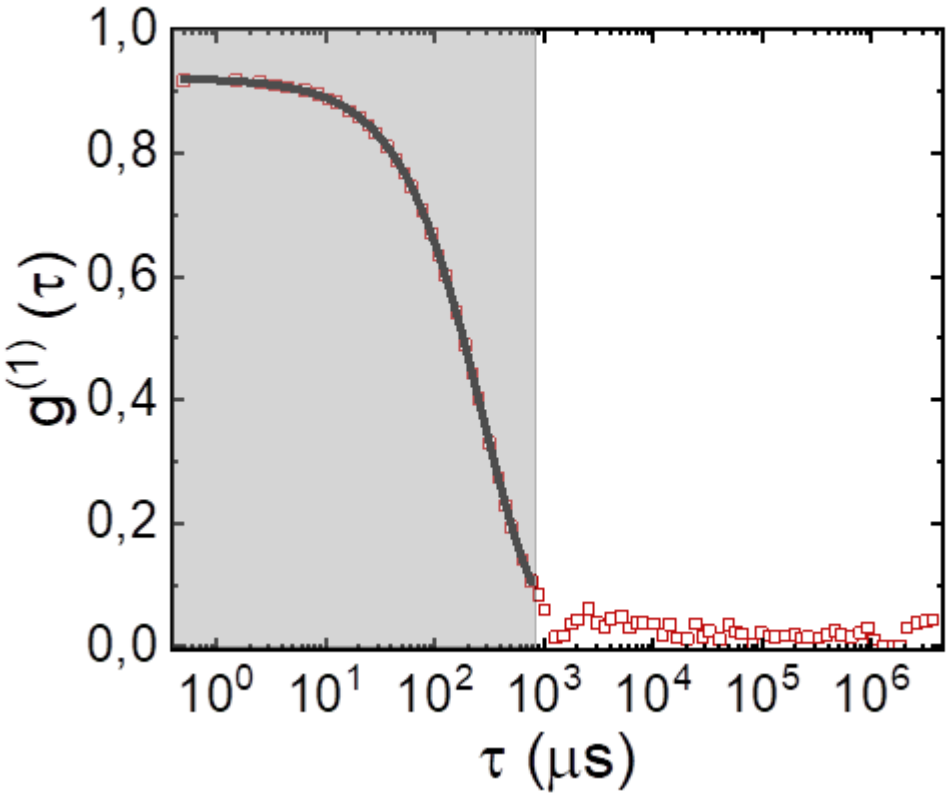

Figure 2.25. Example of g(1)(τ) for a P3HT suspension. The shaded area indicates the section of the curve used to adjust the theory. Half of the points are represented.

The decay rates obtained from the analysis of the correlation function allow for estimating the hydrodynamic diameter as the average z-size of the particles (D_h) using the Stokes-Einstein equation and, considering the particles as rigid spheres[80,82,86]:

$$D_h = \frac{k_B T}{3\pi\eta D} \qquad \text{Eq. 2.11.}$$

where k_B is Boltzmann's constant, T is the temperature, η is the viscosity, and D is the diffusion coefficient. The diffusion coefficient is a value that gives information on how a particle diffuses in a fluid and depends on factors such as the diameter and shape of the particle and its surface structure, concentration, or ionic strength.

However, from a physical point of view, obtaining the hydrodynamic diameter as the number size average (D_n) is more appropriate since it can be compared with the values

obtained by alternative experimental techniques such as AFM[80,82]. Assuming a log-normal distribution shape, a simple relationship exists between D_h and the polydispersity index, Q, given by the expression[80]:

$$D_n = \frac{D_h}{(1+Q)^5} \qquad \text{Eq. 2.12.}$$

In the second approach, a multiple exponential fit is mainly used when the system is suspected to contain a mixture of particles with assorted diameters, although it can also be used for samples where there is a single population. The model assumes that the system is composed of different spherical particle sizes that do not interact with each other and that each population of particles possesses a well-defined and distinct diameter[85]. The particles are assumed to behave independently, and the size distribution can be described as a sum of discrete contributions from each species[85]. In this case, the correlation function is fitted by a linear combination of exponential functions, each corresponding to a species of a particular size:

$$g^{(1)}(\tau) = \sum_i A_i e^{-\Gamma_i \tau} \qquad \text{Eq. 2.13.}$$

where A_i is the intensity fraction corresponding to species with a particular particle diameter, and Γ_i is related to their diffusion coefficient.

Eq. 2.13 describes the case of the correlation function from an ensemble of particles with discrete diameters. In general, real samples have a continuous size distribution, and this analysis is employed to obtain a more detailed particle size distribution, which is especially useful for polydisperse samples. The continuous distribution is obtained by the Tikhonov regularisation method[90,91]. This is achieved by transforming the discrete information into a continuous size distribution. Using the correlation function obtained, a regularisation method is applied:

$$I\ (R_h) = \text{Regularisation}\ (g^{(2)}(\tau)\ ) \qquad \text{Eq. 2.14.}$$

In this procedure, several factors must be taken into account. Primarily, the density and viscosity of the buffer need to be considered to obtain the size distribution. Furthermore, the size range in which the fit is desired, as well as the confidence level, which determines the width of the distribution, can be selected. As shown in Figure 2.26, an example is given, and the fit is performed to obtain a size distribution.

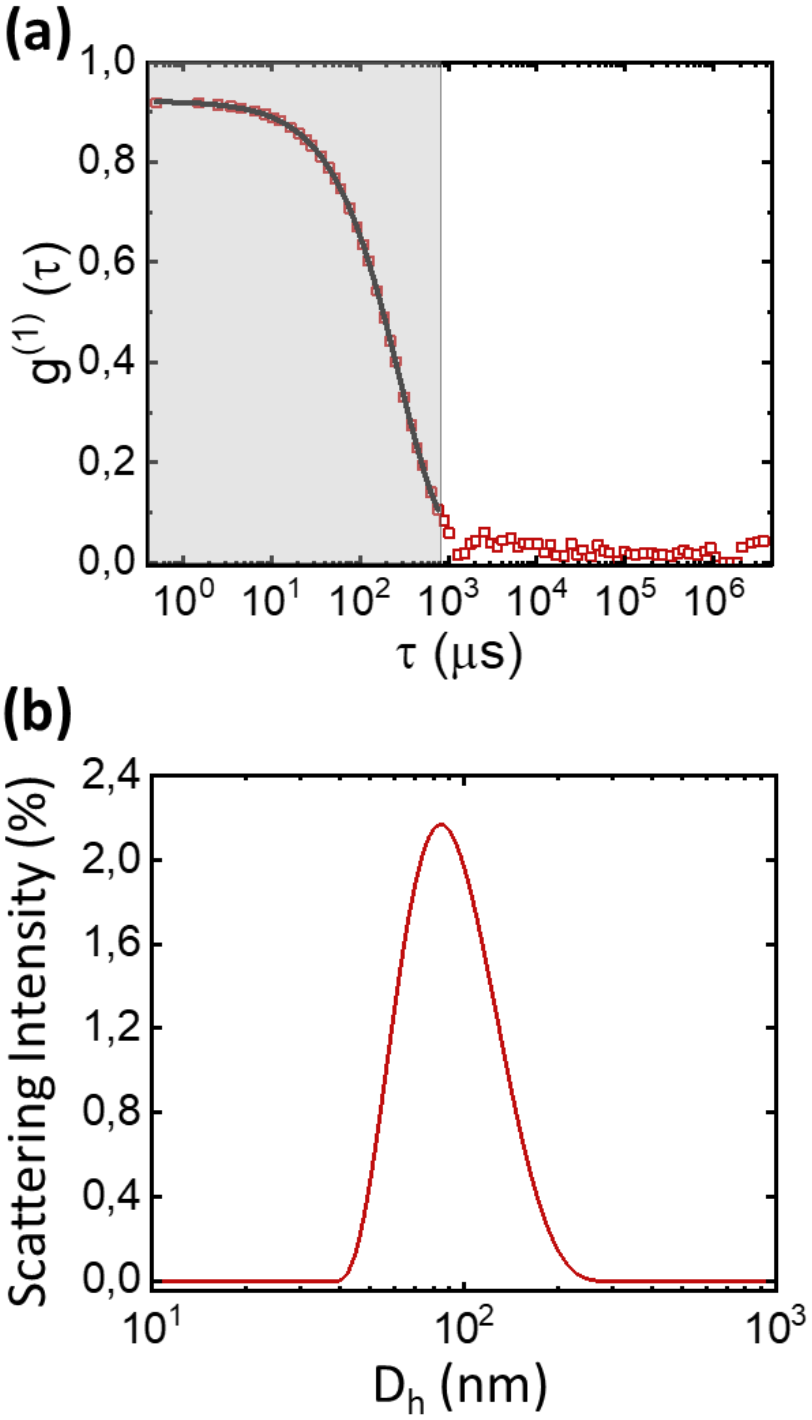

Figure 2.26 (a) Example of a fit using the Tikhonov method with a size range of 8 nm to 1000 nm and a confidence level of 70%. Half of the points are represented. **(b)** Size distribution curve obtained from the Tikhonov method.

In this thesis, backscattering has been measured as it allows the laser to not penetrate through the entire sample, thus minimising the occurrence of multiple scattering. This configuration is particularly advantageous when dealing with concentrated samples, without excessive signal loss. Furthermore, backscattering minimises the laser path length through the sample, which reduces the scattering by the medium and the effects of light absorption by the solvent, which can obscure signals from particles of interest. Additionally, using backscattering is advantageous for studying samples with high turbidity, as it minimises the influence of large particles that could scatter light in multiple directions.

The DLS measurements were performed using a Zetasizer Nano ZS instrument (Malvern Instruments, Worcestershire, UK). Before each measurement, an internal control of the instrument was performed with distilled water to ensure the absence of correlated signals. Disposable cuvettes (2.5 mL, BrandTech) were used to perform the measurements. The Nano ZS instrument incorporates non-invasive backscattering optics (NIBS) and homodyne detection. The sample was illuminated with a laser at a constant power output of 633 nm, and the intensity of the scattered light was measured at an angle of 173° using an avalanche photodiode. The measurements were conducted at a temperature of T = 25 °C and were preceded by sonication of the samples to eradicate any potential aggregates. To ensure the reproducibility of the results, three experiments were performed for each sample, with multiple runs (between 10 and 20) being conducted to obtain an average size. The data processing was carried out using the SEDFIT program[92]. Cumulant analysis and Tikhonov analysis were performed using the SEDFIT program. The approximations of the cumulant analysis are made to a second-degree polynomial.

2.4.4. Optical techniques

Optical spectroscopies are based on the analysis of the interaction of electromagnetic waves with wavelengths in the visible or ultraviolet range with the matter that constitutes the sample (see Figure 2.27). When a beam of light strikes a medium, the molecules or atoms

that comprise it can absorb part of that energy, transform it, re-emit it in the form of fluorescence or other emissions, or scatter it in different directions (Figure 2.27).

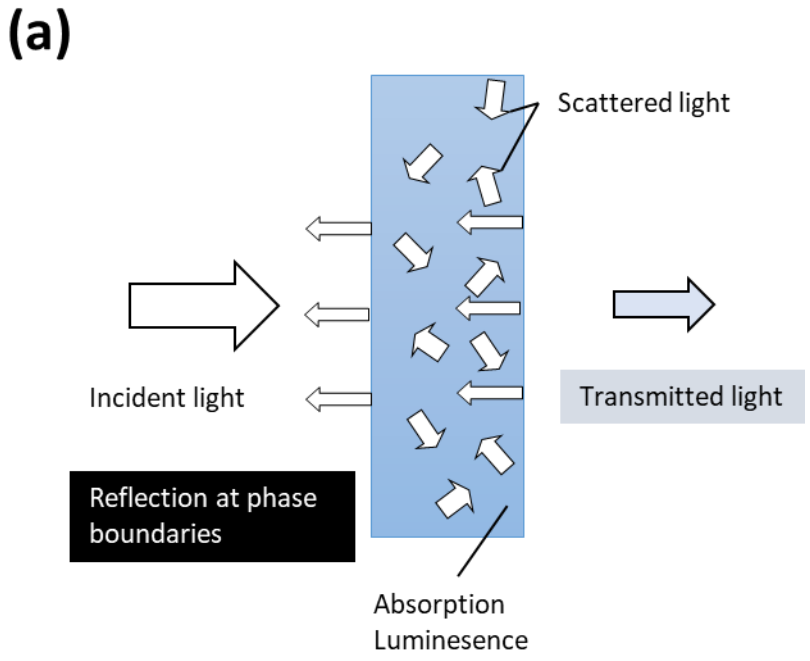

Figure 2.27. Phenomena resulting from the interaction of light with matter are defined by the Lambert-Beer law.

In the context of this thesis, a variety of spectroscopic techniques have been used to characterise the optical properties of the prepared NP suspensions. Of particular interest was the interaction of light with the NPs, including phenomena such as absorption and photoluminescence. These techniques facilitate the analysis of the interaction of visible and ultraviolet light with NPs, thereby providing insights into their electronic structure, morphology, and optical properties. The information obtained through these techniques is fundamental to understanding the absorption and emission mechanisms as a function of the composition, morphology, and size of the NPs.

2.4.4.1. Ultraviolet-Visible Spectroscopy

Ultraviolet-Visible spectroscopy (UV-Vis spectroscopy) studies the absorption of light with wavelengths in the ultraviolet and visible range of the electromagnetic spectrum[93,94]. If

the incident light has a wavelength corresponding to transitions between the electronic states of atoms or molecules of the illuminated sample, it is absorbed, and the electronic transition occurs[93,94]. In the case of polyatomic molecules, quasicontinuous spectra are obtained due to the overlap of vibrational transitions. Moreover, the vibrational structure can become indiscernible in solution due to interactions with the solvent, resulting in broadened electronic spectra.

The relationship between the attenuation of light passing through a medium and the properties of that material, as well as the concentration of the substances that absorb or scatter that light in the medium[93], is dictated by the Lambert-Beer law (Eq. 2.15).

The usual expression for the Beer-Lambert law for monochromatic radiation in the case of molecule solutions or nanoparticle dispersions is as follows[95]:

$$A = \log\left(\frac{I_0}{I}\right) = \varepsilon(\lambda) l c_0 \qquad \text{Eq. 2.15.}$$

Where: A is the absorbance (dimensionless magnitude), defined as the logarithm of the ratio between the incident (I_0) and transmitted light intensities (I), at a wavelength λ, and c_0 is the molar concentration ($mol \cdot L^{-1}$) of the substance, l is the optical path length of the cell, and $\varepsilon(\lambda)$ is the molar absorptivity or molar extinction coefficient ($mol^{-1} \cdot L \cdot m^{-1}$), a constant which only depends on the nature of the molecule and the radiation wavelength[93,95].

In a UV Vis experiment, a spectrometer records the intensity of the transmitted light through a sample at different wavelengths and presents the logarithm of the ratio between the transmitted intensity and the incident one, resulting in a plot of absorbance (A) versus wavelength (λ), which constitutes the absorption spectrum.

In this thesis, the UV-Vis absorption technique is utilised in the 200 to 800 nm wavelength range to identify absorption bands associated with the nanostructure of P3HT in the form of NPs. All spectra were normalised so that the maximum of each spectrum was set to 1 and the minimum to 0.

UV-Vis spectroscopy enables the band gap energy (E_g) of a semiconductor material to be determined by analysing the absorption edge using the Tauc diagram. This method is based on the relationship between the optical absorption coefficient (α) and the photon

energy (hν). For indirect allowed transitions, this relationship is described by the following equation:

$$\alpha h\nu = A(h\nu - E_g)^{n/2} \qquad \text{Eq. 2.16.}$$

where *A* is a proportional constant depending on the transition probabilities and *n* is an exponent characterising the electronic transition nature (*n* = 4 for indirect allowed transitions in semiconductors such as polymers, *n* = 1 for direct allowed transitions, *n* = 2 for indirect forbidden transitions and *n* = 1/2 for direct forbidden transitions). As shown in Figure 2.28, to determine E_g, a graph of $\alpha h\nu^{n/2}$ is constructed as a function of photon energy (hν), and E_g is determined by extrapolating the linear part of the graph to the intersection with the energy axis (abscissas).

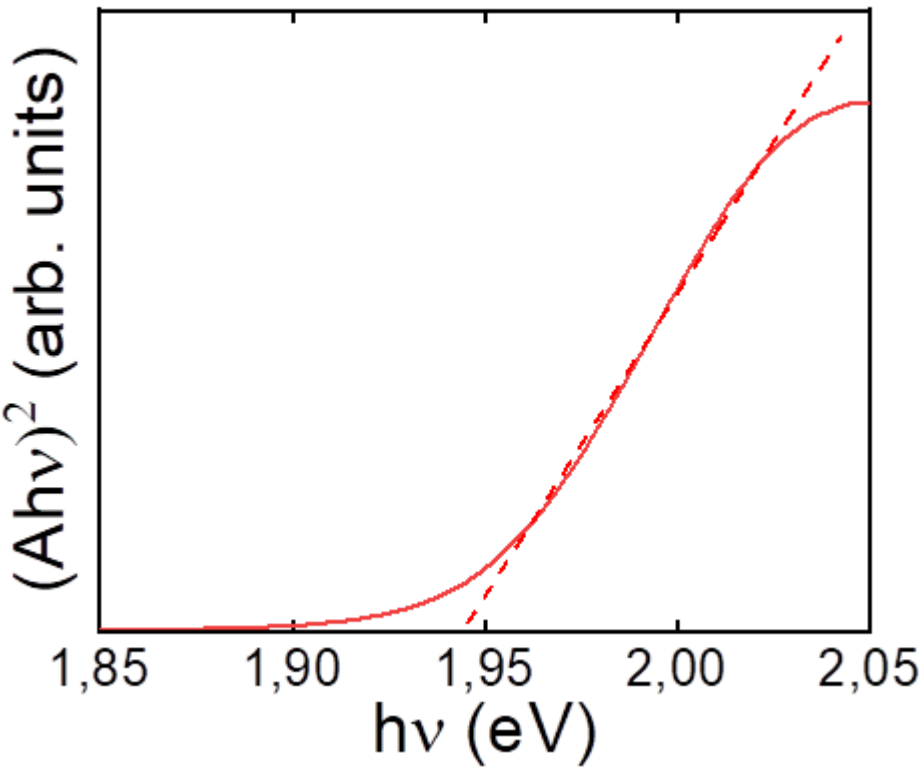

Figure 2.28. Tauc plot for a type of P3HT NPs prepared by miniemulsion.

Furthermore, the E_g value obtained from the Tauc plot can be used to estimate the conduction band edge (E_{CB}) and valence band edge (E_{VB}) potentials of the semiconductor using its electronegativity. These parameters are essential for evaluating the material's ability to induce photochemical reactions as they determine the energy available for oxidation and reduction processes. The equations for estimating E_{CB} and E_{VB} are as follows:

$$E_{CB} = \chi - E^e - 0.5 \cdot E_g \quad \text{Eq. 2.17.}$$

$$E_{VB} = E_{CB} + E_g \quad \text{Eq. 2.18.}$$

For organic polymers such as P3HT, a common approximation is based on the theoretical absolute electronegativity of the constituent monomer (χ), with an approximate value of 3.79 eV, and the energy of the free electrons on the hydrogen scale ($E^e \approx 4.5$ eV). This information is crucial for understanding the photocatalytic mechanism, as the position of the energy bands determines the ability of the semiconductor to generate redox species with the appropriate energy potential for pollutant degradation.

Also, UV-Vis spectroscopy has been used to estimate the concentration of MB dissolved in water during photocatalysis experiments with a semiconducting polymer. The concentration of MB in the solution is directly proportional to the absorption at the band corresponding to a wavelength of 665 nm, as indicated by equation 2.19:

$$A(665) = \varepsilon(665) \cdot c \cdot l \quad \text{Eq. 2.19.}$$

where $A(665)$ denotes the measured absorbance at 665 nm, $\varepsilon(665)$ is the absorption coefficient of MB, with a value of 0.190 $mg^{-1} \cdot L \cdot cm^{-1}$, c is the concentration in $mg \cdot L^{-1}$, and l is the path length in cm. The optical absorption experiments were conducted utilising a double-beam Shimadzu UV-3600 Spectrophotometer (Duisburg, Germany) on liquids contained in quartz cuvettes with 5 mm path length (100QS, HELLMA Analytic, LineLab, S.A., Barcelona, Spain) in the wavelength range from 200 nm to 800 nm. The spectrophotometer is interfaced to a personal computer loaded with the UVProbe software. The baseline was obtained by scanning two clean quartz windows filled with the corresponding solvent.

2.4.4.2. Fluorescence Spectroscopy

Fluorescence spectroscopy, or emission spectroscopy, is an analytical characterisation technique based on the detection of part of the light emitted by a substance after it has been excited at a specific wavelength, usually ultraviolet or visible light[84,96–99]. This technique is widely used in the study of semiconductors[84,96,97] because it can provide information about the electronic structure[84,96,99], chemical environment[84,96,97,99], and intermolecular interactions[84,96–99] within the sample.

Figure 2.29 describes the components of a fluorescence spectrometer[84,96–99]. A light beam with a specific wavelength (typically UV or visible) is absorbed by the sample. The absorbed energy excites the electrons of the sample to a higher-energy excited state (Figure 2.30)[84,96–99]. The excited electrons of the molecule in the sample are energetically unstable with respect to the fundamental state and rapidly relax to their ground state (Figure 2.30). This process may result in the emission of energy in the form of photons with lower energy than the absorbed energy, a process referred to as the "radiative process", leading to light emission of longer wavelengths. The wavelength of this emitted light depends on the energy difference between the excited and ground states[84,96–99]. These transitions can be visualised as vertical transitions in the sense that they involve electronic motions (faster than nuclear, with characteristic times of the order of 10^{-7}-10^{-10} s), i.e., in terms of the Franck-Condon principle (Figure 2.30).

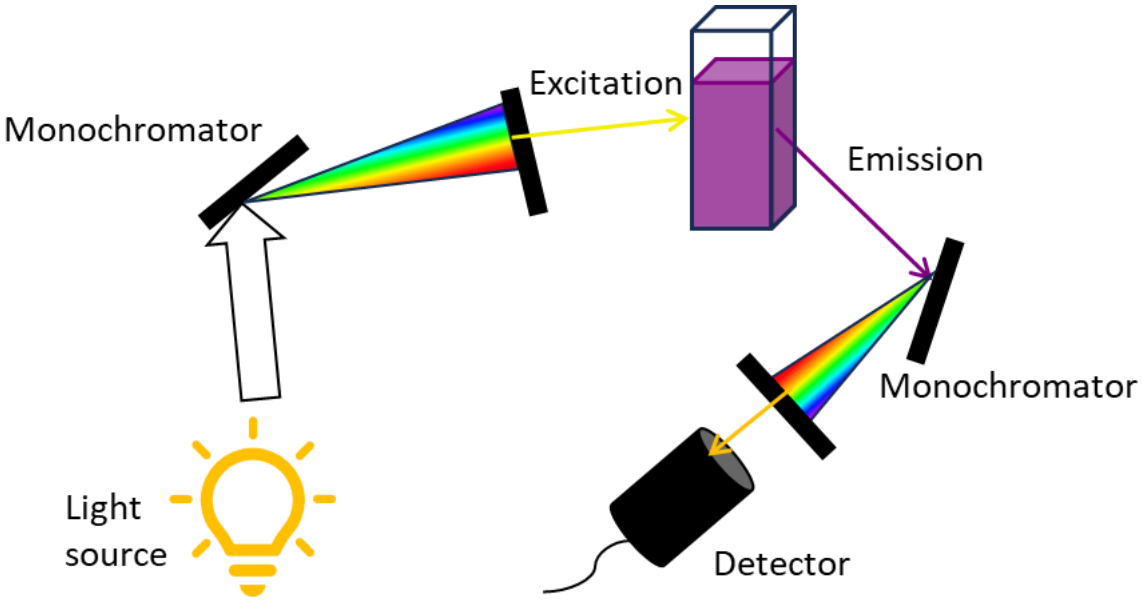

Figure 2.29. Schematic diagram of a fluorescence spectrometer.

In a fluorescence spectrometer, the intensity of emitted light for each wavelength is recorded. In cases where there is minimal difference in the nuclear configuration of the atom nuclei, the most intense emission is 0-0 between the lowest vibrational state of the excited state and the lowest vibrational state of the ground state. In other words, if the molecular structure changes little after excitation, it can relax directly to the lowest vibrational level of the ground state without losing much energy in vibrational rearrangements. Conversely, when the vibrational spacing is analogous in the ground and excited electronic states, the absorption and emission spectra are mirror images. The shift of the emission maximum relative to the absorption maximum is known as the Stokes shift, which is attributable to the difference in geometry between the excited and ground states. This shift can also be caused by interaction with the medium.

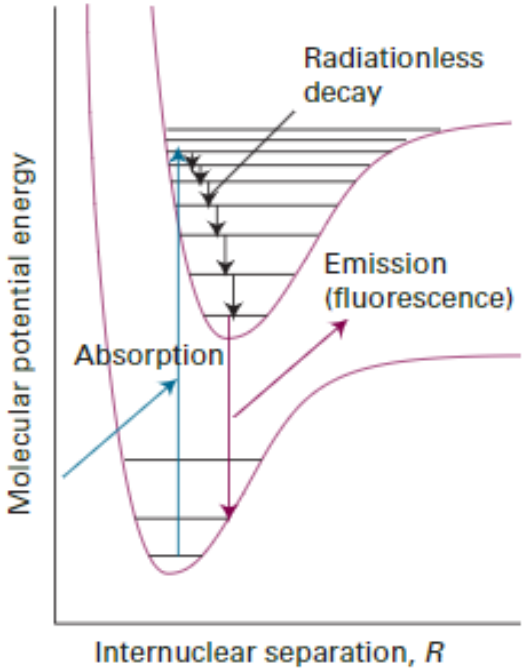

Figure 2.30. The following steps lead to the phenomenon of fluorescence. Following the initial absorption stage, the upper vibrational states undergo radiationless decay by releasing energy into the surrounding environment. This is then followed by a radiative transition from the vibrational ground state of the upper electronic state[93]

Fluorescence spectroscopy can detect extremely low concentrations of fluorescent molecules[84,96–99] and it is used in a wide range of fields, particularly useful for studying the optical properties of semiconductor NPs and functionalised NPs[84,96]:

- The relaxation dynamics of excited states, especially when performing time-dependent fluorescence spectroscopy[96], as will be mentioned later.
- In the context of conjugated polymers, it has been demonstrated that emission spectra can provide insights into the arrangement of the chains. Fluorescence in polymers allows for the elucidation of a number of structural characteristics, including the structure of the polymer, stereoregularity, the dynamics of the chains, their flexibility, and crystallinity.

The present thesis details the performance of photoluminescence experiments in semiconducting polymer colloid and semiconducting polymer solution samples. These experiments were performed utilising a FluoroMax 4 spectrofluorometer (HORIBA Jovin Yvon) at the Blas Cabrera Physical Chemistry Institute. The excitation wavelength used was

555 nm. Water-based samples were loaded in polystyrene cuvettes with a 1 cm-path length in the case of aqueous dispersions of NPs and quartz cuvettes for the case of polymer solutions. The emission or fluorescence spectra were described in the wavelength range from 570 to 900 nm. The process of normalisation was applied to all spectra, to ensure that the maximum value corresponded to 1 and the minimum value to 0.

2.4.4.3. Fluorescence Lifetime Imaging Microscopy (FLIM)

Fluorescence Lifetime Imaging Microscopy (FLIM) is an advanced characterisation technique that provides information on to dynamics of the fluorescence decay processes. FLIM measures not only the intensity of the emitted light but also its time dependency as excited molecules return to their fundamental state after being excited by a light source. Fluorescence lifetime studies provide information about the excited electron microenvironment[100]. Therefore, fluorescence lifetimes are dependent on the chemical composition and chemical environment, polarity, viscosity, presence of reactive species, energy transfer or interaction with other molecules[100,101].

The main elements of this technique are (Figure 2.31):

1. Excitation: FLIM employs a pulsed light source, in the nanosecond range, to repeatedly excite the sample[96,100–102].
2. Decay detection: The fluorescence lifetime is the average time that a molecule remains in the excited state before emitting a photon. The emitted fluorescence decays exponentially after each excitation pulse, and the lifetime is determined from this decay using a time-resolved spectrofluorometer that employs techniques such as Time-Correlated Single Photon Counting (TCSPC) or phase modulation[96,100–102]. These techniques allow the fluorescence decay curve to be reconstructed and, consequently, allow for accurate lifetime determination[96,100–102].
3. Data analysis: From the decay curves obtained, the average fluorescence lifetime is calculated, and, in some cases, multiple decay components can be resolved[100,102].

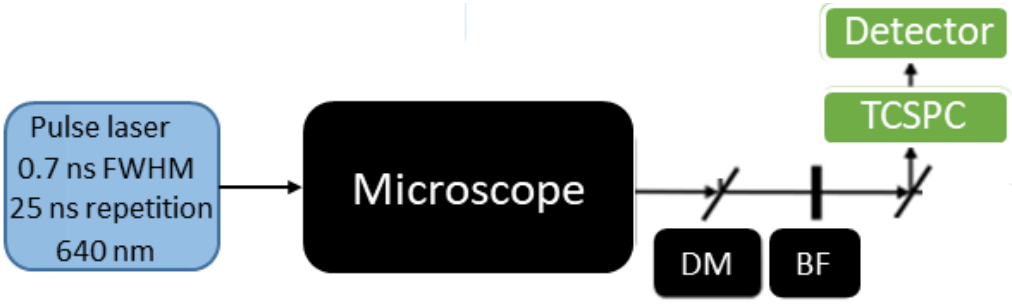

Figure 2.31. The following schematic illustrates the FLIM instrumentation: a 640 nm pulse laser is fed into a microscope in order to excite the sample. The fluorescence emission is then transmitted by a single-mode fibre to a dichroic mirror (DM), which divides the fluorescence signal and passes it through a BP filter (BF). The subsequent conversion of the fluorescence photons into electrical pulses is facilitated by hybrid photomultiplier tube detectors, which are then processed by a TCSPC device for each detector.

FLIM measurements were conducted on a Micro Time 200 confocal microscope (PicoQuant, Berlin, Germany) integrated with an IX73 inverted microscope (Olympus, Hamburg, Germany). The excitation was produced with a diode laser (LDH-D-C-640, PicoQuant, Germany) at an emission wavelength of 640 nm by a PDL-828 pulsed laser diode driver (PicoQuant, Germany). The pulse width was approximately 0.7 ns (IRF FWHM), and a 25 ns repetition window was employed between each pulse. Excitation light was passed through a dichroic mirror (NFD01-532, Semrock, Rochester, USA) and then coupled into a single-mode fibre. The light was focused through either a PLN20X/NA 0.4 or a PLN10X/NA 0.25 lens (Olympus), depending on the type of sample under investigation. Fluorescence emission was collected using the same objective lens and separated from the excitation light using a dichroic mirror (ZT532/640 RPC-UF3, Chroma, Bellows Falls, USA). Subsequent to this, the separated light then passed through a tube lens, a 50 μm pinhole and a 690/70 BP filter (AHF, Germany) onto a hybrid photomultiplier detector (PMA-hybrid-40, PicoQuant). The detector is connected to a TCSPC device (Hydraharp400, PicoQuant) to collect time-tagged data from the laser and detector. The TCSPC technique generates time-, space- and spectrum-resolved fluorescence decay data sets. Before the measurements, the NPs dispersions were ultrasonicated for a period of five minutes. The measurements were conducted on NP suspensions deposited on 0.16–0.19 mm-thick coverslips (purchased from Fisher Scientific, UK) and on films deposited on glass slides. The samples were covered to prevent external light from interfering with the measurements.

The fluorescence decay lifetimes were obtained by fitting the curves with four exponential decays convoluted with the instrument response function (*IRF*) and considering a background (*B*) (Eq. 2.20).

$$I(t) = B + IRF \times \sum_i a_i e^{-\frac{t}{\tau_i}} \quad \text{Eq. 2.20.}$$

The analysis enabled the extraction of representative lifetimes (τ_i) and amplitudes (a_i) of the decay components.

2.4.5. Infrared Spectroscopy (FTIR)

Fourier transform infrared spectroscopy (FTIR) is a widely used technique for analysing the chemical and structural properties of materials[103,104]. FTIR spectroscopy is based on the interaction of infrared radiation with matter[104–106]. The frequency of the infrared light is in resonance with the natural vibrational frequency of a chemical bond, and energy is absorbed, causing vibrations in the covalent bonds of the molecules. This energy absorption is reflected in the spectrum as a peak. The analysis of the positions and intensities of the absorption spectrum, specifically the relationship between absorption and frequency, provides detailed information about the molecular structure, including the identification of functional groups and other structural features and the molecular orientation[103–105,107,108]. This is achieved by employing an interferometer to measure the intensity of infrared light transmitted through the sample (Figure 2.32)[103,105]. The resulting interference pattern is mathematically converted into a spectrum using a Fourier transform[103,105]. This spectrum displays absorbance as a function of wavelength, or wavenumber, which can be used to identify the presence of specific chemical groups within the sample[103].

Each chemical bond in the material has characteristic vibrational modes[103,106,107], such as stretching, bending, twisting, and rocking[103,104,106–108], that absorb infrared radiation at specific frequencies[103,106]:

- Stretching: The bond stretches and contracts[103,104,106–108]. This phenomenon is particularly observable in molecules with double bonds (C=C, C=O)[104,106,107].

    - Symmetry: The atoms move symmetrically towards or away from the point of symmetry of the bond[104,106,107].
    - Asymmetric: Atoms move in opposite directions to each other, causing unequal displacement[104,106,107].
- Bending: The bond angle changes while the bond length remains constant[103,104,106–108]. This phenomenon is commonly observed in molecules with single bonds (C-C, C-H) or aromatic rings and large functional groups[104,106,107].
    - In-plane: The atoms move within the plane of the molecule (e.g., rocking or scissoring)[104,106–108].
    - Out-of-plane: Atoms move out of the plane of the molecule (e.g., twisting or flapping)[104,106–108].

It is important to note that although it is possible to describe each vibration as a single mode, in polyatomic molecules, the vibrational spectra are more complex due to the presence of multiple vibrational modes, as bond lengths and angles can be modified[104]. However, some bonds and groups within a molecule retain certain characteristics, known as group vibrations. The presence of these vibrations in the spectrum facilitates the confirmation of the existence of the group within the molecule[104].

There are several measurement modes for the acquisition of IR spectra, including specular reflection, diffuse reflectance, transmission or attenuated total reflectance (ATR)[103,105]. In this thesis, the latter two measurement modes are utilised:

- Transmission: Infrared radiation passes directly through the sample, and the transmitted light is measured[103,105]. This method requires samples to be thin or in the form of films[103,105]. Samples are deposited on infrared "transparent" silicon substrates to facilitate light transmission[103,105].
- Attenuated Total Reflectance (ATR): Infrared radiation is incident on the surface of a high refractive index optical crystal (such as germanium or diamond) at an angle greater than the critical angle and in contact with the sample[103,105]. The infrared light is reflected within the crystal, and the reflected radiation penetrates slightly (1-2 μm) into the sample surface and is absorbed, allowing a spectrum to be obtained[103,105]. This method is ideal for solid, liquid, or pasty samples without prior preparation[105] and it is less sensitive to variations in the sample than transmission spectroscopy, but more versatile and faster.

The FTIR spectra were obtained with Bruker Alpha II Compact FT-IR spectrometer in both transmission geometry for PVDF NPs deposited on the silicon-float zone window (Korth Kristalle, Germany) and ATR for PVDF films using lasers in the wavenumber range of 400 to 4000 cm^{-1} with a resolution of 4 cm^{-1} to quantify and identify the phases present in PVDF.

2.4.6. Liquid chromatography coupled with mass spectrometry (LC-MS)

Liquid chromatography coupled with mass spectrometry (LC-MS) is a highly sensitive and selective analytical technique that combines the separation capability of liquid chromatography (LC) with the molecular detection and identification capability of mass spectrometry (MS)[109–114]. In essence, at the initial stage, the sample is introduced into the chromatographic system, wherein the components are separated based on their interactions with a stationary phase (typically a chromatographic column) and a mobile phase (a solvent)[110,112,113]. Following separation, each fraction of the eluted compounds is introduced directly into the mass spectrometer, where they are ionised and subsequently detected based on their mass-to-charge ratio (m/z)[109–111,113,114]. This process enables structural identification and quantitative determination of the analytes[109–111,113,114].

The analysis of the dye degradation products was conducted through separation using a HyPurity C18 column (100 mm × 2.1 mm, 3 μm particle size, Thermo Fisher Scientific) at a flow rate of 0.2 mL/min. Before analysis, the samples were subjected to a centrifugal process at a speed of 12000 revolutions per minute for a duration of one minute. Subsequently, the samples were diluted in Milli-Q water to a ratio of 1:10 and then filtered. The gradient employed comprised water (eluent A), acetonitrile (eluent B), and HCOOH 5% (eluent C). The elution programme commenced with a two-minute isocratic period (88% A; 10% B; 2% C). Thereafter, the percentage of B was increased to 90% over a period of 10 minutes, while the 2% C eluent was maintained constant. Consequently, the percentage of A eluent was reduced. These final conditions were maintained for 10 minutes. The injection volume for all LC analyses was set at 100 μL. The detection process was conducted in the electrospray ionisation mode. The Bruker Compass 1.2 software was utilised for the acquisition and processing of LC-MS/MS data.

2.5. Photodegradation test

Aliquots with a volume of 0.1 mL of NP suspensions of P3HT used as photocatalysts were mixed with a solution of 1 mL of MB in water (15 mg/L). The mixture was then poured into a quartz cuvette (100QS, HELLMA Analytics, LineaLab) with a 5 mm path length. The samples were then exposed to a lamp (EQ-99X LDLS Laser-Driven Light Source) with emission in the range 170-2400 nm, located at a distance of 70 cm. The samples were thermostatted at 30 °C during their radiation time. In each experiment, a control cuvette containing the MB solution without NPs was also irradiated. Before the photocatalytic degradation experiment, the suspension of MB and the NPs was magnetically stirred in the dark to achieve adsorption equilibrium. At the given irradiation time, the samples were studied using a UV–Vis spectrophotometer. The photodegradation efficiency was determined by calculating the MB concentration at a given irradiation time through the UV-Vis absorption peak maximum of MB located at 665 nm, using the Lambert-Beer law (Eq. 2.19).

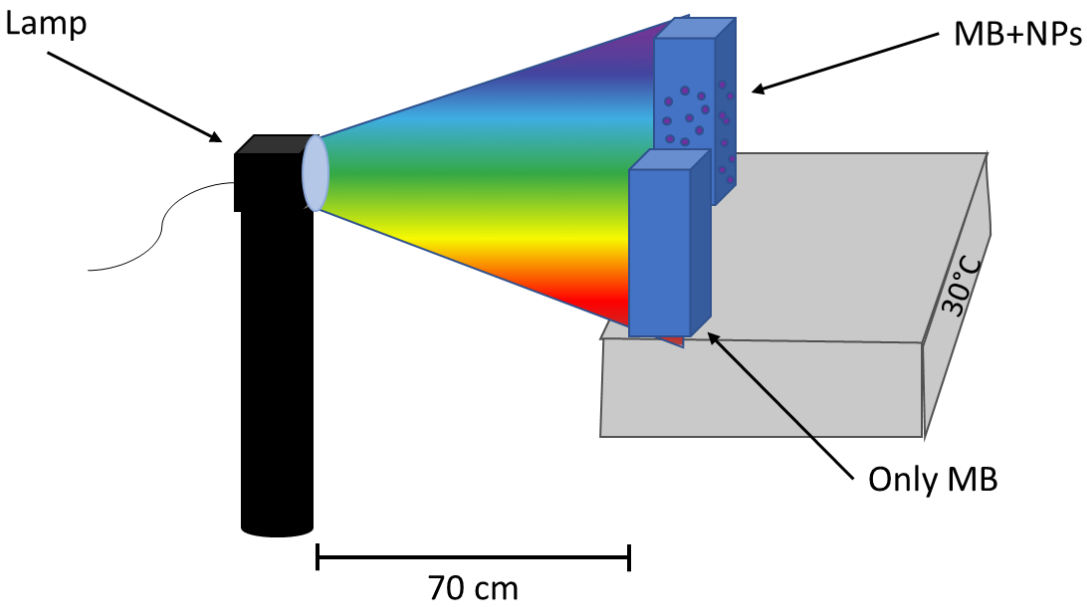

Figure 2.32. Schematic diagram of the photodegradation setup. A UV-Vis lamp irradiates two cuvettes placed 70 cm from the lamp on a hot plate at 30°C. One cuvette contains methylene blue solution, while the other contains methylene blue solution with NPs.

2.6. Bibliography

(1) R. C. Hiorns; R. J. Boucher; R. Duhlev; K.-H. Hellwich; P. Hodge; A. D. Jenkins; R. G. Jones; J. Kahovec; G. Moad; C. K. Ober; D. W. Smith; R. F. T. Stepto; J.-P. Vairon; J. Vohlídal. A Brief Guide to Polymer Nomenclature. *Pure and Applied Chemistry* **2012**, *84*, 2167–2169. https://doi.org/10.1351/PAC-REP-12-03-05.

(2) *Compendium of Polymer Terminology and Nomenclature.*, 2nd ed.; Richard G. Jones, Jaroslav Kahovec, Robert Stepto, Edward S. Wilks, Michael Hess, Tatsuki Kitayama, W. Val Metanomski, Eds.; Royal Society of Chemistry: Cambridge, 2008.

(3) Myers, D. *Surfactant Science and Technology*, 3rd ed.; John Wiley & Sons: New Jersey, 2006.

(4) Rosen, M. J.; Kunjappu, Joy. T. *Surfactants and Interfacial Phenomena*, 4th ed.; Wiley: New Jersey, 2012.

(5) Binks, B. P. Particles as Surfactants Similarities and Differences. *Colloid & Interface Science* **2002**, *7* (1–2), 21–41. https://doi.org/10.1016/S1359-0294(02)00008-0.

(6) Shaban, S. M.; Kang, J.; Kim, D. H. Surfactants: Recent Advances and Their Applications. *Composites Communications* **2020**, *22*. https://doi.org/10.1016/j.coco.2020.100537.

(7) Khan, I.; Saeed, K.; Zekker, I.; Zhang, B.; Hendi, A. H.; Ahmad, A.; Ahmad, S.; Zada, N.; Ahmad, H.; Shah, L. A.; Shah, T.; Khan, I. Review on Methylene Blue: Its Properties, Uses, Toxicity and Photodegradation. *Water* **2022**, *14* (2). https://doi.org/10.3390/w14020242.

(8) Rao, J. P.; Geckeler, K. E. Polymer Nanoparticles: Preparation Techniques and Size-Control Parameters. *Prog Polym Sci* **2011**, *36* (7), 887–913. https://doi.org/10.1016/j.progpolymsci.2011.01.001.

(9) Zhang, C.; Chung, J. W.; Priestley, R. D. Dialysis Nanoprecipitation of Polystyrene Nanoparticles. *Macromol Rapid Commun* **2012**, *33* (20), 1798–1803. https://doi.org/10.1002/marc.201200335.

(10) Gutiérrez-Fernández, E.; Cui, J.; Martínez-Tong, D. E.; Nogales, A. Preparation, Physical Properties, and Applications of Water-Based Functional Polymer Inks. *Polymers* **2021**, *13* (9). https://doi.org/10.3390/polym13091419.

(11) Zhang, C.; Pansare, V. J.; Prud'Homme, R. K.; Priestley, R. D. Flash Nanoprecipitation of Polystyrene Nanoparticles. *Soft Matter* **2012**, *8* (1), 86–93. https://doi.org/10.1039/c1sm06182h.

(12) Landfester, K.; Montenegro, R.; Scherf, U.; Güntner, R.; Asawapirom, U.; Patil, S.; Neher, D.; Kietzke, T. Semiconducting Polymer Nanospheres in Aqueous Dispersion Prepared by a Miniemulsion Process. *Advanced Materials* **2002**, *14* (9), 651–655. https://doi.org/10.1002/1521-4095(20020503)14:9<651::AID-ADMA651>3.0.CO;2-V.

(13) McClements, D. Julian. *Food Emulsions: Principles, Practices, and Techniques*, 3rd ed.; Taylor & Francis: Boca Raton, 2016.

(14) Dang, Y.; Guan, J. Nanoparticle-Based Drug Delivery Systems for Cancer Therapy. *Smart Mater Med* **2020**, *1*, 10–19. https://doi.org/10.1016/j.smaim.2020.04.001.

(15) Reed, R.; Holmes, D.; Weyers, J.; Jones, A. *Practical Skills in Biomolecular Sciences*, 3rd ed.; Pearson Education Limited: London, 2007.

(16) Pustulka, K. M.; Wohl, A. R.; Lee, H. S.; Michel, A. R.; Han, J.; Hoye, T. R.; McCormick, A. V.; Panyam, J.; Macosko, C. W. Flash Nanoprecipitation: Particle Structure and Stability. *Mol Pharm* **2013**, *10* (11), 4367–4377. https://doi.org/10.1021/mp400337f.

(17) Aubry, J.; Ganachaud, F.; Addad, J. P. C.; Cabane, B. Nanoprecipitation of Polymethylmethacrylate by Solvent Shifting: 1. Boundaries. *Langmuir* **2009**, *25* (4), 1970–1979. https://doi.org/10.1021/la803000e.

(18) Bollag, D. M.; Rozycki, M. D.; Edelstein, S. J. *Protein Methods*, 2nd ed.; John Wiley & Sons: New Jersey, 1996.

(19) Van Keuren, E. R. Polymer Nanoparticles Synthesized with Solvent Shifting. *J Dispers Sci Technol* **2004**, *25* (4), 547–553. https://doi.org/10.1081/DIS-200025730.

(20) Hornig, S.; Heinze, T.; Becer, C. R.; Schubert, U. S. Synthetic Polymeric Nanoparticles by Nanoprecipitation. *J Mater Chem* **2009**, *19* (23), 3838–3840. https://doi.org/10.1039/b906556n.

(21) Williams, R. O.; Davies Jr., D. A.; Miller, D. A. *Formulating Poorly Water Soluble Drugs*, 3rd ed.; AAPS Advances in the Pharmaceutical Sciences Series, Ed.; Springer: Cham, 2022; Vol. 50.

(22) Horn, D.; Rieger, J. Organic Nanoparticles in the Aqueous Phase - Theory, Experiment, and Use. *Angewandte Chemie-International Edition* **2001**, *40* (23), 4330–4361. https://doi.org/10.1002/1521-3773(20011203)40:23<4330::AID-ANIE4330>3.0.CO;2-W.

(23) Bilati, U.; Allémann, E.; Doelker, E. Nanoprecipitation Versus Emulsion-Based Techniques for the Encapsulation of Proteins Into Biodegradable Nanoparticles and Process-Related Stability Issues. *AAPS PharmSciTech* **2005**, *6* (74), 594–604.

(24) Sharratt, W. N.; Lee, V. E.; Priestley, R. D.; Cabral, J. T. Precision Polymer Particles by Flash Nanoprecipitation and Microfluidic Droplet Extraction. *ACS Appl Polym Mater* **2021**, *3* (10), 4746–4768. https://doi.org/10.1021/acsapm.1c00546.

(25) Liu, D.; Zhang, H.; Cito, S.; Fan, J.; Mäkilä, E.; Salonen, J.; Hirvonen, J.; Sikanen, T. M.; Weitz, D. A.; Santos, H. A. Core/Shell Nanocomposites Produced by Superfast Sequential Microfluidic Nanoprecipitation. *Nano Lett* **2017**, *17* (2), 606–614. https://doi.org/10.1021/acs.nanolett.6b03251.

(26) Chaudhary, V.; Sharma, S. Suspension Polymerization Technique: Parameters Affecting Polymer Properties and Application in Oxidation Reactions. *Journal of Polymer Research* **2019**, *26* (5). https://doi.org/10.1007/s10965-019-1767-8.

(27) Fitch, R. M. *Polymer Colloids: A Comprehensive Introduction*, 1st ed.; Academic Press: New York, 1997.

(28) Harkins, W. D. A General Theory of the Mechanism of Emulsion Polymerization. *J Am Chem Soc* **1947**, *69* (6), 1428. https://doi.org/10.1021/ja01198a053.

(29) Staff, R.; Landfester, K.; Crespy, D. Recent Advances in the Emulsion Solvent Evaporation Technique for the Preparation of Nanoparticles and Nanocapsules. In *Hierarchical Macromolecular Structures: 60 Years after the Staudinger Nobel Prize II*; Percec, V., Ed.; Springer Cham, 2013; Vol. 262, p 329. https://doi.org/10.1007/12_2013_233.

(30) Barrè, M.; Landfester, K. High Molecular Weight Polyurethane and Polymer Hybrid Particles in Aqueous Miniemulsion. *Macromolecules* **2003**, *36*, 5119–5125. https://doi.org/10.1021/ma025981.

(31) Kietzke, T.; Neher, D.; Landfester, K.; Montenegro, R.; Güntner, R.; Scherf, U. Novel Approaches to Polymer Blends Based on Polymer Nanoparticles. *Nat Mater* **2003**, *2* (6), 408–412. https://doi.org/10.1038/nmat889.

(32) Hiemenz, Paul.; Rajagopalan, Raj. *Principles of Colloid and Surface Chemistry*; Taylor & Francis: Boca Raton, 2016.

(33) Shaw, D. J. *Introduction to Colloid and Surface Chemistry Fourth Edition*, 4th ed.; Butterworth-Heinemann: Oxford, 1992.

(34) Hunter, R. J. *Foundations of Colloid Science*, 2nd ed.; Oxford University Press: Oxford, 2001.

(35) Shaikh, J.; Patil, N. D.; Sharma, A.; Bhardwaj, R. Numerical Simulations and Experiments on Droplet Coalescence Dynamics over a Liquid–Air Interface: Mechanism and Effect of Droplet-Size/Surface-Tension. *SN Appl Sci* **2021**, *3* (3). https://doi.org/10.1007/s42452-021-04275-3.

(36) Mukherjee, S.; Safdari, A.; Shardt, O.; Kenjereš, S.; Van Den Akker, H. E. A. Droplet-Turbulence Interactions and Quasi-Equilibrium Dynamics in Turbulent Emulsions. *J Fluid Mech* **2019**, *878*, 221–276. https://doi.org/10.1017/jfm.2019.654.

(37) Chen, M.; Jafvert, C. T. Application of Cross-Linked Stearic Acid Nanoparticles with Dialysis Membranes for Methylene Blue Recovery. *Sep Purif Technol* **2018**, *204*, 21–29. https://doi.org/10.1016/j.seppur.2018.04.053.

(38) van Leeuwen, T.; Kuchel, R. P.; Knothe Tate, M. L.; Zetterlund, P. B. Paclitaxel Release from Hollow PMMA Nanoparticles: Factors Affecting Release Rate as Quantified via Dialysis and Membrane Centrifugation. *Colloids Surf A Physicochem Eng Asp* **2023**, *675*. https://doi.org/10.1016/j.colsurfa.2023.131992.

(39) Nah, J.-W.; Paek, Y.-W.; Jeong, Y.-I.; Kim, D.-W.; Cho, C.-S.; Kim, S.-H.; Kim, M.-Y. Clonazepam Release from Poly(DL-Lactide-Co-Glycolide) Nanoparticles Prepared by Dialysis Method. *Arch. Pharm. Res* **1998**, *21* (4), 418–422. https://doi.org/10.1007/BF02974636.

(40) Hossain, M. I.; Mansour, S. A Critical Overview of Thin Films Coating Technologies for Energy Applications. *Cogent Eng* **2023**, *10* (1). https://doi.org/10.1080/23311916.2023.2179467.

(41) Pichumani, M.; Bagheri, P.; Poduska, K. M.; González-Viñas, W.; Yethiraj, A. Dynamics, Crystallization and Structures in Colloid Spin Coating. *Soft Matter* **2013**, *9* (12), 3220–3229. https://doi.org/10.1039/c3sm27455a.

(42) Bornside, D. E.; Macosko, C. W.; Scriven, L. E. Spin Coating: One-Dimensional Model. *J Appl Phys* **1989**, *66* (11), 5185–5193. https://doi.org/10.1063/1.343754.

(43) Mouhamad, Y.; Mokarian-Tabari, P.; Clarke, N.; Jones, R. A. L.; Geoghegan, M. Dynamics of Polymer Film Formation during Spin Coating. *J Appl Phys* **2014**, *116* (12). https://doi.org/10.1063/1.4896674.

(44) Hall, D. B.; Underhill, P.; Torkelson, J. M. Spin Coating of Thin and Ultrathin Polymer Films. Polym Eng Sci 2004, 38 (12), 2039–2045.

(45) Shi, Q.; Cheng, W. Free-Standing 2D Nanoassemblies. *Adv Funct Mater* **2020**, *30* (2). https://doi.org/10.1002/adfm.201902301.

(46) Sinha, S.; Kim, H.; Robertson, A. W. Preparation and Application of 0D-2D Nanomaterial Hybrid Heterostructures for Energy Applications. *Mater Today Adv* **2021**, *12*. https://doi.org/10.1016/j.mtadv.2021.100169.

(47) Stadermann, M.; Baxamusa, S. H.; Aracne-Ruddle, C.; Chea, M.; Li, S.; Youngblood, K.; Suratwala, T. Fabrication of Large-Area Free-Standing Ultrathin Polymer Films. *Journal of Visualized Experiments* **2015**, *2015* (100). https://doi.org/10.3791/52832.

(48) Gao, F.; Song, J.; Xu, Z.; Xu, L.; Guo, Y.; Miao, L.; Luo, X. All-Polymer Free-Standing Electrodes for Flexible Electrochemical Sensors. *Sens Actuators B Chem* **2021**, *334*. https://doi.org/10.1016/j.snb.2021.129675.

(49) Fujie, T. Development of Free-Standing Polymer Nanosheets for Advanced Medical and Health-Care Applications. *Polym J* **2016**, *48* (7), 773–780. https://doi.org/10.1038/pj.2016.38.

(50) Sun, L.; Zhang, D.; Cheng, S. Z. D.; Harris, F. W. Thermally Stable Transparent Polymer Films for Flexible Electronics: Properties and Applications. *Giant* **2023**, *14*. https://doi.org/10.1016/j.giant.2023.100156.

(51) Wang, J. Z.; Chou, S. L.; Liu, H.; Wang, G. X.; Zhong, C.; Yen Chew, S.; Kun Liu, H. Highly Flexible and Bendable Free-Standing Thin Film Polymer for Battery Application. *Mater Lett* **2009**, *63* (27), 2352–2354. https://doi.org/10.1016/j.matlet.2009.08.007.

(52) Mizoguchi, T.; Honda, M.; Ida, S.; Koinuma, M. Free Standing Graphene Oxide Membrane with Epoxy Groups for Water Purification. *Chem Lett* **2020**, *49* (4), 376–378. https://doi.org/10.1246/cl.190948.

(53) Cullity, B. D.; Stock, S. R. *Elements of X-Ray Diffraction*; Pearson Education Limited: London, 2001.

(54) Bragg, W. H. The Reflection of X-Rays by Crystals. (II). *Proceedings of the Royal Society of London. Series A, Containing Papers of a Mathematical and Physical Character* **1913**, *89* (610), 246–248. https://doi.org/10.1098/rspa.1913.0082.

(55) Bragg, W. H. The Reflection of X-Rays by Crystals. *Proceedings of the Royal Society of London. Series A, Containing Papers of a Mathematical and Physical Character* **1913**, *88* (605), 428–438. https://doi.org/10.1098/rspa.1913.0040.

(56) Klug, H. P.; Alexander, L. E. *X-Ray Diffraction Procedures for Polycrystalline and Amorphous Materials*, 2nd ed.; John Wiley & Sons: New Jersey, 1974.

(57) Akpalu, Y. A. Scattering from Polymers. *Polymer Reviews* **2010**, *50* (1), 1–13. https://doi.org/10.1080/15583721003624859.

(58) Als-Nielsen, J.; Mcmorrow, D. *Elements of Modern X-Ray Physics*, 2nd ed.; John Wiley & Sons: New Jersey, 2011.

(59) Ezquerra, T. A.; Garcia-Gutierrez, M. C.; Nogales, A.; Gomez, M. *Applications of Synchrotron Light to Scattering and Diffraction in Materials and Life Sciences*; Springer: Verlag, 2009; Vol. 776.

(60) Mahmood, A.; Wang, J. L. A Review of Grazing Incidence Small- and Wide-Angle X-Ray Scattering Techniques for Exploring the Film Morphology of Organic Solar Cells. *Solar RRL* **2020**, *4* (10). https://doi.org/10.1002/solr.202000337.

(61) Rivnay, J.; Noriega, R.; Kline, R. J.; Salleo, A.; Toney, M. F. Quantitative Analysis of Lattice Disorder and Crystallite Size in Organic Semiconductor Thin Films. *Phys Rev B Condens Matter Mater Phys* **2011**, *84* (4). https://doi.org/10.1103/PhysRevB.84.045203.

(62) Rivnay, J.; Mannsfeld, S. C. B.; Miller, C. E.; Salleo, A.; Toney, M. F. Quantitative Determination of Organic Semiconductor Microstructure from the Molecular to Device Scale. *Chem Rev* **2012**, *112* (10), 5488–5519. https://doi.org/10.1021/cr3001109.

(63) Patterson, A. L. The Scherrer Formula for X-Ray Particle Size Determination. *Physical Review* **1939**, *56*. https://doi.org/10.1103/PhysRev.56.978.

(64) Ashiotis, G.; Deschildre, A.; Nawaz, Z.; Wright, J. P.; Karkoulis, D.; Picca, F. E.; Kieffer, J. The Fast Azimuthal Integration Python Library: PyFAI. *J Appl Crystallogr* **2015**, *48* (2), 510–519. https://doi.org/10.1107/S1600576715004306.

(65) Binnig, G.; Rohrer, H. Scanning Tunneling Microscopy. *Helvetica Physica Acta* **1982**, *55* (6), 726–735. https://doi.org/10.5169/seals-115309.

(66) Binnig, G.; Quate, C. F.; Gerber, Ch. Atomic Force Microscope. *Phys Rev Lett* **1986**, *56* (9), 930–933. https://doi.org/10.1103/PhysRevLett.56.930.

(67) Bhushan, B. *Springer Handbook of NanoTechnology*, 3rd ed.; Springer: Berlin, 2010.

(68) Fotiadis, D. Atomic Force Microscopy for the Study of Membrane Proteins. *Curr Opin Biotechnol* **2012**, *23* (4), 510–515. https://doi.org/10.1016/j.copbio.2011.11.032.

(69) Song, Y. J.; Otte, A. F.; Shvarts, V.; Zhao, Z.; Kuk, Y.; Blankenship, S. R.; Band, A.; Hess, F. M.; Stroscio, J. A. Invited Review Article: A 10 MK Scanning Probe Microscopy Facility. *Review of Scientific Instruments* **2010**, *81* (12). https://doi.org/10.1063/1.3520482.

(70) Vickerman, J. C.; Gilmore, I. S. *Surface Analysis: The Principal Techniques*; John Wiley & Sons: New Jersey, 2009.

(71) Dokukin, M. E.; Sokolov, I. Quantitative Mapping of the Elastic Modulus of Soft Materials with HarmoniX and PeakForce QNM AFM Modes. *Langmuir* **2012**, *28* (46), 16060–16071. https://doi.org/10.1021/la302706b.

(72) Schwartz, G. A.; Riedel, C.; Arinero, R.; Tordjeman, P.; Alegría, A.; Colmenero, J. Broadband Nanodielectric Spectroscopy by Means of Amplitude Modulation Electrostatic Force Microscopy (AM-EFM). *Ultramicroscopy* **2011**, *111* (8), 1366–1369. https://doi.org/10.1016/j.ultramic.2011.05.001.

(73) Hu, Z.; Tian, M.; Nysten, B.; Jonas, A. M. Regular Arrays of Highly Ordered Ferroelectric Polymer Nanostructures for Non-Volatile Low-Voltage Memories. *Nat Mater* **2009**, *8* (1), 62–67. https://doi.org/10.1038/nmat2339.

(74) Gutiérrez-Fernández, E.; Rebollar, E.; Cui, J.; Ezquerra, T. A.; Nogales, A. Morphology and Ferroelectric Properties of Semiconducting/Ferroelectric Polymer Bilayers. *Macromolecules* **2019**, *52* (19), 7396–7402. https://doi.org/10.1021/acs.macromol.9b00859.

(75) Karagiannidis, P. G.; Kassavetis, S.; Pitsalidis, C.; Logothetidis, S. Thermal Annealing Effect on the Nanomechanical Properties and Structure of P3HT:PCBM Thin Films. *Thin Solid Films* **2011**, *519* (12), 4105–4109. https://doi.org/10.1016/j.tsf.2011.01.196.

(76) Rodríguez-Rodríguez, Á.; Gutiérrez-Fernández, E.; García-Gutiérrez, M. C.; Nogales, A.; Ezquerra, T. A.; Rebollar, E. Synergistic Effect of Fullerenes on the Laser-Induced Periodic Surface Structuring of Poly(3-Hexyl Thiophene). *Polymers* **2019**, *11* (2). https://doi.org/10.3390/polym11020190.

(77) Schönherr, H.; Vancso, G. J. *Scanning Force Microscopy of Polymers*; Springer: Berlin, 2010.

(78) García, R.; Pérez, R. Dynamic Atomic Force Microscopy Methods. *Surf Sci Rep* **2002**, *47* (6–8), 197. https://doi.org/10.1016/S0167-5729(02)00077-8.

(79) Hansma, P. K.; Cleveland, J. P.; Radmacher, M.; Walters, D. A.; Hillner, P. E.; Bezanilla, M.; Fritz, M.; Vie, D.; Hansma, H. G.; Prater, C. B.; Massie, J.; Fukunaga, L.; Gurley, J.; Elings, V. Tapping Mode Atomic Force Microscopy in Liquids. *Appl Phys Lett* **1994**, *64* (13), 1738–1740. https://doi.org/10.1063/1.111795.

(80) Thomas, J. C. The Determination of Log Normal Particle Size Distributions by Dynamic Light Scattering. *J Colloid Interface Sci* **1987**, *117* (1), 187–192.

(81) Berne, B. J.; Pecora, R. *Dynamic Light Scattering, with Applications to Chemistry, Biology and Physics*; Wiley: New York, 1976.

(82) Vega, J. F.; Vicente-Alique, E.; Núñez-Ramírez, R.; Wang, Y.; Martínez-Salazar, J. Evidences of Changes in Surface Electrostatic Charge Distribution during Stabilization of HPV16 Virus-like Particles. *PLoS One* **2016**, *11* (2). https://doi.org/10.1371/journal.pone.0149009.

(83) *Dynamic Light Scattering DLS*. https://lsinstruments.ch/en/theory/dynamic-light-scattering-dls/introduction (accessed 2024-12-27).

(84) Raja, P. M. V.; Barron, A. R. *Physical Methods in Chemistry and Nano Science*; Connexions, Rice University: Houston, 2012.

(85) Stetefeld, J.; McKenna, S. A.; Patel, T. R. Dynamic Light Scattering: A Practical Guide and Applications in Biomedical Sciences. *Biophys Rev* **2016**, *8* (4), 409–427. https://doi.org/10.1007/s12551-016-0218-6.

(86) Hassan, P. A.; Kulshreshtha, S. K. Modification to the Cumulant Analysis of Polydispersity in Quasielastic Light Scattering Data. *J Colloid Interface Sci* **2006**, *300* (2), 744–748. https://doi.org/10.1016/j.jcis.2006.04.013.

(87) Farkas, N.; Kramar, J. A. Dynamic Light Scattering Distributions by Any Means. *Journal of Nanoparticle Research* **2021**, *23* (5). https://doi.org/10.1007/s11051-021-05220-6.

(88) Koppel, D. E. Analysis of Macromolecular Polydispersity in Intensity Correlation Spectroscopy: The Method of Cumulants. *J Chem Phys* **1972**, *57* (11), 4814–4820. https://doi.org/10.1063/1.1678153.

(89) Maulucci, G.; De Spirito, M.; Arcovito, G.; Boffi, F.; Castellano, A. C.; Briganti, G. Particle Distribution in DMPC Vesicles Solutions Undergoing Different Sonication Times. *Biophys J* **2005**, *88* (5), 3545–3550. https://doi.org/10.1529/biophysj.104.048876.

(90) Farkas, N.; Kramar, J. A. Dynamic Light Scattering Distributions by Any Means. *Journal of Nanoparticle Research* **2021**, *23* (5). https://doi.org/10.1007/s11051-021-05220-6.

(91) Liu, Z.; Zhang, X.; Wang, Y.; Shen, J.; Yuan, X.; Mu, T.; Liu, W.; Li, C.; Wang, Z. Research on Tikhonov Regularization Parameter Selection in Dynamic Light Scattering Measurement of Flowing Particles. *Journal of Optics* **2022**, *51* (4), 1038–1051. https://doi.org/10.1007/s12596-022-00847-7.

(92) Sawicki, M. SEDfit: Software for Spectral Energy Distribution Fitting of Photometric Data. *Publications of the Astronomical Society of the Pacific* **2012**, *124* (921), 1208.

(93) Atkins, P.; de Paula, J. *Physical Chemistry*, 9th ed.; Oxford University Press: Oxford, 2009.

(94) Levine, I. N. *Molecular Spectroscopy*, 1st ed.; John Wiley & Sons: New Jersey, 1975.

(95) Jentoft, F. C. Chapter 3 Ultraviolet-Visible-Near Infrared Spectroscopy in Catalysis. Theory, Experiment, Analysis, and Application Under Reaction Conditions. In *Advances in Catalysis*; John Wiley & Sons: New Jersey, 2009; Vol. 52, pp 129–211. https://doi.org/10.1016/S0360-0564(08)00003-5.

(96) Lakowicz, J. R. *Principles of Fluorescence Spectroscopy*, 3rd ed.; Springer: Verlag, 2006.

(97) Müllertz, A.; Perrie, Y.; Rades, T. *Analytical Techniques in the Pharmaceutical Sciences*; Advances in Delivery Science and Technology; Springer: New York, 2016. https://doi.org/10.1007/978-1-4939-4029-5.

(98) Lakowicz, J. R. *Topics in Fluorescence Spectroscopy. Volume 2: Principles*; Springer: New York, 2006; Vol. 2.

(99) Valeur, Bernard. *Molecular Fluorescence: Principles and Applications*, 2nd ed.; John Wiley & Sons: New Jersey, 2002.

(100) Berezin, M. Y.; Achilefu, S. Fluorescence Lifetime Measurements and Biological Imaging. *Chem Rev* **2010**, *110* (5), 2641–2684. https://doi.org/10.1021/cr900343z.

(101) Bastiaens, P. H.; Squire, A. Fluorescence Lifetime Imaging Microscopy: Spatial Resolution of Biochemical Processes in the Cell. *Trends Cell Biol* **1999**, *9* (2), 48–52.

(102) Gratton, E. Fluorescence Lifetime Imaging for the Two-Photon Microscope: Time-Domain and Frequency-Domain Methods. *J Biomed Opt* **2003**, *8* (3), 381–390. https://doi.org/10.1117/1.1586704.

(103) Griffiths, P. R.; de Haseth, J. A. *Fourier Transform Infrared Spectrometry*, 2nd ed.; John Wiley & Sons: New Jersey, 2006. https://doi.org/10.1007/s00216-008-2144-3.

(104) Smith, B. *Infrared Spectral Interpretation*, 1st ed.; John Wiley & Sons: New Jersey, 1998.

(105) Smith, B. C. *Fundamentals of Fourier Transform Infrared Spectroscopy*; John Wiley & Sons: New Jersey, 1995.

(106) Pavia, D. L.; Lampman, G. M.; Kriz, G. S. *Introduction to Spectroscopy*, 3rd ed.; Cengage Learning, 2015.

(107) Colthup, N. B.; Daly, L. H.; Wiberley, S. E. *Introduction to Infrared and Raman Spectroscopy*, 3rd ed.; Academic Press, 1990.

(108) Berthomieu, C.; Hienerwadel, R. Chapter 7: Fourier Transform Infrared (FTIR) Spectroscopy. In *Photosynthesis Research*; 2009; Vol. 101, pp 157–170. https://doi.org/10.1007/s11120-009-9439-x.

(109) Gross, J. H. *Mass Spectrometry: A Textbook*, 3rd ed.; Springer Cham, 2017. https://doi.org/https://doi.org/10.1007/978-3-319-54398-7.

(110) Niessen, W. M. A. State-of-the-Art in Liquid Chromatography-Mass Spectrometry. *J Chromatogr A* **1999**, *856* (1–2), 179–197. https://doi.org/10.1016/S0021-9673(99)00480-X.

(111) de Hoffmann, E.; Stroobant, V. *Mass Spectrometry Principles and Applications*, 3rd ed.; Wiley, 2007.

(112) Snyder, L. R.; Kirkland, J. J.; Dolan, J. W. *Introduction to Modern Liquid Chromatography*; John Wiley & Sons: New Jersey, 2010.

(113) McMaster, M. C. . *LC/MS : A Practical User's Guide*; John Wiley, 2005.

(114) Kebarle, P.; Verkcerk, U. H. Electrospray: From Ions in Solution to Ions in the Gas Phase, What We Know Now. *Mass Spectrom Rev* **2009**, *28* (6), 898–917. https://doi.org/10.1002/mas.20247.

Chapter 3

Flash nanoprecipitation of P3HT nanoparticles: Tuning morphology, crystallinity, and optical properties via concentration, solvent ratio, and aging effects

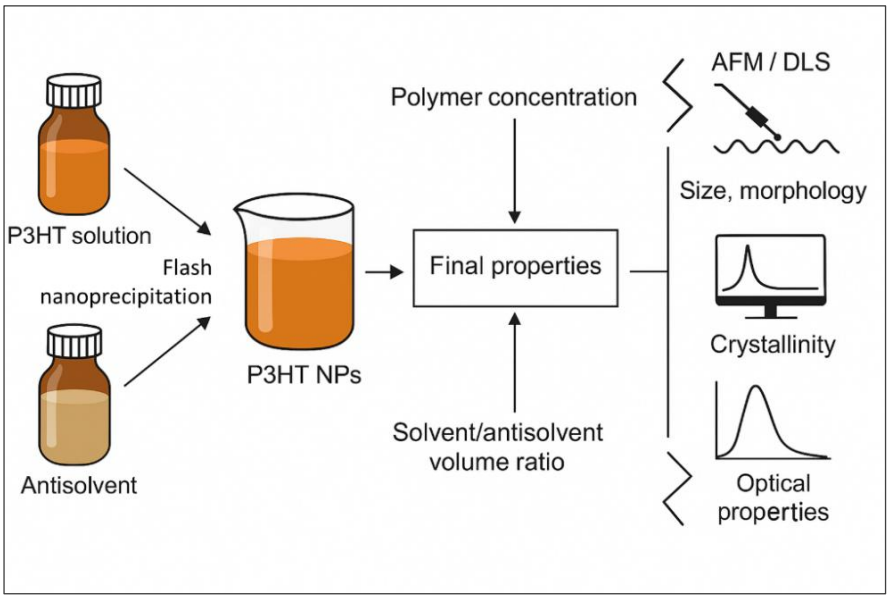

Graphical abstract representing the main idea of Chapter 3

Universidad Complutense de Madrid

Jose Sena Fernández

Micro and Nanoparticles of Functional Polymers: From Fundamentals to Applications

Conjugated polymers such as P3HT have been widely investigated for optoelectronic and photocatalytic applications due to their tunable electronic structure, strong light absorption, and solution processability [1-3]. In recent years, particular attention has been paid to P3HT nanoparticles (NPs), whose nanoscale confinement can significantly modify their structural order, crystallinity, and optical behaviour compared to the bulk material (see Section 1.6). Among the various fabrication techniques, flash nanoprecipitation offers rapid mixing and control over particle size and structure, enabling the tailoring of functional properties[4]. However, systematic studies addressing how processing parameters affect the physical properties of P3HT NPs remain scarce, despite their importance for optimising performance in functional applications. This chapter addresses this gap by providing a thorough evaluation of key parameters, such as polymer concentration, solvent/antisolvent ratio (R) and solution aging, to establish clear structure–property relationships and enable the rational design of P3HT nanoparticles with optimised performance for photocatalysis.

Water suspensions of P3HT NPs were prepared using the flash nanoprecipitation method described in Section 2.2.2.1. The influence of these processing parameters on their morphology, structure, and optical properties was investigated following the scheme shown in Figure 3.1. As illustrated, sample sets were prepared by varying the selected parameters. A comprehensive study was conducted using AFM and DLS to characterize NP size and morphology, XRD to assess crystallinity, and UV-Vis and fluorescence spectroscopy to investigate optical properties.

The first section discusses the impact of polymer concentration. Subsequently, a second section presents the study of the influence of R. Finally, the influence of solution aging on the NPs is studied, highlighting how solution aging further modifies NPs characteristics. The objective of this analysis is to facilitate the identification of the most appropriate NPs for diverse applications such as photocatalysis.

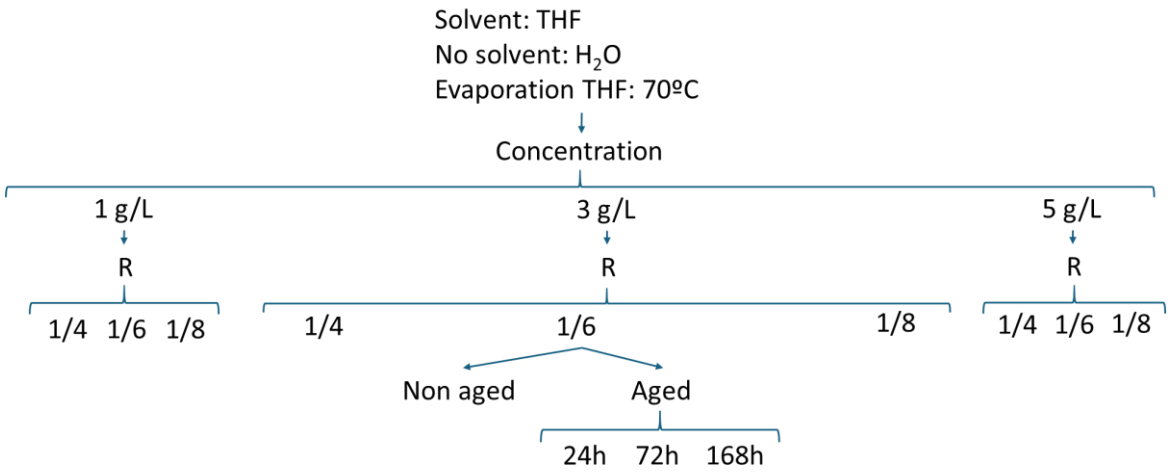

Figure 3.1. Scheme of the preparation conditions of all samples prepared by flash nanoprecipitation, detailing variations in parameters such as concentration, solvent/antisolvent ratio (R), and aging.

3.1. Effect of the P3HT solution concentration on the properties of flash nanoparticles

Flash NPs were prepared as described in Section 2.2.2. Three different concentrations were used. Regardless of the polymer concentration, polymer NPs were obtained for a fixed R value.

Figure 3.2. shows the topographic images obtained by AFM in tapping mode from NPs deposits onto silicon wafers of samples prepared at constant *R* (*R* = 1/6) and varying concentrations (1 g/L, 3 g/L and 5 g/L). The NPs obtained by flash nanoprecipitation are not completely spherical (see Figure 3.2 a-c), but they show sharp edges. This shape has been explained in previous reports as due to the presence of crystalline domains[5,6]. XRD experiments confirm the semicrystalline nature of the NPs, as described below. Depending on the concentration, both dispersed objects with diameters of around 20 to 40 nm for 1 g/L (Figure 3.2 (a)), aggregates of several NPs for 3 g/L (Figure 3.2 (b)) and a more pronounced agglomeration of NPs for 5 g/L (Figure 3.2 (c)), revealing a loose spatial distribution of the NPs.

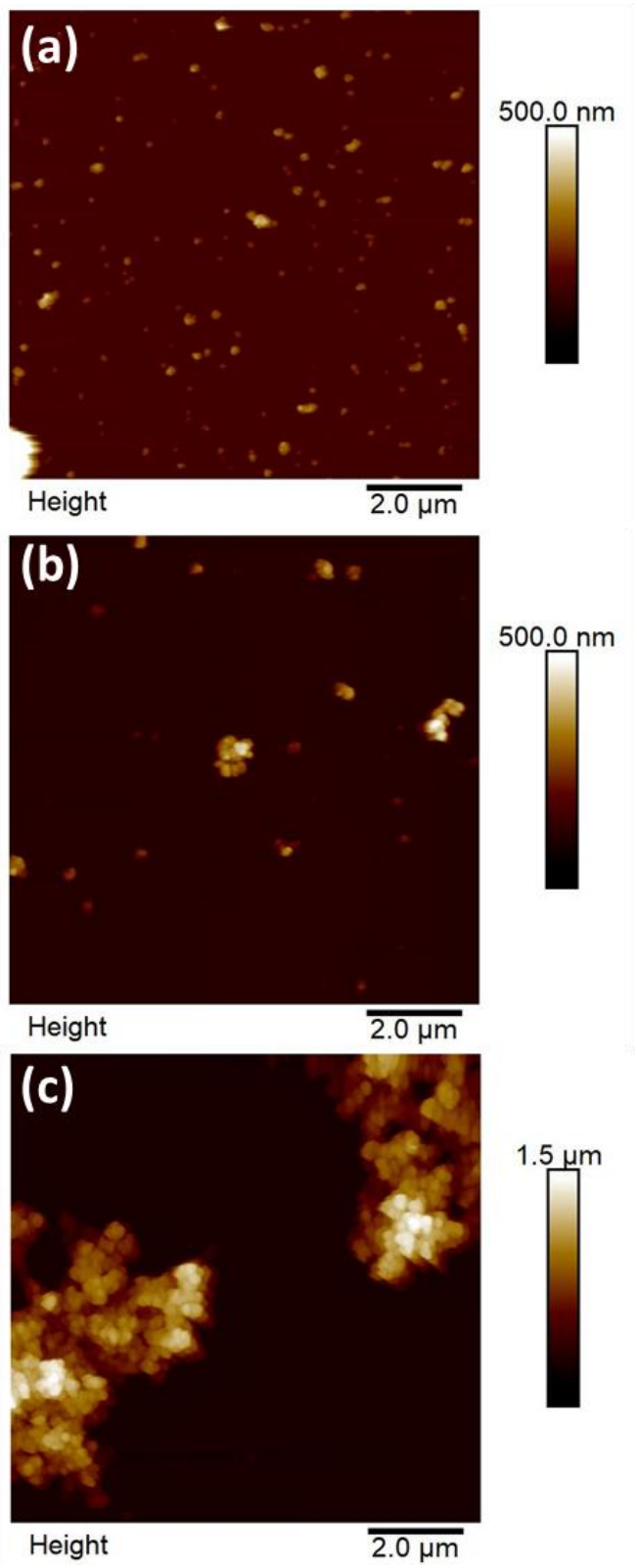

Figure 3.2. AFM topography image obtained from NPs with a volume ratio of R = 1/6 for different concentrations, **(a)** 1 g/L, **(b)** 3 g/L and **(c)** 5 g/L.

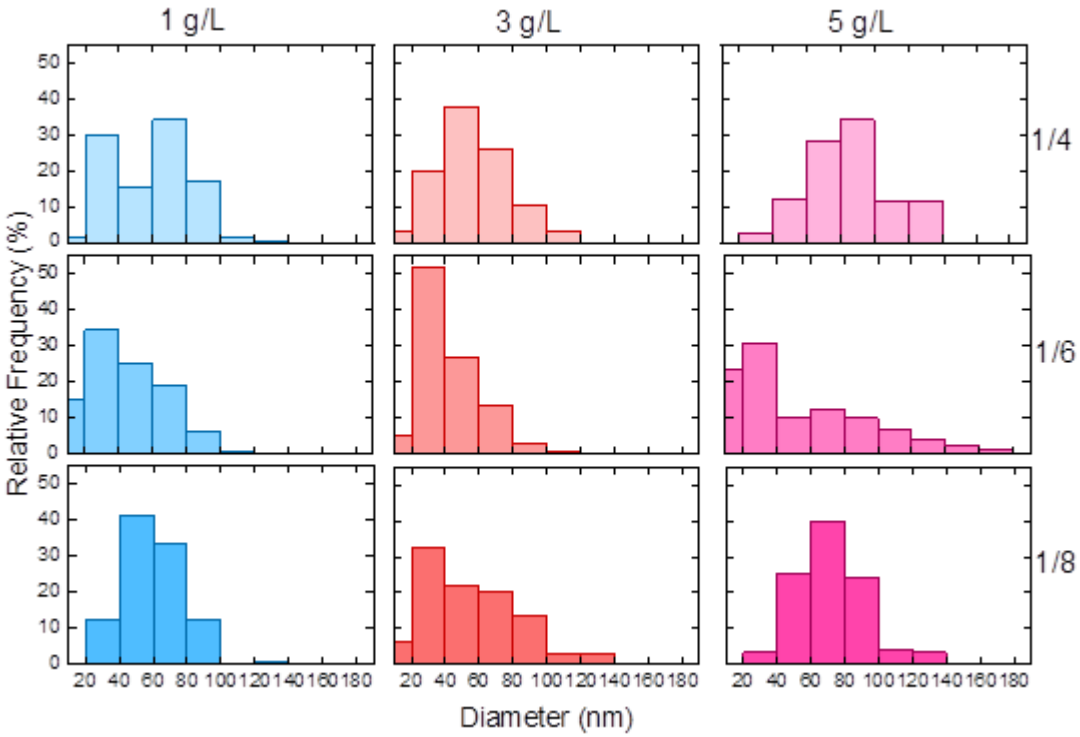

Figure 3.3. Particle diameter histograms of P3HT NPs for different concentrations and different values of *R*. The labels at the top of the figure indicate the polymer concentration, and the labels at the right of the figure indicate different values of *R*.

To estimate the size distribution of the observed NPs, the diameters of at least 100 NPs (and not of the aggregates) were measured. These measurements are presented in the form of histograms in Figure 3.3 for the flash NPs prepared at various *R* (*R* = 1/4, 1/6 and 1/8) and varying concentrations (1 g/L, 3 g/L and 5 g/L). All histograms appear to present a single population, except for the 1 g/L *R*=1/4 histogram and the 5 g/L *R* = 1/6 histogram, which exhibit two populations. The most repeated diameters are presented in Table 3.1. The results suggest that the NPs obtained from a concentration of 3 g/L are those with the smallest particle size, regardless of the value of *R*. In particular, the NPs prepared from a 3 g/L solution and *R*=1/6 exhibit the narrowest size distribution.

Table 3.1. Results of the more repeated diameter values of P3HT NPs obtained by AFM. Those with two populations are marked with an asterisk, indicating the size of each.

R	Diameter (nm)

	1 g/L	3 g/L	5 g/L
1/4	41* 71*	55	84
1/6	40	38	28* 85*
1/8	59	39	69

As outlined in Section 2.4.3, the correlograms obtained by DLS experiments were analysed using cumulant analysis to calculate the polydispersity (Q) and number-average of the hydrodynamic diameter size (D_n). Those values, along with their respective standard deviations, as presented in Table 3.2.

Table 3.2. Results of the number-average of the hydrodynamic diameter (D_n) values and polydispersity (Q) of P3HT NPs obtained using DLS.

R	D_n (nm)	Q ($x10^{-2}$)	D_n (nm)	Q ($x10^{-2}$)	D_n (nm)	Q ($x10^{-2}$)
	1 g/L		3 g/L		5 g/L	
1/4	52 ± 5.7	38 ± 2.8	99 ± 14	18 ± 3.2	56 ± 7.5	49 ± 3.7
1/6	22 ± 4.6	66 ± 7.0	56 ± 27	12 ± 10	78 ± 36	44 ± 13
1/8	61 ± 7.9	33 ± 3.4	74 ± 3.9	26 ± 1.1	127 ± 17.0	23 ± 3.0

DLS results show that the size and distribution of the NPs prepared via the flash nanoprecipitation technique depend strongly on the polymer concentration in the initial solution. It has been proposed that the D_n and the initial polymer concentration (c) in the solvent are described by a power law[7]:

$$D_n \propto 2*c^{1/3} \qquad \text{Eq 2.1.}$$

indicating that the polymer amount per NP scales proportionally with the c. This behaviour is characteristic of non-amphiphilic polymers such as P3HT[7]. Under conditions of low supersaturation, nucleation and subsequent growth are primarily driven by solute depletion[8]. As explained in Chapter 2.2.2, the basis of flash nanoprecipitation underlies the phenomenon of supersaturation[9]. Therefore, in this work, the formation of a limited number of nuclei that grow based on the available solute leads to the emergence of distinct NP populations for a given antisolvent volume (see Figure 3.3). The relation described by Eq. 2.1 is only fulfilled in the present case for R = 1/6 (Figure 3.4). Conversely, at a lower solvent/antisolvent ratio (R = 1/4), no clear influence of polymer concentration on NP size is observed. The findings imply that the quantity of antisolvent employed can also exert an influence on the resulting size, possibly because there is not enough antisolvent for independent growth nuclei to form. Sharratt et al.[10] suggested that polymer solutions must be highly diluted, with final mass fractions on the order of 10^{-3} or less (expressed as the mass of the solute (in this case, the polymer) divided by the total mass of the solution) to achieve a narrow size distribution. Within the context of this thesis, the size distributions of the sample of NPs prepared from the 5g/L solutions for all R are generally wider in AFM (see Figure 3.3), related to the presence of aggregates (Figure 3.2). However, this observation does not hold for 1 g/L and 3 g/L, where no differences are found, indicating that these concentrations are suitable for the formation of stable NPs in dispersion.

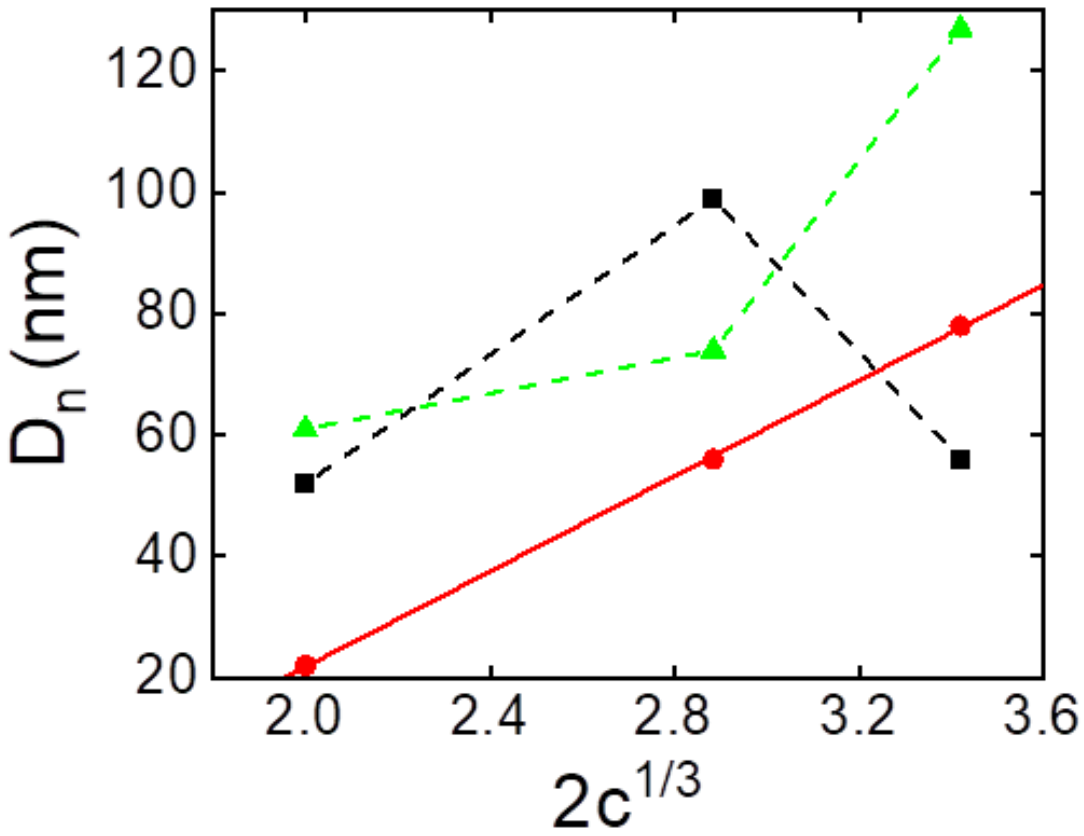

Figure 3.4. NP diameter (D_n) obtained by DLS as a function of $2c^{1/3}$ for P3HT NPs of 1 g/L, 3 g/L and 5 g/L prepared by flash nanoprecipitation at different THF/H_2O volume ratios: R = 1/4 (black), R = 1/6 (red) and R = 1/8 (green). The solid line is the linear fit to Eq. 2.1 for the R = 1/6, while the R = 1/4 and R = 1/8 ratios are connected by the dashed lines.

The results indicated that for elevated polymer concentrations or low R values, the increased number of nuclei leads to an elevated probability of collisions and aggregation rather than independent growth[11] due to strong supersaturation of the solution, once the flash mixing of water and the solution is produced.

3.1.1. Effects of solution concentration on the crystalline structure of the P3HT nanoparticles prepared by flash

As outlined in Section 2.4.1, GIWAXS experiments on P3HT NPs deposited onto silicon wafers were performed to reveal the semicrystalline character of the NPs. Figure 3.5 presents the diffractograms as a function of *q*.

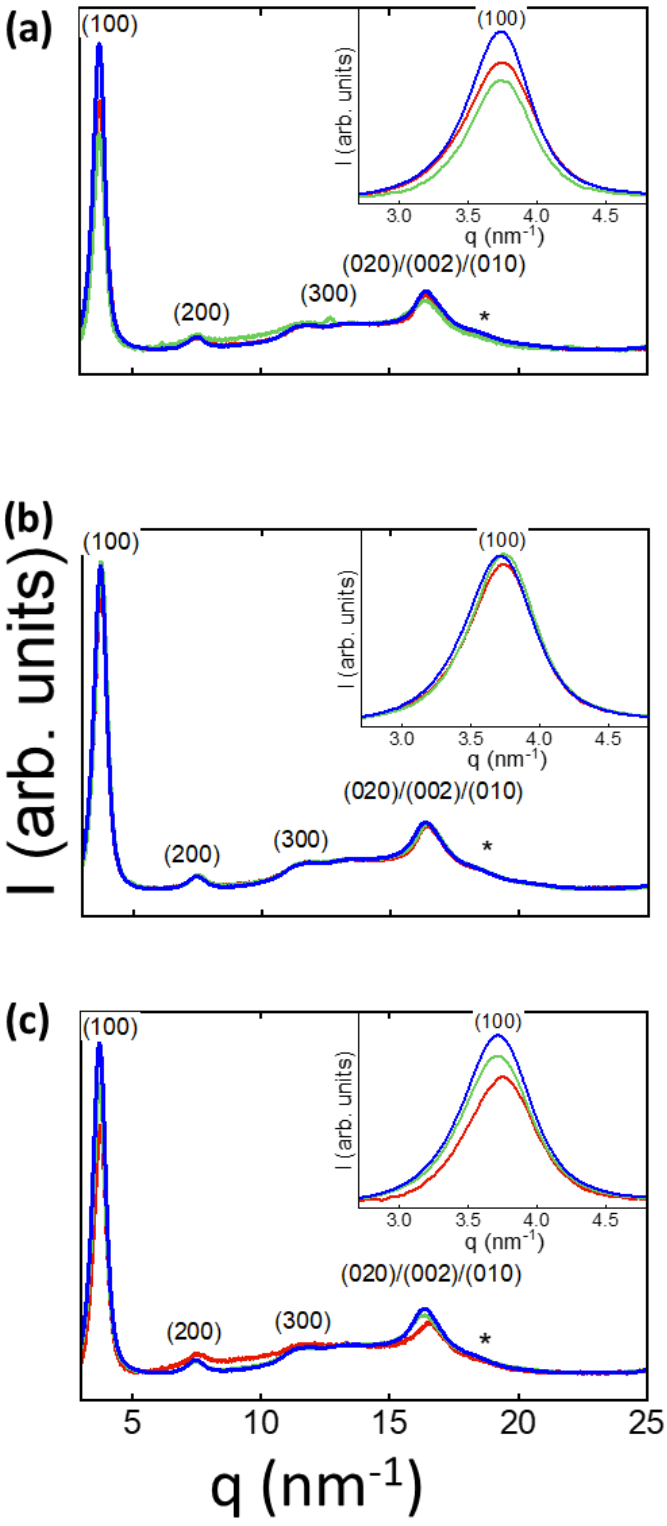

Figure 3.5. X-ray diffraction intensity patterns as a function of *q* of P3HT NPs prepared by flash nanoprecipitation using different conditions **(a)** R = 1/4, **(b)** R = 1/6 and **(c)** R = 1/8. Red corresponds to 1 g/L, green to 3 g/L and blue to 5 g/L. The main crystalline peaks of P3HT are labelled, and the asterisk corresponds to the side chain crystals of low molecular weight. The maximum (100) is shown as an inset within each diffractogram.

All the X-ray diffractograms from NPs prepared by flash nanoprecipitation (Figure 3.5) show the similar diffraction maxima, which correspond to those of the monoclinic unit cell observed in bulk P3HT[12-14] indicating that confining in the form of NPs the molecules of P3HT does not affect its crystalline unit cell[15]. For all preparation conditions, the X-ray diffracted intensity shows Bragg peaks at 3.7 nm^{-1}, 7.6 nm^{-1}, and 11.9 nm^{-1}, which correspond to the (100), (200) and (300) reflections, respectively. Additionally, they show a broad maximum at 16.5 nm^{-1} associated with the Bragg reflection (020)/(002)/(010)[16,17]. The diffraction maxima (h00) are indicative of lamellar stacking or alkyl stacking[18]. The reflections (0k0) indicate chain stacking along the π molecular orbitals, and (002) indicates the periodicity along the conjugated main chain, respectively[18–20]. A small shoulder at 18 nm^{-1} is assigned to the side chain crystals in low molecular weight P3HT[6,17].

Despite the presence of crystallinity in the material, the diffraction maxima demonstrate slight broadening. While both J and H-aggregates exhibited the same crystal structure (see Chapter 1.4.2.1), the predominance of J-aggregates is further substantiated by a slight shift towards a lower *q*, particularly in (020)/(002)/(010), with increasing concentration for all R = 1/6 and 1/8[13]. The crystalline domains, expressed as the coherence length, are closely related to the widths and positions of the diffraction maxima. Figure 3.6 shows the coherence length obtained from the Scherrer equation (see Eq. 2.4 in Chapter 2) at (100) reflection (alkyl stacking) and (020)/(002)/(010) reflection (π stacking)[21]. It is noteworthy that there is a trend towards a reduction in coherence length in R = 1/6 (Figure 3.6) in both reflections.

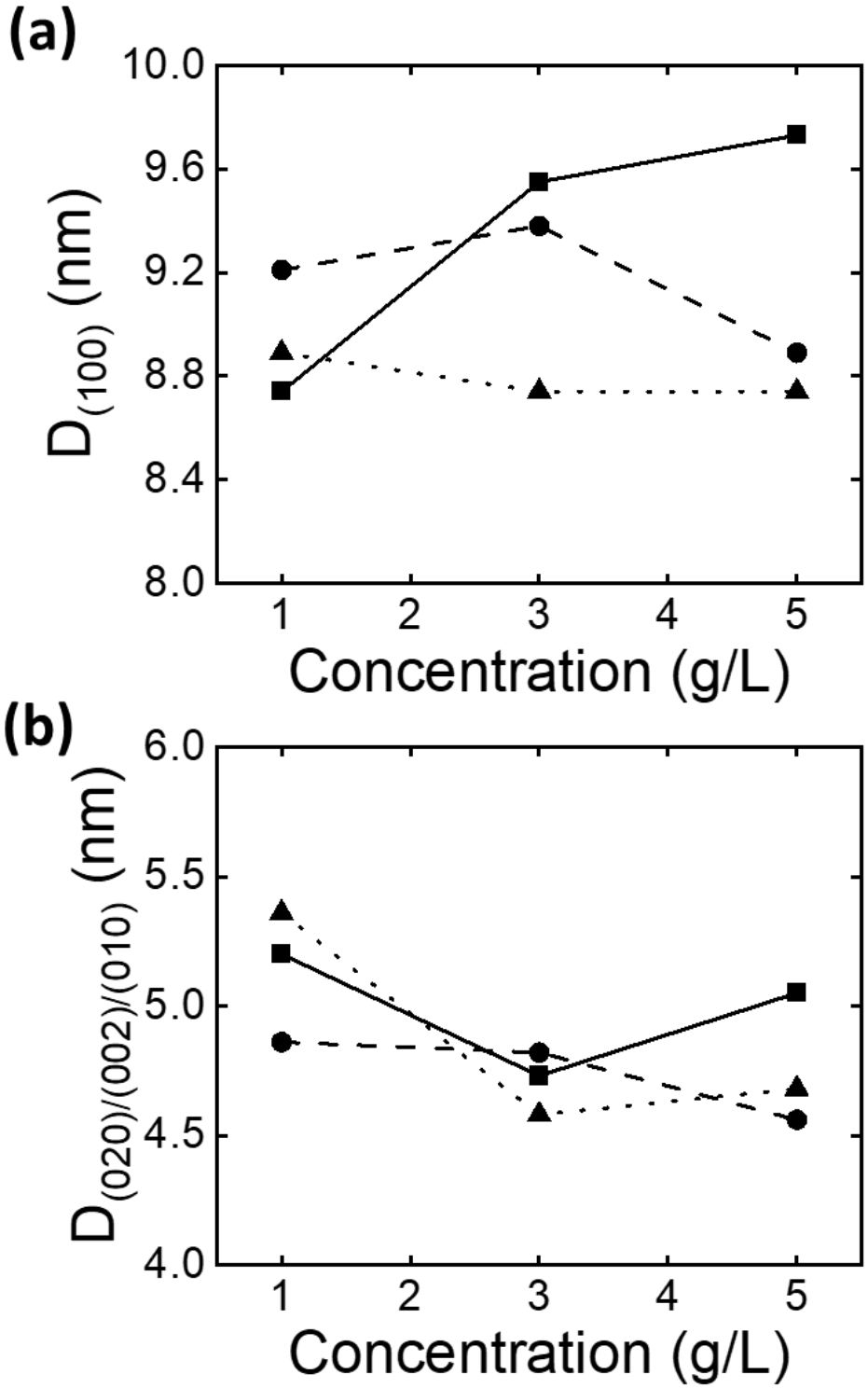

Figure 3.6. Variation of crystallite size along the axis perpendicular to the crystallographic plane associated with reflection **(a)** (100) and **(b)** (020)/(002)/(010). The square symbols connected by a solid line correspond to R = 1/4, the circular symbols with dashed lines correspond to R = 1/6, and the triangular symbols with dotted lines correspond to R = 1/8.

To qualitatively estimate trends in crystallinity, the integrated area of the (100) peak and of the (020)/(002)/(010) peak was calculated and normalised to the total area of the diffractogram. The values obtained from this analysis are presented in Table 3.3. NPs obtained from a 5 g/L concentration exhibit slightly higher integrated peak areas. In fact, with the exception of 3 g/L and R = 1/4, there is a clear trend of increasing crystalline content as the concentration increases. This behaviour can be rationalised by the flash process: at higher concentrations, rapid mixing provides a larger number of nuclei, which promotes the cooperative growth of crystalline domains within the nanoparticles. The higher concentration of the solution thus favours the formation of particles with a higher overall crystallinity. As shown in Table 3.2, there is a general tendency for higher concentrations to produce larger NPs. The X-ray results show that in those larger particles, crystallinity is higher, suggesting that the polymer chains within these particles may be better organised, whereas smaller particles, which are obtained from low concentrations, present lower crystallinity due to confinement effects[22]. In addition to these geometric restrictions, interfacial disorder induced by grain boundaries between crystalline domains can further disrupt long-range order at the nanoscale[23,24]. For smaller P3HT NPs, the higher surface-to-volume ratio implies that a significant fraction of polymer chains resides at or near the particle surface, where reduced packing constraints and increased defect density hinder the adoption of ordered crystalline conformations. In polycrystalline NPs, this effect is magnified by the high density of grain boundaries relative to the total volume, leading to a further reduction in the overall degree of crystallinity (see Figure 3.7).

Table 3.3. Relative integrated area (arbitrary units) values for peaks (100) and (020)/(002)/(010).

Concentration	$A_{(100)}/A_{total}$			$A_{(020)/(002)/(010)}/A_{total}$		
(g/L)	1/4	1/6	1/8	1/4	1/6	1/8
1 g/L	0.404	0.411	0.347	7.19×10^{-2}	7.82×10^{-2}	5.47×10^{-2}
3 g/L	0.325	0.420	0.410	6.50×10^{-2}	8.28×10^{-2}	7.41×10^{-2}
5 g/L	0.423	0.427	0.446	7.96×10^{-2}	8.90×10^{-2}	8.70×10^{-2}

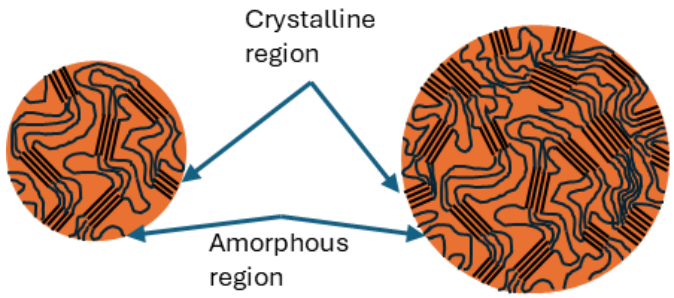

Figure 3.7. Schematic representation of the influence of particle size on the distribution of crystalline domains and surface area. Smaller nanoparticles present a higher relative surface area, which enhances the contribution of surface effects, whereas larger nanoparticles contain a greater proportion of inner volume with higher crystalline order.

3.1.2. Optical properties of the P3HT nanoparticles prepared by flash: absorption and emission

Figure 3.8 shows a photograph of a P3HT solution and of a dispersion of NPs prepared by flash.

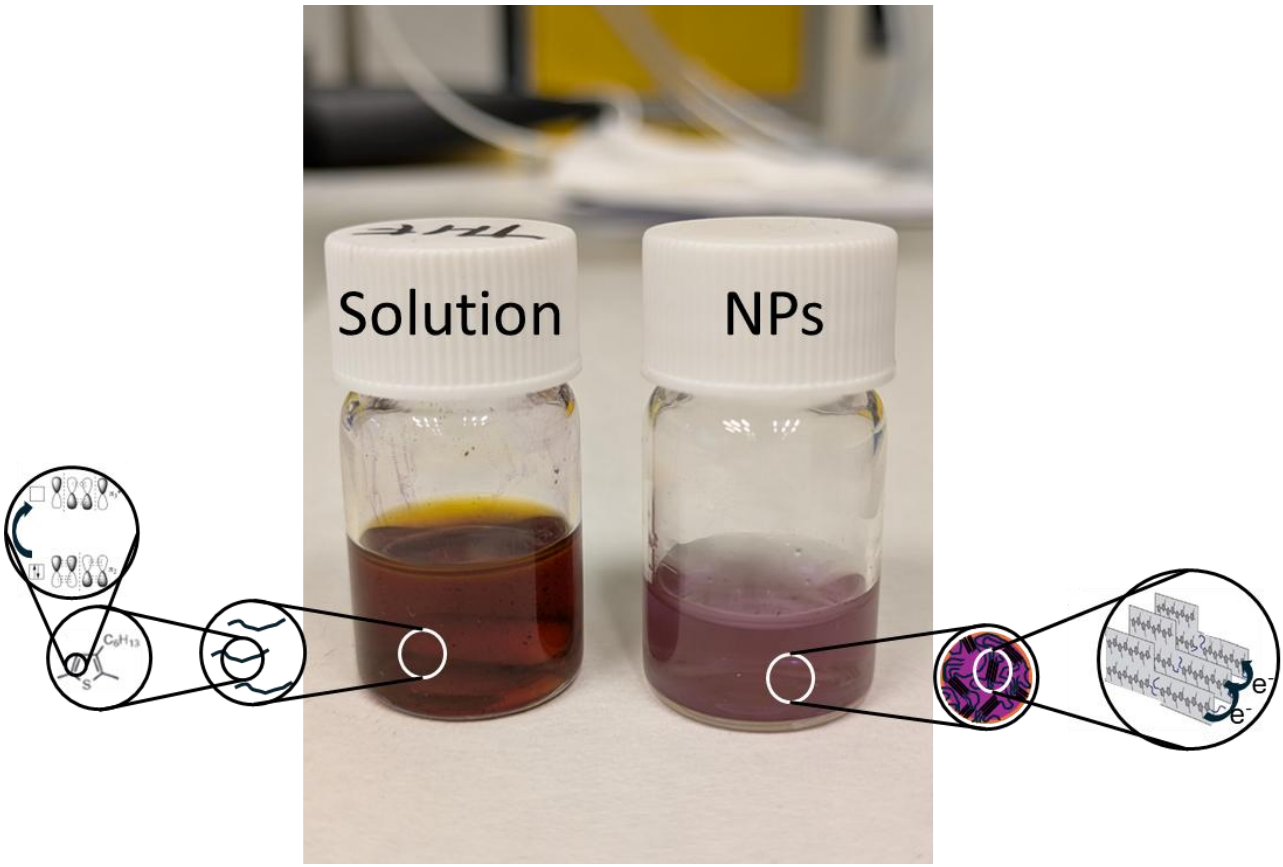

Figure 3.8. Schematic illustration of the optical behaviour of P3HT in different states. On the left, the colour of P3HT 3g/L dissolved in THF is shown. A zoom into the solution reveals isolated and disordered polymer chains, further magnified to depict the molecular structure of P3HT and the intramolecular $\pi \rightarrow \pi^*$ electronic transitions. On the right, the colour of aggregated P3HT 3g/L in the form of NPs is presented. A zoom reveals ordered and closely packed chains within the aggregates, and a final magnification highlights the $\pi \rightarrow \pi^*$ transitions associated with intermolecular interactions in the ordered domains.

The absorption and emission spectrum of dissolved P3HT is shown in Figure 3.9. In the absorption spectrum, some bands in the region below 500 nm are attributed to π–π^* transitions associated with the isolated conjugated chains or the amorphous state (Figure 3.9)[6,25,26]. The π–π^* transitions in conjugated polymers such as P3HT involve the excitation of electrons from full π orbitals to empty π^* orbitals. The energy of these transitions is dependent on the conjugation length of the polymer and the degree of torsion between the thiophene rings[27]. In dilute solutions, the chains adopt more disordered conformations, resulting in less intermolecular interaction and a greater contribution of intramolecular electronic states[20]. Additionally, there is a small band at 613 nm associated with the P3HT in aggregate form (Figure 3.9)[6,28–30].

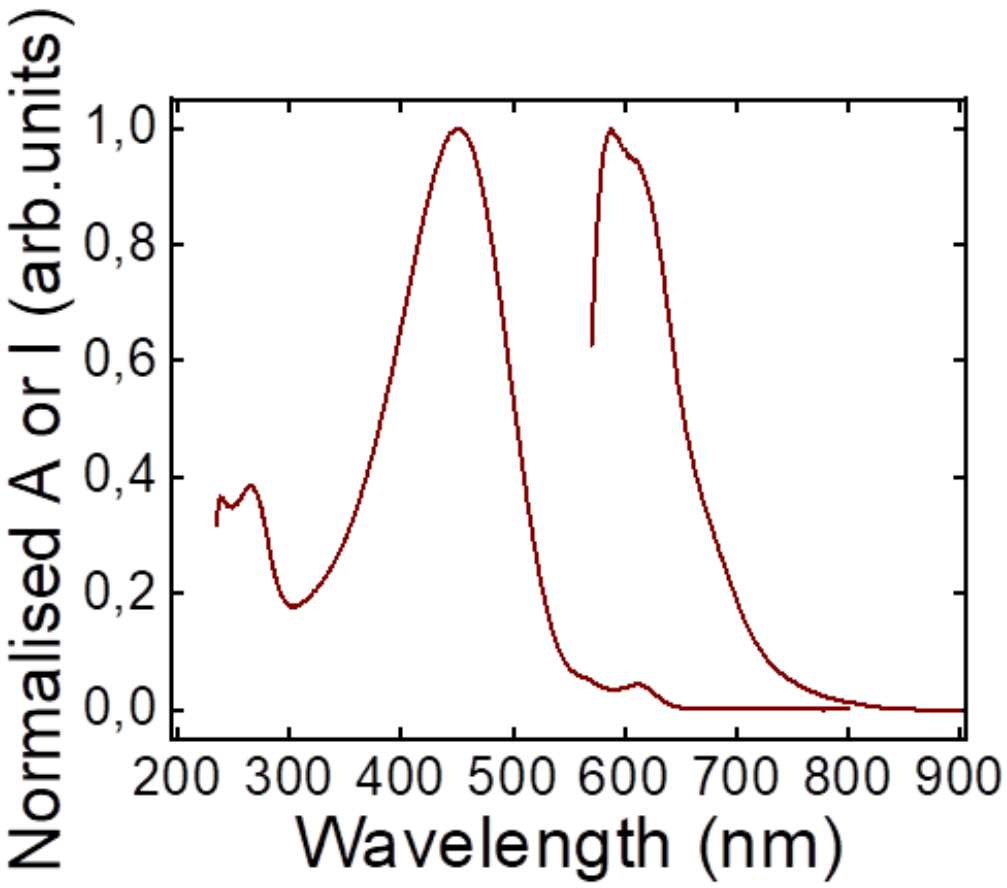

Figure 3.9. Absorption in the 200 to 800 nm range and emission in the 570 to 900 nm range of a P3HT solution in THF.

Conversely, the vibronic structure of the fluorescence emission spectra of dissolved P3HT manifests a predominant emission band centred at 580 nm, accompanied by a shoulder at longer wavelengths, reflecting the interaction between the vibrational modes of the polymer and the electronic excited states. This spectral profile, characteristic of this type of polymer[31], mirrors the heterogeneity of chromophore microenvironments as well as the structural rigidity and energy distribution of the excited state. Such behaviour may be indicative of differences in electronic geometry between the ground and excited states, leading to the presence of additional vibronic bands[32,33]. These bands are attributed to post-excitation conformational rearrangements, such as torsional relaxation[31], as observed in transient absorption studies in the picosecond range[34,35]. This relaxation leads to the stabilisation of the excited state, the appearance of additional vibronic features, and the potential formation of excitons[34,35]. Furthermore, environmental factors such as solvent

polarity, temperature, and the coexistence of coiled and extended P3HT conformations (which favour the formation of H or J aggregates) further modulate these spectral signatures and energy levels of the P3HT electronic states, contributing to the observed Stokes shift[36,37]. The presence of different configurations in the excited states is not only relevant for understanding the emission dynamics but also provides information on the molecular interactions and the stability of the excited states in these polymers.

Figure 3.10 shows the absorption and emission spectra of P3HT NPs prepared by flash nanoprecipitation. Compared to the spectra of P3HT in solution (Figure 3.9), the optical spectra of P3HT NPs prepared by flash exhibit complex behaviour that depends on both polymer concentration and the *R*. For all preparation conditions, the spectra display three bands, which indicates the molecular self-assembly of P3HT chains, corresponding to ≈612 nm in absorption and ≈667 nm in emission, ≈564 nm in absorption and ≈707 nm in emission, and ≈524 nm in absorption and ≈821 nm in emission, that correspond to the 0-0, 0-1 and 0-2 transitions, respectively. The presence of these bands is indicative of the existence of crystalline domains and, consequently, of electronic π–π* transitions at different vibronic levels[6,28-30]. The preparation of NPs results in aggregates that exhibit characteristics comparable to those of thermally or solvent-annealed bulk films of P3HT, which is noteworthy given the absence of any elevated temperature processing during the NPs preparation[38,39].

Figure 3.10 shows that the absorption bands appear primarily in the 500–600 nm region, suggesting a band gap in the approximate range of 1.4 eV to 2.5 eV (886 nm to 496 nm) for P3HT. The 0-0 band is attributed to the finite confinement of the π–π conjugation length and a reduction in the higher-order fine vibrational structure, resulting from reduced electronic interactions of the π orbitals (intrachain interaction)[40]. The 0-1 band is also associated with extended conjugation lengths, i.e., the π–π stacking (interchain interaction), while the 0-2 band corresponds to the π–π* intraband transition in disordered single polymer chains[41,42]. The energy difference between the 0-2 and 0-1 absorption peaks (0.13-0.15 eV) is attributed to the coupling of the π–π* transition with one C=C stretching phonon[43]. This coupling determines the relative intensity of the vibronic bands and reflects the structural stiffness or flexibility of the polymer chain. The P3HT absorption spectra in Figure 3.10 show a low-energy tail extending up to 750 nm (1.65 eV), particularly for all concentrations of $R = 1/4$. This can be interpreted in two ways. The first possibility relates to light scattering and sample reflectance at long wavelengths that give a false signal in absorbance

measurements[44]. Alternatively, the observed phenomenon could be attributed to forbidden sub-band transitions[44], possibly due to the formation of heterogeneous aggregates that increase the degree of site energetic disorder[45]. In this thesis, the latter explanation is favoured, given the correlation between the tail intensity and the aggregation state of the sample. Moreover, a minor contribution is observed at low wavelengths (300-400 nm) (see Figure 3.9), which can be attributable to the fact that the aggregation of P3HT molecules can exhibit crystalline, amorphous, or a combination of both characteristics. The presence of amorphous chain sequences within the P3HT aggregates has been demonstrated to give rise to structural defects, grain boundaries, and coiled-coil chain conformations[46]. However, in NPs (Figure 3.10), this contribution decreases, evidencing a reduction in dissolved P3HT chains.

The fluorescence emission spectra of the NPs reveal a predominant vibronic structure, with a pronounced peak and shoulder, accompanied by a less intense peak at higher wavelengths, which are attributed to the 0-0, 0-1 and 0-2 vibronic transitions[6,38], as depicted in Figure 3.10. This finding is consistent with the spectra of the bulk of the P3HT material[47], indicating that multiple potential energy surfaces contribute to the emission process, reflecting heterogeneity in the local environment of the chromophores. The 0-0 and 0-1 bands are indicative of intrachain and interchain exciton coupling in aggregated P3HT, respectively[48,49]. This dual contribution is linked to different modes of chain organisation, such as aggregated regions with interdigitated or tilted alkyl side chains[48,49]. The separation between the first peaks and the shoulders is approximately 0.07-0.12 eV, which is likely to reflect the stretching frequency of the C=C bond within the conjugated polymer backbone[50].

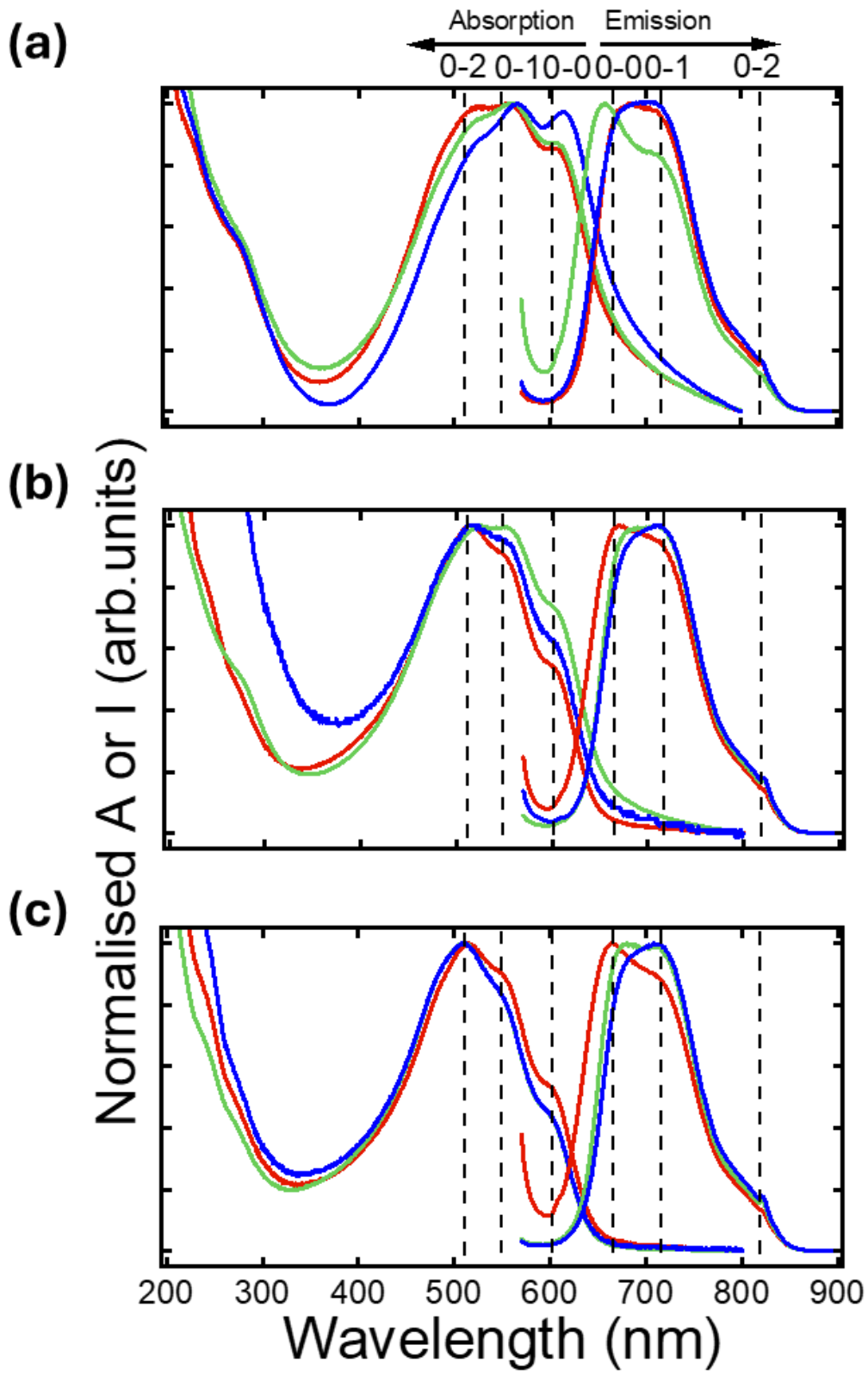

Figure 3.10. Optical absorption and emission spectra of the different volume ratios **(a)** 1/4, **(b)** 1/6 and **(c)** 1/8. Red corresponds to 1 g/L, green to 3 g/L and blue to 5 g/L. Labels correspond to the vibronic transitions between indicated levels.

Subtle differences in the spectra are observed with polymer concentration at fixed *R*. However, these variations do not appear to exhibit any clear trends. At the $R = 1/4$, the X-ray data indicate that the 5 g/L sample has a higher crystallinity (see Table 3.3). This finding is consistent with the information obtained from UV-Vis absorption, where a slight shift towards longer wavelengths is observed in the 5 g/L concentration, indicating a greater degree of chain organisation and the presence of J-aggregates. Spano et al. provide a theoretical framework for understanding how disorder and aggregation influence the vibronic structure in conjugated polymers[37,51–54]. According to the HJ model[32,52,54] (see Chapter 1.4.2.1), J-aggregates, characterised by a "head to tail" arrangement, influence the electronic coupling, thereby favouring greater intrachain exciton coupling and promoting greater molecular planarity of the thiophene rings due to more extended chains[41,43,46]. Sharratt et al.[10] emphasise that even minor variations in the concentration or antisolvent ratio can lead to significant differences in nucleation and growth processes, thus altering the size and structural order of the resulting NPs. For instance, previous studies have observed this behaviour when P3HT films are exposed to methanol vapours[41] or when P3HT NPs prepared by reprecipitation are subjected to hydrothermal post-treatment[43]. In the context of solid films, these changes have been attributed to intermolecular interactions between thiophene chains that extend ground-state conjugation across multiple chains, generating a two-dimensional character to the electron cloud delocalisation[55]. A similar phenomenon has been observed in the aggregation of polymer chains in mixtures of "good" and "bad" solvents[56,57], which promote a more ordered arrangement that favours better electronic organisation. These studies demonstrate that these parameters critically affect the self-assembly and crystallinity of P3HT. The presence of more defined absorption bands is indicative of greater π-conjugation, which in turn suggests more favoured electronic transitions[25,28,40,58]. In addition, an enhancement in the higher-order vibrational fine structure is observed, attributed to the increase in electronic interactions between the π orbitals, resulting in greater vibrational coupling due to a higher degree of long-range order within the material[40]. The aforementioned results are further supported by the absorption tail observed at high wavelengths, thereby facilitating lower energy transitions[43,52].

The ratios between the absorption of the 0-0 and 0-1 bands provide complementary information on the presence of J-H aggregates (see Table 3.4)[52,54]. All $A_{0\text{-}0}/A_{0\text{-}1}$ ratios in absorption are less than 1, indicating that J-aggregates and H-aggregates coexist with non-

aggregated chain sequences[46]. A low intensity of the 0-0 band leads to a higher exciton bandwidth, indicating a shorter conjugation length and a lower planarization of the P3HT main chain associated with the H-aggregates[54,59]. This phenomenon can also be interpreted as the lower the ratio between the two bands, the weaker the intra-chain exciton coupling relative to the inter-chain interactions[60]. For *R* = 1/4, the $A_{0\text{-}0}/A_{0\text{-}1}$ ratios in absorption increase with the concentration, indicating a greater presence of J-aggregates. Furthermore, the ratio of 0-0 and 0-1 bands in emission is greater than 1 for all concentrations except R = 1/4 and 5 g/L, indicating the presence of a mixture of J and H aggregates[52], as observed in absorption. Conversely, for *R* = 1/4 and 5g/L, a greater presence of J-aggregates is observed. Notably, the intensity of the two fluorescence bands is nearly identical for all three ratios, indicating that relaxation to the 0-1 vibronic state is just as probable as the 0-0 transition. This observation indicates the presence of crystalline regions in P3HT, as the transition to the first vibronic state is accessible[49]. However, few electrons are initially promoted from the fundamental electronic state to a vibrationally excited state in the electronically excited molecule.

Table 3.4. The intensity ratios between the 0-0 and 0-1 bands of the absorption and emission spectra for all concentrations at each volume ratio.

R	Concentration (g/L)	$A_{0\text{-}0}/A_{0\text{-}1}$ Absorption	$I_{0\text{-}0}/I_{0\text{-}1}$ Emission
1/4	1	0.854	1.022
	3	0.873	1.196
	5	0.978	0.993
1/6	1	0.595	1.045
	3	0.728	1.002
	5	0.660	1.023
1/8	1	0.593	1.116
	3	0.546	1.013
	5	0.546	1.023

At *R* = 1/6 and 1/8, the most defined absorption bands are observed at 3 g/L and 1 g/L, respectively, and no tendencies have been observed in $A_{0\text{-}0}/A_{0\text{-}1}$ ratios for *R* =1/6 and 1/8 in absorption. In the fluorescence spectra, for *R* = 1/6 and 1/8, a shift towards higher

wavelengths is observed as the concentration increases, which indicates enhanced electronic delocalisation within the solid-state polymer structure and improved intermolecular ordering[26]. This shift is accompanied by the appearance of less-defined bands, with the 0-1 and 0-2 bands becoming more intense (see Figure 3.10). This indicates an increase in the crystallinity (particularly in P3HT NPs with tilted side chains) and the planarization of the chains[43], possibly due to increased interaction between chains and better localised intermolecular ordering[38]. These results are consistent with the X-ray results (see Table 3.3).

The X-ray results suggest that the packing of the chains becomes less efficient as the concentration decreases. In line with observations by Beaujuge et al.[61] and Liu et al.[62], higher molecular organisation has been associated with a reduction in energetic discontinuities between ground and excited states, which can result in a lower band gap. Based on this, it is plausible that samples from lower-concentration solutions, which show reduced crystallinity, may exhibit a slightly larger band gap. The band gap, defined as the energy difference between the HOMO and the LUMO, was determined from absorption and emission spectra (Table 3.5) using two approaches: the intersection of both spectra[37] and the Tauc plot (Chapter 2.4.4.1)[6,63–65].

Table 3.5. Band gaps for all concentrations at each volume ratio, calculated from the intersection of the absorption and emission spectra and the Tauc plot.

R	Concentration	Abs-emis cross	Tauc plot
1/4	1	1.93 ± 0.01 eV (644 nm)	1.89 ± 0.02 eV
	3	1.96 ± 0.01 eV (632 nm)	1.88 ± 0.02 eV
	5	1.91 ± 0.01 eV (648 nm)	1.87 ± 0.02 eV
1/6	1	1.99 ± 0.01 eV (625 nm)	1.97 ± 0.02 eV
	3	1.95 ± 0.01 eV (635 nm)	1.95 ± 0.02 eV
	5	1.94 ± 0.01 eV (638 nm)	1.96 ± 0.02 eV
1/8	1	2.00 ± 0.01 eV (621 nm)	1.96 ± 0.02 eV
	3	1.97 ± 0.01 eV (631 nm)	1.96 ± 0.03 eV
	5	1.96 ± 0.01 eV (633 nm)	1.96 ± 0.03 eV

All values fall within the visible range, as expected. For example, the 5 g/L sample shows a slightly lower band gap by the intersection method, consistent with its marginally higher

crystallinity measured by XRD and UV-Vis spectroscopy. For $R = 1/6$ and $1/8$, the band gap decreases slightly with increasing concentration. By contrast, the Tauc plot yields similar values for all concentrations within each R.

Moreover, in the context of photodegradation, it is of interest to determine the values of the conduction band edge potential (E_{CB}) and the valence band edge potential (E_{VB}) (see Chapter 2.4.4.1) obtained from the Tauc plot[63,64]:

The values obtained for E_{CB} and E_{VB} agree with those reported in other studies[63,66] (Table 3.6), and are very similar to each other, observing that when the band gap diminishes, E_{CB} increases in energy, and E_{VB} decreases in energy.

Table 3.6. Conduction band edge potential (E_{CB}) and the valence band edge potential (E_{VB}) for all concentrations at each volume ratio, calculated from the intersection of the absorption and emission spectra and the Tauc plot.

Volume ratio	Concentration	E_{CB}	E_{VB}
1/4	1	-1.66 eV	0.23 eV
	3	-1.65 eV	0.23 eV
	5	-1.65 eV	0.22 eV
1/6	1	-1.70 eV	0.27 eV
	3	-1.69 eV	0.26 eV
	5	-1.69 eV	0.27 eV
1/8	1	-1.69 eV	0.27 eV
	3	-1.69 eV	0.27 eV
	5	-1.69 eV	0.27 V

3.2. Effect of the THF/water ratio (R) on the morphology and characteristics of the nanoparticles

The crystalline and microstructural properties of P3HT NPs can be modulated by controlling the crystallisation conditions. This section will examine the structural and optical differences that appear in NPs when the THF/water volume ratio (R) is varied (1/4, 1/6, 1/8) while keeping the concentration constant during the preparation process (Figure 3.1).

3.2.1. Effects of R on the size, morphology and aggregation

For this study, similar deposition and imaging conditions as those shown in section 3.1.1.1 were utilised. Figure 3.11 presents the AFM images obtained in tapping mode from P3HT NPs deposited onto silicon wafers from a 5 g/L solution, illustrating the presence of aggregates at all volume ratios, particularly at 1/4, where there is less antisolvent in the injection step.

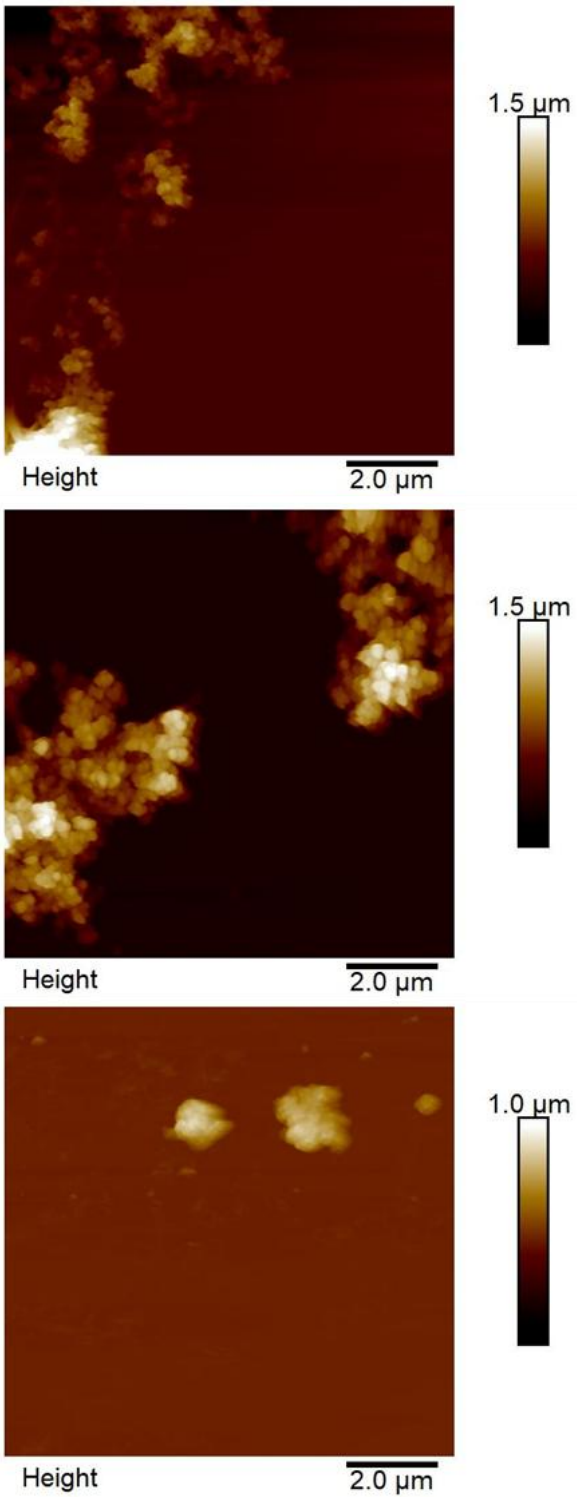

Figure 3.11. AFM topographic images of (a) R = 1/4, (b) R = 1/6, (c) R = 1/8 for P3HT 5 g/L.

The corresponding size distributions (Figure 3.2) and size results (Table 3.1) indicate no clear linear trend with *R*. However, it is evident that, for the *R* = 1/6, a smaller size is observed for all ratios (see Table 3.1), a trend also confirmed by DLS measurements (Table

3.2). The variation in NP size can be attributed to the fact that flash is a very sensitive technique to the injection rate, as noted in the review by Liu[67], which generates different flow rates and supersaturation conditions, which directly affect the final size. The lack of precise control of the injection rate results in a lack of clear trends. One potential solution to this challenge is the utilisation of microfluidic machines, which have been demonstrated to enhance the control of the mixing rate between solvent and antisolvent (see Chapters 2 and 6 for further details). In this instance, the 1/6 ratio has been identified as optimal with respect to injection rate; however, probably, this *R* may also represent an optimal solvent-to-antisolvent balance for achieving favourable supersaturation conditions, which promote rapid nucleation while limiting growth time, ultimately yielding smaller NPs[67]. In essence, high supersaturation enables the growth of a multitude of nuclei, thereby yielding a higher NP yield with reduced particle size, while low supersaturation results in larger particles[67]. However, when the number of nuclei is very high, growth occurs mainly through random collisions of existing particles, leading to the presence of aggregates[67]. Consequently, utilising a reduced proportion of antisolvent (e.g., 1/4) can result in elevated supersaturation, thereby prolonging the nucleation period and enhancing the probability of aggregation between particles. Conversely, employing an increased proportion of antisolvent (1/8) leads to diminished supersaturation, which, in turn, increases the growth rate and produces larger particles.

3.2.2. Effects of R on the crystalline structure of the P3HT nanoparticles prepared by flash.

As illustrated in Figure 3.5, the diffractograms are presented as a function of *R*. Concerning the degree of crystallinity for 3g/L and 5g/L, the *R* = 1/6 is identified as the most crystalline (Table 3.3). However, for a concentration of 5 g/L, all volume ratios demonstrate similar crystallinity (see Table 3.3). This may be due to the concentration effect, which is possibly very oversaturated for all *R*, so that the *R* ratio becomes less determinant. As previously mentioned, the 1/6 ratio provides an optimal balance, giving rise to a higher crystallinity of the NPs. Conversely, at *R* = 1/4 or *R* = 1/8, the presence of a greater number of aggregates or larger particle size results in lower crystallinities.

Additionally, there is an increase in the widths of the (100) Bragg peaks as *R* increases for 3 g/L and 5 g/L, which indicates a decrease in the size of the crystalline domains (Figure 3.12), confining crystal growth to smaller domains.

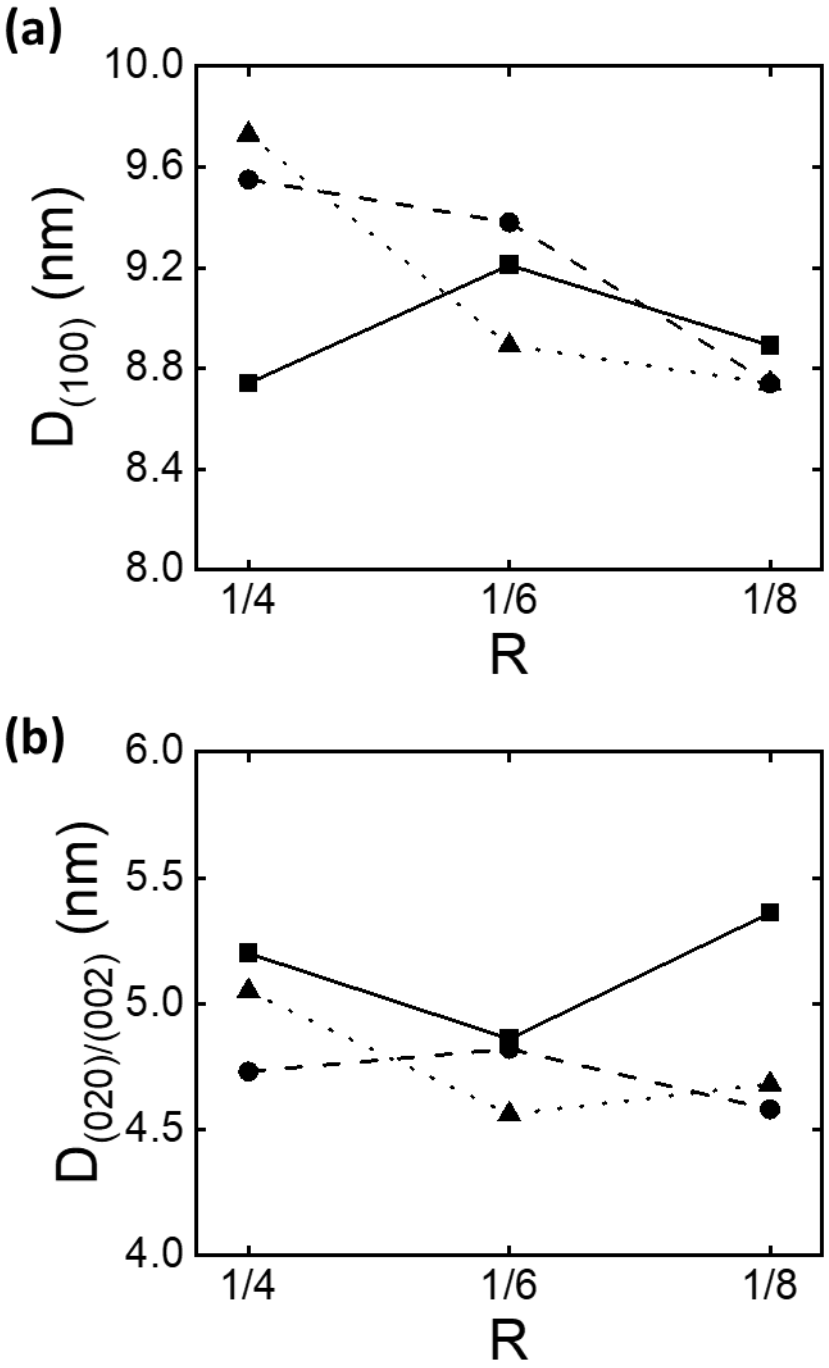

Figure 3.12. Variation of crystallite with R size along the axis perpendicular to the crystallographic plane associated with reflection **(a)** (100) and **(b)** (020)/(002). The square symbols connected by a solid line correspond to 1 g/L,

the circular symbols with dashed lines correspond to 3 g/L, and the triangular symbols with dotted lines correspond to 5 g/L.

3.2.3. Optical properties of P3HT nanoparticles: absorption and emission

As demonstrated in Figure 3.10, distinct trends in the absorption spectra become discernible when the *R* is varied. For all samples, the 1/4 ratio appears to be more ordered due to the more defined bands at high wavelengths and a slight shift to longer wavelengths[25,28,40,58]. This observation is also interpreted as evidence of greater intrachain exciton coupling resulting from enhanced π–π interactions and improved chain planarization in these samples (J-aggregates)[53,59]. In addition, for the 1/4 ratio, a more pronounced tail extending towards higher wavelengths is observed. Lee et al.[43] also report this increase in the tail in P3HT NPs when J-aggregate formation was promoted. Despite the absence of explicit explanations in the literature concerning the relationship between this tail and the presence of H and J aggregates, the observed enhancement of the high-wavelength tail can be hypothesised to suggest that its occurrence is favoured by a higher proportion of J-aggregates. Conversely, the sample prepared at $R = 1/8$ exhibits a reduced degree of order and a diminished π–π interaction, a finding corroborated by the slight increase in the band gap (see Table 3.5) and a reduction in the ratio between the 0-0 and 0-1 vibronic bands (Table 3.4), suggesting that the crystalline domains are less well developed[42].

The fluorescence spectra (see Figure 3.10) further reinforce these findings. A shift towards shorter wavelengths as *R* passes from 1/8 to 1/4, particularly for 1 g/L, suggests a reduction in electronic delocalisation within the solid state[26]. This is supported by the intensity ratio in fluorescence between 0-0 and 0-1. These exceed 1, thereby corroborating the absorption results that indicate the presence of H- and J-aggregates[52], and there is a general decrease in the 0-0/0-1 ratio as *R* decreases that is often associated with lower planarity and weaker intrachain coupling. This may be due to an increase in structural defects or twists that disrupt conjugation along the chain. It can thus be concluded that an optimised *R* (e.g., 1/4) promotes more efficient chain packing and stronger intermolecular interactions than less favourable conditions (e.g., $R = 1/8$). The observed spectral trends (ranging from the defined absorption bands and lower band gap values to the specific fluorescence band ratios) provide strong evidence that processing conditions, particularly the volume ratio,

critically affect the crystalline order and excitonic dynamics of P3HT NPs. However, these aggregates may not pack efficiently into extended three-dimensional crystals, as evidenced by a reduction in crystallinity.

3.3. Effect of aging on the morphology and characteristics of the nanoparticles

In the preceding sections, it was demonstrated that the preparation conditions can influence the properties of P3HT NPs. In the literature, the impact of the changes in solution has previously been investigated by, for example, lowering the temperature, adding a small amount of poor solvent or using external mechanical stimuli[60,68–70]. Another determining factor to consider is the aging of the polymer solutions. The present section will discuss the influence of aging P3HT solutions on the properties of the prepared NPs prepared from a 3 g/L polymer solution and flash precipitated at a ratio R = 1/6, including size, morphology, aggregation, crystallinity and optical properties.

To explore this, the protocol detailed in Chapter 2.2.2.1 (Flash Nanoprecipitation) was employed for the preparation of the aged solutions. But, in this case, the solution was left to stand for a specific period of time, which covers intervals of 1 h, 1.5 h, 2 h, 24 h, 72 h, and 168 h (see Figure 3.1). These times were selected based on previous studies suggesting that significant changes in optical properties can occur on time scales of hours to days[71–73]. The optical properties of the solutions aged at different times were evaluated through UV-Vis absorption spectroscopy to detect any significant spectral shifts or changes in the vibronic features. The aging times where notable changes occur were then selected for NP preparation using the flash nanoprecipitation method, with a *R* = 1/6. The concentration of 3g/L and *R* = 1/6 was selected because these conditions produce the smallest NPs and less polydispersity in size when prepared from fresh solutions.

3.3.1. Effect of the P3HT solution aging on the optical properties

In other studies, different techniques have been explored to induce the aggregation of P3HT in solution (from now referred to as pre-aggregation, to differentiate from aggregation in the preparation of NPs)[74,75]. Pre-aggregation and solution crystallisation depend on several parameters, of which the polymer-solvent interactions appear to be the most significant and the most easily controllable[18,75,76]. In suitable solvents where solute-solvent interactions are notably strong, P3HT chains tend to be extended and with high mobility. The tendency for these chains to assemble competes with their solvation. Enhanced solvation increases the interaction between the molecular chains and the solvent, thereby reducing the possibility of chain aggregation and interchain packing.

Figure 3.13 shows the UV-Vis spectra of the P3HT solutions in THF aged for different times. Besides the broadband centred around 450 nm, as aging proceeds, a series of absorption bands at 612 nm, 564 nm and 524 nm are observed, and their intensity increases with aging time. These bands indicate the formation of ordered aggregates (by $\pi-\pi$ stacking) with long-range order[60]. These modifications are also visible by eye, as a perceptible colour change in the solution is observed, from an initial orange state of low viscosity to a final thick dark red/purple tone, indicating that aggregation leads to significant alterations in the optical properties[76,77]. Notably, this transformation occurs rapidly as the sample is cooled down from the temperature used to prepare the solution to room temperature. This aggregation is slower in other solvents such as $CHCl_3$ or chlorobenzene[20,78]. In fact, a small band is observed in the solution at 0 hours, corresponding to the presence of ordered aggregates. In contrast, this band will not be observable in fresh solutions prepared with $CHCl_3$, as will be demonstrated later, thus showing that THF is not such a good solvent. Additionally, Chu et al.[45] reported that the pre-aggregation time is affected by concentration, being shorter at higher concentrations, suggesting that in this case, chain interactions are favoured. In Figure 3.13, the bands observed in aged solutions that are indicate the presence of aggregates that have been reported to have different shapes, like spirals, fibres or fibrils, lamellas, rods, wires or other crystalline species[18,26,69,78]. Studies have also shown that conjugated polymers exhibit physical gelation during aging due to the fact that aggregation slows down the structural reorganisation dynamics[26]. The broadband observed at 430 nm and associated with non-aggregated chains[45] (see Figure 3.13) exhibits a reduction in the intensity and a shift towards higher wavelengths during the aging process. It has been suggested in the literature that these

aggregates are transformed directly from individual polymer chains without going through an intermediate stage[79].

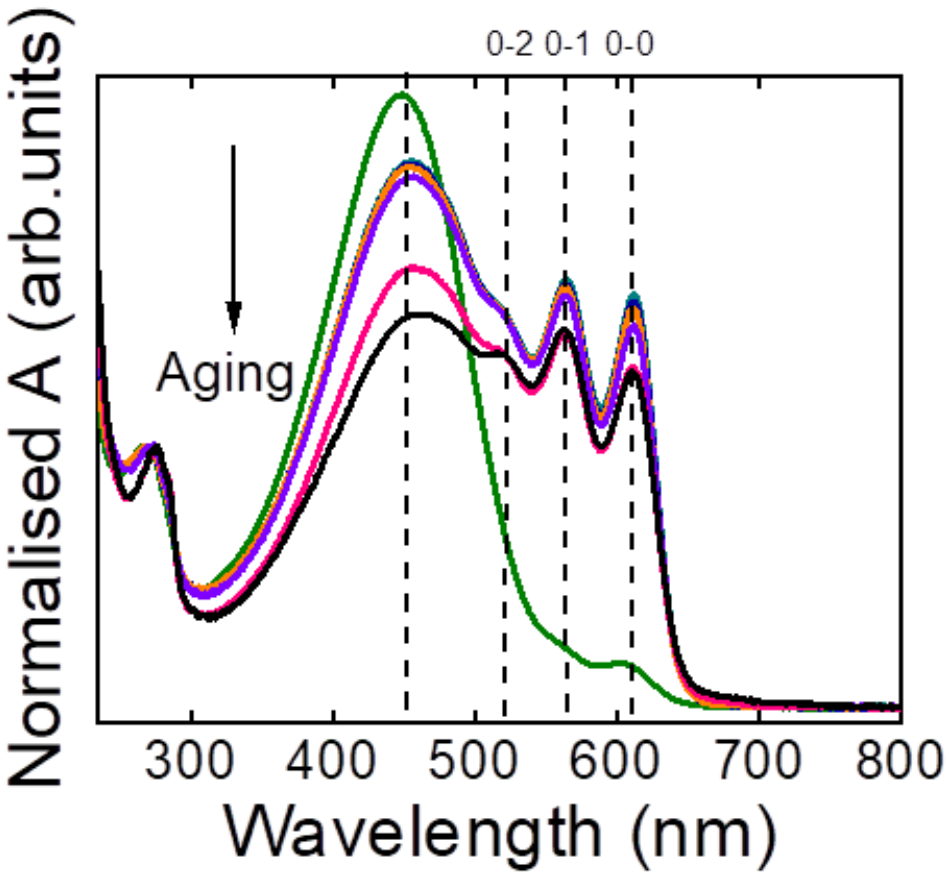

Figure 3.13. UV-Vis absorption spectra of P3HT solutions at varying aging periods: olive colour 0 hours, cyan 1 hour, blue 1.5 hours, orange 3 hours, violet 24 hours, red 72 hours, and black 168 hours. The data was normalised to the maximum at 274 nm to facilitate analysis and interpretation.

Similar analysis of the spectra, in terms of the A_{00}/A_{01} ratio, can be performed here. The A_{00}/A_{01} ratio (Table 3.7) decreases as aging progresses. This observation indicates an increased propensity for the presence of H aggregates[46,52,59,60], which implies parallel stacking of the P3HT chains.

Table 3.7. Ratio of absorption intensities between the 0-0 and 0-1 vibronic transitions for different aging times.

Aged (h)	A_{00}/A_{01}
0	-

1.0	0.963
1.5	0.954
3.0	0.948
24	0.921
72	0.908
168	0.887

In order to better understand the formation of these ordered aggregates, several mechanisms were considered, including possible chain fragmentation due to solvent-related effects, conformational collapse, and supramolecular reorganisation. In addition, photo-oxidation processes arising from hydroperoxides formed in THF upon light exposure could also contribute, potentially favouring polymer crystallisation[80,81]. To probe variations in apparent chain size in a coiled conformation, three P3HT solutions were studied via DLS (Table 3.8): one fresh, one aged for 48 hours, and another aged for 744 hours (one month). Prior to measurement, all solutions were heated and stirred to dissolve existing aggregates, ensuring comparable initial conditions. As explained above, P3HT in THF shows rapid aggregation, making measurements without pre-aggregation and their reproducibility challenging. Correlograms were analysed by the cumulant method (Section 2.4.3). Table 3.8 shows a reduction in apparent chain size with increasing solution age. This decrease may result from physical changes such as conformational collapse or aggregate reorganisation, or from partial chemical modification (e.g., oxidation or chain scission). Further molecular-weight distribution analysis (e.g., by GPC) would be required to unambiguously distinguish between these scenarios.

Table 3.8. Chain size measured as hydrodynamic diameter for P3HT solutions with different aging: 0 h (unaged), 48 h and 744 hours.

Aged (h)	Chain size (nm)
0	50
48	18
744	8

Once the optical properties of the aged solutions have been discussed, the impact on the NPs prepared from such aged solutions is discussed. In view of the results obtained, three

distinct aging periods were selected for the preparation of NPs. The periods were 24, 72 and 168 hours. The duration of the experiment could not be extended due to the significant gelation of the solution, which impeded the formation of stable NPs. It was observed that this gel is stable, and no precipitates are formed even after a month.

3.3.2. Effect of the P3HT solution aging on the morphology and characteristics of the nanoparticles

Figure 3.14 shows AFM images of the NPs obtained from solutions aged at different times.

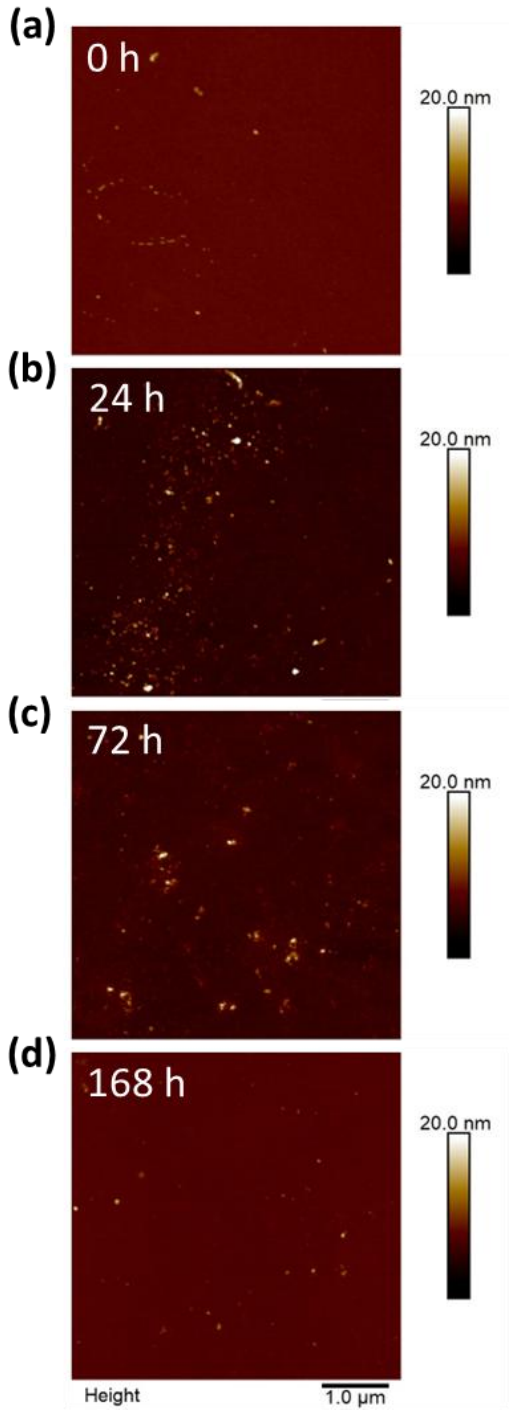

Figure 3.14. AFM topography images of P3HT NPs deposited on silicon wafers. NPs were prepared from solutions with concentrations of 3g/L using different aged solutions: **(a)** 0 hours, **(b)** 24 hours, **(c)** 72 hours and **(d)** 168 hours. Scale bars: 1 µm

The topography images of P3HT NPs from the aged solutions (Figure 3.14) in the same conditions as in previous sections, and histograms of the size distribution were obtained from the NPs sizes (Figure 3.15). Similar to what happens for NPs prepared from fresh

solutions, they are not perfectly spherical, due to the presence of crystalline domains, as confirmed by X-ray scattering experiments in the following section. The results obtained by AFM (see Figures 3.14 and 3.15) demonstrate dispersed NPs with more repeated diameters of around 20-40 nm for all samples. All histograms appear to present a single population with a general tendency to decrease in size as the aging of the initial solution increases. This phenomenon is attributed to the nucleation process being driven by the formation of numerous pre-aggregates that act as nucleation centres, thereby yielding smaller particles by depletion of the solute in the vicinity of the nuclei.

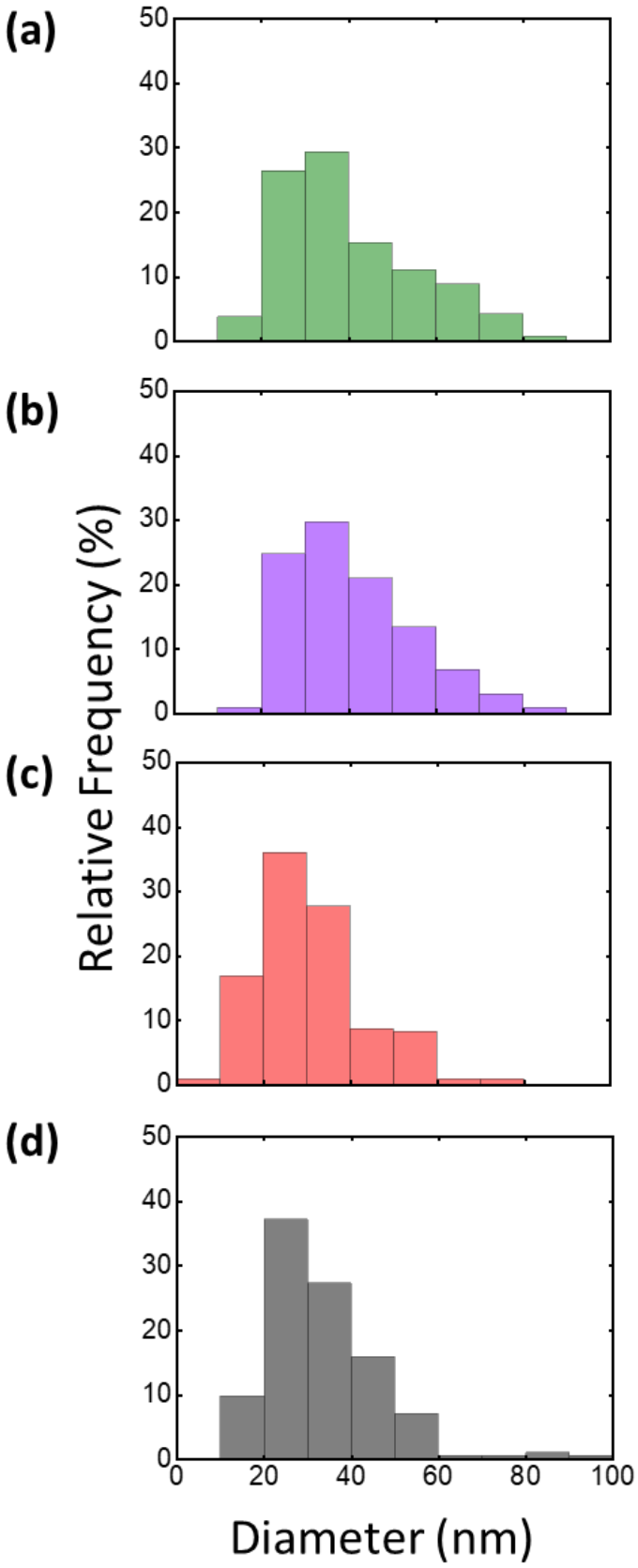

Figure 3.15. The corresponding size distribution histograms of **(a)** 0 hours, **(b)** 24 hours, **(c)** 72 hours and **(d)** 168 hours.

Figure 3.16 shows the dependence of the most repeated diameter obtained by AFM as a function of the aging time.

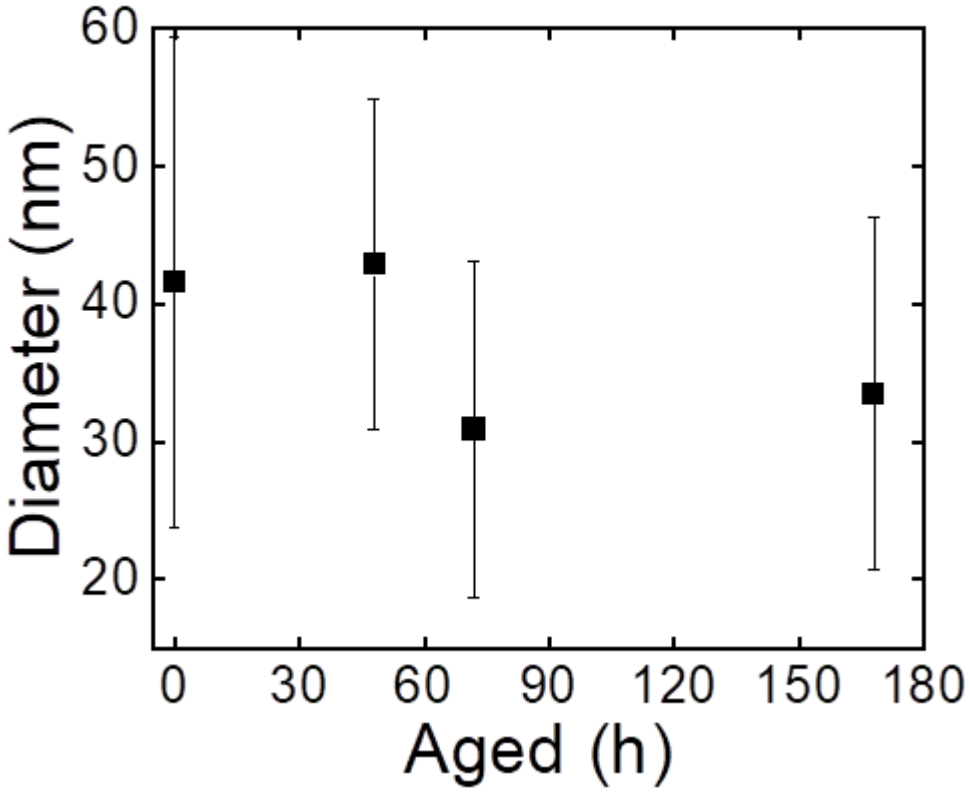

Figure 3.16. Variation of the mean diameter obtained by AFM for NPs prepared from aged solutions. Error bars have been incorporated to indicate the standard deviation.

While the size of individual NPs slightly decreases, as observed in Figure 3.16 for AFM, there is also an increase in the presence of aggregates of multiple associated NPs, as observed in Figure 3.17.

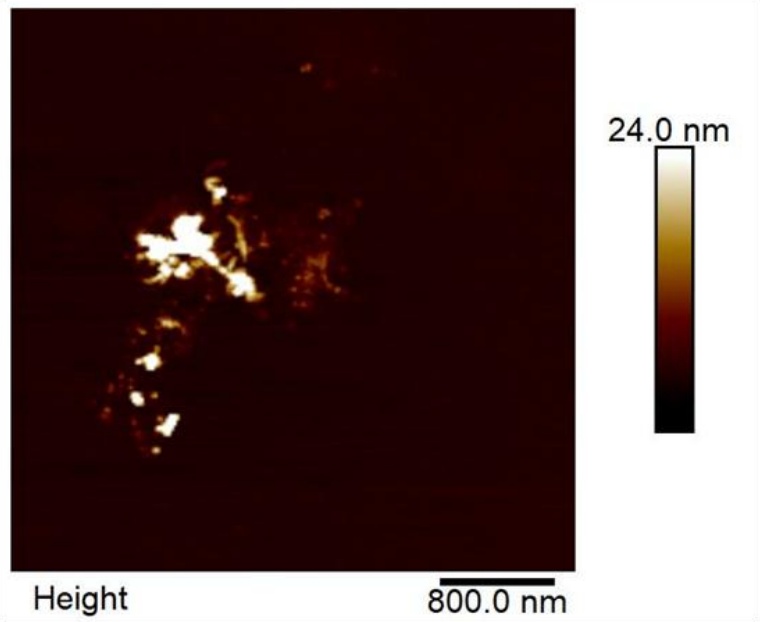

Figure 3.17. AFM image of a sample of P3HT NPs aggregates corresponding to aging of 168 hours.

In addition, the size of the NPs in dispersion was studied by DLS. The D_n and Q obtained from these results are presented in Table 3.9. It can be observed that the NP diameter is reduced in comparison with NPs prepared by unaged solutions and increases slightly as the aged solution increases. However, an increase in D_n is accompanied by an increase in Q. This result lends support to the hypothesis that certain aggregates are present during the ageing process of the solution in preparation for NPs.

Table 3.9. Results of the D_n values and Q of P3HT NPs prepared using aging solutions obtained using DLS.

Aged solution (h)	D_n (nm)	Q ($x10^{-2}$)
0	56 ± 27	12 ± 10
24	12 ± 12	$13*10^{1}$ ± 40
72	31 ± 7.5	66 ± 8.1
168	55 ± 4.3	53 ± 1.4

This phenomenon could be attributed to the formation of crystalline aggregates within the solution, resulting in its thickening, as postulated by Chen et al[26]. This thickening can be attributed to the gelation of the P3HT solution during the aging process. The nucleation and growth model suggests that the longer the solution ages, the more nucleation occurs, leading to the increased gelation (or thickness) of the solution, thereby restricting the mobility of the chains. Under these thermodynamic conditions, the formation of solid crystallites is facilitated, ultimately leading to the precipitation of smaller, more ordered NPs during nanoprecipitation. It has been hypothesised that the pre-aggregation of P3HT in solution, caused by specific solvent-polymer interactions, directly precedes the formation of solid crystals, i.e., pre-aggregates act as nucleation sites[18]. However, in the context of flash nanoprecipitation, where rapid solvent exchange is essential, the accelerated aggregation and gelation during the aging process could also impede the rapid displacement of the solvent by the antisolvent, resulting in an increased number of aggregates and broader NP size distributions (kinetic effect) due to different degrees of supersaturation and limited chain mobility. It is crucial to note that this dual kinetic-thermodynamic control mechanism is pivotal in determining the final NP properties.

3.3.3. Crystalline structure of aged P3HT nanoparticles

Figure 3.18 (a) shows the diffraction patterns from NPs obtained from aged solutions. The curves were normalised to the region around 14 nm^{-1} and corrected for the background to the profile found in the 20-25 nm^{-1} region.

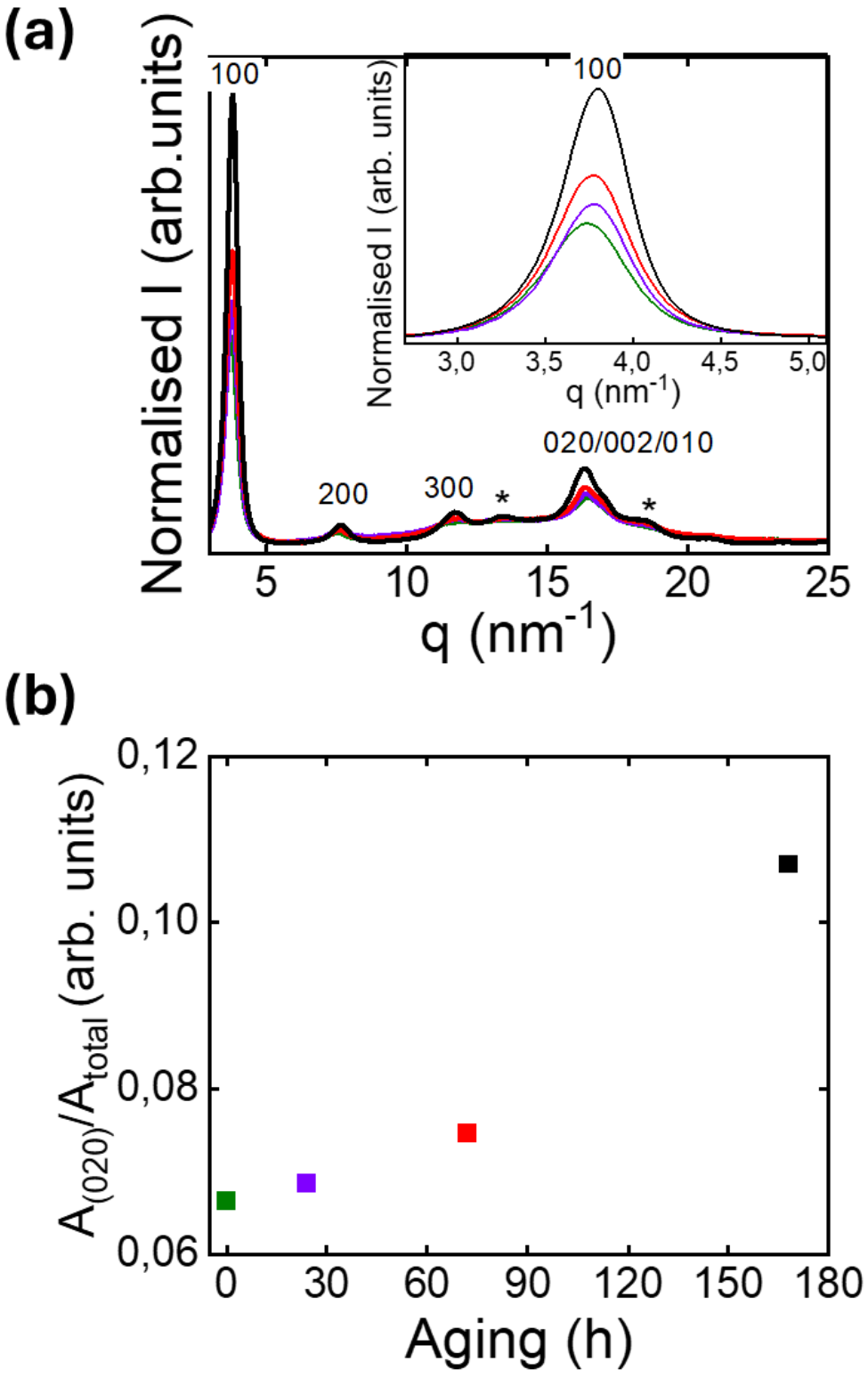

Figure 3.18. (a) Diffractograms of semicrystalline NPs of P3HT at different ages. Green corresponds to 0 h, violet to 24 h, red to 72 h and black to 168 h. The labels and asterisks indicate the crystalline reflections. Inset of maximum (100) within each diffractogram. **(b)** Relative integrated area corresponding to reflection (020) for NPs from aged solutions.

All the X-ray diffractograms in Figure 3.18 correspond to those of the monoclinic unit cell observed in bulk P3HT[12–15]. Labels in Figure 3.18 (a) indicate the indexes of the Bragg reflections from the form I crystalline phase of P3HT at 3.7 nm^{-1}, 7.6 nm^{-1}, 11.9 nm^{-1}, and 16.5 nm^{-1}, which correspond to the (100), (200), (300) reflections and (020)/(002)/(010), respectively. However, with increasing aging, two additional reflections located at approximately 13.3 nm^{-1} and 18.5 nm^{-1} become more prominent (Figure 3.18 (a)). These diffraction maxima do not correspond to typical bulk P3HT reflections. The maximum near 18.5 nm^{-1} is assigned to the side chain crystallites in low molecular weight P3HT[6,17], suggesting that enhancement in crystallisation may be attributable to the fact that the polymer chains are susceptible to fragmentation in solution, as observed by DLS, and subsequently find it easier to aggregate. It is hypothesised that shorter chains may exhibit greater mobility and consequently, a higher probability of aligning their side chains to optimise van der Waals interactions. Moreover, a reduction in the main chain length could result in a decrease in steric repulsions between the chains, thereby facilitating the packing of the side chains. In addition, Berson et al.[79] observed that aging and nanofiber formation are accompanied by a decrease in molecular weight and even a decrease in Q.

The results of this study demonstrate that the aging process has a significant effect on the arrangement of the chains in the NPs, especially in increasing the crystallinity (Figure 3.18 (a)). In order to verify this, the reflection (020)/(002)/(010) at a q = 16.3 nm^{-1} was selected, and the area was integrated for each aging time and divided by the total area obtained (Figure 3.18 (b)). This demonstrated that the area increases with aging by more than double the integrated area from 0 h to 168 h, and, consequently, the crystallinity of the NPs also increases. This result is consistent with the findings of Kleinhenz et al[82], who reported that the fraction of pre-aggregates in solution increases with aging, thereby promoting crystalline nucleation. This phenomenon could be attributed to the discussion in the previous section. The fact that nucleation is determined by thermodynamic control may promote the formation of crystalline aggregates; hence, the pre-aggregation of P3HT in solution can be considered a strategy to enhance the ordering of the polymer in the solid state, as in the case of NPs. This increase in crystallinity can be attributed to either an increase in the size of individual crystallites, the number of crystallites, or both. The coherence length calculated using the Scherrer equation (see Eq. 2.4 in Chapter 2) for the (100) and (020)/(002)/(010) diffraction maxima, shows significant trends (see Table 3.10). NPs prepared from aged solutions exhibit an increased (100) coherence length, which is evidence that aging promotes the growth of larger crystalline domains and enhances chain alignment along this main axis.

However, when examining only NPs prepared from aged solutions, the coherence length of (020)/(002)/(010) decreases with increasing aging, indicating that the crystals become smaller in the π–π stacking direction. This phenomenon may be attributed to the presence of chain fragments of varying lengths, which impede the optimal long-range π–π stacking.

Table 3.10. Coherence length values for (100) (lamellar stacking) and (020) (π-π stacking) reflections in P3HT NPs prepared from aged solutions. These values were obtained using the Scherrer equation (Eq. 2.3).

Aging (h)	$D_{(100)}$ (nm)	$D_{(020)}$ (nm)
0	7.3	4.0
24	8.8	5.4
72	8.9	4.7
168	8.9	4.4

3.3.4. Optical properties of aged P3HT nanoparticles: absorption and emission

Finally, the optical properties of P3HT NPs prepared from an aged solution are shown in Figure 3.19, revealing significant alterations in both absorption and emission spectra.

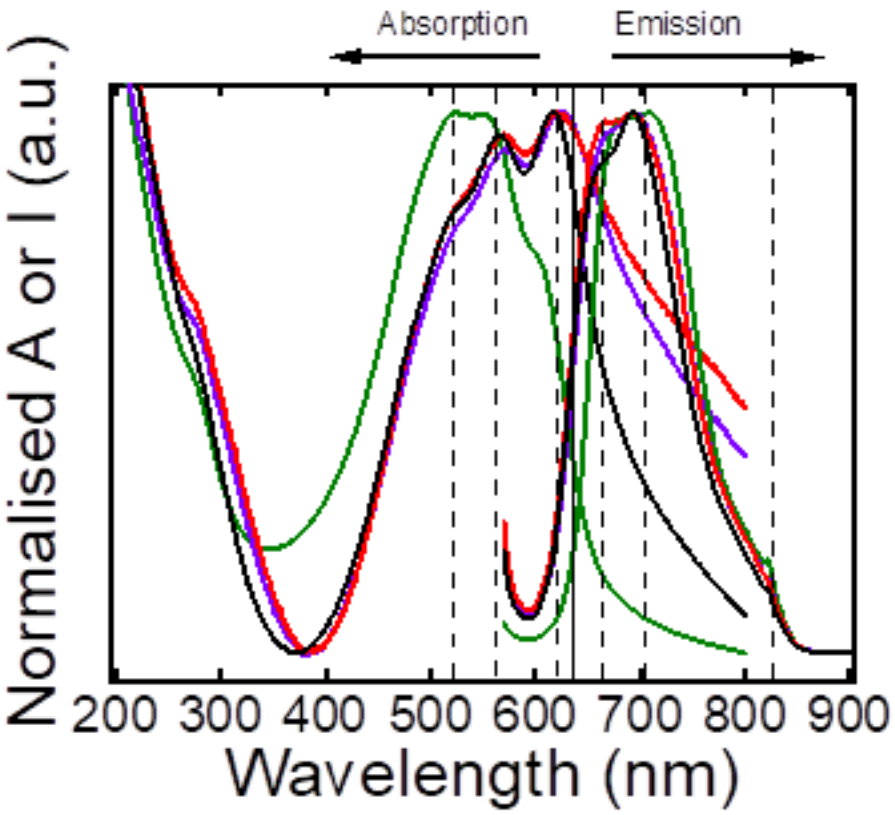

Figure 3.19. UV-Vis absorption spectra as a function of aging for P3HT NPs prepared by flash. Green corresponds to 0 h, violet to 24 h, red to 72 h and black to 168 h.

Both the UV-Vis absorption and emission present three clear maxima, which are associated with the π–π^* electronic transitions to different vibronic levels (0-0,0-1 and 0-2 transitions). In the case of the absorption spectrum, the NPs prepared from aged solutions exhibit a lower amorphous content (Figure 3.19) since, in the 400-500 nm region, associated with the intramolecular π–π^* transitions of torsionally disordered chain segments, presents a lower contribution[52,83]. This observation indicates an enhancement in the degree of chain aggregation or supramolecular organisation of the polymer concerning aged P3HT solutions. Additionally, an improved arrangement of the chains is manifested through the more pronounced maxima, which is facilitated by an increase in crystallinity, as evidenced by X-ray analysis. Furthermore, Figure 3.19 shows an increase in the 0-0 band (624 nm). Since the 0-0 band represents interchain transitions with no vibrational changes, its increase indicates greater interchain ordering and crystallinity in the aged NPs, favouring the formation of more stable excitons[72,84]. The accompanying redshift when the aging increases further supports this better ordering of the crystalline aggregates and an increase in the extension of conjugation[47].

Finally, the tail at high wavelengths is more intense, indicating that there are heterogeneous ordered aggregates or stronger intermolecular interactions that allow forbidden low-energy transitions[44,45].

The emission spectrum, also shown in Figure 3.19, displays significant changes that are consistent with those discussed in the absorption spectrum. In the emission region of lower wavelengths (600 nm), there is a greater contribution from NPs prepared from aged solutions, indicating a higher presence of aggregated states in which excitons are produced. Furthermore, the 0-1 band (670 nm) again gains intensity, indicating greater interchain ordering[47], while the 0-2 maximum (820 nm) loses intensity as the NPs age. This behaviour is indicative of a reduced participation of vibrational excited states, favouring the relaxation of excitation towards lower states. This is attributed to an increased rigidity of the system or a reduced contribution of amorphous domains, which favours more direct and less disordered transitions[38,43].

Table 3.11. Table displaying the intensity ratios between the 0-0 and 0-1 bands of the absorption and emission spectra for NPs prepared with aging solutions.

Aged (h)	Absorption	Emission
	A_{0-0}/A_{0-1}	I_{0-0}/I_{0-1}
0	0.728	1.002
24	1.071	0.965
72	1.041	0.986
168	1.042	0.906

The direct relationship between 0-0 and 0-1 reflections, as detailed in Table 3.11, also provides complementary information for the formation of ordered aggregates[51]. As discussed in section 3.1.3 on the properties of P3HT NPs, the value obtained for the absorption ratio for a P3HT 3g/L and *R*=1/6 (corresponding to 0 hours) sample is less than 1, and greater than 1 in emission, implying a coexistence of J and H aggregates with amorphous zones, being the intra-molecular interactions more characteristic. Conversely, in aggregated NPs, this ratio is greater than 1 in absorption and less than 1 in emission, indicating that the long-range intrachain exciton coupling is higher due to the greater presence of J-aggregates, which are more ordered structures with larger conjugation length[51,60]. These findings also imply that a conformational change occurs in the chains when transitioning from the aged solution (see

Table 3.7) (where there was a reduction in the ratio of absorption intensities) to the NPs (see Table 3.11) (where this ratio increases). One potential explanation for this phenomenon is that the polymer chains, which were initially free in solution, begin to pre-aggregate. This is consistent with the increase in the degree of stacking of H-type molecular packing[46]. The change from pre-aggregates to NPs forms disrupts the dominant forces of π-stacking, thereby favouring those that increase chain planarity and intra-chain order[59]. Additionally, both the redshift in absorption and blueshift in emission and the lower contribution at about 500 nm and the longer tail at higher wavelengths suggest that there is less presence of H-aggregates[51,83]. As the solution ages, these H-aggregates could dissociate or rearrange into more ordered structures, such as J-aggregates, indicating an increase in the ordering of the P3HT chains within the NPs.

Finally, the band gap is also reduced in the aged NPs, especially the one obtained by the Tauc plot (Section 2.4.4.1), as shown in Table 3.12. This further validates the presence of a higher crystalline order, while at 168 h, the band gap is slightly larger than at other aging times, possibly due to the packing may partially restrict electronic delocalisation, decreasing the quantum efficiency of the emission process[47].

Table 3.12. The band gap for all NPs was calculated from the intersection of the absorption and emission spectra, as well as from the Tauc plot.

Aged (h)	Abs-emis cross	Tauc plot
0	1.95eV (635 nm)	1.95 eV
24	1.90 eV (653 nm)	1.71 eV
72	1.90 eV (653 nm)	1.69 eV
168	1.92 eV (645 nm)	1.85 eV

The results obtained in this study are consistent with the findings reported in previous sections, which demonstrated that the process of aging facilitates the formation of ordered aggregates through enhanced organisation of P3HT chains. This process is known to promote J-type packing, resulting in an increased intensity of specific electronic transitions and an enhancement in intramolecular order, characterised by an extended conjugation length[46,59]. The correlation between the XRD data and the optical properties lends further support to this interpretation, suggesting that the enhancement in crystallinity is directly associated with the growth in both the number and size of P3HT aggregates.

3.4. Conclusions

In summary, this chapter has investigated the influence of different preparation conditions on the properties of P3HT NPs produced via flash nanoprecipitation. The study emphasises the importance of factors such as concentration, *R* and solution aging on NP size, morphology, crystallinity, and optical characteristics. The main findings are:

-Increasing the concentration above 3 g/L leads to the formation of NP aggregates due to the supersaturation of the solution. Notably, the 5 g/L NPs have a slightly higher crystallinity, probably due to their larger particle size, which has a lower ratio of surface defects. This conclusion is also corroborated to be extracted by the UV-Vis and emission spectra.

-Varying the antisolvent volume does not significantly affect the NP size, with the intermediate volume ratio ($R = 1/6$) having the smallest NP size and the highest crystalline content. However, the optical properties indicate that it is the 1/4 ratio that shows a greater planarization of the chains, which implies better intrachain charge transport.

-The aging of P3HT solutions further influences NP formation. Aging leads to the formation of ordered pre-aggregates in solution, predominantly in the form of H-aggregates. However, prolonged aging (beyond 7 days) induces gelation, which does not allow the preparation of NPs adequately. Regarding the NPs, the particle size tends to decrease slightly with increasing aging due to enhanced nucleation and crystallisation from pre-aggregated chains, while a higher presence of aggregates and size dispersion has also been observed. This phenomenon may be attributed to the gelation of the solution, which impedes the rapid displacement of the solvent by the non-solvent, resulting in less homogeneous sizes. Furthermore, aged solutions yield NPs with higher crystallinity. The hypothesis that pre-aggregates in solution could act as nucleation centres during nanoprecipitation is investigated in this study. The pre-ordering of these structures could facilitate the alignment of new precipitating P3HT chains, leading to faster growth of existing crystalline domains and the formation of NPs with higher overall crystallinity. In the context of absorption, there is a reduced contribution of amorphous content and an enhanced assembly of chains, a phenomenon that is further substantiated by the diminished band gap, once more attributable to the thermodynamically controlled formation of pre-aggregates.

Finally, some of the samples studied and discussed in this chapter will be applied in Chapter 6 to assess how their structural and optical properties, particularly crystallinity, size, and aggregation, affect the photodegradation of a model organic pollutant. It is hypothesised that NPs with higher crystallinity and a greater proportion of J-aggregates will facilitate more efficient charge separation and free radical formation, thus exhibiting superior photocatalytic activity. The findings of this study emphasise the critical role of NP preparation parameters in tuning the properties essential for environmental remediation applications.

3.5. Bibliography

(1) Kim, H.; So, W. W.; Moon, S. J. The Importance of Post-Annealing Process in the Device Performance of Poly(3-Hexylthiophene): Methanofullerene Polymer Solar Cell. *Solar Energy Materials and Solar Cells* **2007**, *91* (7), 581–587. https://doi.org/10.1016/j.solmat.2006.11.010.

(2) Sirringhaus, H. Device Physics of Solution-Processed Organic Field-Effect Transistors. *Advanced Materials* **2005**, *17* (20), 2411–2425. https://doi.org/10.1002/adma.200501152.

(3) Fichou, D. *Handbook of Oligo- and Polythiophenes*; Wiley-VCH: Verlag, 1998. https://doi.org/10.1002/9783527611713.

(4) Zhang, C.; Pansare, V. J.; Prud'Homme, R. K.; Priestley, R. D. Flash Nanoprecipitation of Polystyrene Nanoparticles. *Soft Matter* **2012**, *8* (1), 86–93. https://doi.org/10.1039/c1sm06182h.

(5) Holmes, N. P.; Marks, M.; Cave, J. M.; Feron, K.; Barr, M. G.; Fahy, A.; Sharma, A.; Pan, X.; Kilcoyne, D. A. L.; Zhou, X.; Lewis, D. A.; Andersson, M. R.; Van Stam, J.; Walker, A. B.; Moons, E.; Belcher, W. J.; Dastoor, P. C. Engineering Two-Phase and Three-Phase Microstructures from Water-Based Dispersions of Nanoparticles for Eco-Friendly Polymer Solar Cell Applications. *Chemistry of Materials* **2018**, *30* (18), 6521–6531. https://doi.org/10.1021/acs.chemmater.8b03222.

(6) Gutiérrez-Fernández, E.; Ezquerra, T. A.; Rebollar, E.; Cui, J.; Marina, S.; Martín, J.; Nogales, A. Photophysical and Structural Modulation of Poly(3-Hexylthiophene) Nanoparticles via Surfactant-Polymer Interaction. *Polymer* **2021**, *218*. https://doi.org/10.1016/j.polymer.2021.123515.

(7) Nikoubashman, A.; Lee, V. E.; Sosa, C.; Prud'homme, R. K.; Priestley, R. D.; Panagiotopoulos, A. Z. Directed Assembly of Soft Colloids through Rapid Solvent Exchange. *ACS Nano* **2016**, *10* (1), 1425–1433. https://doi.org/10.1021/acsnano.5b06890.

(8) Vitale, S. A.; Katz, J. L. Liquid Droplet Dispersions Formed by Homogeneous Liquid-Liquid Nucleation: "The Ouzo Effect." *Langmuir* **2003**, *19* (10), 4105–4110. https://doi.org/10.1021/la026842o.

(9) Rao, J. P.; Geckeler, K. E. Polymer Nanoparticles: Preparation Techniques and Size-Control Parameters. *Prog Polym Sci* **2011**, *36* (7), 887–913. https://doi.org/10.1016/j.progpolymsci.2011.01.001.

(10) Sharratt, W. N.; Lee, V. E.; Priestley, R. D.; Cabral, J. T. Precision Polymer Particles by Flash Nanoprecipitation and Microfluidic Droplet Extraction. *ACS Appl Polym Mater* **2021**, *3* (10), 4746–4768. https://doi.org/10.1021/acsapm.1c00546.

(11) Dirksen, J. A.; Ring, T. A. Fundamentals of Crystallization: Kinetic Effects on Particle Size Distributions and Morphology. *Chemical Enginering Science* **1991**, *46* (10), 2389–2427. https://doi.org/10.1016/0009-2509(91)80035-W.

(12) Müller-Buschbaum, P. The Active Layer Morphology of Organic Solar Cells Probed with Grazing Incidence Scattering Techniques. *Advanced Materials* **2014**, *26* (46), 7692–7709. https://doi.org/10.1002/adma.201304187.

(13) Agbolaghi, S.; Zenoozi, S. A Comprehensive Review on Poly(3-Alkylthiophene)-Based Crystalline Structures, Protocols and Electronic Applications. *Org Electron* **2017**, *51*, 362–403. https://doi.org/10.1016/j.orgel.2017.09.038.

(14) Yang, H.; Shin, T. J.; Yang, L.; Cho, K.; Ryu, C. Y.; Bao, Z. Effect of Mesoscale Crystalline Structure on the Field-Effect Mobility of Regioregular Poly(3-Hexyl Thiophene) in Thin-Film Transistors. *Adv Funct Mater* **2005**, *15* (4), 671–676. https://doi.org/10.1002/adfm.200400297.

(15) Millstone, J. E.; Kavulak, D. F. J.; Woo, C. H.; Holcombe, T. W.; Westling, E. J.; Briseno, A. L.; Toney, M. F.; Fréchet, J. M. J. Synthesis, Properties, and Electronic Applications of Size-Controlled Poly(3-Hexylthiophene) Nanoparticles. *Langmuir* **2010**, *26* (16), 13056–13061. https://doi.org/10.1021/la1022938.

(16) Gutiérrez-Fernández, E.; Cui, J.; Martínez-Tong, D. E.; Nogales, A. Preparation, Physical Properties, and Applications of Water-Based Functional Polymer Inks. *Polymers* **2021**, *13* (9). https://doi.org/10.3390/polym13091419.

(17) Wu, Z.; Petzold, A.; Henze, T.; Thurn-Albrecht, T.; Lohwasser, R. H.; Sommer, M.; Thelakkat, M. Temperature and Molecular Weight Dependent Hierarchical Equilibrium Structures in Semiconducting Poly(3-Hexylthiophene). *Macromolecules* **2010**, *43* (10), 4646–4653. https://doi.org/10.1021/ma902566h.

(18) Janasz, L.; Chlebosz, D.; Gradzka, M.; Zajaczkowski, W.; Marszalek, T.; Müllen, K.; Ulanski, J.; Kiersnowski, A.; Pisula, W. Improved Charge Carrier Transport in Ultrathin Poly(3-Hexylthiophene) Films via Solution Aggregation. *J Mater Chem C Mater* **2016**, *4* (48), 11488–11498. https://doi.org/10.1039/c6tc02142e.

(19) Brinkmann, M.; Wittmann, J. C. Orientation of Regioregular Poly(3-Hexylthiophene) by Directional Solidification: A Simple Method to Reveal the Semicrystalline Structure of a Conjugated Polymer. *Advanced Materials* **2006**, *18* (7), 860–863. https://doi.org/10.1002/adma.200501838.

(20) Ahmad, H.; Zhang, S.; Liu, C. T.; Ma, G.; Azoulay, J. D.; Gu, X.; Gangishetty, M. K.; Kundu, S. Effects of Poly(3-Hexylthiophene) Molecular Weight and the Aging of Spinning Solution on the Electrospun Fiber Properties. *ACS Appl Polym Mater* **2022**, *4* (12), 8812–8824. https://doi.org/10.1021/acsapm.2c01229.

(21) Chiu, M. Y.; Jeng, U. S.; Su, C. H.; Liang, K. S.; Wei, K. H. Simultaneous Use of Small- and Wide-Angle X-Ray Techniques to Analyze Nanometerscale Phase Separation in Polymer Heterojunction Solar Cells. *Advanced Materials* **2008**, *20* (13), 2573–2578. https://doi.org/10.1002/adma.200703097.

(22) Wang, H.; Keum, J. K.; Hiltner, A.; Baer, E.; Freeman, B.; Rozanski, A.; Galeski, A. Confined Crystallization of Polyethylene Oxide in Nanolayer Assemblies. *Science (1979)* **2009**, *323* (5915), 757–760. https://doi.org/10.1126/science.1165857.

(23) Saber, M.; Koch, C. C.; Scattergood, R. O. Thermodynamic Grain Size Stabilization Models: An Overview. *Mater Res Lett* **2015**, *3* (2), 65–75. https://doi.org/10.1080/21663831.2014.997894.

(24) Locci, A. M. Theoretical Assessment of Thermodynamic Stability in Nanocrystalline Metallic Alloys. *Materials* **2019**, *12* (20). https://doi.org/10.3390/ma12203408.

(25) Nagarjuna, G.; Baghgar, M.; Labastide, J. A.; Algaier, D. D.; Barnes, M. D.; Venkataraman, D. Tuning Aggregation of Poly(3-Hexylthiophene) within Nanoparticles. *ACS Nano* **2012**, *6* (12), 10750–10758. https://doi.org/10.1021/nn305207b.

(26) Chen, J. H.; Li, J. Y.; Chen, L. C.; Su, C. I. Morphology and Microstructure of Aggregates and Gelation Behaviour of Poly (3-Hexylthiophene) in Xylene Solution. In *Applied Mechanics and Materials*; 2014; Vol. 479–480, pp 115–120. https://doi.org/10.4028/www.scientific.net/AMM.479-480.115.

(27) Böckmann, M.; Schemme, T.; De Jong, D. H.; Denz, C.; Heuer, A.; Doltsinis, N. L. Structure of P3HT Crystals, Thin Films, and Solutions by UV/Vis Spectral Analysis. *Physical Chemistry Chemical Physics* **2015**, *17* (43), 28616–28625. https://doi.org/10.1039/c5cp03665h.

(28) Chambon, S.; Schatz, C.; Sébire, V.; Pavageau, B.; Wantz, G.; Hirsch, L. Organic Semiconductor Core-Shell Nanoparticles Designed through Successive Solvent Displacements. *Mater Horiz* **2014**, *1* (4), 431–438. https://doi.org/10.1039/c4mh00021h.

(29) Wang, H. S.; Lin, L. H.; Chen, S. Y.; Wang, Y. L.; Wei, K. H. Ordered Polythiophene/Fullerene Composite Core-Shell Nanorod Arrays for Solar Cell Applications. *Nanotechnology* **2009**, *20* (7). https://doi.org/10.1088/0957-4484/20/7/075201.

(30) Holmes, N. P.; Nicolaidis, N.; Feron, K.; Barr, M.; Burke, K. B.; Al-Mudhaffer, M.; Sista, P.; Kilcoyne, A. L. D.; Stefan, M. C.; Zhou, X.; Dastoor, P. C.; Belcher, W. J. Probing the Origin of Photocurrent in Nanoparticulate Organic Photovoltaics. *Solar Energy Materials and Solar Cells* **2015**, *140*, 412–421. https://doi.org/10.1016/j.solmat.2015.04.044.

(31) Ferreira, B.; Da Silva, P. F.; Seixas De Melo, J. S.; Pina, J.; MaçAnita, A. Excited-State Dynamics and Self-Organization of Poly(3-Hexylthiophene) (P3HT) in Solution and Thin Films. *J Phys Chem B* **2012**, *116* (8), 2347–2355. https://doi.org/10.1021/jp207418q.

(32) Wells, N. P.; Boudouris, B. W.; Hillmyer, M. A.; Blank, D. A. Intramolecular Exciton Relaxation and Migration Dynamics in Poly(3-Hexylthiophene). *J Phys Chem C* **2007**, *111* (42), 15404–15414. https://doi.org/10.1021/jp074657j.

(33) Yamamoto, T.; Komarudin, D.; Arai, M.; Lee, B.-L.; Suganuma, H.; Asakawa, N.; Inoue, Y.; Kubota, K.; Sasaki, S.; Fukuda, T.; Matsuda, H. Extensive Studies on π-Stacking of Poly(3-Alkylthiophene-2,5-Diyl)s and Poly(4-Alkylthiazole-2,5-Diyl)s by Optical Spectroscopy, NMR Analysis, Light Scattering Analysis, and X-Ray Crystallography. *J Am Chem Soc* **1998**, *120* (9), 2047–2058. https://doi.org/10.1021/ja973873a.

(34) Dimitriev, O. P. Effect of Confinement on Photophysical Properties of P3HT Chains in PMMA Matrix. *Nanoscale Res Lett* **2017**, *12*. https://doi.org/10.1186/s11671-017-2270-y.

(35) Tapping, P. C.; Kee, T. W. Optical Pumping of Poly(3-Hexylthiophene) Singlet Excitons Induces Charge Carrier Generation. *J Phys Chem Lett* **2014**, *5* (6), 1040–1047. https://doi.org/10.1021/jz500217f.

(36) Weaver, M. J.; McManis, G. E.; Jarzeba, W.; Barbara, P. F. Importance of Fast Solvent Relaxation Components to Electron-Transfer Rates: Comparisons between Barrier-Crossing Frequencies and Subpicosecond Time-Resolved Solvation Dynamics. *J Phys Chem* **1990**, *94* (5), 1715–1719. https://doi.org/10.1021/j100368a001.

(37) Spano, F. C. The Spectral Signatures of Frenkel Polarons in H- And J-Aggregates. *Acc Chem Res* **2010**, *43* (3), 429–439. https://doi.org/10.1021/ar900233v.

(38) Ulum, S.; Holmes, N.; Darwis, D.; Burke, K.; David Kilcoyne, A. L.; Zhou, X.; Belcher, W.; Dastoor, P. Determining the Structural Motif of P3HT:PCBM Nanoparticulate Organic Photovoltaic Devices. *Solar Energy Materials and Solar Cells* **2013**, *110*, 43–48. https://doi.org/10.1016/j.solmat.2012.11.015.

(39) Schwarz, K. N.; Farley, S. B.; Smith, T. A.; Ghiggino, K. P. Charge Generation and Morphology in P3HT : PCBM Nanoparticles Prepared by Mini-Emulsion and Reprecipitation Methods. *Nanoscale* **2015**, *7* (47), 19899–19904. https://doi.org/10.1039/c5nr06244f.

(40) Hiorns, R. C.; De Bettignies, R.; Leroy, J.; Bailly, S.; Firon, M.; Sentein, C.; Khoukh, A.; Preud'homme, H.; Dagron-Lartigau, C. High Molecular Weights, Polydispersities, and Annealing Temperatures in the Optimization of Bulk-Heterojunction Photovoltaic Cells Based on Poly(3-Hexylthiophene) or Poly(3-Butylthiophene). *Adv Funct Mater* **2006**, *16* (17), 2263–2273. https://doi.org/10.1002/adfm.200600005.

(41) Jo, G.; Jung, J.; Chang, M. Controlled Self-Assembly of Conjugated Polymers via a Solvent Vapor Pre-Treatment for Use in Organic Field-Effect Transistors. *Polymers* **2019**, *11* (2). https://doi.org/10.3390/polym11020332.

(42) Andrienko, D.; Brinkmann, M.; Daoulas, K.; Djurado, D.; Hartmann, L.; Kayunkid, N.; Ludwigs, S.; Luscombe, C. K.; Moulé, A. J.; Neher, D.; Poelking, C.; Sista, P.; Tremel, K.; Troisi, A.; Turner, S. T.; Zaumseil, J. *P3HT Revisited-from Molecular Scale to Solar Cell Devices*, 1st ed.; Ludwigs, S., Ed.; Springer: Berlin, 2014; Vol. 265. https://doi.org/10.1007/978-3-662-45145-8.

(43) Lee, S. H.; Lee, Y. B.; Park, D. H.; Kim, M. S.; Cho, E. H.; Joo, J. Tuning Optical Properties of Poly(3-Hexylthiophene) Nanoparticles through Hydrothermal Processing. *Sci Technol Adv Mater* **2011**, *12* (2). https://doi.org/10.1088/1468-6996/12/2/025002.

(44) Cook, S.; Furube, A.; Katoh, R. Analysis of the Excited States of Regioregular Polythiophene P3HT. *Energy Environ Sci* **2008**, *1* (2), 294–299. https://doi.org/10.1039/b805643a.

(45) Chu, Z.; Guo, H.; Yu, W.; Sun, Z.; Chen, W. Low Temperature Aging Induced Conjugated Polymers Aggregation by UV–Vis Spectroscopy. *Journal of Polymer Science* **2024**. https://doi.org/10.1002/pol.20240148.

(46) Rahimi, K.; Botiz, I.; Agumba, J. O.; Motamen, S.; Stingelin, N.; Reiter, G. Light Absorption of Poly(3-Hexylthiophene) Single Crystals. *RSC Adv* **2014**, *4* (22), 11121–11123. https://doi.org/10.1039/c3ra47064d.

(47) Brown, P. J.; Thomas, D. S.; Köhler, A.; Wilson, J. S.; Kim, J. S.; Ramsdale, C. M.; Sirringhaus, H.; Friend, R. H. Effect of Interchain Interactions on the Absorption and Emission of Poly(3-Hexylthiophene). *Phys Rev B* **2003**, *67* (6). https://doi.org/10.1103/PhysRevB.67.064203.

(48) Hu, Z.; Gesquiere, A. J. PCBM Concentration Dependent Morphology of P3HT in Composite P3HT/PCBM Nanoparticles. *Chem Phys Lett* **2009**, *476* (1–3), 51–55. https://doi.org/10.1016/j.cplett.2009.05.066.

(49) Holmes, N. P.; Ulum, S.; Sista, P.; Burke, K. B.; Wilson, M. G.; Stefan, M. C.; Zhou, X.; Dastoor, P. C.; Belcher, W. J. The Effect of Polymer Molecular Weight on P3HT:PCBM Nanoparticulate Organic Photovoltaic Device Performance. *Solar Energy Materials and Solar Cells* **2014**, *128*, 369–377. https://doi.org/10.1016/j.solmat.2014.05.046.

(50) Ruseckas, A.; Namdas, E. B.; Ganguly, T.; Theander, M.; Svensson, M.; Andersson, M. R.; Inganäs, O.; Sundström, V. Intra- and Interchain Luminescence in Amorphous and Semicrystalline Films of Phenyl-Substituted Polythiophene. *J Phys Chem B* **2001**, *105* (32), 7624–7631. https://doi.org/10.1021/jp010511n.

(51) Yamagata, H.; Spano, F. C. Interplay between Intrachain and Interchain Interactions in Semiconducting Polymer Assemblies: The HJ-Aggregate Model. *J Chem Phys* **2012**, *136* (18). https://doi.org/10.1063/1.4705272.

(52) Spano, F. C.; Silva, C. H- and J-Aggregate Behavior in Polymeric Semiconductors. *Annu Rev Phys Chem* **2014**, *65*, 477–500. https://doi.org/10.1146/annurev-physchem-040513-103639.

(53) Manas, E. S.; Spano, F. C. Absorption and Spontaneous Emission in Aggregates of Conjugated Polymers. *J Chem Phys* **1998**, *109* (18), 8087–8101. https://doi.org/10.1063/1.477457.

(54) Clark, J.; Silva, C.; Friend, R. H.; Spano, F. C. Role of Intermolecular Coupling in the Photophysics of Disordered Organic Semiconductors: Aggregate Emission in Regioregular Polythiophene. *Phys Rev Lett* **2007**, *98* (20). https://doi.org/10.1103/PhysRevLett.98.206406.

(55) Österbacka, R.; An, C. P.; Jiang, X. M.; Vardeny, Z. V. Two-Dimensional Electronic Excitations in Self-Assembled Conjugated Polymer Nanocrystals. *Science (1979)* **2000**, *287* (5454), 839–842. https://doi.org/10.1126/science.287.5454.839.

(56) Barbarella, G.; Melucci, M.; Sotgiu, G. The Versatile Thiophene: An Overview of Recent Research on Thiophene-Based Materials. *Advanced Materials* **2005**, *17* (13), 1581–1593. https://doi.org/10.1002/adma.200402020.

(57) Scharsich, C.; Lohwasser, R. H.; Sommer, M.; Asawapirom, U.; Scherf, U.; Thelakkat, M.; Neher, D.; Köhler, A. Control of Aggregate Formation in Poly(3-Hexylthiophene) by Solvent, Molecular Weight, and Synthetic Method. *J Polym Sci B Polym Phys* **2012**, *50* (6), 442–453. https://doi.org/10.1002/polb.23022.

(58) Li, G.; Shrotriya, V.; Huang, J.; Yao, Y.; Moriarty, T.; Emery, K.; Yang, Y. High-Efficiency Solution Processable Polymer Photovoltaic Cells by Self-Organization of Polymer Blends. *Nat Mater* **2005**, *4* (11), 864–868. https://doi.org/10.1038/nmat1500.

(59) Clark, J.; Chang, J. F.; Spano, F. C.; Friend, R. H.; Silva, C. Determining Exciton Bandwidth and Film Microstructure in Polythiophene Films Using Linear Absorption Spectroscopy. *Appl Phys Lett* **2009**, *94* (16). https://doi.org/10.1063/1.3110904.

(60) Persson, N. E.; Chu, P. H.; McBride, M.; Grover, M.; Reichmanis, E. Nucleation, Growth, and Alignment of Poly(3-Hexylthiophene) Nanofibers for High-Performance OFETs. *Acc Chem Res* **2017**, *50* (4), 932–942. https://doi.org/10.1021/acs.accounts.6b00639.

(61) Beaujuge, P. M.; Fréchet, J. M. J. Molecular Design and Ordering Effects in π-Functional Materials for Transistor and Solar Cell Applications. *J Am Chem Soc* **2011**, *133* (50), 20009–20029. https://doi.org/10.1021/ja2073643.

(62) Liu, X.; Sun, Y.; Hsu, B. B. Y.; Lorbach, A.; Qi, L.; Heeger, A. J.; Bazan, G. C. Design and Properties of Intermediate-Sized Narrow Band-Gap Conjugated Molecules Relevant to Solution-Processed Organic Solar Cells. *J Am Chem Soc* **2014**, *136* (15), 5697–5708. https://doi.org/10.1021/ja413144u.

(63) Zhu, H.; Gong, L.; Li, Z. Construction and Mechanism of a Novel Z-Scheme Photocatalyst α-Fe2O3/P3HT with O-Ti-O for Organic Pollutant Degradation under Visible Light. *Appl Surf Sci* **2020**, *505*. https://doi.org/10.1016/j.apsusc.2019.144639.

(64) Makuła, P.; Pacia, M.; Macyk, W. How To Correctly Determine the Band Gap Energy of Modified Semiconductor Photocatalysts Based on UV-Vis Spectra. *J Phys Chem Lett* **2018**, *9* (23), 6814–6817. https://doi.org/10.1021/acs.jpclett.8b02892.

(65) Tauc, J.; Grigorovici, R.; Vancu, A. Optical Properties and Electronic Structure of Amorphous Germanium. *Physica Status Solidi* **1966**, *15* (2), 627. https://doi.org/10.1002/pssb.19660150224.

(66) Floresyona, D.; Goubard, F.; Aubert, P. H.; Lampre, I.; Mathurin, J.; Dazzi, A.; Ghosh, S.; Beaunier, P.; Brisset, F.; Remita, S.; Ramos, L.; Remita, H. Highly Active Poly(3-Hexylthiophene) Nanostructures for Photocatalysis under Solar Light. *Appl Catal B* **2017**, *209*, 23–32. https://doi.org/10.1016/j.apcatb.2017.02.069.

(67) Liu, Y.; Yang, G.; Zou, D.; Hui, Y.; Nigam, K.; Middelberg, A. P. J.; Zhao, C. X. Formulation of Nanoparticles Using Mixing-Induced Nanoprecipitation for Drug Delivery. *Ind Eng Chem Res* **2020**, *59* (9), 4134–4149. https://doi.org/10.1021/acs.iecr.9b04747.

(68) Skrypnychuk, V.; Wetzelaer, G. J. A. H.; Gordiichuk, P. I.; Mannsfeld, S. C. B.; Herrmann, A.; Toney, M. F.; Barbero, D. R. Ultrahigh Mobility in an Organic Semiconductor by Vertical Chain Alignment. *Advanced Materials* **2016**, *28* (12), 2359–2366. https://doi.org/10.1002/adma.201503422.

(69) Kim, J. S.; Lee, J. H.; Park, J. H.; Shim, C.; Sim, M.; Cho, K. High-Efficiency Organic Solar Cells Based on Preformed Poly(3- Hexylthiophene) Nanowires. *Adv Funct Mater* **2011**, *21* (3), 480–486. https://doi.org/10.1002/adfm.201000971.

(70) Chang, M.; Choi, D.; Fu, B.; Reichmanis, E. Solvent Based Hydrogen Bonding: Impact on Poly(3-Hexylthiophene) Nanoscale Morphology and Charge Transport Characteristics. *ACS Nano* **2013**, *7* (6), 5402–5413. https://doi.org/10.1021/nn401323f.

(71) Qiu, L.; Wang, X.; Lee, W. H.; Lim, J. A.; Kim, J. S.; Kwak, D.; Cho, K. Organic Thin-Film Transistors Based on Blends of Poly(3-Hexylthiophene) and Polystyrene with a Solubility-Induced Low Percolation Threshold. *Chemistry of Materials* **2009**, *21* (19), 4380–4386. https://doi.org/10.1021/cm900628j.

(72) Hibner-Kulicka, P.; Waliszewski, W.; Borkowski, M.; Luszczynska, B.; Szymanski, M.; Marszalek, T.; Ulanski, J. Influence of P3HT Preaggregation Process on Performance of the P3HT:C60-PCBM Solar Cells. *Molecular Crystals and Liquid Crystals* **2019**, *693* (1), 82–96. https://doi.org/10.1080/15421406.2020.1723914.

(73) Kleinhenz, N.; Persson, N.; Xue, Z.; Chu, P. H.; Wang, G.; Yuan, Z.; McBride, M. A.; Choi, D.; Grover, M. A.; Reichmanis, E. Ordering of Poly(3-Hexylthiophene) in Solutions and Films: Effects of Fiber Length and Grain Boundaries on Anisotropy and Mobility. *Chemistry of Materials* **2016**, *28* (11), 3905–3913. https://doi.org/10.1021/acs.chemmater.6b01163.

(74) Aiyar, A. R.; Hong, J. Il; Izumi, J.; Choi, D.; Kleinhenz, N.; Reichmanis, E. Ultrasound-Induced Ordering in Poly(3-Hexylthiophene): Role of Molecular and Process Parameters on Morphology and Charge Transport. *ACS Appl Mater Interfaces* **2013**, *5* (7), 2368–2377. https://doi.org/10.1021/am3027822.

(75) Hu, H.; Zhao, K.; Fernandes, N.; Boufflet, P.; Bannock, J. H.; Yu, L.; De Mello, J. C.; Stingelin, N.; Heeney, M.; Giannelis, E. P.; Amassian, A. Entanglements in Marginal Solutions: A Means of Tuning Pre-Aggregation of Conjugated Polymers with Positive Implications for Charge Transport. *J Mater Chem C Mater* **2015**, *3* (28), 7394–7404. https://doi.org/10.1039/c5tc01425e.

(76) Bielecka, U.; Lutsyk, P.; Janus, K.; Sworakowski, J.; Bartkowiak, W. Effect of Solution Aging on Morphology and Electrical Characteristics of Regioregular P3HT FETs Fabricated by Spin Coating and Spray Coating. *Org Electron* **2011**, *12* (11), 1768–1776. https://doi.org/10.1016/j.orgel.2011.06.027.

(77) Wolf, C. M.; Guio, L.; Scheiwiller, S. C.; O'Hara, R. P.; Luscombe, C. K.; Pozzo, L. D. Blend Morphology in Polythiophene-Polystyrene Composites from Neutron and X-Ray Scattering. *Macromolecules* **2021**, *54* (6), 2960–2978. https://doi.org/10.1021/acs.macromol.0c02512.

(78) Zhao, K.; Ding, Z.; Xue, L.; Han, Y. Crystallization-Induced Phase Segregation Based on Double-Crystalline Blends of Poly(3-Hexylthiophene) and Polyethylene Glycolsa. *Macromol Rapid Commun* **2010**, *31* (6), 532–538. https://doi.org/10.1002/marc.200900770.

(79) Berson, S.; De Bettignies, R.; Bailly, S.; Guillerez, S. Poly(3-Hexylthiophene) Fibers for Photovoltaic Applications. *Adv Funct Mater* **2007**, *17* (8), 1377–1384. https://doi.org/10.1002/adfm.200600922.

(80) Gruendling, T.; Pickford, R.; Guilhaus, M.; Barner-Kowollik, C. Degradation of RAFT Polymers in a Cyclic Ether Studied via High Resolution ESI-MS: Implications for Synthesis, Storage, and End-Group Modification. *J Polym Sci A Polym Chem* **2008**, *46* (22), 7447–7461. https://doi.org/10.1002/pola.23050.

(81) Rabek, J. F.; Shurh, Y. J.; Ranby, B. Studies of the Photooxidation Mechanism of Polymers. III. Role of Tetrahydrofuran in the Photooxidative Degradation of Poly(Vinyl Chloride). *J Polym Sci: Polym Chem* **1975**, *13* (6), 1285–1295. https://doi.org/10.1002/pol.1975.170130602.

(82) Kleinhenz, N.; Rosu, C.; Chatterjee, S.; Chang, M.; Nayani, K.; Xue, Z.; Kim, E.; Middlebrooks, J.; Russo, P. S.; Park, J. O.; Srinivasarao, M.; Reichmanis, E. Liquid Crystalline Poly(3-Hexylthiophene) Solutions Revisited: Role of Time-Dependent Self-Assembly. *Chemistry of Materials* **2015**, *27* (7), 2687–2694. https://doi.org/10.1021/acs.chemmater.5b00635.

(83) Bhattacharjee, U.; Elshobaki, M.; Santra, K.; Bobbitt, J. M.; Chaudhary, S.; Smith, E. A.; Petrich, J. W. Characterizing Electric Field Exposed P3HT Thin Films Using Polarized-Light Spectroscopies. *Macromol Chem Phys* **2016**, *217* (16), 1801–1809. https://doi.org/10.1002/macp.201600113.

(84) Chang, M.; Lee, J.; Kleinhenz, N.; Fu, B.; Reichmanis, E. Photoinduced Anisotropic Supramolecular Assembly and Enhanced Charge Transport of Poly(3-Hexylthiophene) Thin Films. *Adv Funct Mater* **2014**, *24* (28), 4457–4465. https://doi.org/10.1002/adfm.201400523.

Chapter 4

Physical properties of P3HT nanoparticles prepared by Miniemulsion

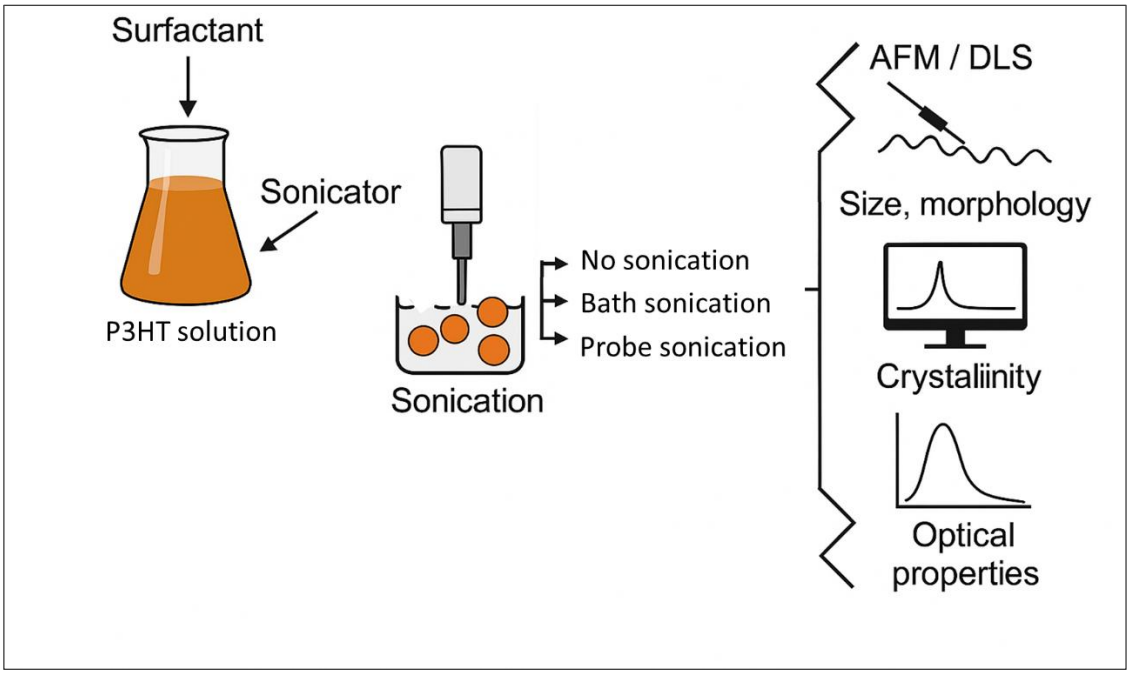

Graphical abstract representing the main idea of Chapter 4

Universidad Complutense de Madrid

Jose Sena Fernández

Micro and Nanoparticles of Functional Polymers: From Fundamentals to Applications

Miniemulsion is a versatile technique widely employed for the preparation of polymer NPs, where the use of surfactants and sonication is essential to stabilise the droplets and prevent coalescence during the process[1-5]. In this method, sonication not only dictates the droplet size distribution but also strongly influences the resulting NP characteristics, including morphology, crystallinity, and optical properties[6-10]. Sonication conditions, such as time and intensity can significantly impact the size uniformity and stability of polymer NPs, which in turn govern their performance in applications ranging from optoelectronics to photocatalysis[11]. In the case of P3HT, whose nanoscale structuring critically determines its photophysical and electronic behaviour, the miniemulsion method is particularly attractive for preparing aqueous dispersions due to its scalability and ability to fine-tune particle characteristics. In this case, sonication is a crucial step: insufficient energy may lead to unstable dispersions, whereas excessive input may disrupt polymer chains or promote undesired aggregation, altering structural and optical properties. Nevertheless, systematic investigations into the effect of sonication intensity, particularly comparing ultrasonic baths and probe sonication at varying amplitudes, remain scarce. Addressing this gap is essential for optimising NP performance in functional applications such as photocatalysis.

This chapter addresses this by systematically investigating the effect of varying sonication intensity on P3HT NPs prepared via miniemulsion. SDS was used as a surfactant, and different sonication strategies were employed: an ultrasonic bath (15 min) and a sonication probe at amplitudes of 10 %, 25 %, and 35 %, with a constant sonication time of 1 min. The results are also compared with particles prepared without sonication, allowing to elucidate the role of this step-in NP formation. As schematised in Figure 4.1, the study systematically examines the influence of sonication conditions on NP size and morphology (AFM, DLS), crystallinity (XRD), and optical properties (UV–Vis and fluorescence spectroscopy). The insights obtained provide valuable guidelines for tailoring P3HT NPs and identifying the most suitable processing conditions for applications such as photocatalysis.

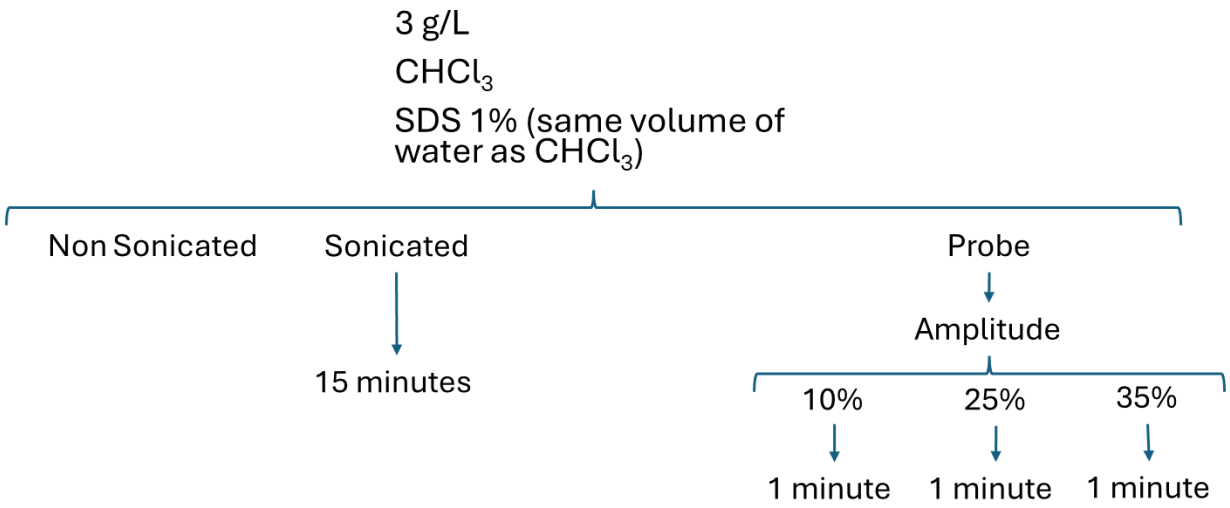

Figure 4.1. Schematic representation of the preparation conditions for all P3HT nanoparticle dispersions produced by miniemulsion. The figure highlights the various sonication methods employed, including non-sonicated samples, those sonicated in a water bath, and probe-sonicated samples at different amplitudes (10%, 25% and 35%).

4.1. Effect of sonication on the size, morphology and aggregation of the nanoparticles

The AFM topographic images of the different samples deposited onto silicon wafers are shown in Figure 4.2. The size distribution histograms for each condition were derived from the NP diameters (Figure 4.2), and the histograms obtained for samples non-sonicated and bath sonicated through DLS are also plotted (Figure 4.3). In addition, the polydispersity (Q) and the average size by number of the hydrodynamic diameter (D_h) for better normalisation were obtained, following the formula in Section 2.4.3.

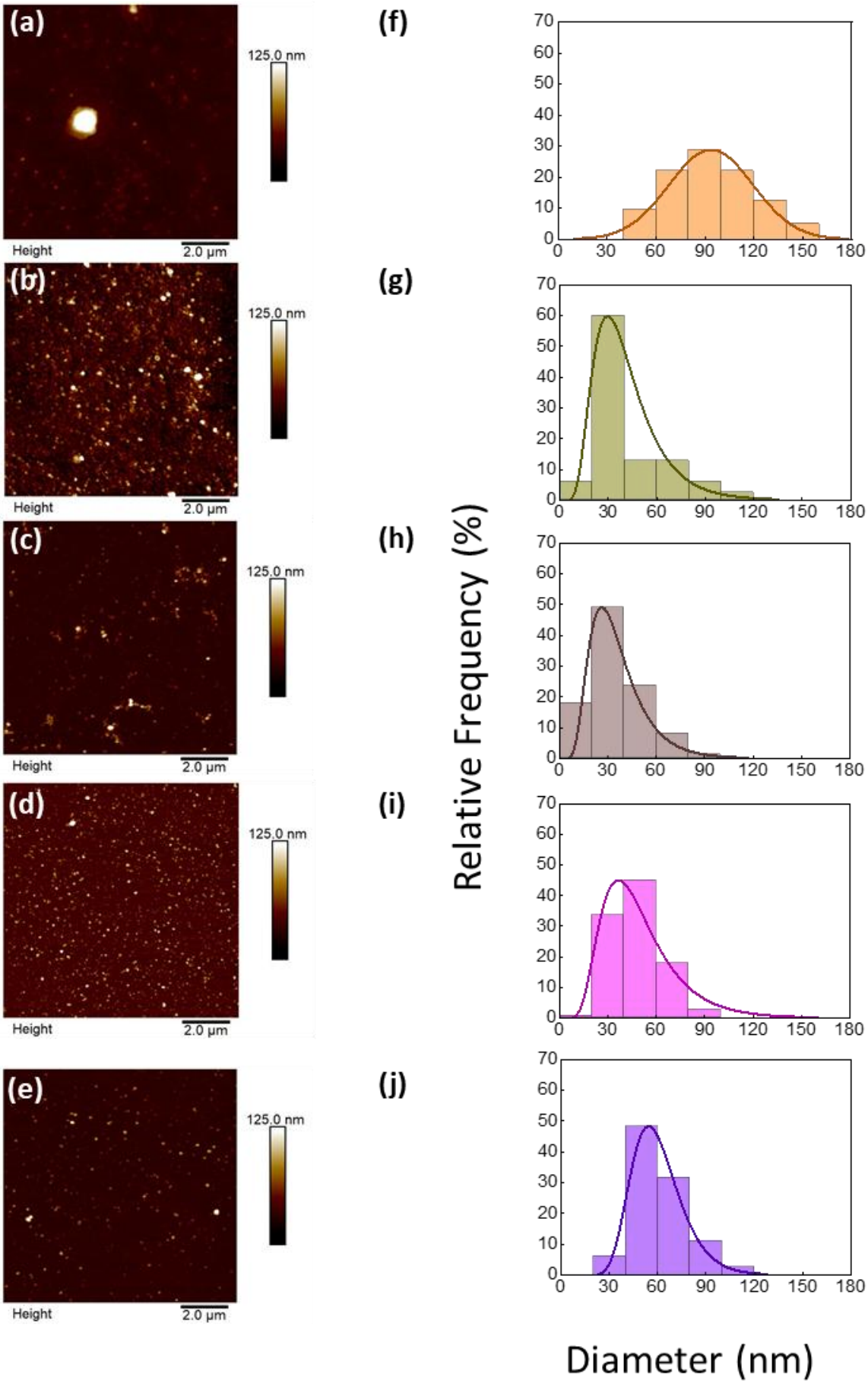
(a)
125.0 nm
Height
2.0 µm
(b)
125.0 nm
Height
2.0 µm
(c)
125.0 nm
Height
2.0 µm
(d)
125.0 nm
Height
2.0 µm
(e)
125.0 nm
Height
2.0 µm
(f)
(g)
(h)
(i)
(j)
Relative Frequency (%)
0 10 20 30 40 50 60 70
0 30 60 90 120 150 180
Diameter (nm)

Figure 4.2. AFM images of P3HT NPs prepared by the miniemulsion protocol **(a)** without sonication, **(b)** with bath sonication, **(c)** with probe sonication at 10% amplitude, **(d)** 25% amplitude and **(e)** 35% amplitude. The corresponding diameter distributions with the distribution curve type (**(f) to (j)**) are shown on the right.

As revealed in Figure 4.2, the shape of the NPs in all samples is nearly spherical. In the absence of sonication, larger particle size (Figure 4.2 (a)) and aggregates are observed. This fact contrasts with the sonicated samples in both the water bath and the probe. Therefore, it can be concluded that sonication generates a greater number of growth nuclei and a greater disentanglement of the polymer chains[12–14], resulting in a smaller size for the NPs. The size of the NPs prepared with sonication is similar, exhibiting little dependence on the sonication conditions. Also, NPs prepared with sonication show minimal aggregation (Figure 4.2 (b) to (e)). The reduced aggregation in sonicated NPs suggests the enhanced dispersion efficiency achieved through this method, resulting in a more uniform NP distribution. The size distribution obtained by AFM in Figure 4.2 (f) is notably more Gaussian-type, with more repeated diameters of 90 nm. In sonicated samples, the size distributions obtained from AFM are more homogeneous and have a lognormal type (see Figures 4.2 (g) to 4.2 (j)). A comparison of the sonicated samples reveals a shift in diameter distribution towards larger sizes in the samples sonicated by probe in comparison to those sonicated by ultrasonic bath. Indeed, in NPs sonicated by the probe, an increase in amplitude results in a shift of the diameter distribution towards larger diameters. Consequently, the most frequently observed sizes in water bath sonication and at a sonication amplitude of 10% are 30 nm. However, when the amplitude is increased to 25% and 35%, the most frequently observed size is 50 nm in both cases.

The effect of sonication in producing smaller and more monodisperse particles is clearly observed in Figure 4.3, where the size distribution obtained by DLS is compared for NPs prepared without sonication and those prepared by sonication in the bath. Here, hydrodynamic diameters (D_h) obtained from the intensity distribution are reported to highlight the effect of sonication. The D_h, corresponding to the maximum of the distribution, is significantly reduced from 195 nm for the non-sonicated sample to 109 nm for the sonicated one due to the presence of aggregates observed by AFM. Furthermore, the monodispersity is drastically improved, as evidenced by the full width at half maximum (FWHM) of the distributions, which decreases from 342.9 nm to just 13.9 nm after sonication.

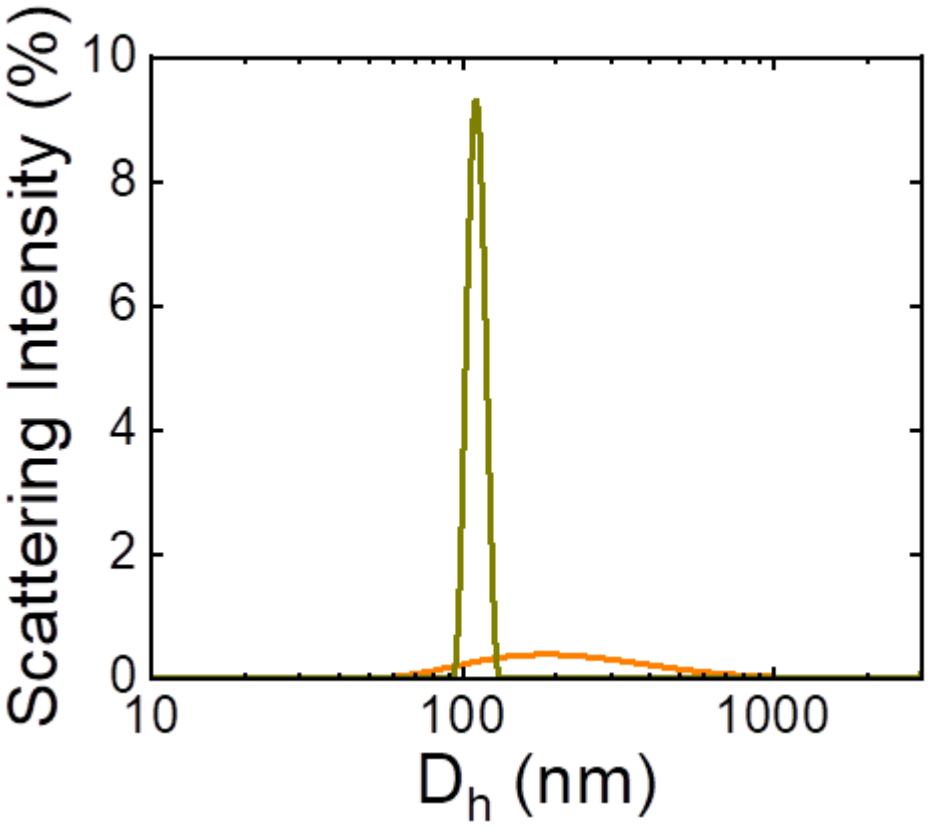

Figure 4.3. Size distributions obtained by DLS of P3HT NPs prepared by miniemulsion with different sonication conditions. The orange colour corresponds to non-sonicated, and dark yellow corresponds to sonicated in the bath.

The finding that sonication reduces NP size and improves monodispersity is further reinforced by a comparison of number-average diameters obtained from both AFM and DLS (see Section 2.4.3.) measurements (Figure 4.4), which show a close similarity. As can be seen, both techniques (with the exception of the bath-sonicated sample due to its monodispersity and no presence of aggregates) tend to yield a smaller NP size until a minimum of approximately 40 nm is reached at a 10% sonication amplitude, after which the size increases slightly.

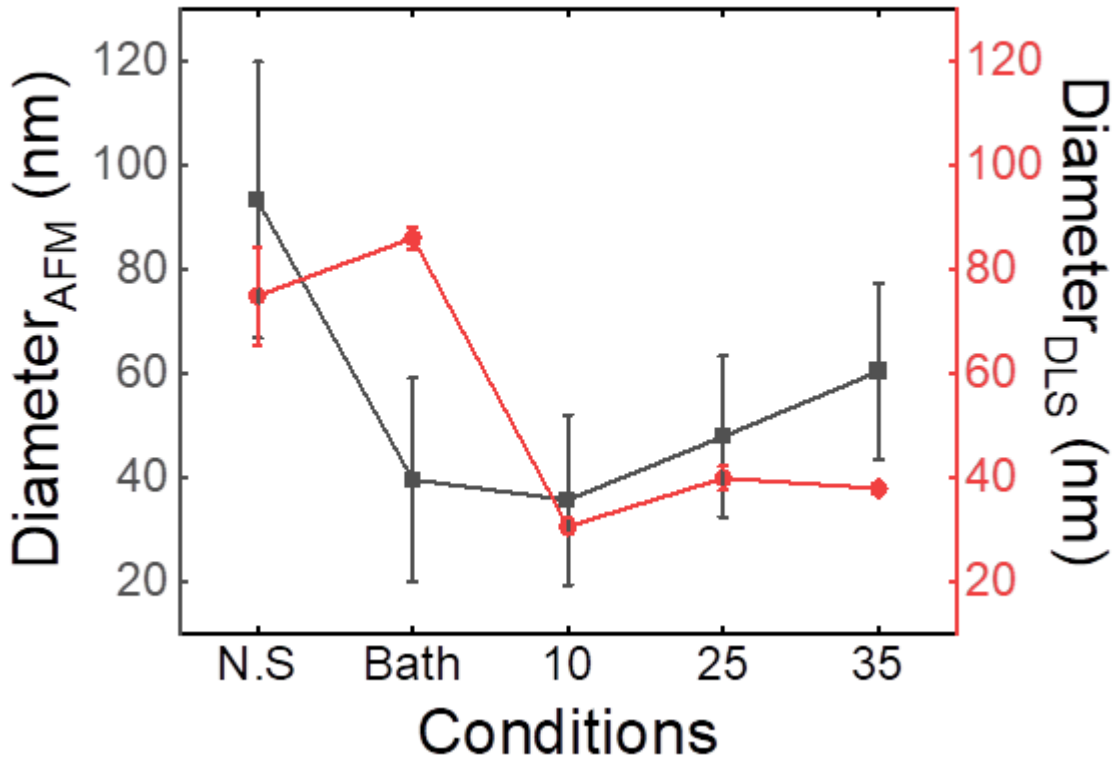

Figure 4.4. Variation in particle size diameter obtained by AFM (dark grey) and DLS (D_n) (red) for samples prepared by miniemulsion. The sample that is not sonicated is referenced as N.S., the sample that is sonicated in the ultrasonic bath is referenced as Bath, and the samples that are sonicated by the probe are referenced as a function of amplitude percentage.

Kleinhenz et al.[15] observed that thin films prepared from aged solutions resulted in the formation of fibres that were shorter when sonicated. Also, in the literature, it has been reported that a short sonication time favours more crystalline structures, whereas long times may limit growth, leading to an increase in the number of grain boundaries[16]. This effect may also occur with increasing sonication intensity. Pao et al.[17] found that high-intensity sonication can produce smaller particles, but in turn, damage the polymer and generate excessive heat in the solution, which should be avoided. In this thesis, to verify that the intensity of the sonication did not break the polymer chains, changes in the molecular weight were estimated by analysing the size of the chains in sonicated and non-sonicated solutions by DLS. The cumulant analysis did not give smaller coiled chain sizes in the sonicated one (14 nm in the non-sonicated versus 17 nm in the sonicated by probe at 35% amplitude).

4.2. Crystalline structure of the P3HT nanoparticles prepared by miniemulsion

Figure 4.5 shows the XRD patterns as a function of the scattering vector *q* for the NPs prepared with different sonication conditions. In Figure 4.5 (a), results for NPs prepared without sonication and those prepared with bath sonication are presented. In both cases, the reflections of the form I crystalline phase of P3HT are observed: an intense (100) diffraction maximum at q = 3.8 nm^{-1} and its higher orders (200) and (300) reflections observed at q = 7.6 nm^{-1} and 11.4 nm^{-1}, respectively[18–21]. The (020)/(002)/(010) reflection is observed at q = 16.7 nm^{-1}.[18–21]

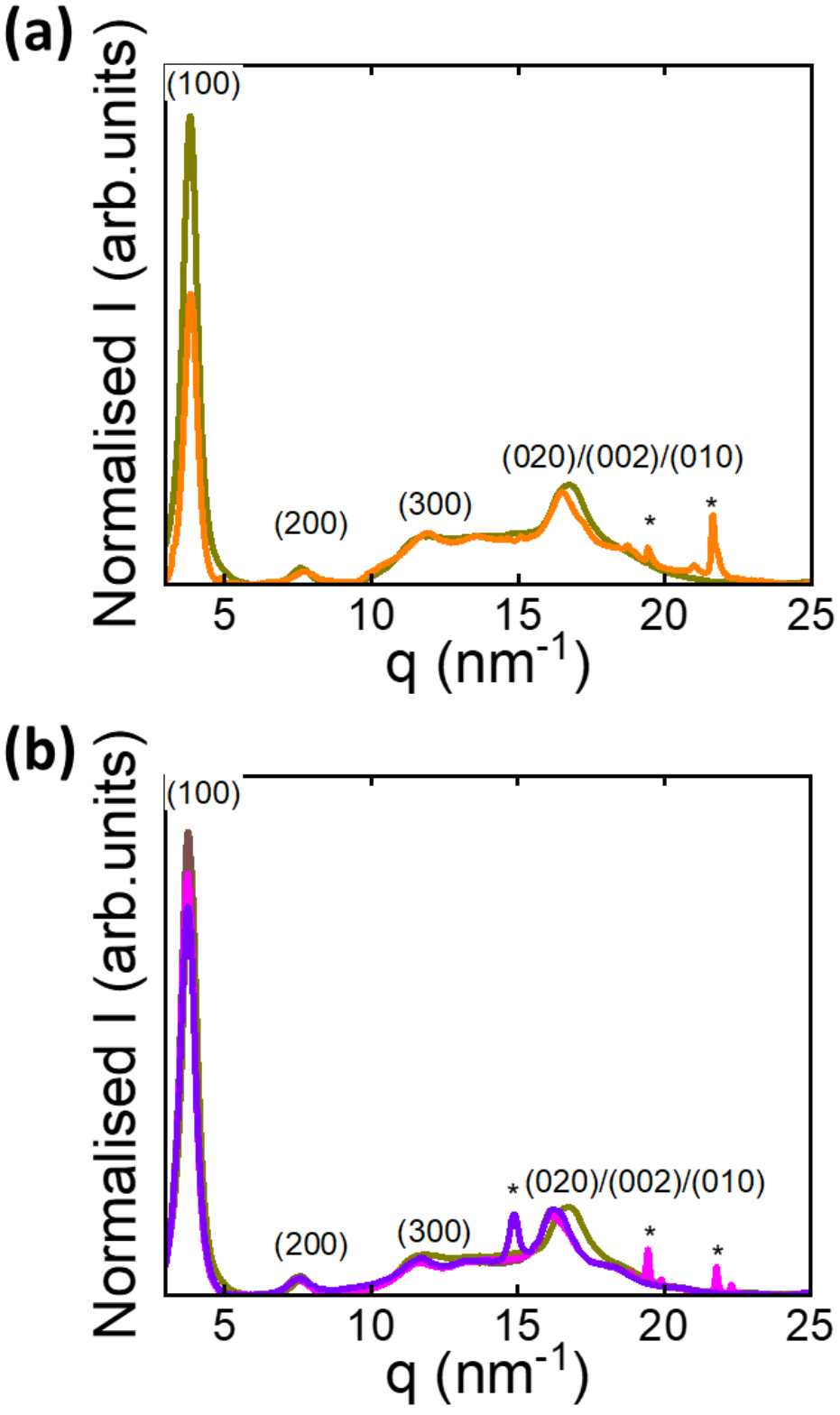

Figure 4.5. (a) X-ray diffraction patterns for non-sonicated (orange lines) and bath-sonicated (dark yellow lines) NPs and **(b)** for bath-sonicated (dark yellow) and probe-sonicated samples (brown for 10%, magenta for 25% and violet for 35%). Several narrow rings between 14.8 and 25 nm^{-1}, labelled with an asterisk, can be attributed to residual crystalline SDS[22].

However, it is interesting to note that the ultrasonication induces changes in the π-π stacking as revealed by the shift towards higher *q* of the (020)/(002)/(010) reflection in the NPs prepared by bath sonication. As discussed in the preceding chapter concerning the crystalline analysis by diffraction, this shift may be related to a decrease in the distance between crystalline planes, that is, a more compact structure[18]. The interplanar distance corresponding to the π–π stacking (reflection 020) was estimated to be 0.382 nm for the non-sonicated sample and 0.378 nm for the sample sonicated in a bath[18,23]. The results obtained provide corroboration for the more compact structure.

Figure 4.5 (b) shows the XRD results for the NPs prepared by bath sonication and by probe ultrasonication at different intensities. Again, the reflections corresponding to the form I crystalline phase of P3HT are observed[18–21]. And also, variations of the π-π stacking distance with the different sonication conditions are observed. Probe sonication produce a decrease in the *q* position of the (020) peak, revealing a larger π-π stacking distance compared with those prepared from low-intensity sonicated samples[18].

In order to estimate possible variations in the crystallinity of the samples, the area of the (020)/(002)/(010) and (100) reflections was calculated. Figure 4.6 presents the area integrated of the (100) and (020)/(002)/(010) peaks for all samples. Results show that the non-sonicated NPs exhibit a significantly lower degree of crystallinity in comparison to those sonicated. When comparing the integrated areas of samples prepared under different sonication conditions, the results show that the samples prepared with the ultrasonic probe show a slight decrease in the integrated areas, and this decrease is more pronounced with increasing probe intensity. These results indicate that probe sonication induces a less ordered molecular organisation, hindering the formation of new domains during nucleation and growth or dispersing more of the individual chains[15].

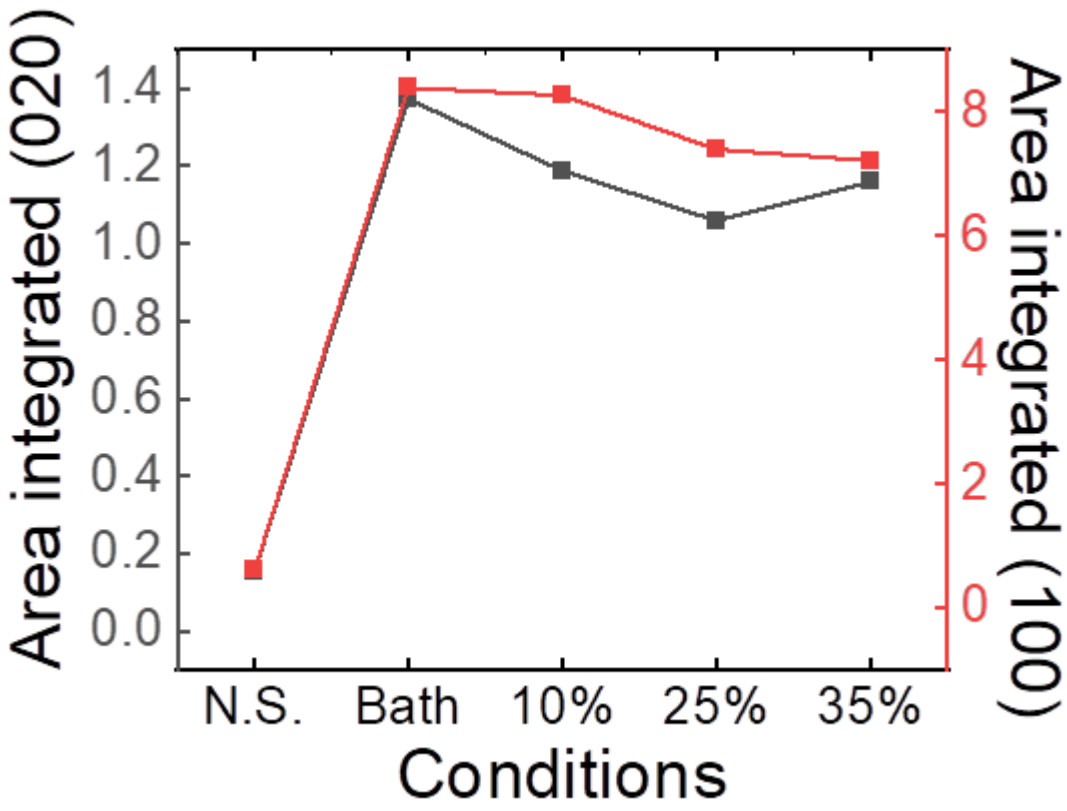

Figure 4.6. Values obtained from the integrated area of the (100) and (020) diffraction maxima for all samples prepared by minimulsion. The non-sonicated sample is referenced as N.S., the ultrasonic bath sonicated sample is referenced as Bath, and the probe sonicated samples are referenced as a function of amplitude percentage.

It was proposed that sonication induces planarization of the P3HT chains, which can facilitate the rearrangement of the chains and their packing, promoting the formation of more ordered aggregates in solution and favouring the crystallinity and a longer conjugation length of the NPs[24]. Furthermore, the distribution of the surfactant when the sample is sonicated can be more homogeneous, facilitating the self-assembly of the chains. However, these results indicate that high-intensity sonication does not further improve the π-π stacking and the crystallinity. On the other hand, the presence of the surfactant could be considered. A plausible hypothesis is that the high, localized energy and turbulence produced by probe sonication generate a significant amount of localized heat, which may affect the interactions between the polymer chains and the surfactant molecules. This intense energy input could induce the segregation of the surfactant molecules and their subsequent re-crystallization. The fact that we observe maxima (marked with asterisks in Figure 4.5 (b)) corresponding to

crystalline SDS strongly supports this reasoning. In contrast, bath sonication provides a more homogeneous and less energetic input, which facilitates the removal of SDS during dialysis rather than its recrystallisation. Residual SDS crystals, if present, could potentially influence the exciton diffusion of the NPs, and therefore are a relevant aspect to consider.

4.3. Optical properties of P3HT nanoparticles at different sonication levels: absorption and emission

As was the case for the flash NPs presented in the previous chapter, colour differences are observed between the dissolved P3HT (orange) and the miniemulsion NPs dispersions (purple) (Figure 4.7).

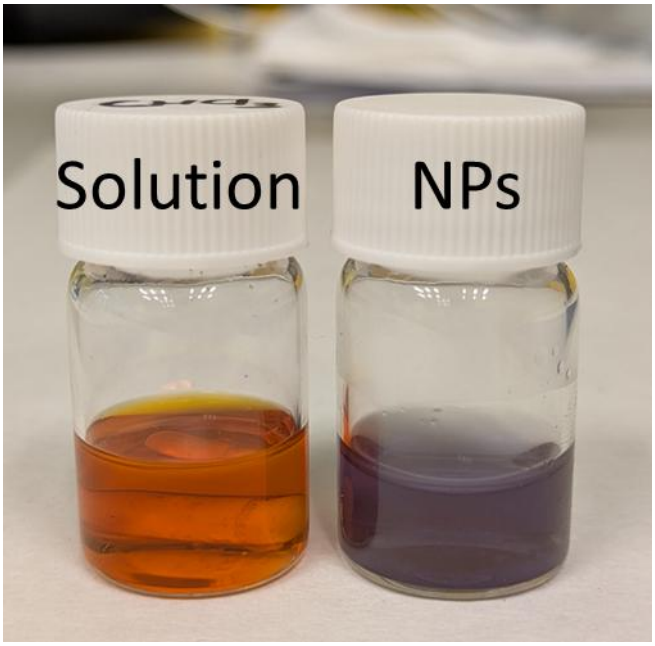

Figure 4.7. Solutions of P3HT 3g/L in $CHCl_3$ on the left and NPs prepared by miniemulsion on the right. The observed colour change is a consequence of the aggregation state of P3HT.

The UV-Vis and fluorescence spectrum of a P3HT solution in $CHCl_3$ is presented in Figure 4.8. The absorption spectrum shows a broad band centred at 450 nm, which is associated with the intrachain π–π^* transitions[25–27]. No aggregates are observed at high

wavelengths. In addition, the fluorescence emission spectrum shows a band at 580 nm and a shoulder that are associated with the ground and first singlet excited states, as previously mentioned in the previous Chapter, indicative of the heterogeneity of the local environment of the chromophores[28,29].

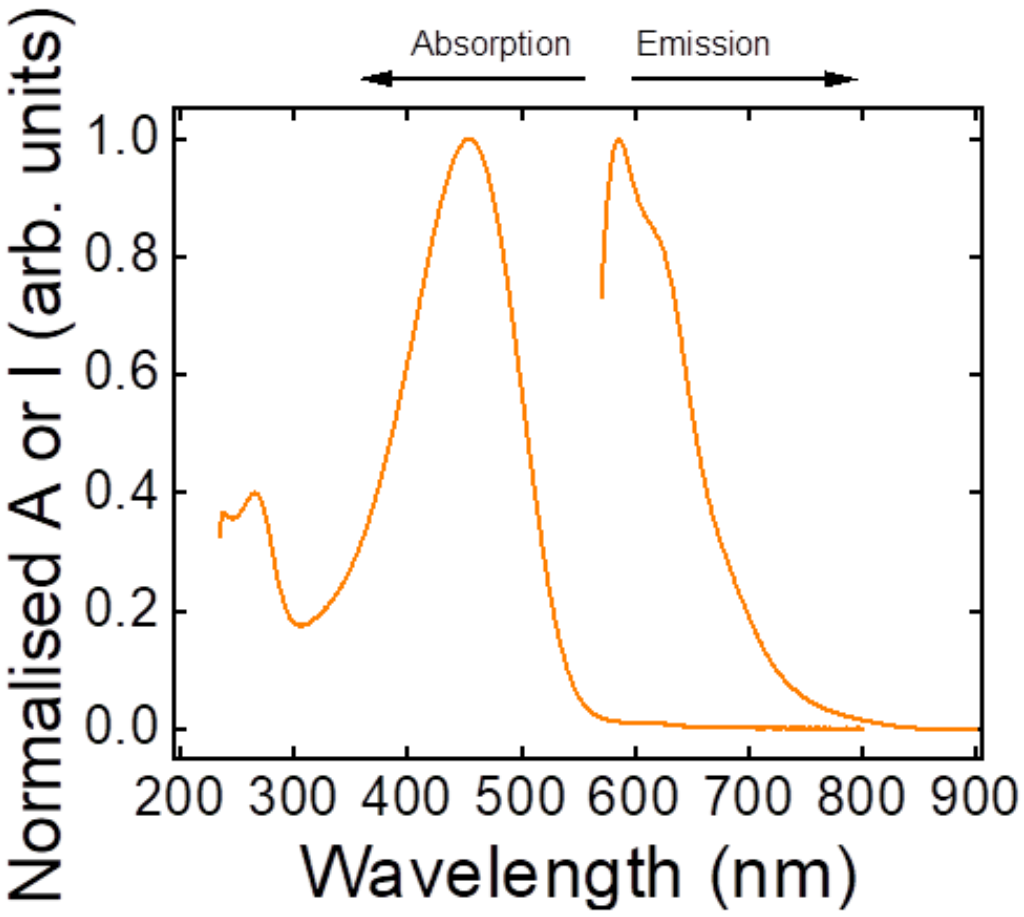

Figure 4.8. Absorption and emission spectrum of P3HT dissolved in $CHCl_3$.

Figure 4.9 shows the absorption and emission spectra of all NPs prepared by miniemulsion. In all cases, the UV-Vis spectra exhibit three bands, located at 525 nm, 556 nm, and 607 nm, associated with specific electronic transitions attributed to the presence of crystalline domains in P3HT[25,30,31]. However, depending on the preparation conditions of the NPs, these bands show differences. Figure 4.9 (a) displays a comparison between the UV-Vis and emission spectra of NPs prepared from non-sonicated and bath-sonicated solutions. The UV-Vis spectrum of the non-sonicated sample is shifted towards longer wavelengths compared to that of the sonicated NPs. The ratio between the 0-0 and 0-1 transitions also shows differences in samples prepared with and without sonication. The values of the 0-0/0-

1 ratios are presented in Table 4.1, indicative of enhanced intrachain exciton coupling[32]. The non-sonicated sample has a value greater than 1, suggesting a higher presence of J aggregates[33,34]. A high intensity of the 0-0 vibronic transition is associated with a low exciton bandwidth, indicating an increase in the conjugation length, as previously mentioned, and a higher intrachain ordering along an individual polymer chain[27,32,35]. Another important difference in the UV-Vis spectra of non-sonicated and bath sonicated NPs appears in the high wavelength regions, where a tail can be observed in the non-sonicated NPs, while in the sonicated ones, this tail does not appear. The presence of this tail has been attributed to lower energy transitions due to the formation of heterogeneous aggregates[36,37]. In the case of emission, as in absorption, the same transitions are identified for all samples[25].

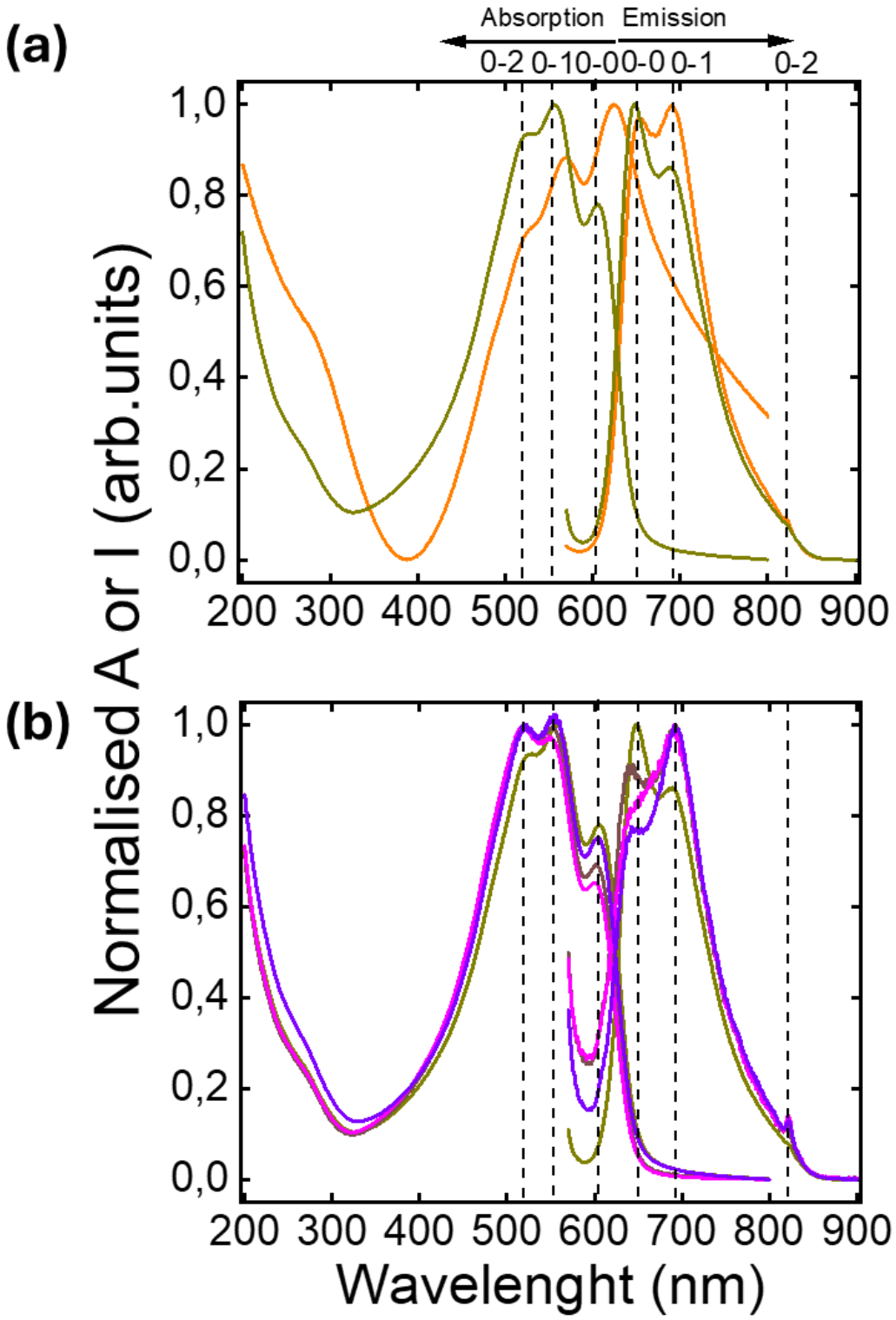

Figure 4.9. (a) UV-Vis absorption and emission spectra for non-sonicated (orange lines) and bath-sonicated (dark yellow lines) samples, and **(b)** UV-Vis absorption and emission spectra for bath-sonicated (dark yellow) and probe-sonicated samples (10%: brown, 25%: magenta and 35%: violet). The colour gradient becomes darker as the amplitude increases. In the emission, all samples were measured under the same excitation wavelength (555 nm). The spectra are normalised to the more intense band.

To address the effect of the sonication on the optical properties of the colloidal suspensions, Figure 4.9 (b) shows the absorption and emission spectra for bath sonicated NPs and those sonicated with the ultrasonic probe at different amplitudes. Firstly, compared to the bath sonicated NPs, the NPs prepared by the ultrasonic probe show very similar UV-Vis spectra with a slight blue shift (displacement towards lower wavelength values), indicating lower planarity of the chains and a larger presence of H-aggregates. The 0-0 and 0-1 ratio (Table 4.1) corroborates these results, exhibiting values less than 1 in absorption[38]. The sonicated samples in the probe display an even lower value compared to those sonicated in an ultrasonic bath. This observation indicates that the transition to the first vibronic state is accessible[39], and more electrons are initially promoted from the fundamental electronic state to a vibrational excited state in the electronically excited molecule in sonicated NPs by the probe. Moreover, the 0-2 band is less intense in the sample prepared in the ultrasonic bath.

Table 4.1. The intensity ratios between the 0-0 and 0-1 bands of the absorption spectra for non-sonicated and sonicated samples.

Conditions	Absorption
	$A_{0\text{-}0}/A_{0\text{-}1}$
Non sonicated	1.135
Bath	0.782
10%	0.686
25%	0.670
35%	0.750

Among the NPs prepared with probe sonication, several significant differences can be appreciated in Figure 4.9 (b). The most significant of these is that the 0-0 bands gain intensity as sonication amplitude increases, implying greater planarization of the rings and better intermolecular order[40,41].

The band gaps[36,42,43] estimated from the emission and absorption spectra and calculated through the Tauc plot, as explained in Chapter 2.4.4.1, are present in Table 4.2. The lowest band gap is that of the non-sonication NPs, despite their lower crystallinity. The band gaps

of the NPs prepared from sonicated solutions have comparable values, although slightly higher for the NPs prepared with the ultrasonic probe.

Table 4.2. Band gap for non-sonicated and sonicated samples, calculated from the intersection of the absorption and emission spectra and the Tauc plot.

Conditions	Abs-emis cross	Tauc plot
Non sonicated	1.93 eV (644 nm)	1.78 eV
Bath	1.98 eV (626 nm)	1.94 eV
10 %	2.01 eV (618 nm)	1.96 eV
25 %	2.01 eV (618 nm)	1.96 eV
35 %	1.99 eV (624 nm)	1.95 eV

Moreover, the values of the conduction band edge potential (E_{CB}) and the valence band edge potential (E_{VB}) obtained from the Tauc plot[43–45] (see Chapter 2.4.4.1) have been calculated and are presented in Table 4.3. The NPs with a smaller band gap are those prepared without sonication, which is reflected in the closer proximity of the E_{CB} and E_{VB} values. The edges obtained for all the sonicated samples are very similar.

Table 4.3. Calculated energy levels of the conduction band edge (E_{CB}) and valence band edge (E_{VB}) for P3HT nanoparticles prepared under different sonication conditions. The estimations are based on the intersection energy of the absorption and emission spectra and the optical band gap determined via Tauc plot analysis.

Conditions	E_{CB}	E_{VB}
Non sonicated	-1.67 eV	0.24 eV
Bath	-1.69 eV	0.27 eV
10 %	-1.70 eV	0.28 eV
25 %	-1.70 eV	0.28 eV
35 %	-1.70 eV	0.27 eV

4.4. Conclusions

In summary, this chapter has investigated the influence of sonication conditions on the preparation of P3HT NPs by miniemulsion, revealing the significant impact of this parameter on various properties crucial for their applications. The following key conclusions have been drawn:

-Sonication significantly affected the NP diameter and aggregation. NPs prepared from non-sonicated solutions exhibited the largest average particle diameter and a higher degree of aggregation. In contrast, the sonication also led to a more uniform dispersion. Sonication in the ultrasonic bath resulted in the smallest NPs, while sonication in the probe led to size distributions that shifted towards larger diameters.

-Sonicating the solutions produces more crystalline NPs, especially the bath sonicated NPs. NPs prepared from probe-sonicated solutions show a trend towards a slight decrease in crystallinity as probe amplitude increases.

-The bath-sonicated NPs, which exhibit higher crystallinity compared to the probe sonicated NPs, also showed spectral features suggesting a higher degree of interchain order and J-aggregate formation.

Some of the NPs studied and discussed in this chapter will be applied in Chapter 7, where their structural and optical properties, including crystallinity, size, and aggregation state, will be correlated with their efficiency in the degradation of a model organic pollutant. The subsequent evaluation of the impact of these characteristics on the degradation efficiency and mechanism will provide a deeper understanding of the structure-function relationship in these nanomaterials for environmental applications, underscoring the importance of controlled preparation for developing sustainable pollutant remediation strategies.

4.5. Bibliography

(1) Chaudhary, V.; Sharma, S. Suspension Polymerization Technique: Parameters Affecting Polymer Properties and Application in Oxidation Reactions. *Journal of Polymer Research* **2019**, *26* (5). https://doi.org/10.1007/s10965-019-1767-8.

(2) Fitch, R. M. *Polymer Colloids: A Comprehensive Introduction*, 1st ed.; Academic Press: New York, 1997.

(3) Hiemenz, Paul.; Rajagopalan, Raj. *Principles of Colloid and Surface Chemistry*; Taylor & Francis: Boca Raton, 2016.

(4) Shaw, D. J. *Introduction to Colloid and Surface Chemistry Fourth Edition*, 4th ed.; Butterworth-Heinemann: Oxford, 1992.

(5) Mukherjee, S.; Safdari, A.; Shardt, O.; Kenjereš, S.; Van Den Akker, H. E. A. Droplet-Turbulence Interactions and Quasi-Equilibrium Dynamics in Turbulent Emulsions. *J Fluid Mech* **2019**, *878*, 221–276. https://doi.org/10.1017/jfm.2019.654.

(6) Gutiérrez-Fernández, E.; Cui, J.; Martínez-Tong, D. E.; Nogales, A. Preparation, Physical Properties, and Applications of Water-Based Functional Polymer Inks. *Polymers* **2021**, *13* (9). https://doi.org/10.3390/polym13091419.

(7) Hunter, R. J. . *Foundations of Colloid Science*, 2nd ed.; Oxford University Press: Oxford, 2001.

(8) Shaikh, J.; Patil, N. D.; Sharma, A.; Bhardwaj, R. Numerical Simulations and Experiments on Droplet Coalescence Dynamics over a Liquid–Air Interface: Mechanism and Effect of Droplet-Size/Surface-Tension. *SN Appl Sci* **2021**, *3* (3). https://doi.org/10.1007/s42452-021-04275-3.

(9) Guo, R.; Yu, E.; Liu, J.; Wei, Z. Agitating Transformation during Vinyl Chloride Suspension Polymerization: Aggregation Morphology and PVC Properties. *RSC Adv* **2017**, *7* (39), 24022–24029. https://doi.org/10.1039/c7ra01914a.

(10) Schwarz, K. N.; Farley, S. B.; Smith, T. A.; Ghiggino, K. P. Charge Generation and Morphology in P3HT : PCBM Nanoparticles Prepared by Mini-Emulsion and Reprecipitation Methods. *Nanoscale* **2015**, *7* (47), 19899–19904. https://doi.org/10.1039/c5nr06244f.

(11) Vitale, S. A.; Katz, J. L. Liquid Droplet Dispersions Formed by Homogeneous Liquid-Liquid Nucleation: "The Ouzo Effect." *Langmuir* **2003**, *19* (10), 4105–4110. https://doi.org/10.1021/la026842o.

(12) Choi, D.; Chang, M.; Reichmanis, E. Controlled Assembly of Poly(3-Hexylthiophene): Managing the Disorder to Order Transition on the Nano- through Meso-Scales. *Adv Funct Mater* **2015**, *25* (6), 920–927. https://doi.org/10.1002/adfm.201403708.

(13) Zhao, K.; Khan, H. U.; Li, R.; Su, Y.; Amassian, A. Entanglement of Conjugated Polymer Chains Influences Molecular Self-Assembly and Carrier Transport. *Adv Funct Mater* **2013**, *23* (48), 6024–6035. https://doi.org/10.1002/adfm.201301007.

(14) Kleinhenz, N.; Persson, N.; Xue, Z.; Chu, P. H.; Wang, G.; Yuan, Z.; McBride, M. A.; Choi, D.; Grover, M. A.; Reichmanis, E. Ordering of Poly(3-Hexylthiophene) in Solutions and Films: Effects of Fiber Length and Grain Boundaries on Anisotropy and Mobility. *Chemistry of Materials* **2016**, *28* (11), 3905–3913. https://doi.org/10.1021/acs.chemmater.6b01163.

(15) Kleinhenz, N.; Persson, N.; Xue, Z.; Chu, P. H.; Wang, G.; Yuan, Z.; McBride, M. A.; Choi, D.; Grover, M. A.; Reichmanis, E. Ordering of Poly(3-Hexylthiophene) in Solutions and Films: Effects of Fiber Length and Grain Boundaries on Anisotropy and Mobility. *Chemistry of Materials* **2016**, *28* (11), 3905–3913. https://doi.org/10.1021/acs.chemmater.6b01163.

(16) Aiyar, A. R.; Hong, J. Il; Izumi, J.; Choi, D.; Kleinhenz, N.; Reichmanis, E. Ultrasound-Induced Ordering in Poly(3-Hexylthiophene): Role of Molecular and Process Parameters on Morphology and Charge Transport. *ACS Appl Mater Interfaces* **2013**, *5* (7), 2368–2377. https://doi.org/10.1021/am3027822.

(17) Pan, H.; Tan, B.; Yazdani, A.; Budhlall, B.; Sobkowicz, M. J. Controlling the Particle Size of Aqueous Conjugated Polymer Colloids and Impact on Transistor Performance. *Colloids Surf A Physicochem Eng Asp* **2020**, *594*. https://doi.org/10.1016/j.colsurfa.2020.124633.

(18) Müller-Buschbaum, P. The Active Layer Morphology of Organic Solar Cells Probed with Grazing Incidence Scattering Techniques. *Advanced Materials* **2014**, *26* (46), 7692–7709. https://doi.org/10.1002/adma.201304187.

(19) Agbolaghi, S.; Zenoozi, S. A Comprehensive Review on Poly(3-Alkylthiophene)-Based Crystalline Structures, Protocols and Electronic Applications. *Org Electron* **2017**, *51*, 362–403. https://doi.org/10.1016/j.orgel.2017.09.038.

(20) Yang, H.; Shin, T. J.; Yang, L.; Cho, K.; Ryu, C. Y.; Bao, Z. Effect of Mesoscale Crystalline Structure on the Field-Effect Mobility of Regioregular Poly(3-Hexyl Thiophene) in Thin-Film Transistors. *Adv Funct Mater* **2005**, *15* (4), 671–676. https://doi.org/10.1002/adfm.200400297.

(21) Millstone, J. E.; Kavulak, D. F. J.; Woo, C. H.; Holcombe, T. W.; Westling, E. J.; Briseno, A. L.; Toney, M. F.; Fréchet, J. M. J. Synthesis, Properties, and Electronic Applications of Size-Controlled Poly(3-Hexylthiophene) Nanoparticles. *Langmuir* **2010**, *26* (16), 13056–13061. https://doi.org/10.1021/la1022938.

(22) Summerton, E.; Hollamby, M. J.; Zimbitas, G.; Snow, T.; Smith, A. J.; Sommertune, J.; Bettiol, J.; Jones, C.; Britton, M. M.; Bakalis, S. The Impact of N,N-Dimethyldodecylamine N-Oxide (DDAO) Concentration on the Crystallisation of Sodium Dodecyl Sulfate (SDS) Systems and the Resulting Changes to Crystal Structure, Shape and the Kinetics of Crystal Growth. *J Colloid Interface Sci* **2018**, *527*, 260–266. https://doi.org/10.1016/j.jcis.2018.05.058.

(23) Chiu, M. Y.; Jeng, U. S.; Su, C. H.; Liang, K. S.; Wei, K. H. Simultaneous Use of Small- and Wide-Angle X-Ray Techniques to Analyze Nanometerscale Phase Separation in Polymer Heterojunction Solar Cells. *Advanced Materials* **2008**, *20* (13), 2573–2578. https://doi.org/10.1002/adma.200703097.

(24) Aiyar, A. R.; Hong, J. Il; Nambiar, R.; Collard, D. M.; Reichmanis, E. Tunable Crystallinity in Regioregular Poly(3-Hexylthiophene) Thin Films and Its Impact on Field Effect Mobility. *Adv Funct Mater* **2011**, *21* (14), 2652–2659. https://doi.org/10.1002/adfm.201002729.

(25) Gutiérrez-Fernández, E.; Ezquerra, T. A.; Rebollar, E.; Cui, J.; Marina, S.; Martín, J.; Nogales, A. Photophysical and Structural Modulation of Poly(3-Hexylthiophene) Nanoparticles via Surfactant-Polymer Interaction. *Polymer* **2021**, *218*. https://doi.org/10.1016/j.polymer.2021.123515.

(26) Nagarjuna, G.; Baghgar, M.; Labastide, J. A.; Algaier, D. D.; Barnes, M. D.; Venkataraman, D. Tuning Aggregation of Poly(3-Hexylthiophene) within Nanoparticles. *ACS Nano* **2012**, *6* (12), 10750–10758. https://doi.org/10.1021/nn305207b.

(27) Chen, J. H.; Li, J. Y.; Chen, L. C.; Su, C. I. Morphology and Microstructure of Aggregates and Gelation Behaviour of Poly (3-Hexylthiophene) in Xylene Solution. In *Applied Mechanics and Materials*; 2014; Vol. 479–480, pp 115–120. https://doi.org/10.4028/www.scientific.net/AMM.479-480.115.

(28) Wells, N. P.; Boudouris, B. W.; Hillmyer, M. A.; Blank, D. A. Intramolecular Exciton Relaxation and Migration Dynamics in Poly(3-Hexylthiophene). *J Phys Chem C* **2007**, *111* (42), 15404–15414. https://doi.org/10.1021/jp074657j.

(29) Yamamoto, T.; Komarudin, D.; Arai, M.; Lee, B.-L.; Suganuma, H.; Asakawa, N.; Inoue, Y.; Kubota, K.; Sasaki, S.; Fukuda, T.; Matsuda, H. Extensive Studies on π-Stacking of Poly(3-Alkylthiophene-2,5-Diyl)s and Poly(4-Alkylthiazole-2,5-Diyl)s by Optical Spectroscopy, NMR Analysis, Light Scattering Analysis, and X-Ray Crystallography. *J Am Chem Soc* **1998**, *120* (9), 2047–2058. https://doi.org/10.1021/ja973873a.

(30) Chambon, S.; Schatz, C.; Sébire, V.; Pavageau, B.; Wantz, G.; Hirsch, L. Organic Semiconductor Core-Shell Nanoparticles Designed through Successive Solvent Displacements. *Mater Horiz* **2014**, *1* (4), 431–438. https://doi.org/10.1039/c4mh00021h.

(31) Holmes, N. P.; Nicolaidis, N.; Feron, K.; Barr, M.; Burke, K. B.; Al-Mudhaffer, M.; Sista, P.; Kilcoyne, A. L. D.; Stefan, M. C.; Zhou, X.; Dastoor, P. C.; Belcher, W. J. Probing the Origin of Photocurrent in Nanoparticulate Organic Photovoltaics. *Solar Energy Materials and Solar Cells* **2015**, *140*, 412–421. https://doi.org/10.1016/j.solmat.2015.04.044.

(32) Persson, N. E.; Chu, P. H.; McBride, M.; Grover, M.; Reichmanis, E. Nucleation, Growth, and Alignment of Poly(3-Hexylthiophene) Nanofibers for High-Performance OFETs. *Acc Chem Res* **2017**, *50* (4), 932–942. https://doi.org/10.1021/acs.accounts.6b00639.

(33) Rahimi, K.; Botiz, I.; Agumba, J. O.; Motamen, S.; Stingelin, N.; Reiter, G. Light Absorption of Poly(3-Hexylthiophene) Single Crystals. *RSC Adv* **2014**, *4* (22), 11121–11123. https://doi.org/10.1039/c3ra47064d.

(34) Spano, F. C.; Silva, C. H- and J-Aggregate Behavior in Polymeric Semiconductors. *Annu Rev Phys Chem* **2014**, *65*, 477–500. https://doi.org/10.1146/annurev-physchem-040513-103639.

(35) Clark, J.; Chang, J. F.; Spano, F. C.; Friend, R. H.; Silva, C. Determining Exciton Bandwidth and Film Microstructure in Polythiophene Films Using Linear Absorption Spectroscopy. *Appl Phys Lett* **2009**, *94* (16). https://doi.org/10.1063/1.3110904.

(36) Cook, S.; Furube, A.; Katoh, R. Analysis of the Excited States of Regioregular Polythiophene P3HT. *Energy Environ Sci* **2008**, *1* (2), 294–299. https://doi.org/10.1039/b805643a.

(37) Chu, Z.; Guo, H.; Yu, W.; Sun, Z.; Chen, W. Low Temperature Aging Induced Conjugated Polymers Aggregation by UV–Vis Spectroscopy. *Journal of Polymer Science* **2024**. https://doi.org/10.1002/pol.20240148.

(38) Manas, E. S.; Spano, F. C. Absorption and Spontaneous Emission in Aggregates of Conjugated Polymers. *J Chem Phys* **1998**, *109* (18), 8087–8101. https://doi.org/10.1063/1.477457.

(39) Holmes, N. P.; Ulum, S.; Sista, P.; Burke, K. B.; Wilson, M. G.; Stefan, M. C.; Zhou, X.; Dastoor, P. C.; Belcher, W. J. The Effect of Polymer Molecular Weight on P3HT:PCBM Nanoparticulate Organic Photovoltaic Device Performance. *Solar Energy Materials and Solar Cells* **2014**, *128*, 369–377. https://doi.org/10.1016/j.solmat.2014.05.046.

(40) Lee, S. H.; Lee, Y. B.; Park, D. H.; Kim, M. S.; Cho, E. H.; Joo, J. Tuning Optical Properties of Poly(3-Hexylthiophene) Nanoparticles through Hydrothermal Processing. *Sci Technol Adv Mater* **2011**, *12* (2). https://doi.org/10.1088/1468-6996/12/2/025002.

(41) Ulum, S.; Holmes, N.; Darwis, D.; Burke, K.; David Kilcoyne, A. L.; Zhou, X.; Belcher, W.; Dastoor, P. Determining the Structural Motif of P3HT:PCBM Nanoparticulate Organic Photovoltaic Devices. *Solar Energy Materials and Solar Cells* **2013**, *110*, 43–48. https://doi.org/10.1016/j.solmat.2012.11.015.

(42) Tauc, J.; Grigorovici, R.; Vancu, A. Optical Properties and Electronic Structure of Amorphous Germanium. *Physica Status Solidi* **1966**, *15* (2), 627. https://doi.org/10.1002/pssb.19660150224.

(43) Makuła, P.; Pacia, M.; Macyk, W. How To Correctly Determine the Band Gap Energy of Modified Semiconductor Photocatalysts Based on UV-Vis Spectra. *J Phys Chem Lett* **2018**, *9* (23), 6814–6817. https://doi.org/10.1021/acs.jpclett.8b02892.

(44) Zhu, H.; Gong, L.; Li, Z. Construction and Mechanism of a Novel Z-Scheme Photocatalyst α-Fe2O3/P3HT with O-Ti-O for Organic Pollutant Degradation under Visible Light. *Appl Surf Sci* **2020**, *505*. https://doi.org/10.1016/j.apsusc.2019.144639.

(45) Floresyona, D.; Goubard, F.; Aubert, P. H.; Lampre, I.; Mathurin, J.; Dazzi, A.; Ghosh, S.; Beaunier, P.; Brisset, F.; Remita, S.; Ramos, L.; Remita, H. Highly Active Poly(3-Hexylthiophene) Nanostructures for Photocatalysis under Solar Light. *Appl Catal B* **2017**, *209*, 23–32. https://doi.org/10.1016/j.apcatb.2017.02.069.

Chapter 5

Comparative preparation of P3HT nanoparticles: flash versus miniemulsion and effects on structural, optical and FLIM properties

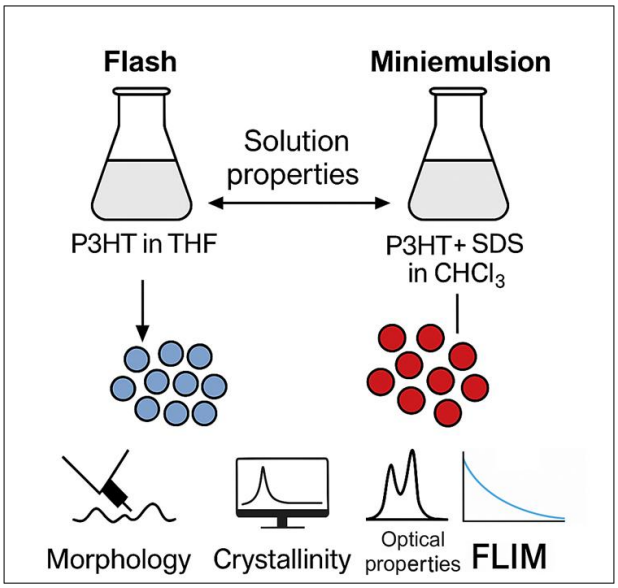

Graphical abstract representing the main idea of Chapter 5

Universidad Complutense de Madrid

Jose Sena Fernández

Micro and Nanoparticles of Functional Polymers: From Fundamentals to Applications

Flash nanoprecipitation and miniemulsion are two widely used techniques for producing polymer NPs, each relying on distinct physical principles for particle formation (see Sections 2.2.2 and 2.2.3). Although both have been successfully applied to P3HT, direct, and systematic comparisons of the resulting NP properties remain scarce in the literature[1,2]. Building on the previous chapters of this thesis, which investigated P3HT NPs obtained by flash nanoprecipitation (Chapter 3) and by miniemulsion (Chapter 4), this chapter aims to address this gap by analysing the intrinsic differences between P3HT NPs prepared by each method, from the properties of their precursor solutions to their final morphology, crystallinity, and optical behavior. The analysis also employs fluorescence lifetime imaging microscopy (FLIM) to gain further insight into exciton dynamics and charge separation pathways, providing a more in-depth understanding of the physical processes that govern NP formation by each method.

5.1. Effects of the solvent on P3HT solutions

As mentioned in previous chapters, flash nanoprecipitation of P3HT NPs involves an initial solution of the polymer in THF. For the preparation of miniemulsion P3HT NPs, the solvent used is $CHCl_3$. At the same concentration (3 g/L), the visual inspections reveal differences in the colour of the solutions (Figure 5.1). In a first approach, the observed variations can be attributed to the different solubility of the polymer in these solvents.

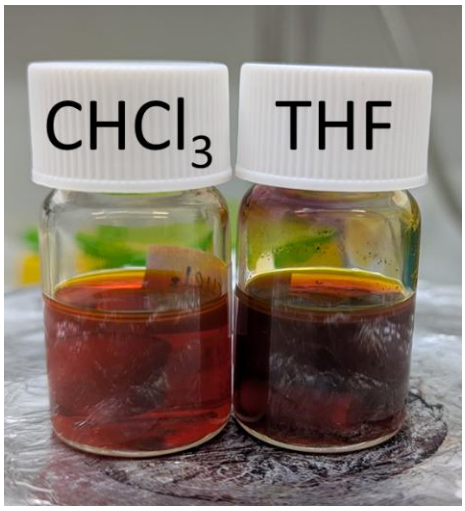

Figure 5.1. Solutions of P3HT 3 g/L in: $CHCl_3$ on the left and THF on the right.

The observed differences in colour are better quantified by UV-Vis absorption experiments (Figure 5.2). A broad band centred at 450 nm is observed, which is attributed to π–π^* transitions occurring in the coiled polymer chains in solution[3–5]. A small difference in the position of this broad peak is observed when comparing the two solvents. Interactions of P3HT molecules with the solvent are affected by polarity, viscosity, and electrostatic effects, which are all relevant to the solvation process. All these interactions influence the conformation of the chains, their rigidity, or the local chemical environment, affecting the energy of the polymer states and causing this shift[6]. Furthermore, in the absorption spectrum of P3HT in THF, a band is present at high wavelengths (613 nm), suggesting the presence of ordered aggregates[3,7,8] as observed in NPs prepared in previous chapters. This is due to the limited solubility of P3HT in this solvent. The Hansen solubility parameters or R_a (see Chapter 1.2.2) are useful for determining the theoretical solubility of a compound in a solvent. These parameters confirm that P3HT has a higher solubility in $CHCl_3$ (R_a = 1.7 $MPa^{1/2}$) than in THF (R_a = 6.2 $MPa^{1/2}$)[9,10].

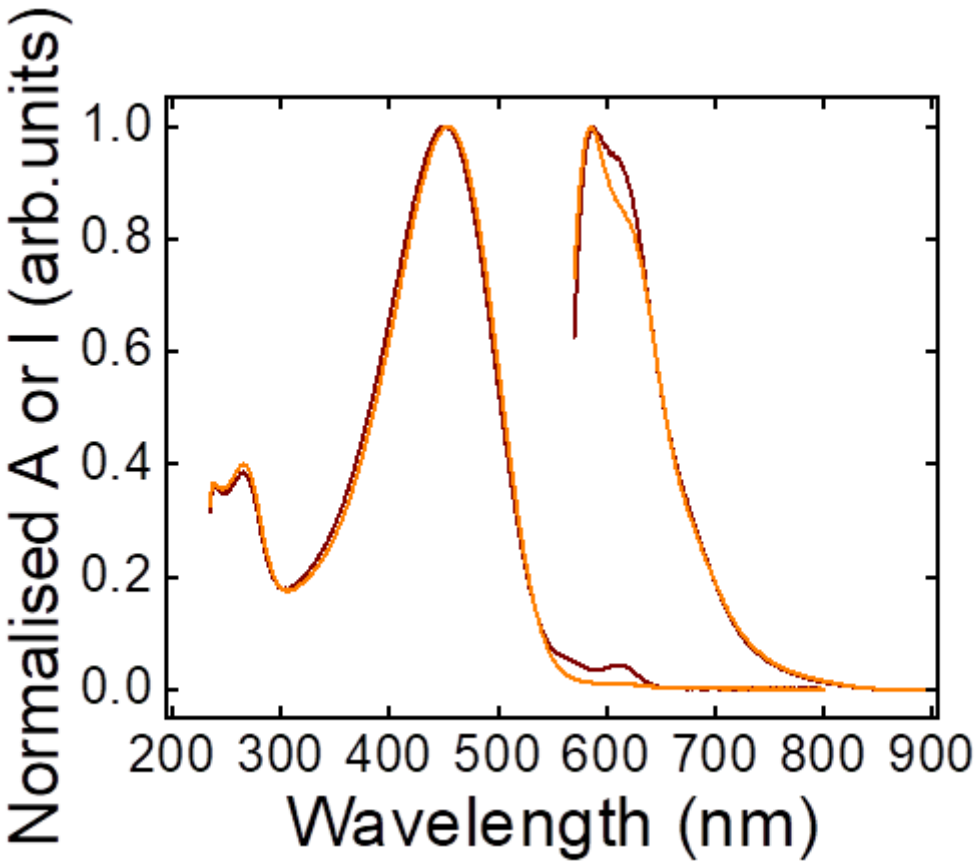

Figure 5.2. UV-Vis absorption and emission spectra of P3HT solutions in THF (curves in wine colour) and in $CHCl_3$ (curves in orange colour).

There are also differences between the two solvents in the emission spectrum (Figure 5.2). A peak centred at 580 nm is observed in both samples, accompanied by a shoulder. The intensity of this shoulder is dependent on the solvent, and its presence is attributed to the existence of ordered aggregates. The higher contribution of THF in this region is consistent with the absorption results[11]. Furthermore, apart from the coexistence of coiled and extended P3HT conformations, environmental factors such as solvent polarity modulate these spectral signatures and energy levels of the P3HT electronic states[8,12].

In order to detect possible changes in the molecular weight of the polymer due to the solvent, the size of the molecules was determined by DLS. In the case of $CHCl_3$, the size obtained corresponds to about 22.7 nm, a value consistent with other materials of similar molecular weight. In contrast, the result changes when P3HT is measured in THF, obtaining a value of chain size of 50 nm. This indicates that P3HT tends to aggregate very rapidly when the heat source is removed, as mentioned in Chapter 3. This makes obtaining values for the free chains in the solvent difficult.

The assembly behaviour of P3HT in solution is a determining factor in the properties and characteristics observed in the solid state. This assembly behaviour is associated with the molecular structure and preparation conditions in the solution, as previously observed. As previously mentioned, P3HT exhibits different intramolecular and intermolecular interactions in solution, resulting in a complex structure of crystalline P3HT. This transition from conformational disorder to ordered aggregation is of particular interest in this study. This transition covers different dimensions, ranging from intramolecular conformations (e.g., twisted angles, chain folding) to intermolecular ordering (e.g., π–π stacking).

The ensuing sections will thus comprise a study of P3HT in the solid state, focusing on these two solvents.

5.2. Comparison of the size and aggregation of the nanoparticles depending on the preparation method

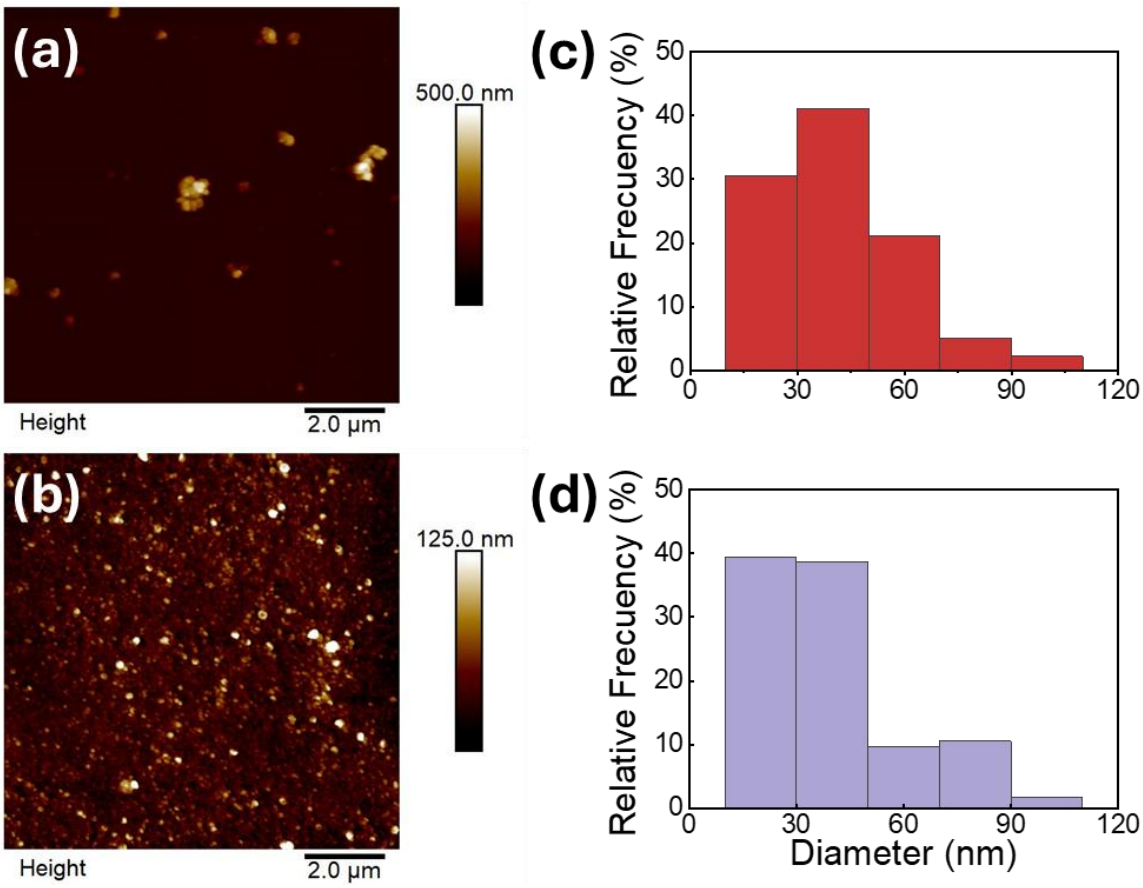

Figure 5.3. AFM topography images of P3HT NPs deposited on a silicon wafer for **(a)** flash NPs and **(b)** miniemulsion NPs. along with the corresponding histograms of particle diameter distribution of **(c)** flash P3HT NPs (red histogram), and **(d)** miniemulsion P3HT NPs (violet histogram).

Figure 5.3 shows an AFM topography image of deposits of P3HT prepared by flash, by miniemulsion and their corresponding diameter distributions. Size intensity distributions obtained by DLS are shown in Figure 5.4. It can be seen that the NPs produced by both methods are very similar in size, with a clear tendency towards spherical morphology (Figure 5.3 (a) and (b)). The size distribution for both techniques does not exceed 100 nm, with the highest frequency of diameters around 20 to 40 nm. The average diameters in NPs prepared by miniemulsion and flash NPs are shown in Table 5.1. It is important to note that, in the case of miniemulsion, the size of the NPs is not only influenced by the concentration of the

polymer solution but also by the concentration of the surfactant in water[13]. Furthermore, both P3HT and SDS are present in the NPs, with SDS acting as a stabilising agent. Consequently, in Figure 5.4, changes in NP diameters in DLS are observed. A plot of the size distribution is shown in Figure 5.4.

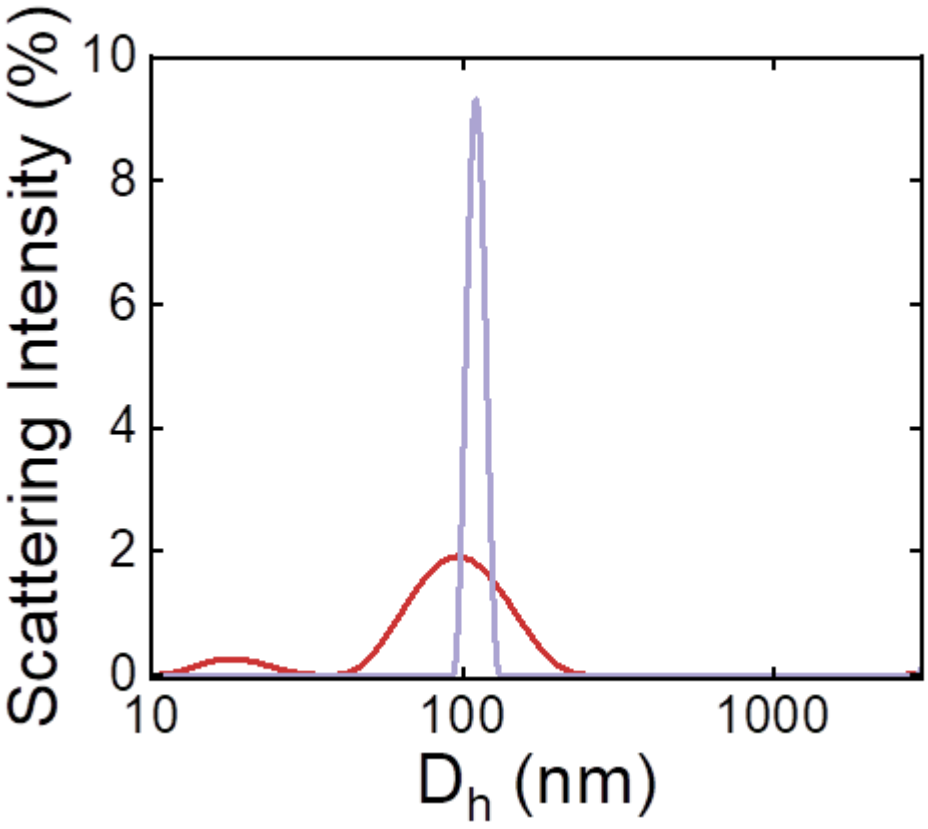

Figure 5.4. Size distribution of the P3HT NPs prepared by flash (red) and miniemulsion (violet) in suspension obtained by DLS.

Table 5.1 shows the diameter of both types of NPs by AFM and by DLS, as well as the Q obtained by DLS. In the case of both preparation methods, the D_n is larger than that obtained by AFM due to the presence of some aggregates. In the context of miniemulsion, there is a potential for the polymer to become swollen within a colloidal system, particularly in the presence of a water-soluble surfactant. Furthermore, the miniemulsion sample exhibits a minimal Q index, indicating a monodisperse population (see Table 5.1). By contrast, the flash-prepared sample exhibits a higher Q, although the value remains within acceptable range.

Table 5.1. Results of the diameter obtained by AFM and the D_n values and Q obtained using DLS of P3HT NPs prepared by flash and by miniemulsion.

Preparation method	AFM	DLS	
	Diameter (nm)	D_n (nm)	Q ($\times 10^{-2}$)
Flash	42 ± 18	56 ± 18	12
Miniemulsion	40 ± 20	86 ± 2	4.7

The tendency to form aggregates can also be explained by the zeta potential, which is also known as electrokinetic potential[14-16]. The zeta potential is a measure of the magnitude of the electric charge on the surface of particles in a colloidal dispersion and is measured in millivolts (mV)[14–17]. It is fundamental to understand and evaluate the stability of colloidal dispersions: a particle immersed in a liquid attracts oppositely charged ions, forming a layer around it (electric double layer)[15-17]. High values (positive or negative) indicate a greater repulsion between particles, which prevents them from agglomerating or precipitating and, therefore, is a more stable dispersion[16]. Conversely, values close to zero suggest a tendency to aggregation. In general, the value that differentiates between highly stable and unstable suspensions is generally taken at either +30 or -30 mV[14,16]. P3HT NPs prepared by miniemulsion are more stable than flash NPs, since their potential in absolute terms is higher (33 mV vs 24 mV). This could account for the broader size distribution and increased tendency toward aggregation observed in flash-prepared NPs.

5.3. Changes in crystalline structure in nanoparticles: GIWAXS

The impact of the NPs preparation method on their structure has been studied by XRD. Figure 5.5 shows the diffractograms of both types of NPs. As mentioned in Chapters 3 and 4, in both cases, the reflections corresponding to the crystalline phase I of P3HT are observed[18,19]. However, significant differences have been identified. NPs preparation via miniemulsion are more crystalline, as indicated by the more intense and narrower reflections. Also, a marginal increase in the position of the (100) reflection (3.83 nm^{-1} for miniemulsion vs. 3.77 nm^{-1} for flash NPs), attributed to enhanced interdigitation or a variation in the tilt of the alkyl side chains[20,21]. Additionally, for miniemulsion, the (020)/(002)/(010) reflection is observed at a higher value of the scattering vector. This reflection is related to the π–π

stacking[2,22], and therefore, these results indicate closer interchain stacking for miniemulsion NPs[23]. As discussed in preceding chapters, this shift signifies a more compact structure along this axis[24], most likely attributable to the presence of SDS between the chains. Similarly, the interplanar distance obtained by means of the Bragg law also changes. In the (100) direction, miniemulsion NPs had an interplanar distance of 1.63 nm, in comparison to 1.69 nm exhibited in flash NPs. In the (020) atomic plane is 0.378 nm in miniemulsion NPs and 0.382 nm in flash NPs. These results support that the polymer chains in miniemulsion NPs are more compactly packed. The presence of the surfactant could induce this, as it has been recently suggested[3]. However, it could also be related to the fact that different solvents are used in each type of preparation. For instance, Newbloom et al.[25] examined the structure of the self-assembly of colloidal particles in various aromatic solvents, demonstrating that the observed structure is highly dependent on the selected solvent.

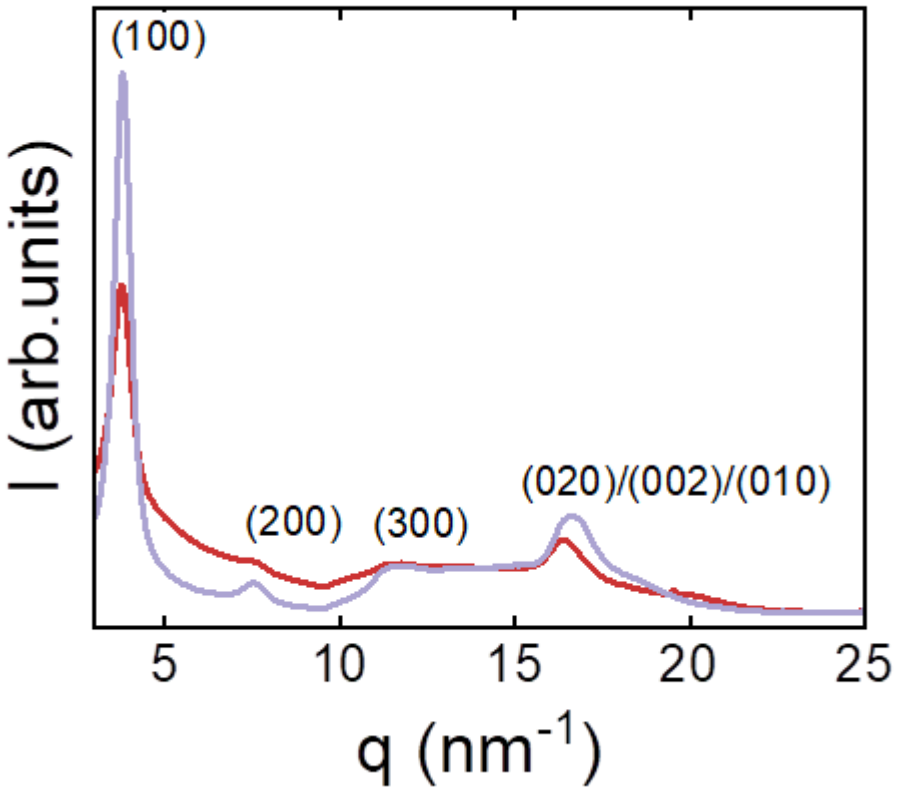

Figure 5.5. XRD intensity of PH3T miniemulsion NPs (purple) and flash NPs (red) deposited on a silicon wafer.

5.4. Changes in optical properties in nanoparticles: absorption and emission

The colour of the water suspension of NPs prepared by miniemulsion and flash nanoprecipitation is different, as illustrated in Figure 5.6. Slight variations in the colour of each suspension are evident, with the miniemulsion displaying a more purple tone and the flash exhibiting a pinkish-violet tint. From these visible colour differences, it can be assumed that the optical properties of both samples are different.

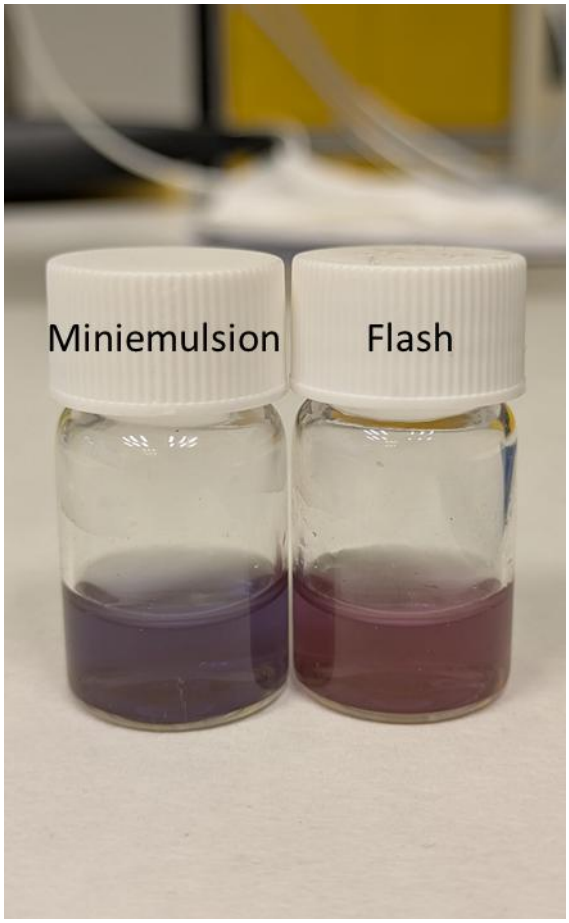

Figure 5.6. Suspensions of P3HT NPs prepared by miniemulsion (left) and P3HT NPs prepared via flash nanoprecipitation (right).

Figure 5.7 shows the absorption and emission spectra of the NPs dispersed in water. In both cases, π–π* electronic transitions corresponding to ordered states of P3HT are observed[3,7,8,12,16]. The spectrum corresponding to the miniemulsion NPs displays more

defined bands than the spectrum of the flash NPs. Also, miniemulsion NPs show a higher ratio between the intensity of the 0-0 and 0-1 bands (0.782 for miniemulsion vs 0.728 for flash) and emission (1.167 for miniemulsion vs 1.002 for flash). These observations are attributed to enhanced molecular organisation and improved interchain coupling in the case of miniemulsion NPs, in agreement with the XRD experiments. Furthermore, the bands exhibit a slight redshift, which lends support to a more effective chain organisation, thereby favouring electronic organisation with enhanced π–π overlap[5] probably due to enhanced planarization of the chains[27,28] and a more extended conjugation length, obtaining more stable excitons[29,30]. Tan et al.[31] reported that an increase in conjugation within surfactant led to elevated levels of chain order and conjugation length in the resultant P3HT colloids, thereby providing support for the results presented here. The contribution at wavelengths of 400-500 nm is more pronounced in flash, a phenomenon associated with this elevated amorphous content[3–5]. Saifuddin et al.[32] also observed that there are differences in the assembly of the chains in thin films depending on the evaporation rate of the solvent. However, in this case, it is not expected that this is a determining factor since there is no significant difference in the boiling point of the solvents (THF: 66°C and $CHCl_3$: 61°C).

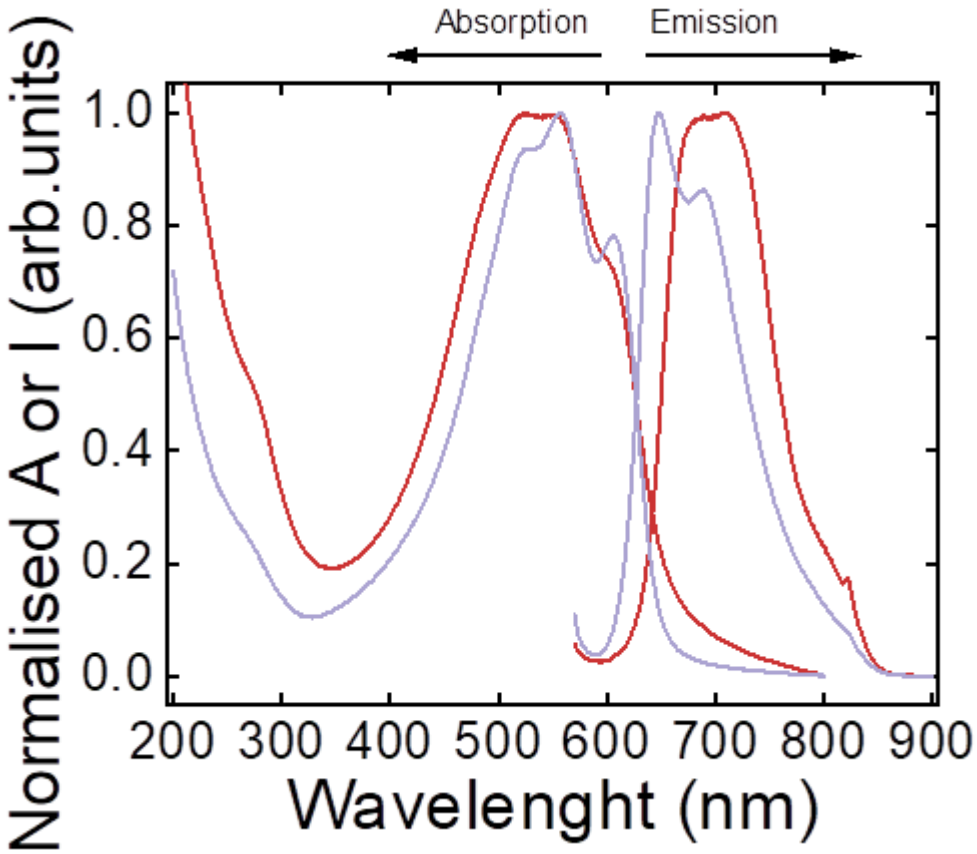

Figure 5.7. UV-Vis absorption and emission spectra for P3HT NPs prepared by two methods: flash method (red), and miniemulsion method (purple). The bands corresponding to the 0-0 transition (at ≈612 nm in absorption and ≈667 nm in emission), the 0-1 transition (at ≈564 nm in absorption and ≈707 nm in emission) and the 0-2 transition (at ≈524 nm in absorption and ≈821 nm in emission) are also identified.

It is important to note that these results align with those previously observed in X-ray studies, which attributed the observed effects to the presence of surfactant. This phenomenon can be attributed to the semicrystalline structure of P3HT, which is influenced by the interactions between SDS and P3HT. These interactions suggest a potential role for SDS in affecting the properties of the NPs. Consequently, changes in the band gap should be expected. The analysis of both absorption spectra, through the construction of a Tauc plot[33–35] (Section 2.4.4.1.), yielded similar values for the band gap of the two types of NPs. However, the band gap for miniemulsion NPs was slightly smaller (1.94 eV) than that for flash NPs (1.95 eV).

5.5. Fluorescence lifetime of the nanoparticle suspensions

To further understand the observed differences in the optical properties of the two types of NPs, fluorescence lifetime measurements were conducted. These experiments provide information about the duration of the excited state in the molecule before it is de-excited, as explained in detail in Section 2.4.4.3. Figure 5.8 shows the fluorescence decay curves following excitation at 640 nm for suspensions of P3HT NPs prepared by the flash and miniemulsion methods. For comparison, the lifetime of a P3HT thin film with a thickness of approximately 300 nm is also presented.

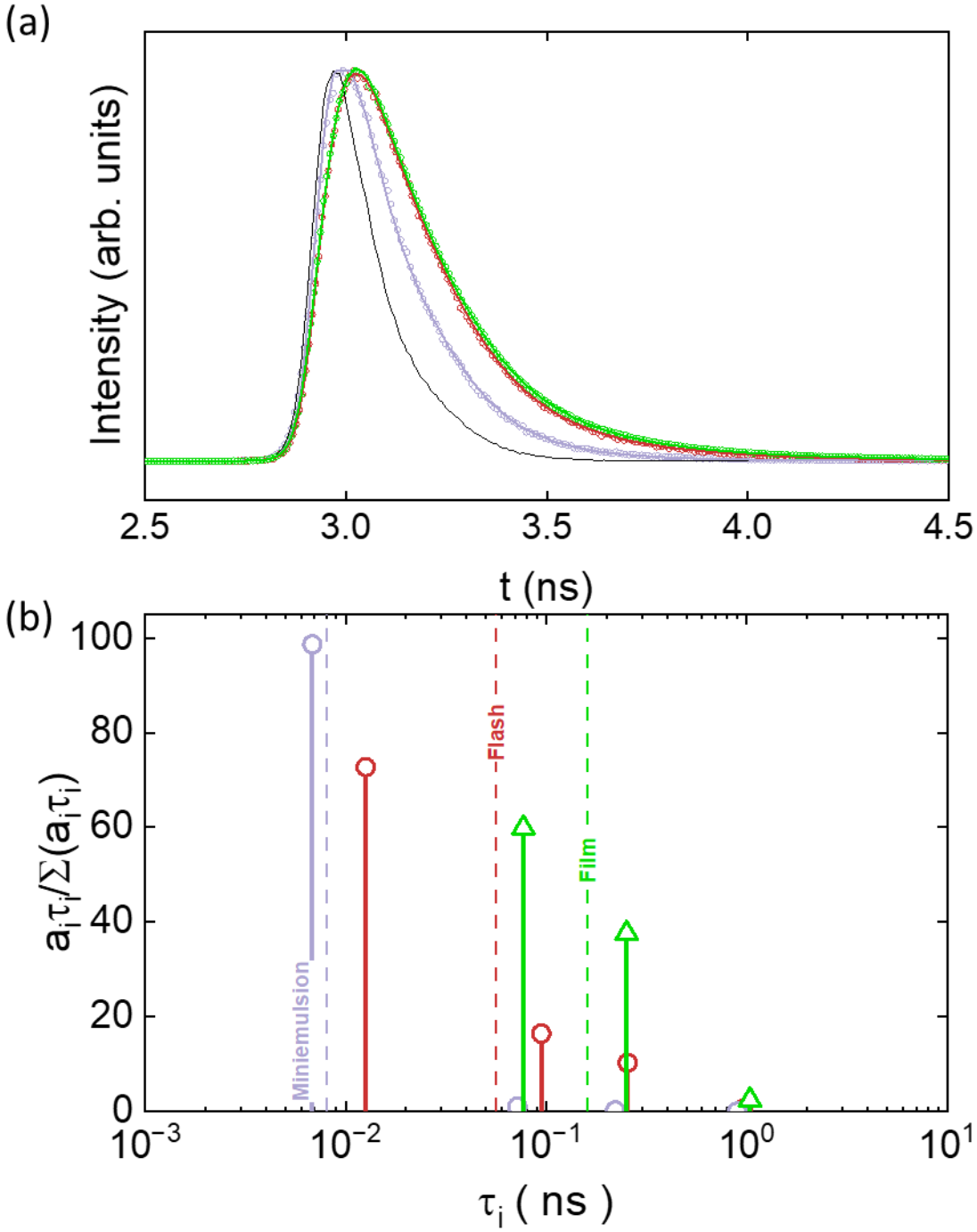

Figure 5.8. (a) Normalised fluorescence decays of P3HT NPs prepared by the flash technique (red symbols), the miniemulsion technique (purple symbols) and the thin film (green symbols) after excitation at 640 nm. The thick solid lines represent the fits obtained to the experimental data, using four exponential terms for the NPs and three exponential terms for the thin film. The thin black line represents the instrumental response function (IRF) of the instrument. **(b)** The resulting decay times (τ_i) and the normalised intensities, calculated from the pre-exponential coefficients (a_i), are presented for each of the systems studied. The same colour code as in (a) is used. The dashed lines indicate the averaged intensity

half-lives obtained from the fits, which allows a clear comparison of the fluorescence dynamics between the different samples.

Fluorescence lifetimes for each system depend on the type of NP, as it is observed in Figure 5.8 (a). This is a signature of differences in the deactivation mechanisms for the respective systems under investigation. Of particular interest is the rapid decay of the fluorescence observed for NPs prepared by miniemulsion, compared to flash NPs and the thin film. The analysis of the decay curves shown in Figure 5.8 (a) was performed by fitting the data to a combination of multiple exponential functions, reflecting the heterogeneity of the relaxation mechanisms. To facilitate comparison, and following the methodology of Ferrari et al.[36], the decay times were grouped into four characteristic regions:

-τ_1: Lifetimes longer than 1 ns, associated with long-lived excited states.

-τ_2: Times close to 0.2 ns, characteristic of de-excitation in ordered aggregates.

-τ_3: Times close to 0.1 ns, associated with relaxation of intermediate emissive states.

-τ_4: Times around 0.01 ns, indicative of ultrafast relaxation processes.

The photophysical behaviour of each system was characterised from these values and the relative contribution of each, as shown in Figure 5.8 (b). Firstly, analysis of the P3HT film, which has been extensively studied in the literature[37–39], shows that the shorter times (τ_4) do not make a significant contribution. Instead, the τ_2 and τ_3 components dominate, with a small contribution at long times (τ_1). These times have previously been associated with the decay of emissive states in ordered aggregates of P3HT,[39] i.e., the de-excitation of excitons confined in crystalline regions. In contrast, the fit for NPs shows a strong contribution from the τ_4 component, which represents the fastest de-excitation process. This de-excitation process is associated with the transition from a hot photoexcited state to a geometrically relaxed aggregate state[37]. Ghosh et al.[40] have suggested that in P3HT NPs dispersed in aqueous media, a considerable proportion of the polymer chain behaves as a hydrophobic material and adopts a coil-like structure, which favours faster de-excitation. This effect is particularly pronounced in NPs prepared by miniemulsion, where practically all the decay occurs by this process. This behaviour can be attributed to the enhanced interaction between the polymer chains in the NPs, facilitated by the presence of SDS. The presence of SDS in the medium stabilises the hydrophobic and hydrophilic arrangement of the polymer chains,

allowing the chromophores to be closer to each other than in the thin film and flash NPs, and consequently enhancing the efficiency in the transition from high-energy excited states to relaxed states. In flash prepared NPs, processes relaxing with longer lifetimes (τ_3 and τ_2) are also important. These processes have been associated with deexcitations of excitons trapped in crystalline regions, and excitons localised in structural defects[36,37].

The optical properties of NPs obtained by flash and miniemulsion methods exhibit notable disparities, suggesting variations in fluorescence lifetimes. The NPs prepared by miniemulsion primarily exhibit fluorescence decay related to the hopping transition to low-energy sites with a conformational planarization of the polymer backbone, resulting in shorter lifetimes[38,41]. In contrast, the fluorescence obtained by the flash method presents contributions from both short and long lifetimes. The fluorescence in flash NPs, therefore, decays via emissive states, attributable to exciton recombination, having lower efficiency in controlled energy transitions. These observations are consistent with the lower crystallinity observed by X-ray and a higher presence of defects observed in the weaker, less structured, and red shift in the emission spectrum in the NPs prepared by flash. In contrast, NPs prepared by miniemulsion exhibit higher intensity in the lower energy bands in the absorption spectrum, indicating a higher proportion of J-aggregates and higher delocalisation of excitons. The presence of J-aggregates in NPs prepared by miniemulsion favours energy transfer between polymer chains and non-radiative deactivation of excitons, explaining the lower weights of τ_3, τ_2 and τ_1 in their fluorescence decay. This is due to the fact that excitons can migrate through high crystallinity regions and become trapped in defects or impurities, which reduces the emission efficiency. Therefore, in NPs obtained by miniemulsion, it is hypothesised that the excited electrons migrate from the inner core of the particle to the external hydrophilic regions. This is consistent with other previous studies that have identified the formation of a reversible charge transfer complex between P3HT and molecular oxygen in the presence of water[42]. Furthermore, in P3HT solutions with electrolytes, it has been observed that the polymer can be polarised, reducing its energy levels, and thus modulating its optical and electronic response[43].

5.6. Conclusions

In summary, this chapter systematically compares the influence of two NP preparation methods, flash and miniemulsion, on the properties of P3HT NPs. A preliminary investigation into the comparison of the P3HT solutions (THF for flash and $CHCl_3$ for miniemulsion) revealed that $CHCl_3$ supports the formation of more extended polymer chains and THF presents few aggregates.

The results indicate that miniemulsion NPs exhibit a more homogeneous size distribution, higher crystallinity, and enhanced chain planarization (evidenced by optical characteristics such as a higher A_{0-0}/A_{0-1} ratio), leading to the predominance of J-aggregates and efficient non-radiative processes. Conversely, flash NPs show lower crystallinity and higher dispersity of sizes. These observations are related to less effective exciton dynamics and elevated rates of exciton recombination.

It is hypothesised that these structural and optical distinctions will have a significant effect on the photocatalytic performance of the NPs. In Chapter 7, the relationship between NP properties, including crystallinity, size, and aggregation, and their efficiency in degrading a model organic pollutant will be further explored.

5.7. Bibliography

(1) Sena-Fernández, J.; Rebollar, E.; Hurtado-Mendoza, A.; Murdoch, T. J.; Vega, J. F.; Martín-Fabiani, I.; Ezquerra, T. A.; Nogales, A. Tuning Photophysical Properties of Semiconducting Polymer Nanoparticles for Improved Photocatalytic Activity. *Nanoscale* **2025**. https://doi.org/10.1039/d5nr01699a.

(2) Gutiérrez-Fernández, E.; Cui, J.; Martínez-Tong, D. E.; Nogales, A. Preparation, Physical Properties, and Applications of Water-Based Functional Polymer Inks. *Polymers* **2021**, *13* (9). https://doi.org/10.3390/polym13091419.

(3) Gutiérrez-Fernández, E.; Ezquerra, T. A.; Rebollar, E.; Cui, J.; Marina, S.; Martín, J.; Nogales, A. Photophysical and Structural Modulation of Poly(3-Hexylthiophene) Nanoparticles via Surfactant-Polymer Interaction. *Polymer* **2021**, *218*. https://doi.org/10.1016/j.polymer.2021.123515.

(4) Nagarjuna, G.; Baghgar, M.; Labastide, J. A.; Algaier, D. D.; Barnes, M. D.; Venkataraman, D. Tuning Aggregation of Poly(3-Hexylthiophene) within Nanoparticles. *ACS Nano* **2012**, *6* (12), 10750–10758. https://doi.org/10.1021/nn305207b.

(5) Chen, J. H.; Li, J. Y.; Chen, L. C.; Su, C. I. Morphology and Microstructure of Aggregates and Gelation Behaviour of Poly (3-Hexylthiophene) in Xylene Solution. In *Applied Mechanics and Materials*; 2014; Vol. 479–480, pp 115–120. https://doi.org/10.4028/www.scientific.net/AMM.479-480.115.

(6) Böckmann, M.; Schemme, T.; De Jong, D. H.; Denz, C.; Heuer, A.; Doltsinis, N. L. Structure of P3HT Crystals, Thin Films, and Solutions by UV/Vis Spectral Analysis. *Physical Chemistry Chemical Physics* **2015**, *17* (43), 28616–28625. https://doi.org/10.1039/c5cp03665h.

(7) Chambon, S.; Schatz, C.; Sébire, V.; Pavageau, B.; Wantz, G.; Hirsch, L. Organic Semiconductor Core-Shell Nanoparticles Designed through Successive Solvent Displacements. *Mater Horiz* **2014**, *1* (4), 431–438. https://doi.org/10.1039/c4mh00021h.

(8) Holmes, N. P.; Nicolaidis, N.; Feron, K.; Barr, M.; Burke, K. B.; Al-Mudhaffer, M.; Sista, P.; Kilcoyne, A. L. D.; Stefan, M. C.; Zhou, X.; Dastoor, P. C.; Belcher, W. J. Probing the Origin of Photocurrent in Nanoparticulate Organic Photovoltaics. *Solar Energy Materials and Solar Cells* **2015**, *140*, 412–421. https://doi.org/10.1016/j.solmat.2015.04.044.

(9) MacHui, F.; Langner, S.; Zhu, X.; Abbott, S.; Brabec, C. J. Determination of the P3HT:PCBM Solubility Parameters via a Binary Solvent Gradient Method: Impact of Solubility on the Photovoltaic Performance. *Solar Energy Materials and Solar Cells* **2012**, *100*, 138–146. https://doi.org/10.1016/j.solmat.2012.01.005.

(10) Roesing, M.; Howell, J.; Boucher, D. Solubility Characteristics of Poly(3-Hexylthiophene). *Journal of Polymer Science Part B-Polymer Physics* **2017**, *55* (14), 1075–1087. https://doi.org/10.1002/polb.24364.

(11) Spano, F. C. The Spectral Signatures of Frenkel Polarons in H- And J-Aggregates. *Acc Chem Res* **2010**, *43* (3), 429–439. https://doi.org/10.1021/ar900233v.

(12) Ulum, S.; Holmes, N.; Darwis, D.; Burke, K.; David Kilcoyne, A. L.; Zhou, X.; Belcher, W.; Dastoor, P. Determining the Structural Motif of P3HT:PCBM Nanoparticulate Organic Photovoltaic Devices. *Solar Energy Materials and Solar Cells* **2013**, *110*, 43–48. https://doi.org/10.1016/j.solmat.2012.11.015.

(13) Colberts, F. J. M.; Wienk, M. M.; Janssen, R. A. J. Aqueous Nanoparticle Polymer Solar Cells: Effects of Surfactant Concentration and Processing on Device Performance. *ACS Appl Mater Interfaces* **2017**, *9* (15), 13380–13389. https://doi.org/10.1021/acsami.7b00557.

(14) Malvern Instruments. *Zeta Potential-Introduction in 30min*; 2015.

(15) Frangenberg, M.; Schmidt, A. M.; Wilkens, J. Impact of Surface Conductivity on the Zeta Potential Determination of Concentrated Aqueous Polymer Dispersions Using Electroacoustics and Electrokinetic Standard Models. *Colloid Polym Sci* **2024**. https://doi.org/10.1007/s00396-024-05301-7.

(16) Bhattacharjee, S. DLS and Zeta Potential - What They Are and What They Are Not? *Journal of Controlled Release* **2016**, *235*, 337–351. https://doi.org/10.1016/j.jconrel.2016.06.017.

(17) Barbosa, J. A. C.; Abdelsadig, M. S. E.; Conway, B. R.; Merchant, H. A. Using Zeta Potential to Study the Ionisation Behaviour of Polymers Employed in Modified-Release Dosage Forms and Estimating Their PKa. *Int J Pharm X* **2019**, *1*. https://doi.org/10.1016/j.ijpx.2019.100024.

(18) Brinkmann, M.; Rannou, P. Molecular Weight Dependence of Chain Packing and Semicrystalline Structure in Oriented Films of Regioregular Poly(3-Hexylthiophene)Revealed by High-Resolution Transmission Electron Microscopy. *Macromolecules* **2009**, *42* (4), 1125–1130. https://doi.org/10.1021/ma8023415.

(19) Millstone, J. E.; Kavulak, D. F. J.; Woo, C. H.; Holcombe, T. W.; Westling, E. J.; Briseno, A. L.; Toney, M. F.; Fréchet, J. M. J. Synthesis, Properties, and Electronic Applications of Size-Controlled

Poly(3-Hexylthiophene) Nanoparticles. *Langmuir* **2010**, *26* (16), 13056–13061. https://doi.org/10.1021/la1022938.

(20) Chang, M.; Choi, D.; Fu, B.; Reichmanis, E. Solvent Based Hydrogen Bonding: Impact on Poly(3-Hexylthiophene) Nanoscale Morphology and Charge Transport Characteristics. *ACS Nano* **2013**, *7* (6), 5402–5413. https://doi.org/10.1021/nn401323f.

(21) Aiyar, A. R.; Hong, J. Il; Nambiar, R.; Collard, D. M.; Reichmanis, E. Tunable Crystallinity in Regioregular Poly(3-Hexylthiophene) Thin Films and Its Impact on Field Effect Mobility. *Adv Funct Mater* **2011**, *21* (14), 2652–2659. https://doi.org/10.1002/adfm.201002729.

(22) Wu, Z.; Petzold, A.; Henze, T.; Thurn-Albrecht, T.; Lohwasser, R. H.; Sommer, M.; Thelakkat, M. Temperature and Molecular Weight Dependent Hierarchical Equilibrium Structures in Semiconducting Poly(3-Hexylthiophene). *Macromolecules* **2010**, *43* (10), 4646–4653. https://doi.org/10.1021/ma902566h.

(23) Agbolaghi, S.; Zenoozi, S. A Comprehensive Review on Poly(3-Alkylthiophene)-Based Crystalline Structures, Protocols and Electronic Applications. *Org Electron* **2017**, *51*, 362–403. https://doi.org/10.1016/j.orgel.2017.09.038.

(24) Müller-Buschbaum, P. The Active Layer Morphology of Organic Solar Cells Probed with Grazing Incidence Scattering Techniques. *Advanced Materials* **2014**, *26* (46), 7692–7709. https://doi.org/10.1002/adma.201304187.

(25) Newbloom, G. M.; Kim, F. S.; Jenekhe, S. A.; Pozzo, D. C. Mesoscale Morphology and Charge Transport in Colloidal Networks of Poly(3-Hexylthiophene). *Macromolecules* **2011**, *44* (10), 3801–3809. https://doi.org/10.1021/ma2000515.

(26) Clark, J.; Silva, C.; Friend, R. H.; Spano, F. C. Role of Intermolecular Coupling in the Photophysics of Disordered Organic Semiconductors: Aggregate Emission in Regioregular Polythiophene. *Phys Rev Lett* **2007**, *98* (20). https://doi.org/10.1103/PhysRevLett.98.206406.

(27) Manas, E. S.; Spano, F. C. Absorption and Spontaneous Emission in Aggregates of Conjugated Polymers. *J Chem Phys* **1998**, *109* (18), 8087–8101. https://doi.org/10.1063/1.477457.

(28) Clark, J.; Chang, J. F.; Spano, F. C.; Friend, R. H.; Silva, C. Determining Exciton Bandwidth and Film Microstructure in Polythiophene Films Using Linear Absorption Spectroscopy. *Appl Phys Lett* **2009**, *94* (16). https://doi.org/10.1063/1.3110904.

(29) Spano, F. C.; Silva, C. H- and J-Aggregate Behavior in Polymeric Semiconductors. *Annu Rev Phys Chem* **2014**, *65*, 477–500. https://doi.org/10.1146/annurev-physchem-040513-103639.

(30) Schwarz, K. N.; Farley, S. B.; Smith, T. A.; Ghiggino, K. P. Charge Generation and Morphology in P3HT : PCBM Nanoparticles Prepared by Mini-Emulsion and Reprecipitation Methods. *Nanoscale* **2015**, *7* (47), 19899–19904. https://doi.org/10.1039/c5nr06244f.

(31) Tan, B.; Li, Y.; Palacios, M. F.; Therrien, J.; Sobkowicz, M. J. Effect of Surfactant Conjugation on Structure and Properties of Poly(3-Hexylthiophene) Colloids and Field Effect Transistors. *Colloids Surf A Physicochem Eng Asp* **2016**, *488*, 7–14. https://doi.org/10.1016/j.colsurfa.2015.10.002.

(32) Saifuddin, M.; Mukhopadhyay, M.; Biswas, A.; Gigli, L.; Plaisier, J. R.; Hazra, S. Tuning the Edge-on Oriented Ordering of Solution-Aged Poly(3-Hexylthiophene) Thin Films. *J Mater Chem C Mater* **2020**, *8* (26), 8804–8813. https://doi.org/10.1039/d0tc02031a.

(33) Tauc, J.; Grigorovici, R.; Vancu, A. Optical Properties and Electronic Structure of Amorphous Germanium. *Physica Status Solidi* **1966**, *15* (2), 627. https://doi.org/10.1002/pssb.19660150224.

(34) Zhu, H.; Gong, L.; Li, Z. Construction and Mechanism of a Novel Z-Scheme Photocatalyst α-Fe2O3/P3HT with O-Ti-O for Organic Pollutant Degradation under Visible Light. *Appl Surf Sci* **2020**, *505*. https://doi.org/10.1016/j.apsusc.2019.144639.

(35) Makuła, P.; Pacia, M.; Macyk, W. How To Correctly Determine the Band Gap Energy of Modified Semiconductor Photocatalysts Based on UV-Vis Spectra. *J Phys Chem Lett* **2018**, *9* (23), 6814–6817. https://doi.org/10.1021/acs.jpclett.8b02892.

(36) Ferreira, B.; Da Silva, P. F.; Seixas De Melo, J. S.; Pina, J.; MaçAnita, A. Excited-State Dynamics and Self-Organization of Poly(3-Hexylthiophene) (P3HT) in Solution and Thin Films. *J Phys Chem B* **2012**, *116* (8), 2347–2355. https://doi.org/10.1021/jp207418q.

(37) Parkinson, P.; Müler, C.; Stingelin, N.; Johnston, M. B.; Herz, L. M. Role of Ultrafast Torsional Relaxation in the Emission from Polythiophene Aggregates. *J Phys Chem Lett* **2010**, *1* (19), 2788–2792. https://doi.org/10.1021/jz101026g.

(38) Banerji, N.; Cowan, S.; Vauthey, E.; Heeger, A. J. Ultrafast Relaxation of the Poly(3-Hexylthiophene) Emission Spectrum. *J Phys Chem C* **2011**, *115* (19), 9726–9739. https://doi.org/10.1021/jp1119348.

(39) Cook, S.; Furube, A.; Katoh, R. Analysis of the Excited States of Regioregular Polythiophene P3HT. *Energy Environ Sci* **2008**, *1* (2), 294–299. https://doi.org/10.1039/b805643a.

(40) Ghosh, S.; Chakraborty, S.; Ghosh, A.; Marjit, K.; Ghosh, G.; Patra, A. Ultrafast Relaxation Dynamics of Conjugated Polymer Nanoparticles by Tuning Their Interchain Interactions. *J Phys Chem C* **2022**, *126* (42), 18177–18187. https://doi.org/10.1021/acs.jpcc.2c06093.

(41) Banerji, N.; Cowan, S.; Leclerc, M.; Vauthey, E.; Heeger, A. J. Exciton Formation, Relaxation, and Decay in PCDTBT. *J Am Chem Soc* **2010**, *132* (49), 17459–17470. https://doi.org/10.1021/ja105290e.

(42) Bellani, S.; Fazzi, D.; Bruno, P.; Giussani, E.; Canesi, E.; Lanzani, G.; Antognazza, M. R. Reversible P3HT/Oxygen Charge Transfer Complex Identification in Thin Films Exposed to Direct Contact with Water. *J Phys Chem C* **2014**, *118* (12), 6291–6299. https://doi.org/10.1021/jp4119309.

(43) Mosconi, E.; Salvatori, P.; Saba, M. I.; Mattoni, A.; Bellani, S.; Bruni, F.; Santiago Gonzalez, B.; Antognazza, M. R.; Brovelli, S.; Lanzani, G.; Li, H.; Brédas, J. L.; De Angelis, F. Surface Polarization Drives Photoinduced Charge Separation at the P3HT/Water Interface. *ACS Energy Lett* **2016**, *1* (2), 454–463. https://doi.org/10.1021/acsenergylett.6b00197.

Chapter 6

Development of polar phases in PVDF deposits and NPs

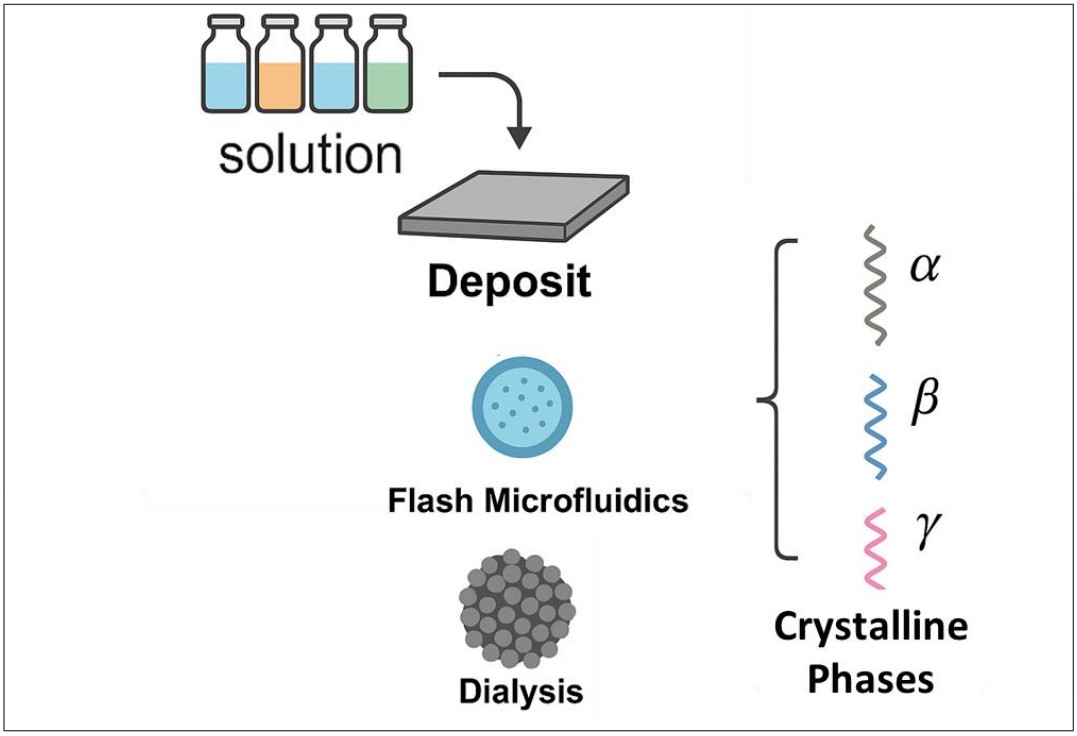

Graphical abstract representing the main idea of Chapter 6

Universidad Complutense de Madrid

Jose Sena Fernández

Micro and Nanoparticles of Functional Polymers: From Fundamentals to Applications

As outlined in Section 1.5.2, the crystalline phase composition of PVDF is strongly influenced by processing conditions, particularly the choice of solvent, which governs chain conformation and nucleation pathways[1–3]. Previous studies have shown that solvent properties can bias crystallisation towards either non-polar α-phase or electroactive β/γ-phases[2-4], with most reports focusing on bulk films or specific NP preparation routes. However, a systematic, side-by-side comparison of bulk deposits and water-dispersed NPs prepared under controlled and comparable solvent conditions is still lacking.

This chapter aims to address this knowledge gap by systematically exploring the role of diverse solvents in the preparation of both bulk PVDF deposits (via solvent casting) and water-dispersed PVDF NPs (via dialysis and flash microfluidics). The objective is to provide fundamental insights into the decisive role of the solvent in dictating ferroelectric phase formation under comparable processing conditions, thereby advancing the field of PVDF polymorphism control at the nanoscale. Following this thread, the chapter is organised as follows:

-Section 6.1 reviews the properties of the solvents used.

-Section 6.2 presents the influence of these properties on the phases of PVDF prepared in bulk as deposits.

-Section 6.3 examines the solvent effect on NP characteristics.

-Section 6.4 compares deposits and NPs to assess the role of solvent–antisolvent transition in phase formation.

-Section 6.5 summarises the conclusions.

6.1. Evaluation of solvent properties for PVDF crystallisation

For this study, solvents in which the polymer is soluble[5–7] have been selected based on the work carried out by Marshall et al.[5], Chan et al.[6], and Bottino et al.[7]. Solvents such as ethanol, methanol and acetone, which are known as "green solvents", have also been used[8,9], all of which are miscible with water. Table 6.1 presents a compilation of different properties of the solvents that may have a role in the development of polar phases of PVDF, including polarity, measured through the dipole moment and dielectric constant; boiling point; and

solubility as determined by the Hansen solubility parameter (R_a). The following properties will be explained in order to determine the reason for the selection of these parameters as variables for consideration:

Table 6.1. Physicochemical properties of various organic solvents: boiling points (T_b), Hansen solubility parameter by R_a[6], dipole moments (μ) in Debyes and dielectric constant (ε_r) at 25ºC. Solvent acronyms: PC: Propylene Carbonate; DMSO: Dimethyl Sulfoxide; DMA: N,N-Dimethylacetamide; MEK: Methyl Ethyl Ketone; THF: Tetrahydrofuran.

Solvent	T_b (ºC)	R_a (MPa$^{1/2}$)	μ (D)	ε_r at 25ºC
PC	242[10]	11.9[11–13]	5.16[14,15]	66.0[15,16]
DMSO	189[17,18]	4.54[12,13,19]	4.00[14,17]	46.9[17]
DMA	165[17]	1.15[12,13,19]	3.73[14,17]	37.8[17]
Acetone	56.0[17]	5.16[11–13]	2.88[20,21]	20.7[17]
MEK	80.0[17]	9.00[12,13]	2.77[14,17]	18.5[17]
EG	197[10]	33.6[12,13]	2.20[22]	37.7
THF	66.0[17,23]	7.22[12,13,19]	1.74[14,17]	7.50[17,24]
MetOH	64.8[17,25]	26.3[12,13,19]	1.70[18,26]	32.7[17]
EtOH	78.0[27]	20.8[12,13,19]	1.69[14,26]	24.8[17,28,29]
FA	101[30]	10.3[12,13]	1.41[31,32]	58.3[30]

- Boiling temperature: The temperature at which the solvent state changes from liquid to vapour at ambient pressure. It depends on several aspects like intermolecular forces, such as hydrogen bonds, Van der Waals forces and dipole-dipole interactions, and chemical composition[33–36].
- Solubility: As outlined in Section 1.2, the solubility of a polymer in a solvent is determined by the distance on the three-dimensional HSP sphere, as defined by Equation 1.6. The equation considers the tendency of each component to form dipolar interactions, dispersion forces or hydrogen bonds. The closer these values are between the two components, the lower the value of *Ra* and the greater the theoretical solubility of the solute in the solvent.

  In the case of PVDF has a high dipole moment due to the highly electronegative C-F bonds. In general, solvents with high dipole moments interact more readily with these polar regions of PVDF, helping to break intermolecular

interactions, such as dipole-dipole or hydrogen bonds, within the polymer, allowing the chains to separate and the polymer to dissolve. Consequently, the determination of R_a facilitates the identification of the most suitable solvent for dissolution, i.e., the solvent that presents the most favourable interactions, thereby enabling the understanding of the phase formation process of PVDF.

- Polarity: Polarity in a molecule is defined by the uneven distribution of electron density[35,37]. In a covalent bond, this means that one atom is attracting the shared electrons more strongly than the other atom, resulting in a negative partial charge on the more electronegative atom and a positive partial charge on the other. This charge separation leads to the formation of an electric dipole[10], a concept of significant importance in molecular behaviour. For instance, polar molecules with distinct positively and negatively charged centres can interact effectively with other polar and ionic species. In the context of solvents, polarity refers to the ability to solvate and stabilise charges, thereby significantly impacting their capacity to dissolve various substances[35,37]. A polar solvent establishes strong electrostatic interactions with polar solute molecules. Two of the most widely used parameters to quantify solvent polarity are:
    1. Dipole moment: The dipole moment (μ) is a quantitative measure of the charge separation within a molecule, determined by the difference in electronegativity between atoms and the molecular geometry[3,10,35,37]. It is represented as a vector pointing from the positive charge to the negative charge, and is defined as the product of the charge difference (δ) and the distance (d) between them, typically measured in Debye (D):

$$\mu = \delta \times d \qquad \text{Eq. 6.1}$$

    Therefore, the dipole moment of a solvent could impact its effectiveness in dissolving polar compounds via electrostatic interactions between the solvent and solute. In the case of PVDF, the solvent polarity plays a crucial role in determining the molecular conformation of the chains in solution, which may affect the formation of the α, β, and γ crystalline phases upon solvent evaporation.
    2. Dielectric constant: The dielectric constant (denoted as ε or ε_r), also known as relative permittivity, is a dimensionless parameter that

quantifies the ability of a material to attenuate the strength of the electric field between two oppositely charged ions compared to a vacuum[38–40]. It is a bulk property that represents the ability of a solvent to reduce the effective electrostatic interactions between charged or polar species. The density and the polarizability of the solvent molecules influence this property[41], and it is defined as the ratio of the permittivity of the solvent (ε) to the permittivity of free space (ε_0)[39]:

$$\varepsilon_r = \frac{\varepsilon}{\varepsilon_0} \qquad \text{Eq. 6.2}$$

A higher dielectric constant indicates the capacity of a solvent to effectively stabilise and solvate ionic or polar species by reducing the electrostatic forces between them, thus enhancing their solubility. In summary, solvents with higher dielectric constants tend to be more polar. In the context of PVDF crystallisation, similarly to what was explained above in relation to the dipole moment, the dielectric constant could influence the strength of solvent–polymer interactions, thereby affecting the conformation of the polymer chains during dissolution and the stabilisation of specific polymer conformations during crystallisation from solution.

6.2. Solvent effects on the morphology and crystallisation of free-standing PVDF deposits

As previously outlined, deposits have been prepared by drop casting using the solvents described in Table 6.1. The concentration of the deposits was 50 g /L.

Figure 6.1 shows a photograph of deposits prepared from casting PVDF solutions in different solvents (DMSO, DMA, MEK, THF and MetOH); their appearance is substantially different. Samples such as MetOH, EtOH or EG, which exhibit high values of R_a (see Table 6.1), require temperature to facilitate the dissolution of PVDF, as they act as swelling agents, and it is necessary to break the Van der Waals forces and weak hydrogen bonds that hold

the chains together[7,42]. The crystallisation of PVDF and the identification of the predominant phases have been studied through XRD (WAXS) (see section 2.4.1) and FTIR (see section 2.4.5).

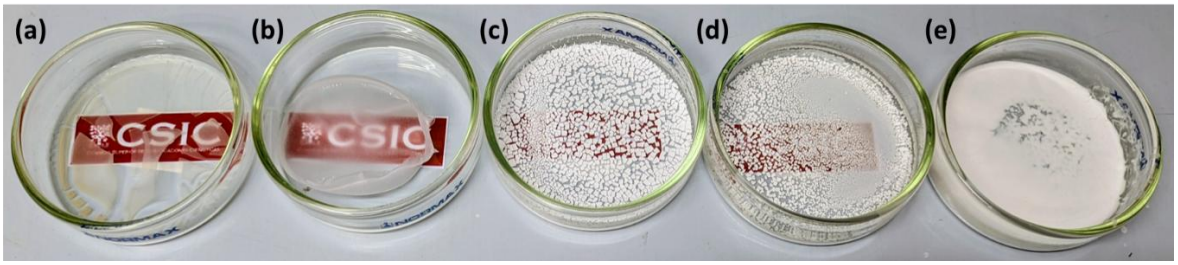

Figure 6.1. Differences in the appearance of deposits prepared using: (a) DMSO, (b) DMA, (c) MEK, (d) THF and (e) MetOH.

6.2.1. Impact of solvent properties on the developed crystalline phases of PVDF deposits

Figure 6.2 shows X-ray diffractograms for deposits of PVDF prepared from solution in selected solvents listed in Table 6.1.

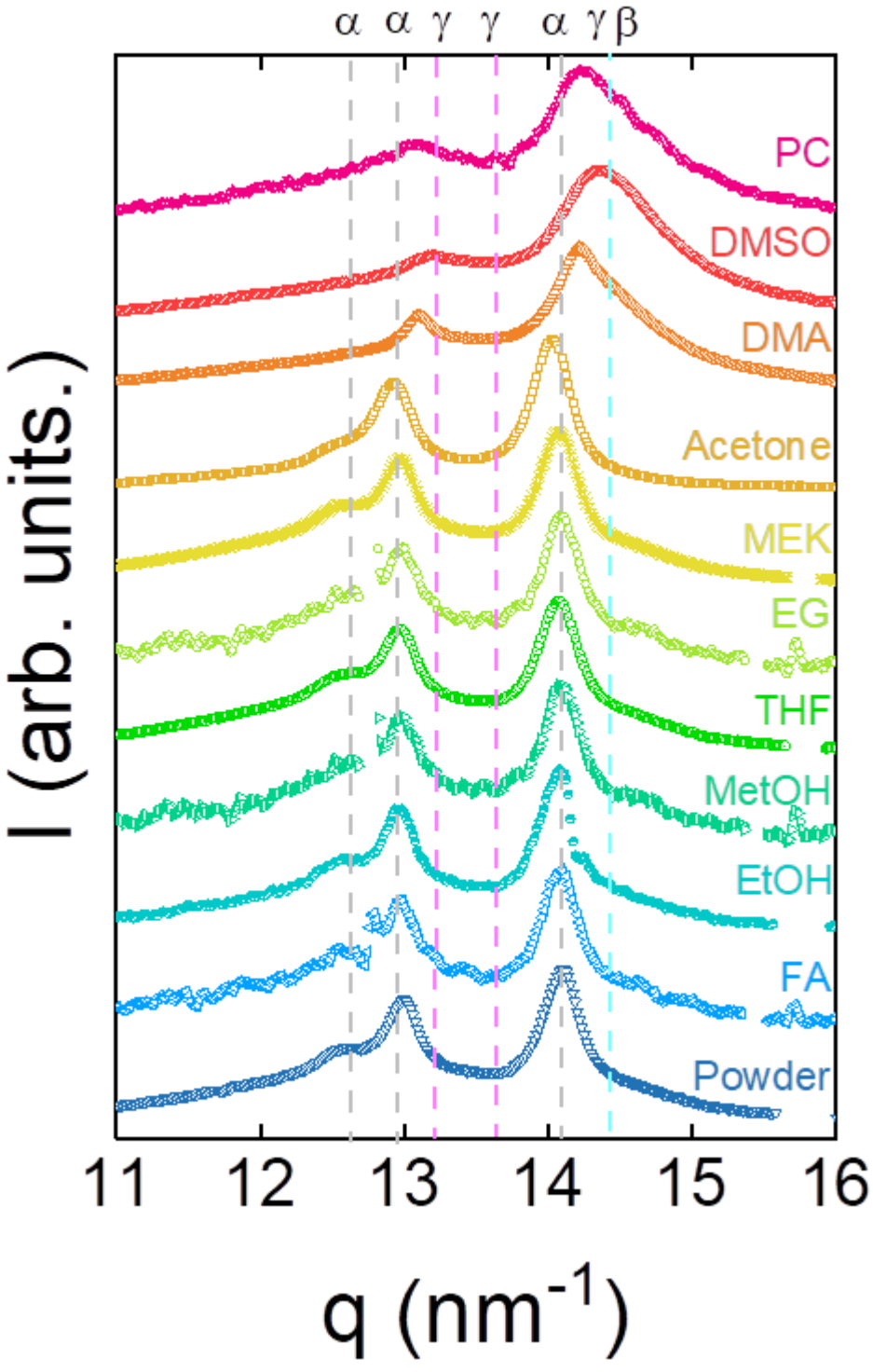

Figure 6.2. Diffraction patterns obtained for PVDF deposits prepared by free-standing using different solvents, as indicated by the labels in the scattering vector (q) range from 11 to 16 nm^{-1}. The label powder refers to the PVDF powder as received. The identified crystalline phases, indicated by dotted lines, correspond to α (grey), γ (pink) and β (blue). Each diffractogram was baseline

corrected to zero intensity and then normalised to the intensity of the most intense peak located between 14.10 and 14.25 nm^{-1}. The spectrum was then separated by 0.6 units.

Diffraction patterns presented in Figure 6.2 demonstrate that the solvent does indeed affect the PVDF phase, resulting in variations in the position and ratio of the intensity maxima. In general, all the diffraction patterns exhibit similar features, with Bragg peaks around 13-13.3 nm^{-1} and 14.1-14.45 nm^{-1}.[2,4,43–45] However, some differences are observed, like the presence of a shoulder at 12.5 nm^{-1} in some samples or clear variations of the central position of the Bragg maxima. Figure 6.2 dotted lines indicate the reported positions for the α, β and γ crystalline phases of PVDF. A detailed description of the crystallographic positions in *q* of the different PVDF crystalline phases is presented in Table 6.2. The observed variations in the positions of the Bragg maxima could indicate a more significant presence of each of those phases. In addition, it is possible to obtain qualitative information on crystallinity. In Figure 6.2, there is a loss of resolution of the maxima, which results in them becoming less defined and wider when transitioning from FA to PC. This finding suggests that the deposits under study are less crystalline and exhibit a greater amorphous contribution[46].

Table 6.2. Position in *q* (nm^{-1}) of the different reflections with their respective Miller indexes and the corresponding crystalline phase. The bibliographical references used for indexing are indicated in the last column.

q (nm^{-1})	Phase/s	*hkl*	References
12.65-12.75	α	100	2,43–45,47,48
12.95-13.05	α	020	2,6,43–45,47–52
13.30-13.40	γ	020	2,43–45,48,49
13.70-13.80	γ	002	2,43–45,47,48
14.05-14.15	α γ	110	2,6,43–45,47–51,53
14.46-14.56	β γ	β: 200/110 γ: 021/101	2,43–45,47–51,53

In order to obtain an estimation of the proportion of each crystalline phase for PVDF deposits prepared using different solvents, a fit of the diffractograms is required in terms of contributions of the different crystalline phases. Figure 6.3 presents an example of different

fits for distinct samples with varying contributions from each phase. The fit of XRD patterns was performed by modelling the amorphous halo using pseudo-Voigt functions, which better account for both instrumental broadening (Gaussian) and sample-induced effects (Lorentzian), while the crystalline peaks were adjusted with Lorentzian functions, suitable for isolated Bragg reflections in semi-crystalline polymers[54–56].

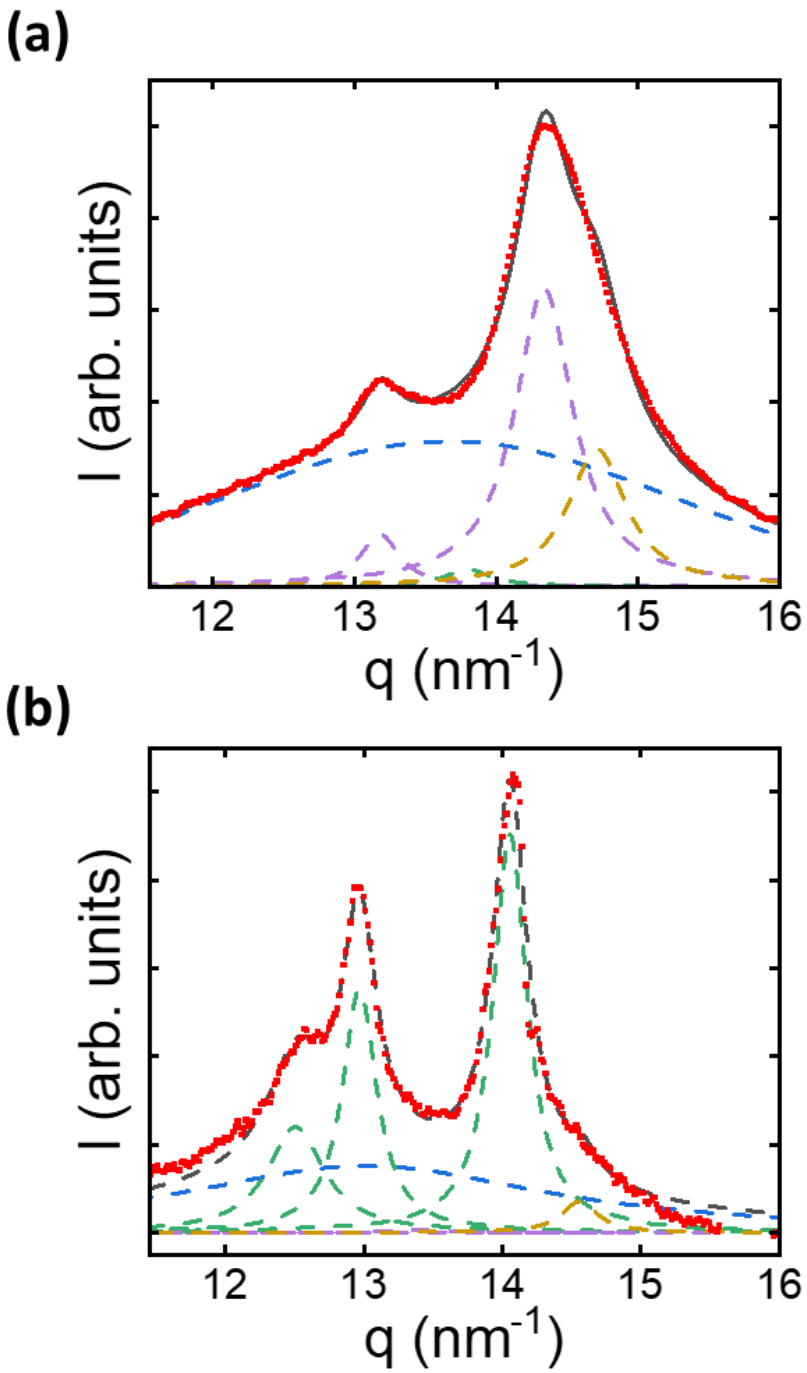

Figure 6.3. Representative examples of the fitted XRD patterns for the analysis of amorphous and crystalline phases in PVDF. Red symbols represent

experimental points. The black lines correspond to the fits obtained by summing the individual contributions of the amorphous halo (blue), the reflections of the α phase (green), the β phase (yellow) and the γ phase (purple). Panels show PVDF deposits prepared using **(a)** DMSO and **(b)** EtOH as solvents. The amorphous halos were modelled using Voigt functions, while crystalline peaks were fitted using Lorentzian profiles. It should be noted that the quality of the fit may vary depending on the complexity of the pattern and the relative contribution of each crystalline phase.

From each fit, the ratio between the area corresponding to the Bragg peaks of each phase and the amorphous halo can be used to quantify fractions of each phase. In this way, one can define the fraction of electroactive phase (χ_{EA}) or the fraction of α phase (χ_{α}) as described in Eq. 6.3 and 6.4.

$$\chi_{EA} = \frac{A_\beta + A_\gamma}{A_\alpha + A_\beta + A_\gamma} \times 100 \qquad \text{Eq. 6.3}$$

$$\chi_{\alpha} = 100 - \chi_{EA} \qquad \text{Eq. 6.4}$$

where the A_α, A_β, and A_γ are the sum of the areas in the diffractogram corresponding to each maximum of associated the α, β, and γ, respectively.

6.2.2. Influence of solvent on the chain conformation in PVDF deposits: A quantitative FTIR spectroscopic study

Figure 6.4 presents the FTIR spectra for PVDF deposits prepared from solutions in the selected solvents listed in Table 6.1. FTIR results show different spectral signatures for deposits prepared from different solvents. Precisely, FTIR spectra exhibit differences in intensity for the characteristic bands of the different crystalline phases of PVDF[43,57].

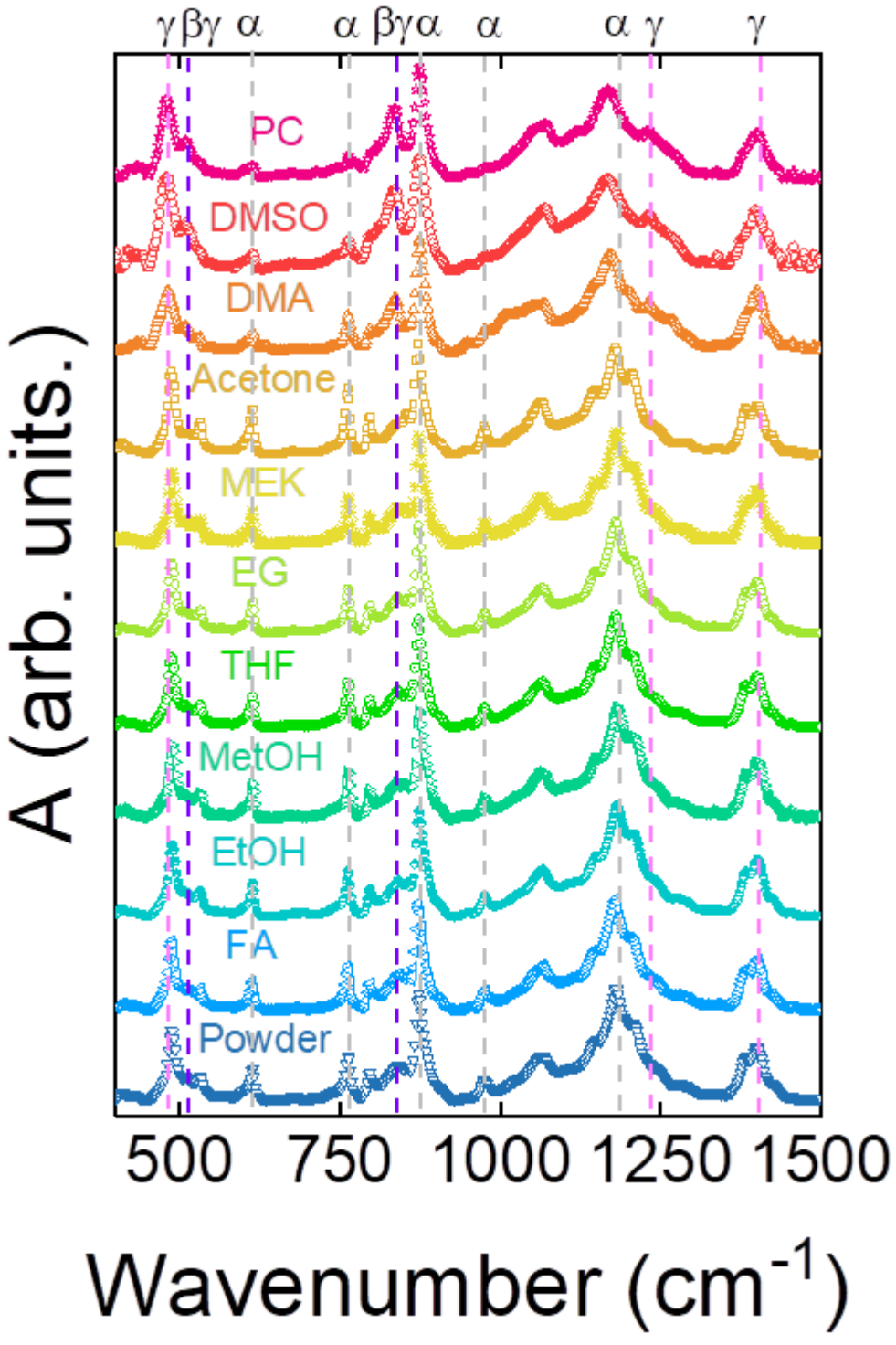

Figure 6.4. Normalised Infrared (IR) spectra of the samples prepared by drop casting deposition from solution in different solvents, indicated by the labels. The spectra labelled as powder correspond to the PVDF sample as received. All spectra have been baseline-corrected and normalised to the intensity of the most prominent absorption band at 873 cm^{-1} to facilitate comparison. A vertical offset

of 0.9 absorbance units has been applied between successive spectra for clarity. The characteristic vibrational bands of the main crystalline phases are marked by dotted lines: α: grey, γ: pink, β and γ: purple.

As observed in Figure 6.4, deposits prepared using PC, DMSO, or DMA exhibit strong absorption bands at approximately 480 cm^{-1} and 1230 cm^{-1}, which are associated with the γ phase. Furthermore, the bands at 510 cm^{-1} and 835 cm^{-1} that are clearly visible in the samples prepared from solution in PC, DMSO and DMA, are associated with the electroactive phases β and γ. It is important to note that many of the IR bands coincide for the β and γ phases due to their *TTT* conformation present in both phases[52]. On the contrary, the bands at 874 cm^{-1}, 975 cm^{-1}, and 1185 cm^{-1}, in these three samples, present lower intensity than in all the other samples. These bands are associated with the non-polar α phase[43,57].

To quantitatively assess these spectral changes, the analysis focuses on the contributions of the electroactive phases (β and γ) by establishing the intensity ratio between the band related to the electroactive phase (840 cm^{-1}) and the band associated with the α phase (763 cm^{-1}) (Figure 6.5), within the same vibrational mode[58–61]. This relationship is expressed by the following equation, explained by Gregorio[61,62]:

$$\Phi_{EA} = \frac{I_{840}}{\frac{K_{840}}{K_{763}} \times I_{763} + I_{840}} \times 100 \qquad \text{Eq. 6.5}$$

$$\Phi_{\alpha} = 100 - \Phi_{EA} \qquad \text{Eq. 6.6}$$

where Φ_{EA} and Φ_{α} in Equations 6.5 and 6.6 are representative of the fraction of the electroactive and α phases, I_{840} is the intensity of the band corresponding to 840 cm^{-1}, I_{763} is the intensity at 763 cm^{-1}, and K_{840} = 7.7x10^4 cm^2/mol and K_{763} = 6.1x10^4 cm^2/mol are the absorption constants at the corresponding wavenumber[60,61,63,64]. These results underscore the critical role of the solvent in modulating the phase composition of PVDF deposits, offering insights into how solvent properties affect the molecular ordering of the material, as described below.

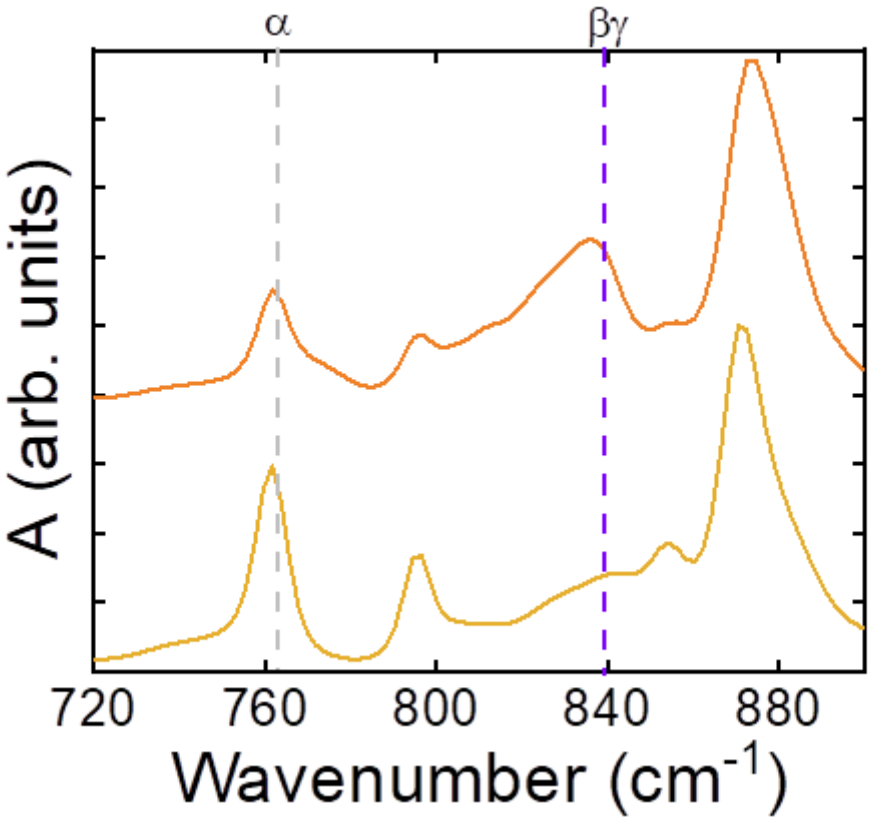

Figure 6.5. IR spectra in the 720-900 cm^{-1} wavenumber region of a PVDF sample prepared from DMA (orange) and acetone (yellow), highlighting the characteristic bands of the non-electroactive (α, grey dashed line) and electroactive (β and γ, purple dashed line) phases. All spectra have been baseline-corrected and normalised to the intensity of the most prominent absorption band at 873 cm^{-1} to facilitate comparison. A vertical offset of 0.8 absorbance units has been applied between successive spectra for clarity.

6.2.3. Influence of solvent properties on the crystalline phase formation of PVDF: role of the boiling point, solubility and polarity

The degree of crystallinity was determined from XRD data by comparing the area of the amorphous halo with the total diffractogram area. For example, Figure 6.3 shows that NPs prepared in DMSO exhibit a crystallinity of 38%, whereas those obtained in EtOH reach 58%. Furthermore, significant variations in the polar phase content are observed when changing the solvent. Figure 6.6 depicts the fractions of the different crystalline phases estimated by both XRD and FTIR for NPs prepared in different solvents. The trends

observed with both techniques are consistent, confirming the solvent-dependent formation of polar phases.

Figure 6.6 (a) shows the dependency of the fraction of electroactive phase on the solubility in the form of R_a. The results indicate an apparent lack of correlation with PVDF crystalline phase formation, suggesting that this property exerts a less direct influence on polymer chain organisation during the crystallisation process. It is important to note that, in contrast to the findings of Kumar et al.[65], which demonstrated that better Hansen parameters resulted in more electroactive phases in thin films, the results of this study indicate that, in the studied solvents, solubility does not significantly influence the formation of the desired phases. This apparent discrepancy stems from the fundamental difference in the crystallization mechanisms employed. The study by Kumar et al.[65] utilized the Langmuir technique, where PVDF chains crystallize at the air-water interface. In this process, the organization and packing of polymer chains are governed by a combination of interfacial interactions, surface pressure, and solvent spreading properties. Conversely, deposits prepared in this Thesis involve crystallization from solution, a bulk process where the key determinant is the interaction between the polymer chains and the solvent molecules themselves. Consequently, all solvents are considered suitable for the study.

Figure 6.6 (b) presents the relationship between the fraction of the electroactive phase and the boiling point of the solvent. As shown in Figure 6.6 (b), the fraction of electroactive phase is larger for the solvents with higher boiling temperature, except for EG. This fact can be related to the process of evaporation, a solvent with a higher boiling point evaporates more slowly, which may allow for a longer rearrangement time of the PVDF chains. This phenomenon may potentially favour crystallisation in the electroactive phase. Chinaglia et al.[66] reported that highly polar solvents can induce a β or γ polar phase in PVDF films, but this seems to occur only in micrometre-thick films, and the fraction of polar phase is highly dependent on the evaporation rate of the solvent. However, Zhang et al.[67] used a low-boiling-point solvent, such as acetone, to favour the β-phase by electrospinning.

A clear trend is observed in the case of the dipolar moment (Figure 6.6 (c)), indicating that the more polar the solvent, the higher the percentage of the electroactive phase, especially from a value of 2.8 D, which coincides with the dipole moment of the electroactive phases (2.1 D)[1]. This finding is consistent with the results reported by other research groups in the context of film preparation[2,6,50,52,53]. While there is a consensus that the polar phases of PVDF are favoured in the presence of polar solvents, the crystallisation of the phases as a function of the polarity of the solvent has not been studied in depth[50,52,68]. However, it should

be noted that crystallisation does not necessarily have to depend solely on one parameter. It is hypothesised that in more polar solvents, the strong dipole-dipole interactions between the solvent and the -CF_2- groups of PVDF may stabilise this conformation, reducing the chain energy in electroactive conformations[1,2,42].

A slight trend is also observed in the case of the dielectric constant (Figure 6.6 (d)). The dielectric constant of the solvent appears to influence the composition of the electroactive phase, with higher dielectric constant solvents resulting in a greater proportion of the electroactive phase, excluding FA. The high dielectric constant of the solvent is indicative of its greater ability to stabilise partial charges. In the case of PVDF, this facilitates the formation of interactions that stabilise the electroactive phases.

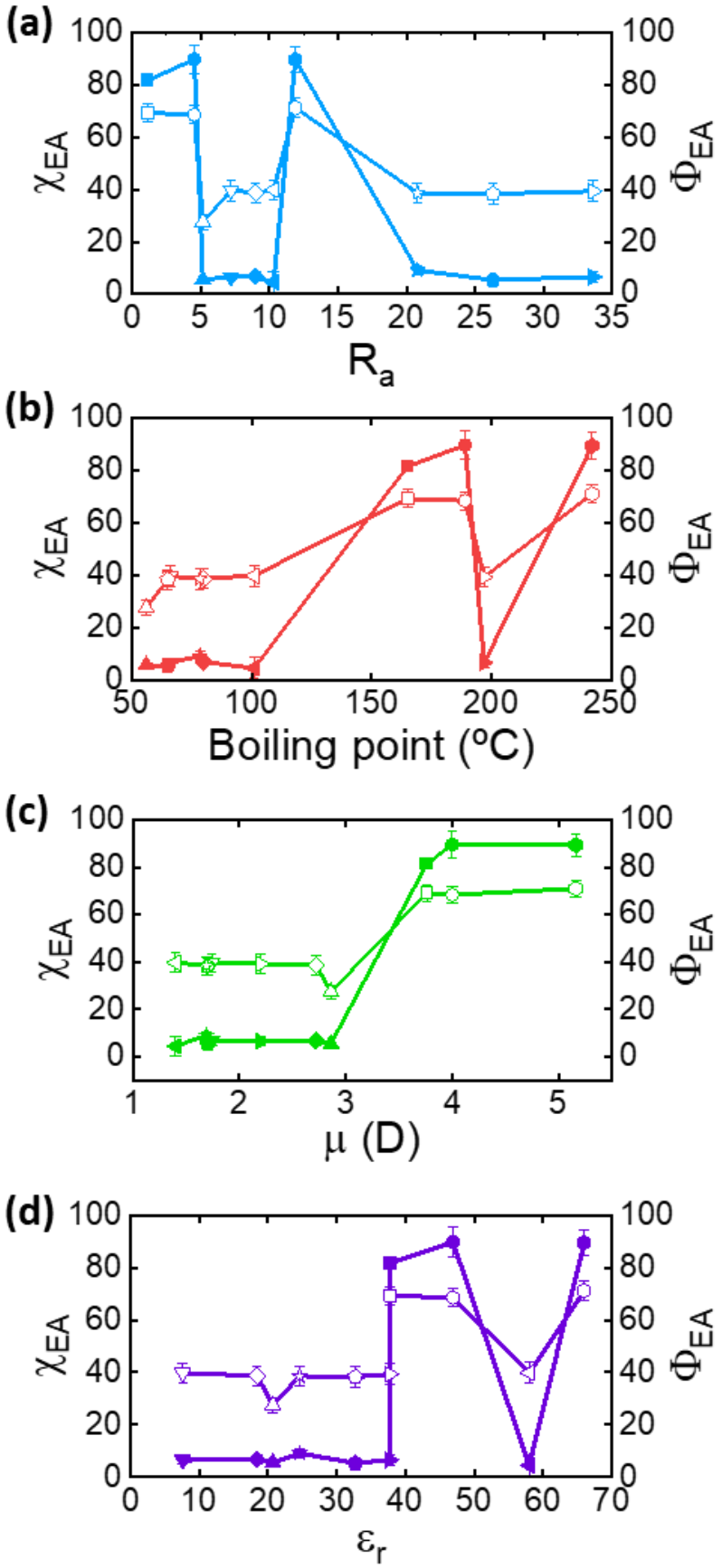
(a)
χEA
ΦEA
Ra
(b)
χEA
ΦEA
Boiling point (ºC)
(c)
χEA
ΦEA
μ (D)
(d)
χEA
ΦEA
εr

Figure 6.6. Variation of the percentage of electroactive phase as a function of different properties of the solvents obtained by XRD (filled symbols) and FTIR (empty symbols): **(a)** solubility (R_a), **(b)** boiling temperature, **(c)** dipole moment and **(d)** dielectric constant. Solvents are represented by the following symbols: DMA (square), DMSO (circle), acetone (triangle), THF (inverted triangle), MEK (rhombus), FA (left-facing triangle), PC (hexagon), EtOH (star), MetOH (pentangle), EG (right-facing triangle). The PVDF in powder form has a χ_{EA} value of 7.7 and Φ_{EA} value of 39.

6.3. Preparation and characterisation of PVDF NPs: Effect of dialysis and flash techniques on morphology, size, and phase formation

NPs were prepared by dialysis (see Section 2.2.1), employing the same solvents utilised in preparing the deposits (see Table 6.3). Additionally, for those solvents with a boiling point lower than that of water, NPs were also prepared via the flash technique (see Table 6.3).

Table 6.3. Description of the methods for preparing NPs using different techniques (dialysis and flash methods). The organic solvent selected for the preparation, the initial concentration (in grams per litre) of the solution utilised, and the preparation method are included.

Solvent	Concentration (g/L)	NP Preparation Method
Acetone	2	Dialysis/Flash
DMA		Dialysis
DMSO		Dialysis
EtOH		Dialysis/Flash
EG		Dialysis
FA		Dialysis
MEK		Dialysis/Flash
MetOH		Dialysis/Flash
PC		Dialysis
THF		Dialysis/Flash

6.3.1. Investigation of solvent effects on PVDF NP by flash nanoprecipitation

6.3.1.1. Morphological and size characterisation of PVDF NPs prepared by flash nanoprecipitation

The size and morphology of the PVDF NPs prepared by flash nanoprecipitation were characterised by AFM after deposition on a silicon substrate by drop casting and spin coating (see sections 2.3.1 and 2.3.2). Figure 6.7 presents images of NPs prepared by microfluidics using five different solvents (acetone, EtOH, MEK and MetOH), accompanied by their respective histograms. The images illustrate the spherical nature of the NPs.

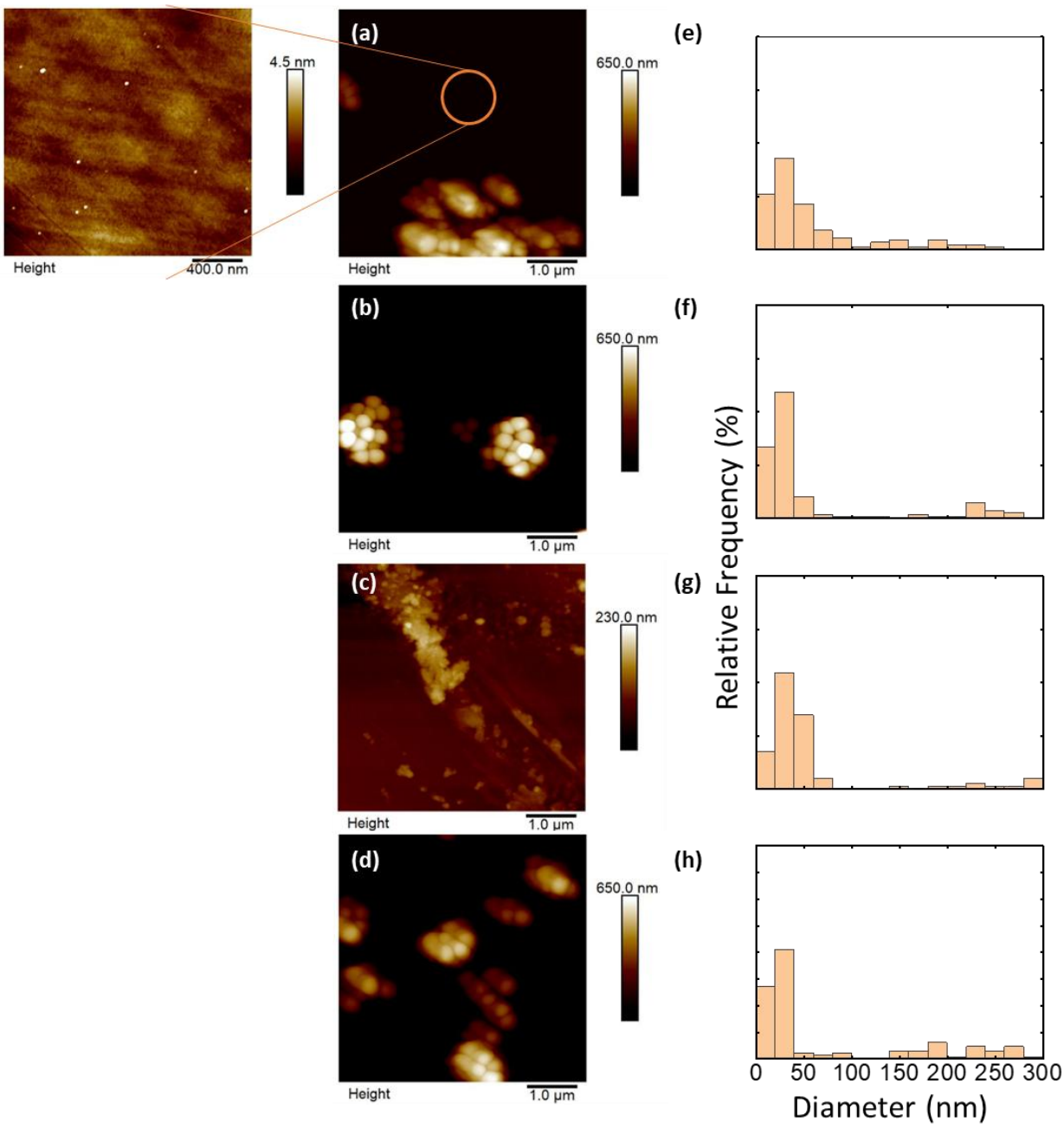

Figure 6.7. (a)-(d) AFM topographical images of PVDF NPs prepared by flash in microfluidics: **(a)** acetone, with an inset showing the two populations, **(b)** EtOH, **(c)** MetOH and **(d)** MEK. **(e)-(h)** Histograms of measured diameters of PVDF NPs prepared by flash in microfluidics: **(e)** acetone, **(f)** EtOH, **(g)** MetOH and **(h)** MEK. A total of at least 100 NPs were measured.

As shown in Figure 6.7, the samples prepared with acetone (Figure 6.7 (a) and (e)), EtOH (Figure 6.7 (b) and (f)), MetOH (Figure 6.7 (c) and (g)), and MEK (Figure 6.7 (d) and (h)) have comparable sizes and distributions. Also, all the images show aggregates of spherical NPs. An analysis of the particle sizes reveals narrow distributions in almost all samples,

although some large particles are also found. In the samples of EtOH, MetOH and MEK, this distribution manifests as different populations, with a population of smaller NPs around 22.5 nm in EtOH (Figure 6.7 (f)) and MetOH (Figure 6.7 (g)), and 35 nm in MEK (Figure 6.7 (h)), and sporadic appearance of larger NPs. The wider distribution in sizes observed for NPs prepared can be related to differences in solubility (Table 6.1), and this may affect the formation of larger aggregates of macromolecules that nucleate larger NPs.

6.3.1.2. Solvent-induced variations in the crystalline structure of PVDF NPs prepared by flash

XRD experiments were performed on PVDF NPs deposited via drop casting from aqueous dispersions to identify the phases formed. Figure 6.8 presents the diffractograms of samples prepared by microfluidics. As observed in Figure 6.8, the Bragg reflections are not well defined, with the exception of the flash NPs prepared from EtOH. This finding suggests a decrease in crystallinity from NPs prepared from MetOH (47% crystallinity) to NPs prepared from acetone (36% crystallinity). In the case of the NPs prepared from solution in THF, the X-ray structure obtained is compatible with that of the α phase. However, for all the rest of the solvents, the Bragg peaks appear to be combinations of more than one phase. The particular case of EtOH is interesting, since it shows clear Bragg reflections corresponding to the α, β and γ phases[69].

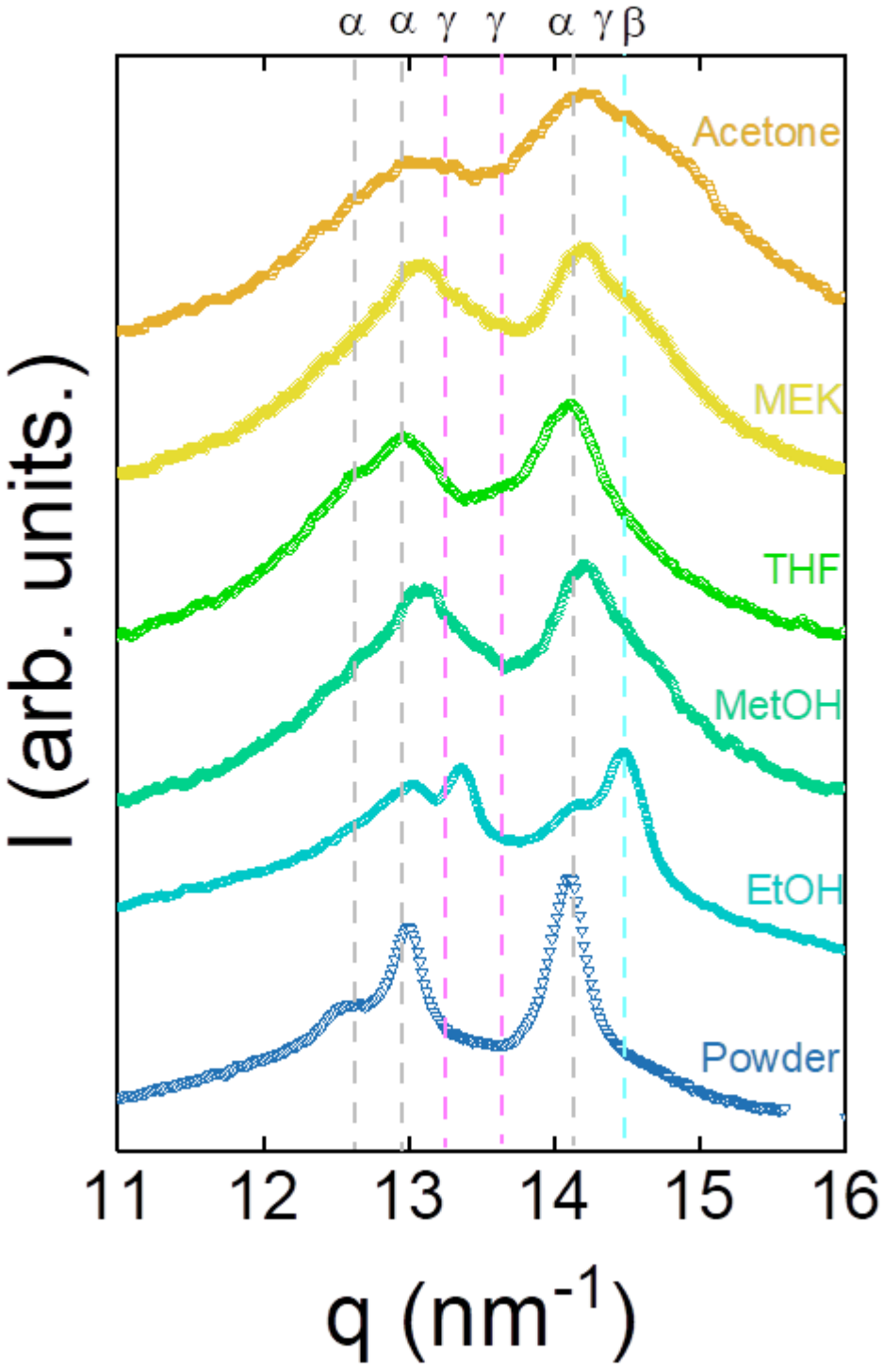

Figure 6.8. Diffraction patterns from NPs prepared via flash microfluidics with different solvents, as indicated by the labels in the scattering vector (*q*) range from 11 to 16 nm^{-1}. The crystalline phases (α: grey, β: blue, γ: pink) are indicated by dotted lines. This illustrates the structural variations affected by this method. The diffractograms were baseline-corrected by setting the minimum intensity to

zero and then normalised to the intensity of the most prominent peak located between 14.10 and 14.25 nm^{-1} for each sample. For clarity, a vertical offset of 1 intensity unit was applied between successive spectra.

6.3.1.3. Modulation of PVDF crystalline phases by solvent: FTIR study

As illustrated in Figure 6.9, FTIR spectra provide additional insight by showing variations in the intensity of the characteristic vibrational bands related to the different crystalline phases of PVDF. For example, differences in the intensity of the bands correlated with the α phase (615 cm^{-1}, 762 cm^{-1}, 874 cm^{-1} and 1189 cm^{-1})[43,57] are detected, representing a lower intensity in samples prepared from acetone and higher in the case of samples prepared from EtOH and powder, confirming the influence of the solvent on the composition of the PVDF crystalline phases. The bands assigned to the electroactive phases remain largely unaltered. Samples exhibiting elevated α phase show a slight blue shift at 1071 cm^{-1}, which is ascribed to the bending of CF_2.

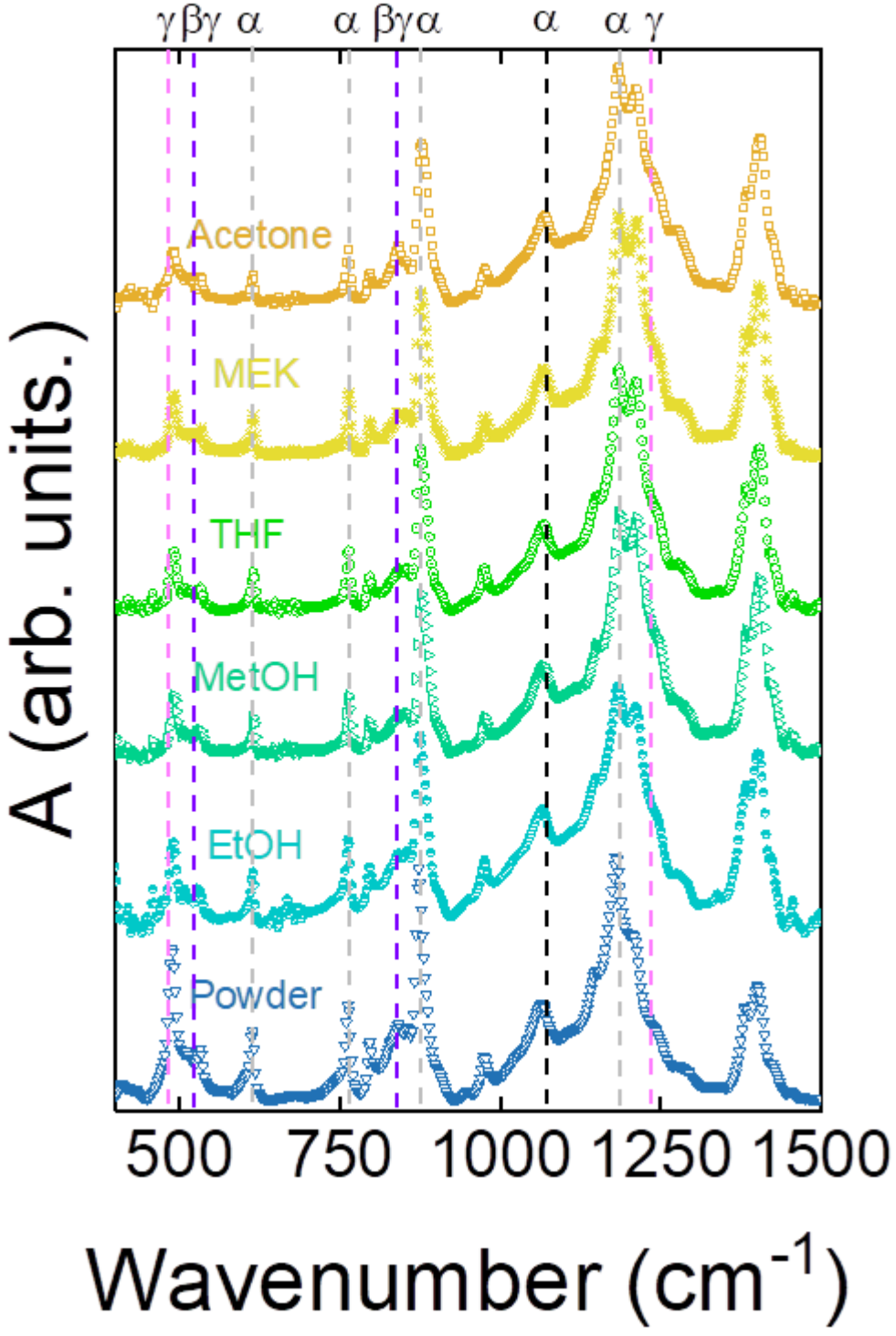

Figure 6.9. IR spectra of the flash-prepared samples from solutions in different solvents, indicated by the labels, highlight the characteristic bands of each crystalline phase. The identified vibration modes of each crystalline phase are indicated by dotted lines, corresponding to α: grey, γ: pink, β and γ: purple, α, β and γ: black. Each spectrum was normalised to its most intense peak at

approximately 873 cm-1. For visual clarity, a vertical offset of 0.7 absorbance units was applied between successive spectra.

6.3.1.4. Influence of solvent properties on crystalline phases of PVDF NPs prepared by flash nanoprecipitation

Figure 6.10 illustrates the trends observed by XRD and FTIR for PVDF NPs obtained by flash microfluidics, as a function of the boiling point (see Figure 6.10 (a)), and polarity, represented by dipole moment (see Figure 6.10 (b)) and dielectric constant (see Figure 6.10 (c)). Both XRD and FTIR experiments consistently show that the fraction of electroactive phases remains relatively constant across the different solvents used. This effect can be attributed to the fact that the flash boiling point is less decisive, since the displacement of the solvent by the antisolvent produces the NPs and, therefore, the assembly of the chains. In the case of polarity, these solvents have polarities that are lower or only slightly higher than the polarity of the electroactive phases of PVDF.

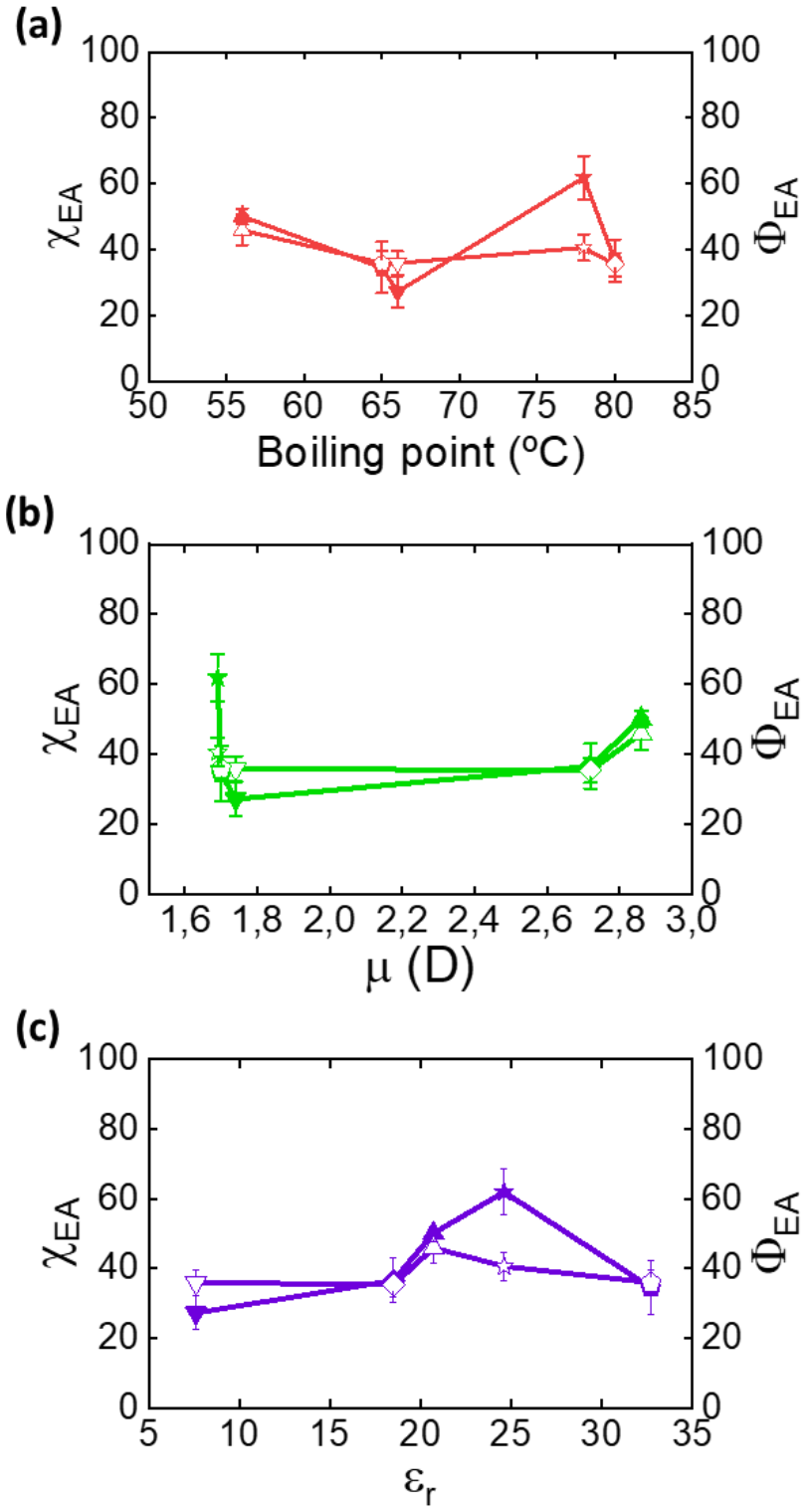

Figure 6.10. Influence of solvent properties on the electroactive phase content in PVDF NPs, as determined by XRD (filled symbols) and FTIR spectroscopy (empty symbols). Samples were prepared by flash nanoprecipitation using microfluidics. The solvent properties examined were: **(a)** boiling point, **(b)** μ, and **(c)** ε_r. Solvents are represented by the following symbols: acetone (triangle), THF (inverted triangle), MEK (rhombus), EtOH (star), MetOH (pentangle). The PVDF in powder form has a χ_{EA} value of 7.7 and Φ_{EA} value of 39.

6.3.2. The influence of solvent on PVDF NPs prepared by dialysis

6.3.2.1. Dialysis NPs prepared at room temperature

6.3.2.1.1. Influence of solvent on the size, morphology, and nucleation mechanisms of PVDF NPs

The size and morphology of the PVDF NPs were characterised by AFM in the same conditions as PVDF flash NPs. Figure 6.11 presents images of NPs prepared by dialysis using five different solvents (acetone, EtOH, EG, MetOH and THF), along with their respective size distributions.

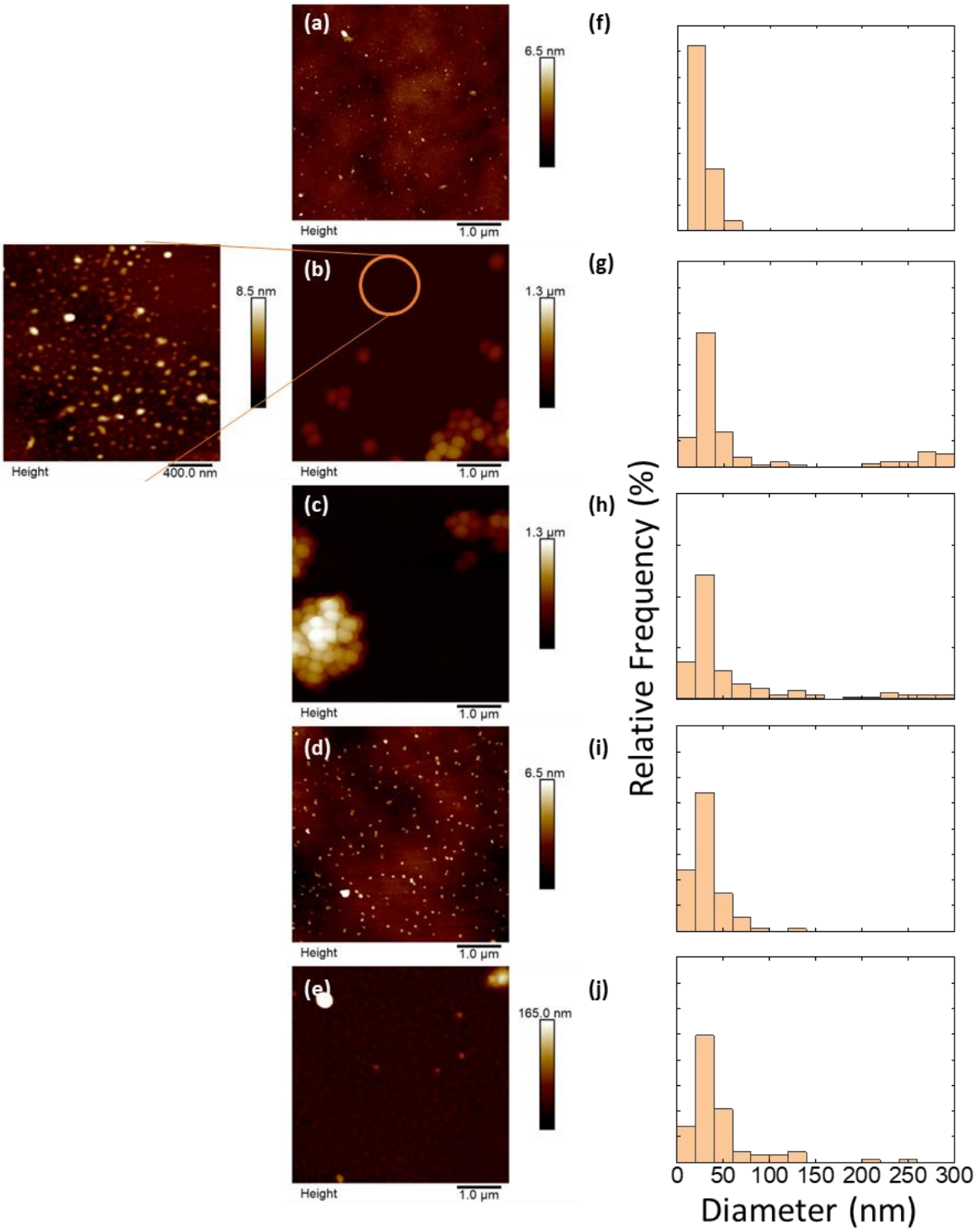

Figure 6.11. (a)-(e) AFM topographical images of PVDF NPs prepared by dialysis. **(a)** corresponds to acetone, **(b)** EtOH, with an inset showing the two populations, **(c)** EG, **(d)** MetOH and **(e)** THF. **(f)** to **(i)** histogram of measured diameters of PVDF NPs prepared by dialysis. **(f)** corresponds to acetone, **(g)** EtOH, **(h)** EG, **(i)** MetOH and **(j)** THF. Total number of NPs counted: at least 100.

In Figure 6.11 is observed that all samples have nearly spherical NPs with nanometric sizes that do not exceed 300 nm. Figure 6.11 (a), corresponding to acetone, shows small NPs with a size of approximately 22.5 nm and monodispersity. A similar observation can be made for MetOH and THF (see Figures 6.11 (d) and (e)), where the size for these samples is found to be approximately 30 nm and 45 nm, respectively. However, it is noted that the size distribution functions for these samples are broader (see Figures 6.11 (i) and (j)). In Figures 6.11 (b) and (c), corresponding to NPs obtained from EtOH and EG, the images show larger sizes, leading to the appearance of bimodal size distributions (Figures 6.11 (g) and (h)), with one of the populations centred at 27.5 for EtOH and 22.5 for EG and the other at 222.5 for EtOH and 232.5 for EG. As it was explained in the previous section, the presence of these two distinct populations could be indicative of the existence of two distinct nucleation and growth mechanisms due to the interaction of the solvent with the PVDF.

6.3.2.1.2. Solvent-dependent crystalline phase composition in dialysis prepared PVDF NPs

The diffractograms for NPs prepared by dialysis with the different solvents are presented in Figure 6.12, revealing notable differences among the samples. As with deposits and microfluidic NPs, all the diffraction patterns show two main diffraction maxima. However, it should be noted that the positions of these maxima exhibit significant shifts depending on the solvent used. Specifically, NPs prepared from PC, DMSO, DMA, acetone and MEK show broad maxima, whose positions are consistent with electroactive phases. However, the NPs prepared from all the rest of the solvents show reflections with positions shifted towards lower *q* values, which are consistent with the non-polar α phase[69]. The degree of crystallinity exhibited by the NPs prepared with varying solvents exhibits marginal variation. For instance, the NPs prepared from DMSO exhibit a higher proportion of an electroactive phase, resulting in a crystallinity of 53%, in comparison to the 56% crystallinity of EtOH, whose predominant phase is α.

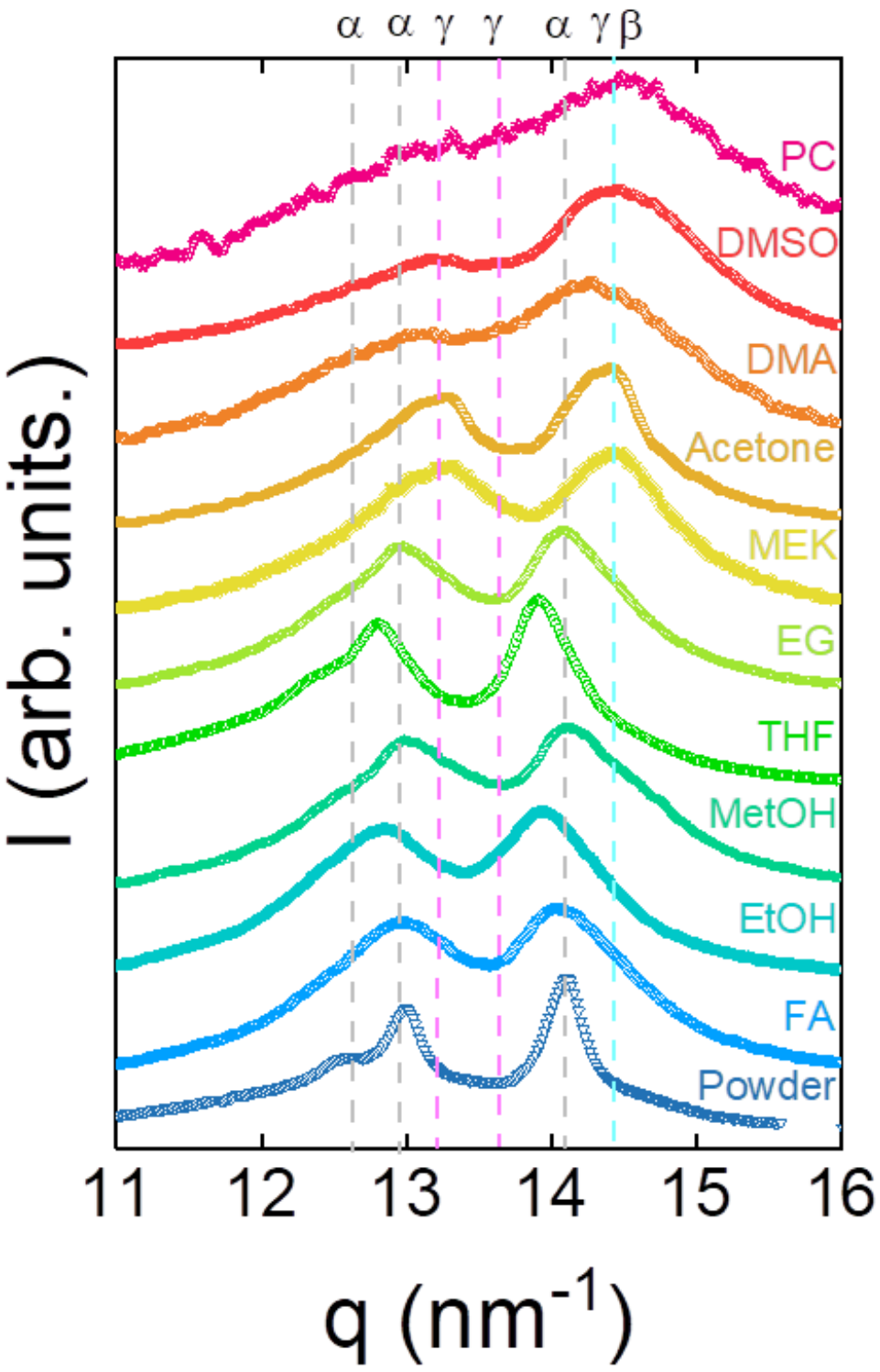

Figure 6.12. Normalised XRD patterns of the samples prepared by dialysis using different solvents, as indicated by the labels, with identified crystalline phases (α: grey, β: blue, γ: pink) indicated by dotted lines. These patterns highlight differences in crystal structure and phase composition. The diffractograms were

baseline corrected to zero and then normalised to the maximum intensity peak observed between 14.10 and 14.25 nm^{-1} for each individual diffractogram. For visual clarity, a vertical offset of approximately 0.5 intensity units was applied between successive spectra.

6.3.2.1.3. Influence of solvent on PVDF crystalline phase composition: FTIR Study

The FTIR spectra of the NPs prepared by dialysis from different solvents are shown in Figure 6.13. Notably, the samples prepared from PC, DMSO and DMA clearly exhibit the bands at 480 cm^{-1} and 1230 cm^{-1} that are characteristic of the γ phase [43,57]. These samples also show other bands associated with electroactive phases (510 cm^{-1} and 835 cm^{-1})[43,57], while those associated with the α phase (610 cm^{-1}, 760 cm^{-1}, 874 cm^{-1}, 974 cm^{-1} and 1186 cm^{-1})[43,57] are detected with lower intensity compared to those from less polar solvents. The appearance of the band at 835 cm^{-1} is associated with the asymmetric oscillation of CH_2 in polar conformation and the shift toward a larger wavenumber at 1071 cm^{-1}, attributed to the bending of CF_2. The results obtained from this study indicate that an increase in the dipole moment of the solvent leads to an enhancement in the torsion of the molecular chains (see Table 6.1).

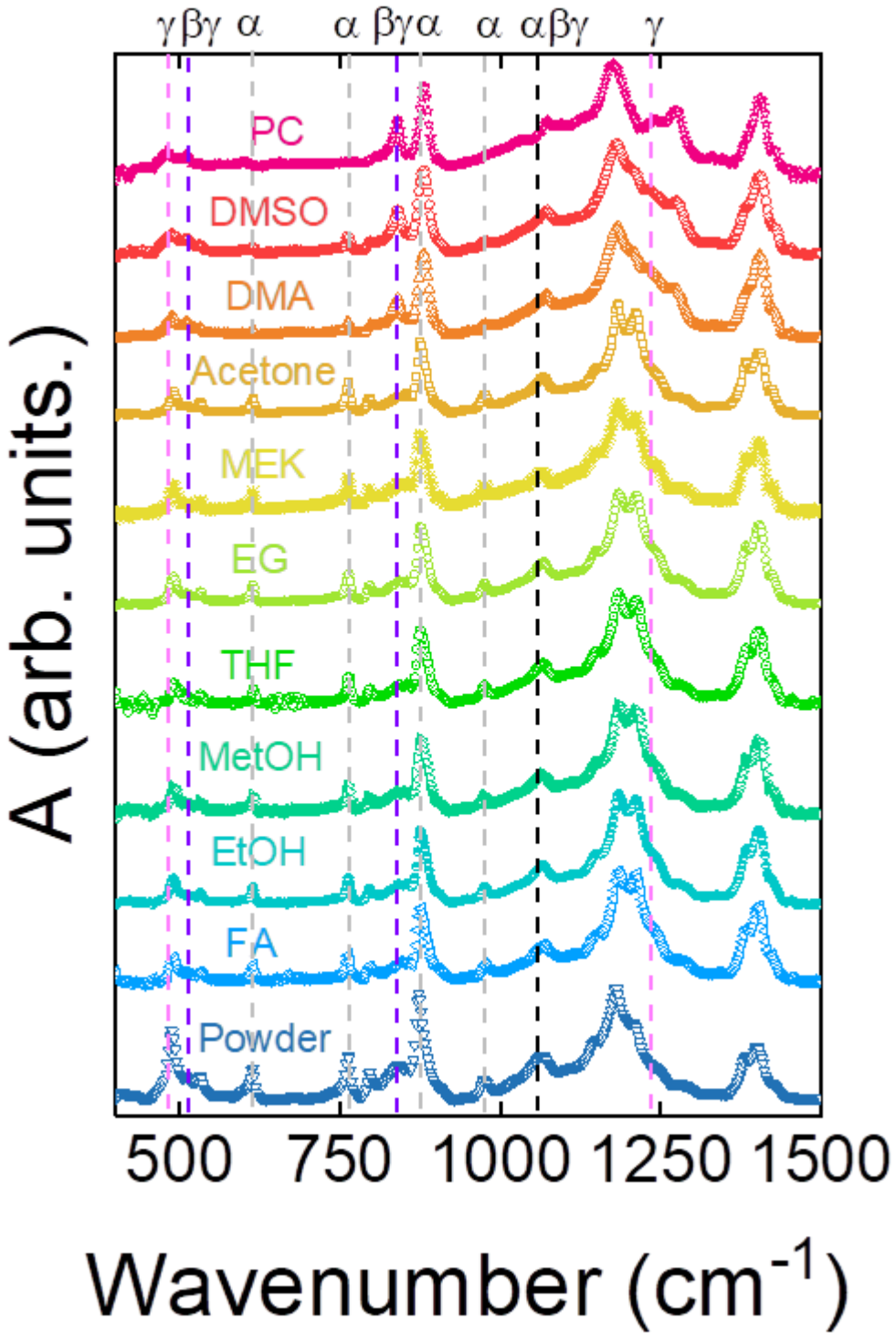

Figure 6.13. IR spectra of the samples prepared by dialysis from solutions in different solvents, indicated by the labels. All spectra were baseline-corrected and normalised to the strongest absorption at 873 cm^{-1}, then vertically offset by 0.8 absorbance units for clarity. Dotted lines mark the characteristic bands of each phase: α: grey, γ: pink, β and γ: purple, α, β and γ: black.

6.3.2.1.4. The role of solvent and antisolvent miscibility and solvent polarity on the crystalline phase formation of dialysis prepared PVDF NPs

The fraction of electroactive phases from XRD and FTIR was calculated as explained above for the case of the deposits. Thus, in the case of dialysis, the boiling point of the solvent is not a significant factor, as no evaporation occurs. Instead, the key step influencing the process is the solvent-antisolvent exchange across the membrane, which is governed by the miscibility between the organic solvent and water. Consequently, the solvent–water miscibility has been calculated using the R_a. Table 6.4 presents the values in terms of R_a of the solubility between the corresponding organic solvent and water. Figure 6.14 illustrates the trends observed by XRD and FTIR for the NPs obtained by dialysis with respect to the solvents R_a (see Figure 6.14 (a)), polarity in the form of dipole moment (Figure 6.14 (b)), and dielectric constant (see Figure 6.14 (c)). When the electroactive phase fraction is plotted as a function of the R_a parameter of the solvents (Figure 6.14 (a)), it is observed that, at low R_a values, indicative of solvents that are highly miscible with water, the predominant phase is the α phase, since the exchange of the solvent with water is rapid. Conversely, for solvents with higher R_a values that are less miscible with water, the PVDF phases that begin to appear are the electroactive ones. This is because a reduced rate of solvent exchange results in a prolonged exposure of the PVDF chains to the organic solvent environment. Consequently, the chains remain in a trans conformation for a greater duration due to the solvent. This prolonged exposure enables the chains to adopt and maintain this conformation more effectively during the gradual desolvation and crystallisation process. For Figures 6.14 (b) and (c), the observed trends are very similar to those obtained from the deposits.

Table 6.4. Miscibility of organic solvents in water expressed in terms of R_a.

Solvent	Solvents R_a ($MPa^{1/2}$)
PC	77
DMSO	64
DMA	66
Acetone	71

MEK	75
EG	33
THF	69
MetOH	40
EtOH	46
FA	57

Consequently, the dipole moment of the solvent can be identified as a pivotal factor (see Figure 6.14 (b)), with the formation of the electroactive phase starting to increase when the dipole moment of the solvent is equal to or greater than the dipole moment of the electroactive phase (2.1D)[1]. This finding suggests that a minimum dipole-dipole interaction between the solvent and the PVDF chain is necessary to stabilise the electroactive conformation. Conversely, if the dipole moment of the solvent is comparable or greater, the energetic interactions could be favourable enough to direct crystallisation toward the electroactive phases. As previously mentioned in the context of deposits, these trends can be attributed to the interactions between the solvent and the PVDF chains. Solvents with higher dipole moments interact through dipole-dipole forces with the -CF_2- groups of PVDF, which can influence the conformation of the chains in solution and during the precipitation process and stabilise the trans conformation associated with the electroactive phase[1,42,68,70]. Conversely, solvents exhibiting lower dipole moments may promote the formation of the α-phase, attributable to their less effective stabilisation of the trans conformation[70].

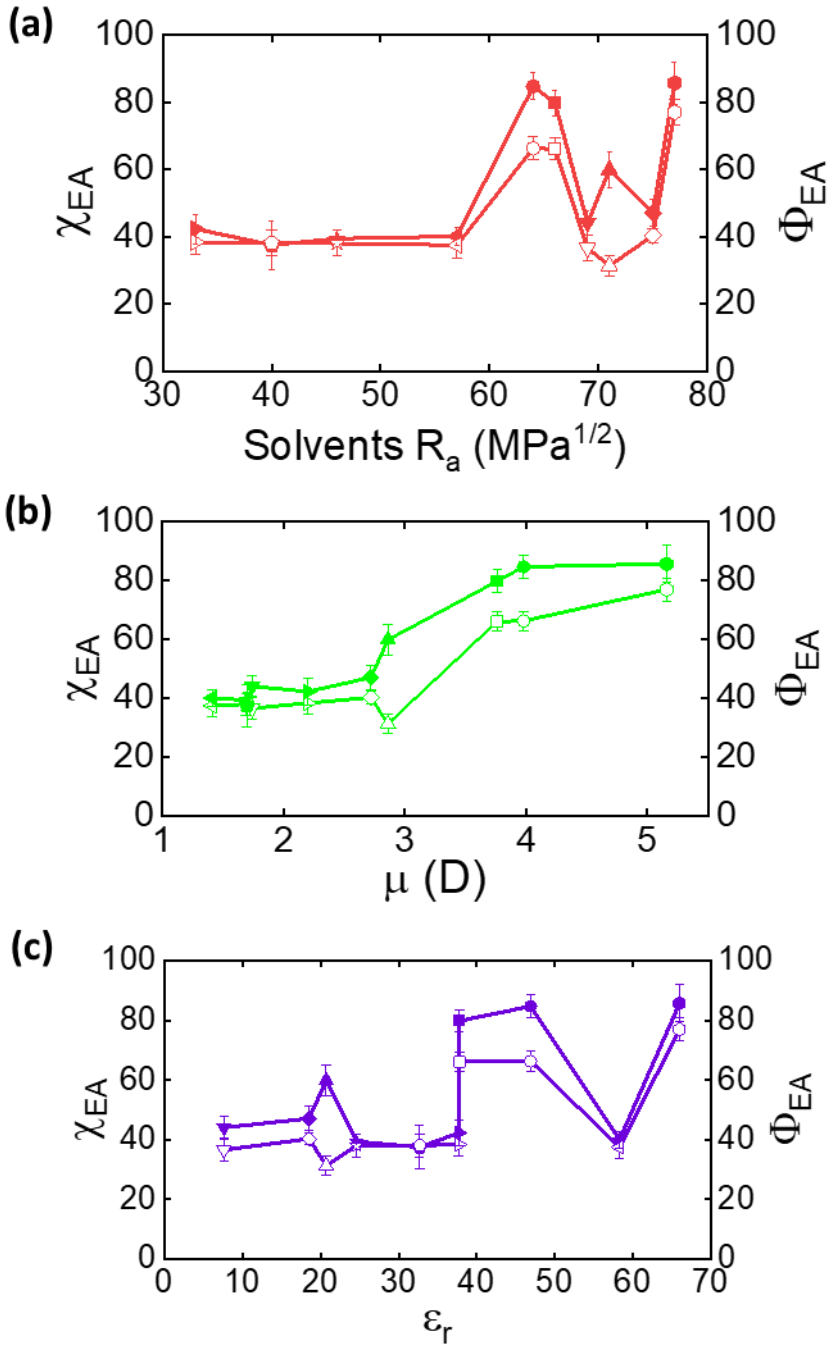

Figure 6.14. Variation of the percentage of electroactive phase as a function of various solvent properties determined by XRD (filled symbols) and FTIR (empty symbols) for NPs prepared by dialysis: **(a)** boiling point; **(b)** dipole moment; **(c)** dielectric constant. A solvent property value of 0 corresponds to PVDF in powder form. Solvents are represented by the following symbols: DMA (square), DMSO (circle), acetone (triangle), THF (inverted triangle), MEK (rhombus), FA (left-facing triangle), PC (hexagon), EtOH (star), MetOH (pentangle), EG (right-facing triangle). The PVDF in powder form has a χ_{EA} value of 7.7 and Φ_{EA} value of 39.

6.3.2.2. Tuning electroactive phase formation in PVDF NPs via binary solvent mixtures of DMA and acetone

Since the above results point towards an influence of the solvent polarity on the amount of electroactive phase of PVDF obtained in the form of bulk deposits or NPs, mixtures of solvents with different polarities were used to prepare NPs and study their fraction of electroactive phases. For instance, research such as that of Ma et al.[50] has obtained a greater amount of electroactive phase in films when two solvents with different polarities are mixed. In particular, DMA has been selected as the more polar solvent, and acetone as the less polar solvent. NPs were prepared by dialysis using these binary mixtures as solvents, in the specific volume ratios of DMA and acetone 2:1, 1:1, and 1:2.

6.3.2.2.1. Influence of binary solvent mixtures on the crystallisation and phase formation of PVDF NPs

The effect of the DMA/Acetone ratio on the formation of the polar phase has been studied using XRD, as previously described. Figure 6.15 shows the diffractograms of NPs obtained by dialysis. Depending on the solvent ratio, slight differences can be observed in the relative intensity of the regions related to the different phases. The NPs prepared in pure DMA exhibit two less-defined and broader maxima, which may indicate lower crystallinity (25%) and positions consistent with electroactive phases. However, as the proportion of acetone in the initial solvent mixture increases, the maxima become more defined and narrower, indicating higher crystallinity (52% in solely acetone), and are more identifiable with a mixture of polar and non-polar phases. This phenomenon is not attributed to a preferential displacement of the more polar solvent (DMA) by the less polar one (acetone). Instead, the observed changes can be explained by the variation in the overall solvating power of the binary mixture, which directly impacts the crystallization kinetics. When the polymer is dissolved in pure DMA, the strong DMA-PVDF interactions promote the formation of polar conformations. However, the slow, gradual solvent exchange during dialysis may lead to a less-ordered structure with lower overall crystallinity. In contrast, as the proportion of acetone is increased, the overall polarity and solvating power of the mixture decrease, leading to a faster polymer collapse and nucleation when exposed to water. This more rapid

crystallization process favors the formation of a more crystalline structure but, due to the reduced control over chain organization, can result in a mixture of both polar and non-polar phases. The fraction of polar phases thus estimated from these diffractograms is presented in Figure 6.17.

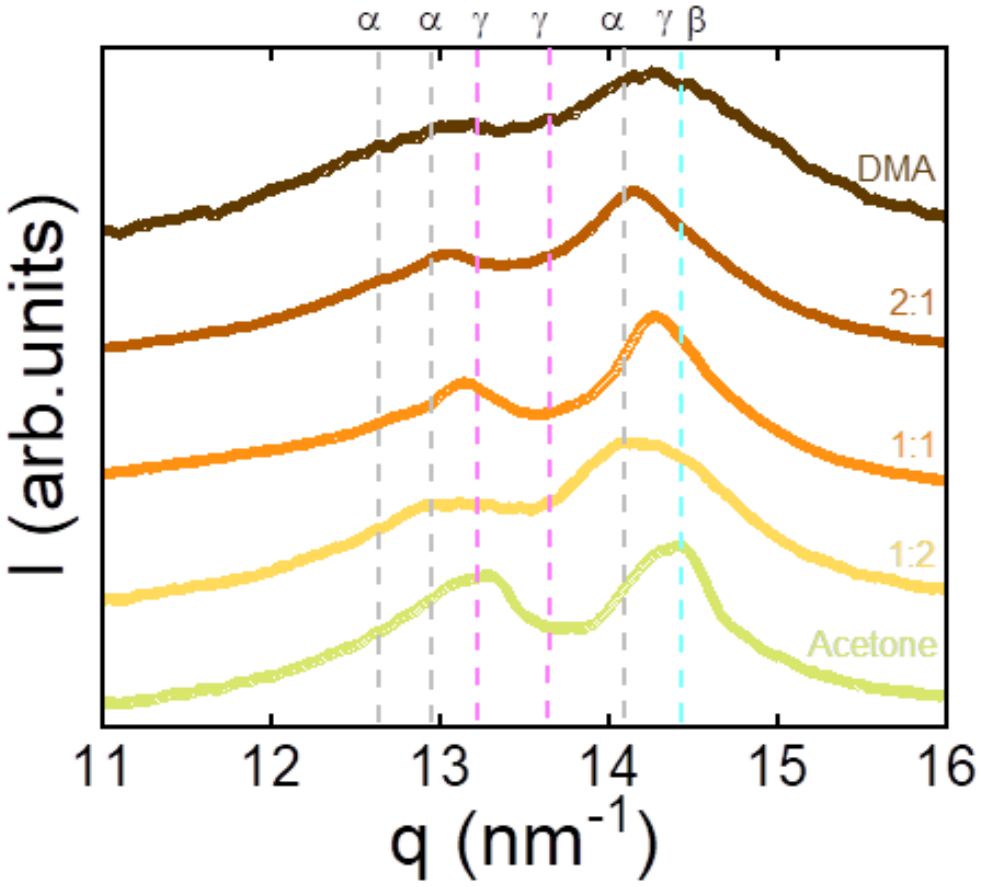

Figure 6.15. Characterisation of the samples by X-ray diffraction for samples with DMA (brown), acetone (green) and binary solvent ratios: 2:1 (caramel colour), 1:1 (orange) and 1:2 (yellow) with characteristic bands of the identified phases highlighted by dotted lines: α: grey, β: blue, γ: pink. All diffractograms have been baseline-corrected and normalised with respect to the most intense diffraction peak located between 14.10 and 14.25 nm^{-1} to allow for direct comparison of relative peak intensities. A vertical offset of 0.7 units has been applied between successive curves to improve visual clarity.

6.3.2.2.2. Tuning PVDF crystalline phases with solvent mixtures: An FTIR spectroscopic investigation

The polar phase formation in dialysis NPs prepared from DMA/Acetone mixtures was also investigated using FTIR spectroscopy in the spectral region of 400-1500 cm^{-1}. Figure 6.16 shows the FTIR spectra of the NPs obtained by dialysis, and again, only subtle variations are observed among samples prepared from different solvent ratios. The presence of all phases of PVDF is confirmed in the samples. Samples prepared from solvent mixtures with a higher proportion of DMA exhibit lower intensities in the bands associated with the α phase at 610, 765, or 978 cm^{-1},[43,57] while bands corresponding to the electroactive phases, such as those at 488, 515, 840, 1233, or 1405 cm^{-1},[43,57] show higher intensities. This suggests support for the idea postulated above those solvents with higher polarity may promote the formation of the β phase (all-trans conformation) and the γ phase (*TTTGTTTG'* conformation)[50,71].

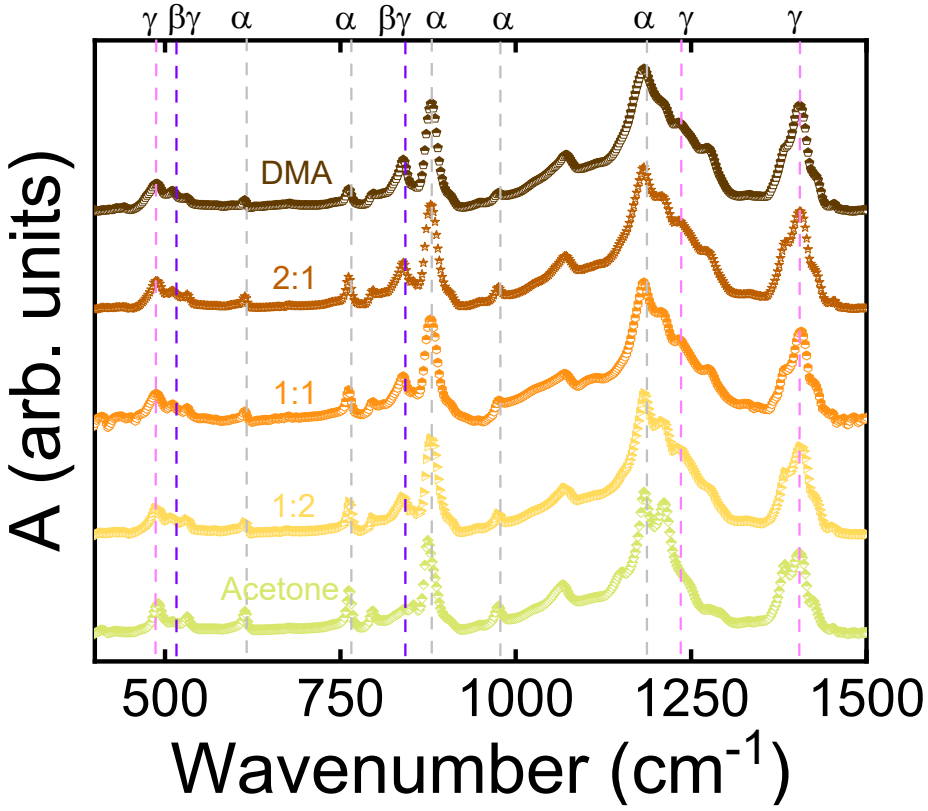

Figure 6.16. IR spectra of the samples prepared with DMA (brown), acetone (green) and binary solvent ratios: 2:1 (caramel colour), 1:1 (orange) and 1:2

(yellow). To facilitate visual comparison of the spectral features and trends, each spectrum was normalised to its most intense peak at approximately 873 cm^{-1}, and a constant vertical offset of 0.7 absorbance units was applied between successive spectra. The characteristic bands of the identified phases are highlighted by dotted lines (α: grey, β: blue, γ: pink).

6.3.2.2.3. Solvent mixtures and their impact on PVDF crystalline phase composition: A comparative WAXS and FTIR study

The proportion of the electroactive phase is illustrated in Figure 6.17. Figure 6.17 show a slight trend for an increased proportion of the electroactive phase in the presence of a solvent mixture for XRD. These observations are consistent with the findings reported in the extant literature on films[50]. This tendency is more pronounced in the electroactive phase obtained when compared with the less polar solvent (acetone), but slightly higher than that obtained with the more polar solvent (DMA), reaching a maximum value when the ratio is 1:1. This observation aligns with the conclusions drawn by Ma et al.[50], who reported that a 1:1 ratio in DMF as more polar solvent and acetone as less polar solvent is optimal for film preparation, leading to the highest electroactive content. The underlying mechanism for this phenomenon is attributed to the dipolar interactions and hydrogen bonding between the highly electronegative part of the solvent molecules (in this case, the $O^{\delta-}$ of DMA) with the partial positive charge of the hydrogens ($H^{\delta+}$) of the PVDF chain, thereby stabilising the trans conformation associated with the electroactive phase[42,50,52,68]. Conversely, repulsive interactions between the $O^{\delta-}$ of DMA and the fluorine ($F^{\delta-}$) of the chain further modulate this effect[50,52]. This phenomenon would explain why a solvent of lower polarity as acetone, is required to interact with DMA, and why a 1:1 ratio is more effective because it seems to achieve an optimal balance between the favourable and unfavourable interactions between the solvent and PVDF to control the process that maximises the formation of the electroactive phase. Other studies refer to the interaction of the NH_2 group, instead of oxygen, with the fluorine atoms of the chain through hydrogen bonds, which favoured the presence of the trans conformation[72–74]. However, both explanations may be plausible, and the polar solvent molecules may orient themselves based on the interaction with the corresponding part of the chain, but the effect of acetone would be diminished. A theoretical study on the interactions between solvent molecules and the PVDF chain could provide

further insights into the mechanism. Conversely, in the context of FTIR spectra, a different trend can be observed. In this case, a tendency towards a lower proportion of electroactive phase is observed when there is a greater amount of acetone, indicating that an optimal balance between polar and less polar solvents is critical. The differences between XRD and FTIR may be due to the fact that both techniques are sensitive to different aspects of the crystal structure. XRD provides information about long-range ordering, while FTIR is sensitive to local molecular conformations.

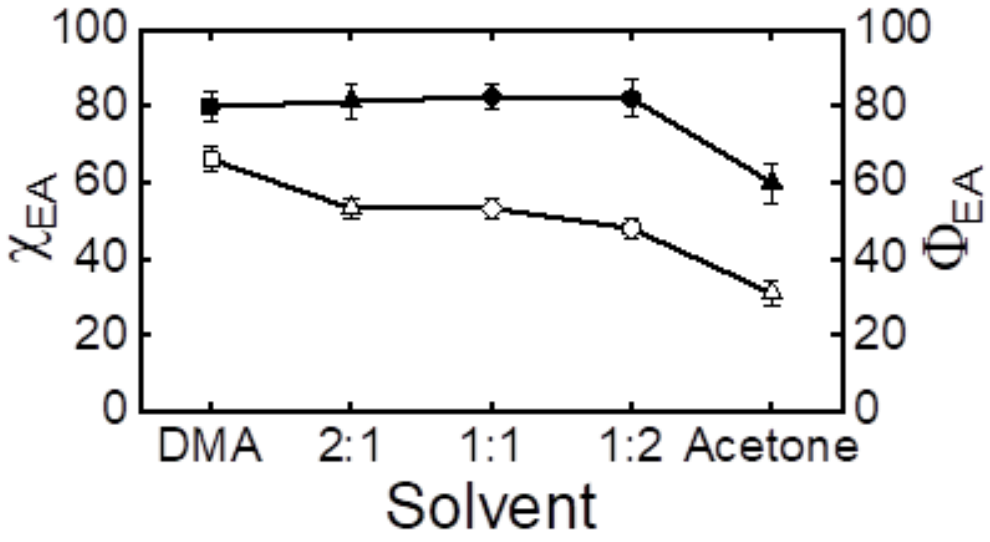

Figure 6.17. Variation of the electroactive phase of PVDF NPs as a function of solvent composition: pure solvents of DMA and acetone and mixtures with ratios of 2:1, 1:1 and 1:2 (DMA:Acetone) by XRD (filled symbols) and FTIR (empty symbols) analysis. Solvents are represented by the following symbols: DMA (square), acetone (triangle), DMA:Acetone (2:1) (triangle), DMA:Acetone (1:1) (rhombus), DMA:Acetone (1:2) (hexagon).

6.3.2.3. Impact of dialysis bath temperature on crystalline structure of PVDF NPs processed from DMA

Li et al.[75] reported that, in PVDF films, increasing the crystallisation temperature increases the degree of crystallinity, whereas the content of the electroactive phase is maximised when crystallisation occurs at lower temperatures. In this section, NPs were prepared by dialysis using DMA as an organic solvent while varying the water bath

temperature. Three distinct procedures were employed for this purpose. The first procedure was to use a bath at room temperature (around 20 °C). This method has been employed in all previous preparations. The second procedure involved using an ice bath that provides a dialysis bath of approximately 15 °C. A third preparation was carried out using a plate that heated the water bath to a temperature of 70 °C. The objective of this study is to determine whether the effect of the temperature of the water bath affects the crystalline structure of PVDF NPs.

6.3.2.3.1. Effect of bath temperature on PVDF phase formation and crystallinity

Figure 6.18 shows the X-ray diffractograms for the three sets of NPs, prepared by dialysing at three different temperatures. It is notable that NPs formed by dialysis at elevated temperatures exhibit the most intense maximum at 12.9 nm^{-1}, corresponding to the α phase. It is important to note that the maximum intensity decreases as the dialysis bath temperature decreases. In addition, a reduction in bath temperature has been shown to result in an increase in the intensity of the peaks that are associated with the electroactive phases. Finally, the sample dialysed at the room temperature appears to be the least crystalline (44% at high and low temperatures, and 25% at room temperature), although no major variations are observed.

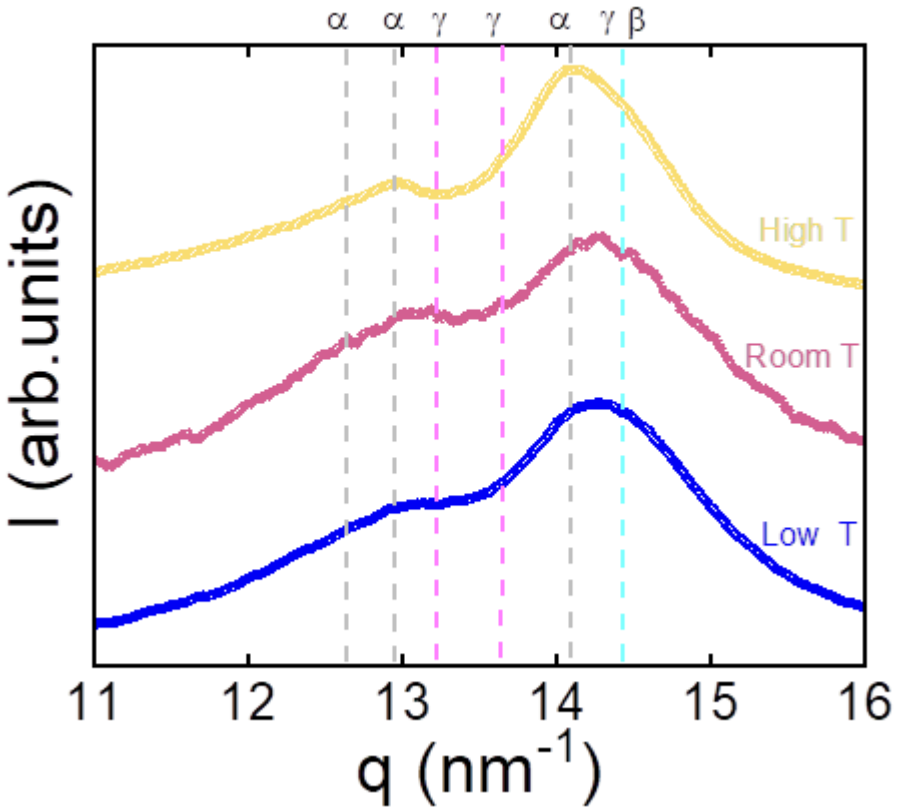

Figure 6.18. Sample characterisation by WAXS of three samples prepared by dialysis at different water bath temperatures: low (15 ℃, blue), room (20 ℃, pink) and high (70 ℃, yellow), highlighting the characteristic bands of the identified phases, marked with dotted lines (α: grey, β: blue, γ: pink), and showing the changes in phase composition as a function of water bath temperature. Each pattern was baseline-corrected to zero intensity, normalised to the most intense peak in the q-range 14.10–14.25 nm^{-1}, and vertically offset by 0.6 relative intensity units for clarity

6.3.2.3.2. Investigation of temperature effects on PVDF crystalline phases: An FTIR perspective

Similarly, the FTIR data (Figure 6.19) reveal differences in band intensities. Specifically, bands associated with the electroactive phases, such as those at 488, 512, and 843, or 1235 cm^{-1}, exhibit decreased intensity at room temperature. Conversely, the intensity of bands characteristic of the α phase, such as those at 615, 764, or 882 cm^{-1}, increases with increasing dialysis bath temperature. Furthermore, the band associated with the interaction between DMA and PVDF at 675 cm^{-1} shows enhanced intensity when the dialysis is performed at a

higher temperature, suggesting a stronger interaction between the solvent and the polymer under these conditions.

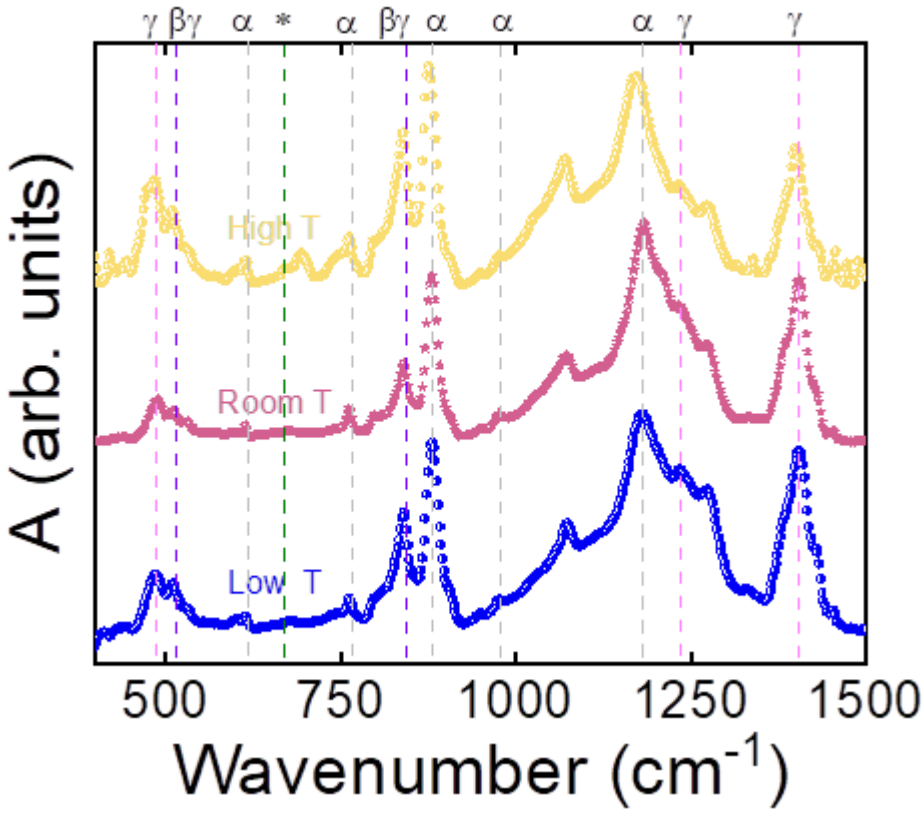

Figure 6.19. FTIR spectra of the three samples (low temperature (blue), room temperature (pink) and high temperature (yellow)), highlighting the characteristic bands of the identified phases (α: grey, γ: pink, β and γ: purple) and the band associated with the interaction between DMA and PVDF (green band with asterisk), marked with dotted lines. All spectra have been baseline-corrected and normalised with respect to the most intense vibrational band located at 873 cm^{-1}, characteristic of the electroactive phases. A vertical offset of 0.8 units has been applied between spectra to enhance visual distinction.

6.3.2.3.3. Influence of dialysis bath temperature on electroactive phase formation in PVDF NPs: A GIWAXS and FTIR Study

As illustrated in Figure 6.20, the percentages of the electroactive phase for three samples have been determined by XRD (Figure 6.20 (a)) and FTIR (Figure 6.20 (b)). The sample dialysed at room temperature exhibits the lowest electroactive phase contribution in both

XRD and FTIR. This observation suggests that the temperature of the water bath does not significantly affect the thermodynamic or kinetic aspects governing the formation of the electroactive phase. Rather, it influences the overall crystallinity by modulating the rate of solvent exchange across the membrane and chain mobility during crystallisation. A bath at a lower temperature (20 ℃) could favour rapid nucleation and limit crystal growth due to the reduced mobility of the chains, thereby potentially favouring the formation of less ordered, electroactive-rich phases. Conversely, at higher temperatures (70 ℃), a more prolonged growth is favoured, which can induce changes in the conformation of the chains and the distribution of the phases. Gregorio et al.[61] analysed these effects in films, concluding that high temperatures and long formation times give rise to more electroactive phases. Li et al.[75] investigated the impact of crystallisation temperature on PVDF films prepared from DMSO, observing an increased proportion of polar phase at 60°C. However, at lower and higher temperatures, this fraction decreases. Concurrently, Gutierrez-Fernandez et al.[51] investigated the impact of temperature on NPs prepared by dialysis utilising DMA as an organic solvent. This work demonstrates how the increase in temperature favours the electroactive phases due to α to γ phase transitions[51]. Okada et al.[46] also obtained a higher percentage of electroactive phase when they subjected the DMF-prepared NPs to acetone and an ionic liquid at elevated temperatures. However, it should be noted that the temperatures at which differences were observed in both studies exceeded 145 ℃, which was not possible to achieve in the present study. Consequently, in contrast to the influence of the temperature in the formation of the films as explained by Li et al.[75] or Gregorio et al.[61], the alteration in bath temperature to prepare NPs could not influence the kinetic energy of the chains, thereby maintaining the degree of ordering during the solvent displacement stage. Furthermore, the investigation revealed that temperature does not appear to influence the rate of exchange of DMA through water. Therefore, the formation of the electroactive phase appears to depend primarily on the dissolution stage and the conformation adopted by the PVDF chains or the precipitation rate, which are not significantly affected by temperature.

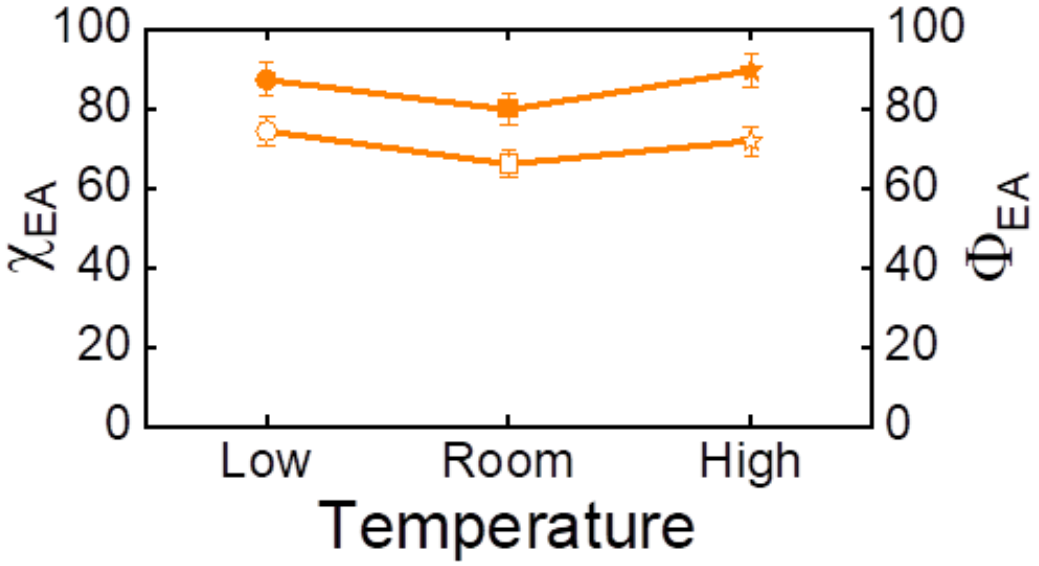

Figure 6.20. Variation of the proportion of electroactive phase in PVDF NPs prepared by dialysis at different water bath temperatures, as determined by XRD (filled symbols) and FTIR analysis (empty symbols). Solvents are represented by the following symbols: low (circle), room temperature (square), high (star).

6.3.3. Comparative analysis of flash microfluidic and dialysis for PVDF NPs formation

6.3.3.1. The effect of solvent on PVDF NP morphology

As shown in Figures 6.7 and 6.11, the overall tendency of NPs to adopt a spherical shape is observed. Figure 6.21 shows that the diameter of the smaller population corresponding to the preparation with all the solvents used, both by dialysis and by flash. Furthermore, it is observed that the sizes obtained for solvents such as acetone, EtOH, and THF are smaller in microfluidic flash than those in dialysis. These differences may be related to the mixing conditions of the solvent and antisolvent, which affect the nucleation and growth of the NPs. In the flash method, the displacement of the solvent by the antisolvent is faster than in dialysis, but less controlled. This could generate smaller NP sizes, but in turn, broader distributions. Additionally, the solvent removal process in flash is more rapid than in dialysis, with evaporation being faster than diffusion.

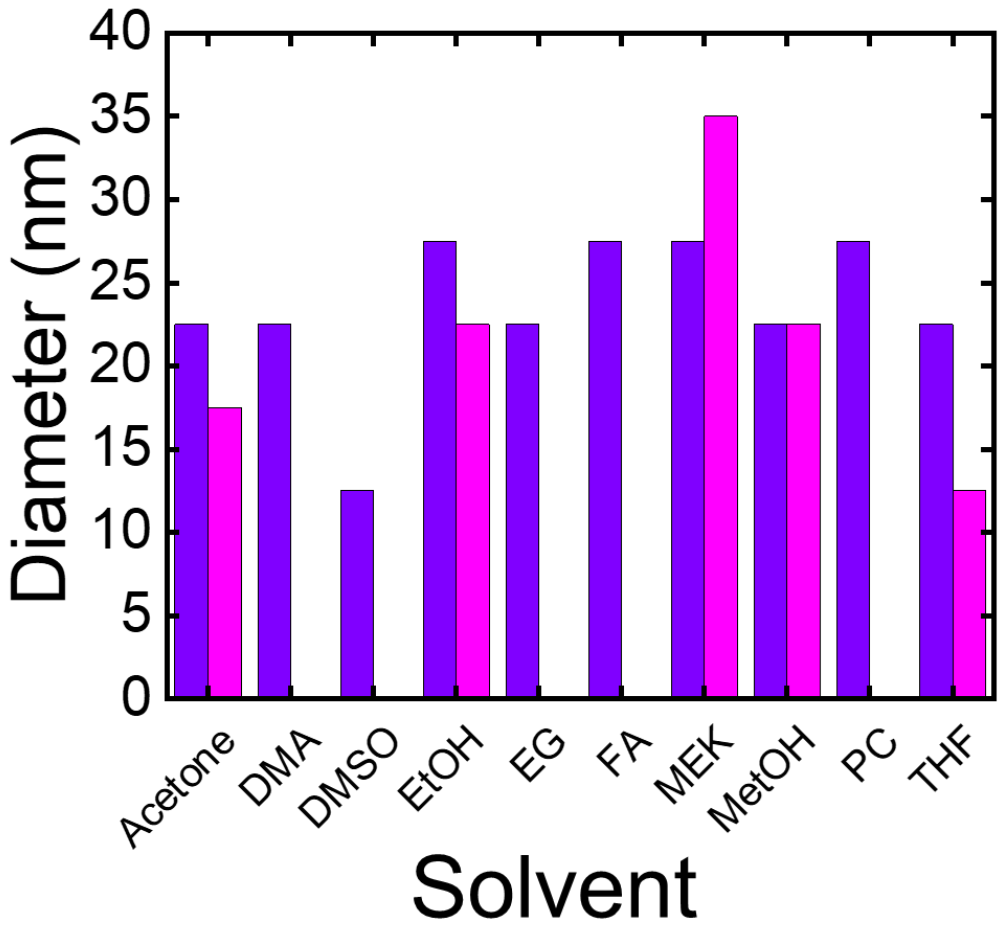

Figure 6.21. Particle diameters for the different organic solvents used to prepare PVDF NPs: dialysis (black) and flash microfluidics (red).

6.3.3.2. Comparative study of PVDF NPs crystallinity and electroactive phase formation

This section aims to provide a comparative analysis of the influence of the preparation methods on PVDF NPs produced by flash microfluidics versus those prepared by dialysis. Figure 6.22 shows the diffractograms of the NPs prepared by microfluidics (Figure 6.22 (a)) and those obtained by dialysis (Figure 6.22 (b)) for the same solvents. The spectra corresponding to the same solvents are similar. The degree of crystallinity is dependent on the method of preparation, though no clear trend has been identified as to which method

favours greater crystallinity. For instance, the crystallinity value of NPs prepared through acetone as a solvent is 36% in microfluidics and 52% in dialysis. The crystallinity value of NPs prepared through methanol as a solvent is 47% in microfluidics and 39% in dialysis. With regard to the position of the maxima, in the context of dialysis, the maxima associated with the electroactive phases are observed to be slightly more intense in the case of acetone and MEK. In the case of EtOH, the application of microfluidics to the diffractogram results in more clearly differentiated maxima. In THF and MetOH, no significant changes are observed.

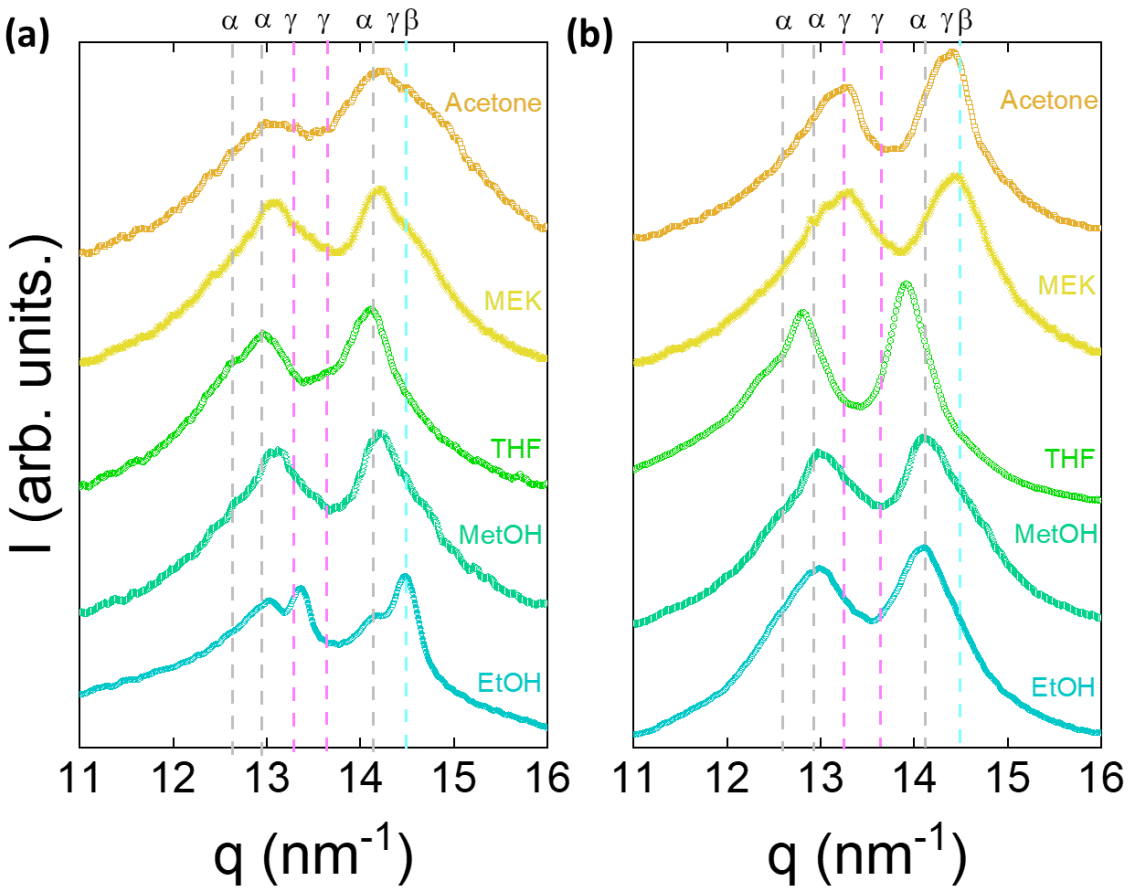

Figure 6.22. Diffractograms of PVDF NPs obtained by: **(a)** flash and **(b)** dialysis.

In the case of the crystalline phases, Figure 6.23 compares the fraction of electroactive phases obtained by XRD (Figure 6.23 (a)) and FTIR (Figure 6.23 (b)) for both types of NPs, as a function of the dipole moment. FTIR results show that the electroactive phase fraction is constant for NPs prepared with solvents with dipolar moment below 2.1 D, for both types

of NPs. For solvents with higher values of the dipolar moment, the fraction of electroactive phase increases as the dipolar moment increases. XRD results also show this trend, although the trend is less pronounced than in the dialysis case. However, by FTIR, this trend is very similar, with coinciding values, obtaining similar electroactive phase values up to a dipole moment value of 2.1 D, as discussed above, where a slight increase in the electroactive phase is appreciated. In the case of flash, the application of this trend cannot be tested with more polar solvents due to their boiling point.

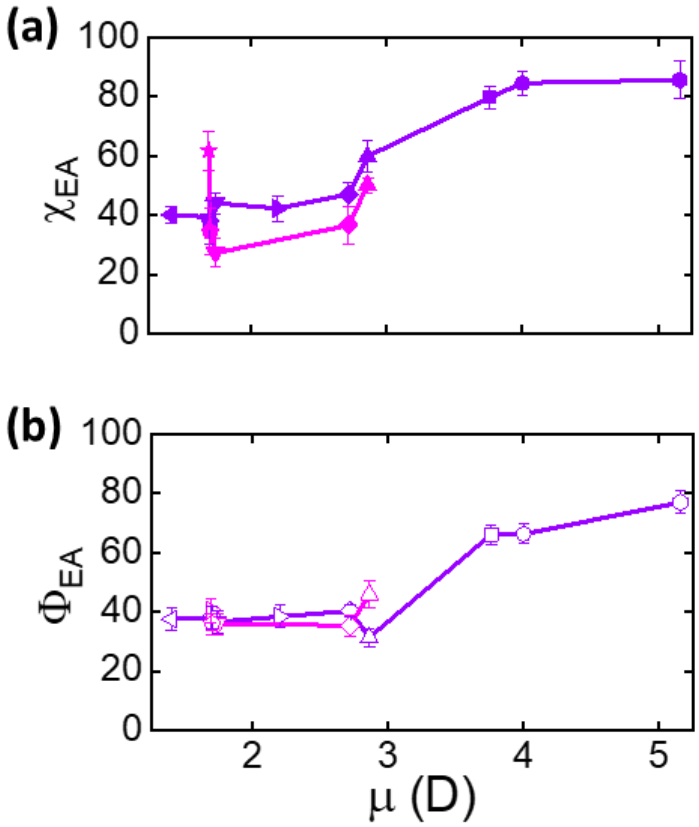

Figure 6.23. (a) Variation of the electroactive phase in PVDF NPs prepared by dialysis (purple) and in flash (magenta) versus the dipole moment of the different solvents used, obtained from X-ray diffractograms and from **(b)** FTIR. Solvents are represented by the following symbols: DMA (square), DMSO (circle), acetone (triangle), THF (inverted triangle), MEK (rhombus), FA (left-facing triangle), PC (hexagon), EtOH (star), MetOH (pentangle), EG (right-facing triangle)

6.4. A comparative analysis of solvent influence on crystallinity and crystalline phases of PVDF deposits and dialysis-prepared NPs

This section evaluates the effect of NP preparation by dialysis when compared to the deposits prepared from the same solvent. For this study, NPs prepared by dialysis were selected for comparison, since the flash NPs were prepared only in low-polarity solvents, due to the limitation of the solvent boiling point in the preparation method, resulting in no significant changes in the percentage of electroactive phase.

In terms of crystallinity, no trends are observed in terms of crystalline content (see Figure 6.24). The confinement of polymer chains within the NPs could potentially induce alterations in crystallinity.

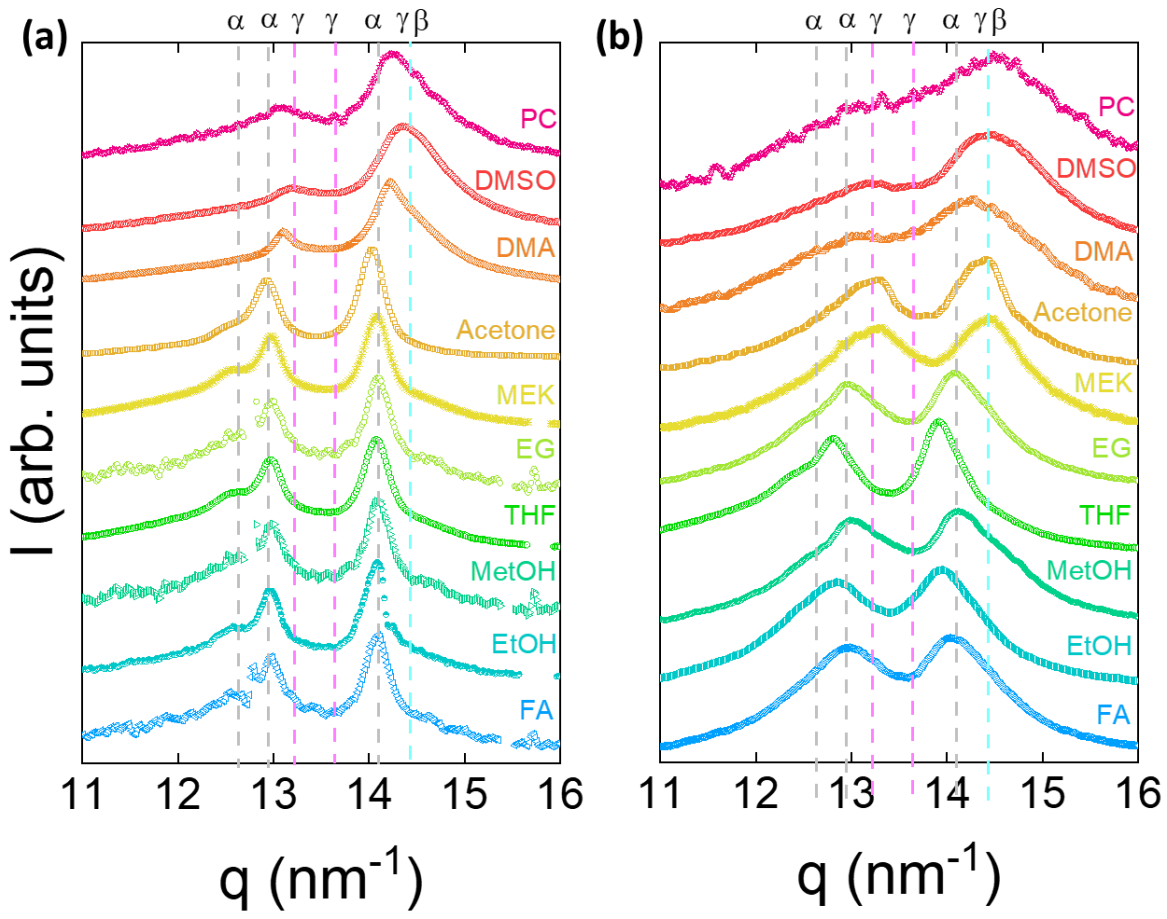

Figure 6.24. Diffractograms of PVDF NPs obtained by: **(a)** deposits and **(b)** dialysis.

In the case of the crystalline phases, the trend observed in the X-ray diffractograms (Figure 6.25 (a)) and FTIR spectra (Figure 6.25 (b)) is shown for the deposits and NPs. In the case of the information obtained by X-ray analysis, a greater contribution of the electroactive phase is observed for the less polar solvents in NPs. However, the trend of increasing percentage of electroactive phase starts at a very similar dipole moment, which corresponds to the dipole moment of the electroactive phase of PVDF[1], as mentioned above. Similarly, in FTIR, both the deposits and the NPs show very similar results, with coinciding electroactive phase values for all solvents. These results indicate that the change from solvent to antisolvent does not affect the phase obtained, nor the precipitation technique. The decisive step is the dissolution of the polymer in the solvent and the molecular arrangement of the chains in solution. It is also noteworthy that the polymer concentration, which is 50 g/L in the deposits and 2 g/L in the NPs, does not have a significant impact on either the crystallinity or the phases obtained.

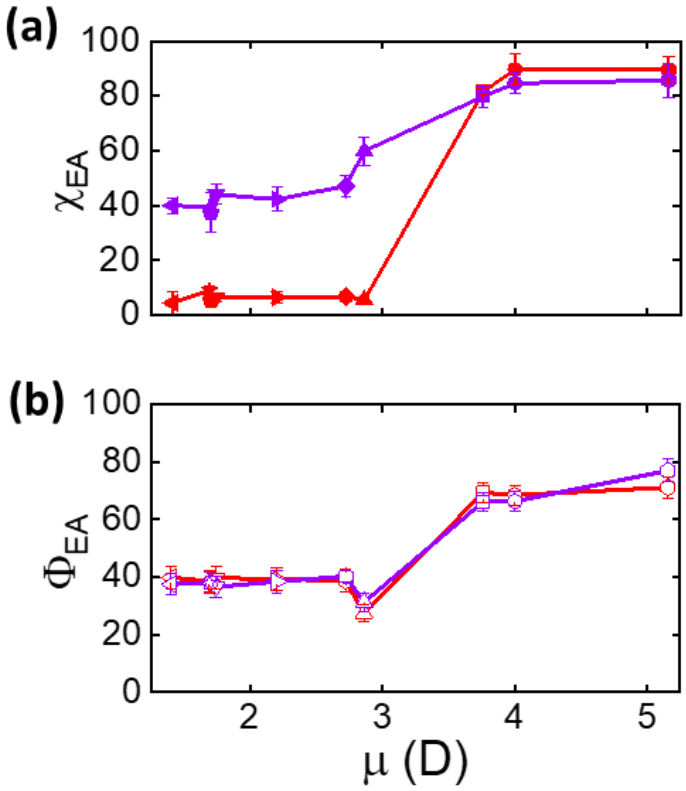

Figure 6.25. Variation of the electroactive phase in PVDF NPs prepared by dialysis (purple) and in deposits (red) versus the dipole moment of the different

solvents used, obtained from: **(a)** X-ray diffractograms. **(b)** FTIR. Solvents are represented by the following symbols: DMA (square), DMSO (circle), acetone (triangle), THF (inverted triangle), MEK (rhombus), FA (left-facing triangle), PC (hexagon), EtOH (star), MetOH (pentangle), EG (right-facing triangle)

6.5. Conclusions

This chapter comprehensively examined the impact of solvent properties on the formation of PVDF deposits and NPs, prepared by two distinct methods: dialysis and flash microfluidics. The utilisation of a combination of XRD and FTIR has facilitated the establishment of significant correlations between the physicochemical properties of the solvents and the ensuing crystalline phases. Based on the experimental findings, the following conclusions were drawn:

- The formation of polar phases is governed by solvent polarity and boiling point: The formation of polar phases in PVDF is strongly influenced by solvent polarity, particularly as reflected by the dipole moment and dielectric constant, as well as by the boiling point.
- Achievement of nanoscale sizes on a universal scale: In all cases, the presence of particles in the nanometric range was obtained, regardless of the preparation method (dialysis or flash) or solvent utilised.
- Dipole moment as a key determinant for NPs: For PVDF NPs, the dipole moment emerged as the most relevant parameter governing the appearance of the electroactive phase, although this trend is less pronounced in flash-prepared NPs due to the lower polarity of the solvents used.
- The minimal impact of binary solvents in dialysis: The utilisation of binary solvent systems in NPs prepared by dialysis yielded no significant effect on the appearance of polar phases.
- The temperature's minimal impact in dialysis: Modifications to the temperature of the dialysis bath exhibited minimal influence on the formation of electroactive phases.
- Method-independent polar phase formation: Minimal variations in polar phase formation were observed when comparing PVDF deposits (prepared by solvent casting, where solvent evaporation is key) and PVDF NPs (prepared by dialysis/flash, driven by solvent exchange).

The results obtained demonstrate the pivotal function of the dissolution stage in regulating the conformation of PVDF chains and the crystalline phase of PVDF in both deposits and NPs. Specifically, polar solvents have been shown to promote strong dipole-dipole interactions, thereby stabilising the trans chain conformation and favouring electroactive phase formation. This emphasises the critical importance of optimising the solvent-mediated dissolution stage. In conclusion, this work provides a solid foundation for future investigations focused on the molecular-level understanding of PVDF crystallisation. It is proposed that the integration of advanced spectroscopic studies and molecular simulations will further elucidate the intricate PVDF crystallisation mechanisms.

6.6. Bibliography

(1) Lovinger, A. J. Ferroelectric Polymers. *Science* **1983**, *220* (4602), 1115–1121. https://doi.org/10.1126/science.220.4602.1115.

(2) Martins, P.; Lopes, A. C.; Lanceros-Mendez, S. Electroactive Phases of Poly(Vinylidene Fluoride): Determination, Processing and Applications. *Prog Polym Sci* **2014**, *39* (4), 683–706. https://doi.org/10.1016/j.progpolymsci.2013.07.006.

(3) Nalwa, H. S. *Ferroelectric Polymers: Chemistry, Physics and Applications*, 1st ed.; Taylor & Francis: Boca Raton, 1995. https://doi.org/10.1201/9781482295450.

(4) Gregorio, R. Determination of the α, β, and γ Crystalline Phases of Poly(Vinylidene Fluoride) Films Prepared at Different Conditions. *J Appl Polym Sci* **2006**, *100* (4), 3272–3279. https://doi.org/10.1002/app.23137.

(5) Marshall, J. E.; Zhenova, A.; Roberts, S.; Petchey, T.; Zhu, P.; Dancer, C. E. J.; McElroy, C. R.; Kendrick, E.; Goodship, V. On the Solubility and Stability of Polyvinylidene Fluoride. *Polymers* **2021**, *13* (9). https://doi.org/10.3390/polym13091354.

(6) Chan, K. Y.; Li, C. L.; Wang, D. M.; Lai, J. Y. Formation of Porous Structures and Crystalline Phases in Poly(Vinylidene Fluoride) Membranes Prepared with Nonsolvent-Induced Phase Separation—Roles of Solvent Polarity. *Polymers* **2023**, *15* (5). https://doi.org/10.3390/polym15051314.

(7) Bottino, A.; Capannelli, G.; Munari, S.; Turturro, A. Solubility Parameters of Poly(Vinylidene Fluoride). *Journal of Polymer Science Part B-Polymer Physics* **1988**, *26* (4), 785–794. https://doi.org/10.1002/polb.1988.090260405.

(8) Byrne, F. P.; Jin, S.; Paggiola, G.; Petchey, T. H. M.; Clark, J. H.; Farmer, T. J.; Hunt, A. J.; Robert McElroy, C.; Sherwood, J. Tools and Techniques for Solvent Selection: Green Solvent Selection Guides. *Sustainable Chemical Processes* **2016**, *4* (1). https://doi.org/10.1186/s40508-016-0051-z.

(9) Prat, D.; Hayler, J.; Wells, A. A Survey of Solvent Selection Guides. *Green Chemistry* **2014**, *16* (10), 4546–4551. https://doi.org/10.1039/c4gc01149j.

(10) Haynes, W. M. *Handbook of Chemistry and Physics*, 97th ed.; Taylor & Francis: New York, 2016.

(11) Mihalovits, M. Determination of the Hansen Solubility Parameters from Solubility Data Using an Improved Evaluation Approach, the Concentric Spheroids Method. *J Mol Liq* **2022**, *364*. https://doi.org/10.1016/j.molliq.2022.119911.

(12) Abbott, S. *HSP Basics*. https://www.stevenabbott.co.uk/practical-solubility/hsp-basics.php (accessed 2025-04-30).

(13) *Surface Tension, Hansen Solubility Parameters, Molar Volume, Enthalpy of Evaporation, and Molecular Weight of Selected Liquids*. https://www.accudynetest.com/solubility_table.html (accessed 2025-04-30).

(14) *Dipole Moment*. https://macro.lsu.edu/Howto/solvents/dipole%20moment.html (accessed 2025-05-02).

(15) Chernyak, Y. Dielectric Constant, Dipole Moment, and Solubility Parameters of Some Cyclic Acid Esters. *J Chem Eng Data* **2006**, *51* (2), 416–418. https://doi.org/10.1021/je050341y.

(16) You, X.; Chaudhari, M. I.; Rempe, S. B.; Rick, S.; Pratt, L. R. Dielectric Properties of Ethylene Carbonate and Propylene Carbonate Using Molecular Dynamics Simulations. *ECS Trans* **2015**, *69* (1). https://doi.org/10.1149/06901.0107ecst.

(17) Chandrasekaran, A. *Solvent Physical Properties*. https://people.chem.umass.edu/xray/solvent.html (accessed 2025-05-02).

(18) *The Merck Index - An Encyclopedia of Chemicals, Drugs, and Biologicals*, 14th ed.; O'Neil, M. J., Heckelman, P. E., Koch, C. B., Roman, K. J., Eds.; Royal Society of Chemistry: New Jersey, 2013.

(19) Li, M.; Ren, T.; Sun, Y.; Xiao, S.; Wang, Y.; Lu, M.; Zhang, S.; Du, K. New Parameter Derived from the Hansen Solubility Parameter Used to Evaluate the Solubility of Asphaltene in Solvent. *ACS Omega* **2022**, *7* (16), 13801–13807. https://doi.org/10.1021/acsomega.2c00018.

(20) Pereyra, R. G.; Asar, M. L.; Carignano, M. A. The Role of Acetone Dipole Moment in Acetone-Water Mixture. *Chem Phys Lett* **2011**, *507* (4–6), 240–243. https://doi.org/10.1016/j.cplett.2011.04.015.

(21) Oster, G. The Dielectric Properties of Liquid Mixtures. *J Am Chem Soc* **1946**, *68* (10), 2036–2041. https://doi.org/10.1021/ja01214a050.

(22) Lewis, R. J. Sr. *Hawley's Condensed Chemical Dictionary*, 15th ed.; John Wiley & Sons: New Jersey, 2007.

(23) Lide, D. R. *CRC Handbook of Chemistry and Physics*, 88th ed.; Taylor & Francis: New York, 2007.

(24) *Industrial Solvents Handbook*, 4th ed.; Flick, E. W., Ed.; Taylor & Francis: Boca Raton, 1991.

(25) Serjeant, E. P.; Dempsey B. *Ionisation Constants of Organic Acids in Aqueous Solution*, 23rd ed.; Elsevier Science & Technology: Oxford, 1979.

(26) Jorge, M.; Gomes, J. R. B.; Barrera, M. C. The Dipole Moment of Alcohols in the Liquid Phase and in Solution. *J Mol Liq* **2022**, *356*. https://doi.org/10.1016/j.molliq.2022.119033.

(27) *CRC Handbook of Chemistry and Physics.*, 95th ed.; Haynes, W. M., Ed.; Taylor & Francis: New York, 2014.

(28) *Dielectric Constant of Common solvents*. https://depts.washington.edu/eooptic/linkfiles/dielectric_chart%5B1%5D.pdf (accessed 2025-05-06).

(29) *Liquids - Dielectric Constants*. The Engineering ToolBox. https://www.engineeringtoolbox.com/liquid-dielectric-constants-d_1263.html (accessed 2025-05-06).

(30) *CRC Handbook of Chemistry and Physics.*, 91st ed.; Haynes, W. M., Ed.; Taylor & Francis: New York, 2010.

(31) Gray, C. G.; Gubbins, K. E. *Theory of Molecular Fluids*; Oxford University Press: Oxford, 1984; Vol. 1.

(32) Kim, H.; Keller, R.; Gwinn, W. D. Dipole Moment of Formic Acid, HCOOH and HCOOD. *J Chem Phys* **1962**, *37* (12), 2748–2750. https://doi.org/10.1063/1.1733099.

(33) Chang, R.; Overby, J. *General Chemistry: The Essential Concepts*, 6th ed.; McGraw-Hill: New York, 2010.

(34) Atkins, P.; de Paula, J. *Physical Chemistry*, 9th ed.; Oxford University Press: Oxford, 2009.

(35) Bursten Brown, L. *Química: La Ciencia Central*; Prentice Hall Mexico, 2004.

(36) Harris, D. C. *Quantitative Chemical Analysis*, 9th ed.; W. H. Freeman and Company: New York, 2015.

(37) Mark, J. E. *Physical Properties of Polymers Handbook*, 2nd ed.; Springer: New York, 2006.

(38) Marenich, A. V.; Cramer, C. J.; Truhlar, D. G. Universal Solvation Model Based on Solute Electron Density and on a Continuum Model of the Solvent Defined by the Bulk Dielectric Constant and Atomic Surface Tensions. *J Phys Chem B* **2009**, *113* (18), 6378–6396. https://doi.org/10.1021/jp810292n.

(39) Mills, I.; Cvitas, T.; Homann, K.; Kallay, N.; Kuchitsu, K. *Quantities, Units and Symbols in Physical Chemistry*, 2nd ed.; Blackwell Science: Oxford, 1993.

(40) *Handbook of Low and High Dielectric Constant Materials and Their Applications*; Singh Nalwa, H., Ed.; Academic Press: San Diego, 1999.

(41) Lee, Y. I. Various Dielectric Constants. *Ferroelectrics* **2015**, *482* (1), 54–59. https://doi.org/10.1080/00150193.2015.1056706.

(42) Benz, M.; Euler, W. B.; Gregory, O. J. The Influence of Preparation Conditions on the Surface Morphology of Poly(Vinylidene Fluoride) Films. *Langmuir* **2001**, *17* (1), 239–243. https://doi.org/10.1021/la001206g.

(43) Cai, X.; Lei, T.; Sun, D.; Lin, L. A Critical Analysis of the α, β and γ Phases in Poly(Vinylidene Fluoride) Using FTIR. *RSC Adv* **2017**, *7* (25), 15382–15389. https://doi.org/10.1039/c7ra01267e.

(44) Lei, T.; Cai, X.; Wang, X.; Yu, L.; Hu, X.; Zheng, G.; Lv, W.; Wang, L.; Wu, D.; Sun, D.; Lin, L. Spectroscopic Evidence for a High Fraction of Ferroelectric Phase Induced in Electrospun Polyvinylidene Fluoride Fibers. *RSC Adv* **2013**, *3* (47), 24952–24958. https://doi.org/10.1039/c3ra42622j.

(45) Esterly, D. M.; Love, B. J. Phase Transformation to β-Poly(Vinylidene Fluoride) by Milling. *Journal of Polymer Science Part B-Polymer Physics* **2003**, *42* (1), 91–97. https://doi.org/10.1002/polb.10613.

(46) Okada, D.; Kaneko, H.; Kato, K.; Furumi, S.; Takeguchi, M.; Yamamoto, Y. Colloidal Crystallization and Ionic Liquid Induced Partial β-Phase Transformation of Poly(Vinylidene Fluoride) Nanoparticles. *Macromolecules* **2015**, *48* (8), 2570–2575. https://doi.org/10.1021/acs.macromol.5b00337.

(47) Jurczuk, K.; Galeski, A.; Mackey, M.; Hiltner, A.; Baer, E. Orientation of PVDF α and γ Crystals in Nanolayered Films. *Colloid Polym Sci* **2015**, *293* (4), 1289–1297. https://doi.org/10.1007/s00396-015-3542-7.

(48) Gutiérrez-Fernández, E.; Cui, J.; Martínez-Tong, D. E.; Nogales, A. Preparation, Physical Properties, and Applications of Water-Based Functional Polymer Inks. *Polymers* **2021**, *13* (9). https://doi.org/10.3390/polym13091419.

(49) Liang, C. L.; Mai, Z. H.; Xie, Q.; Bao, R. Y.; Yang, W.; Xie, B. H.; Yang, M. B. Induced Formation of Dominating Polar Phases of Poly(Vinylidene Fluoride): Positive Ion-CF2 Dipole or Negative Ion-

CH2 Dipole Interaction. *J Phys Chem B* **2014**, *118* (30), 9104–9111. https://doi.org/10.1021/jp504938f.

(50) Ma, W.; Zhang, J.; Chen, S.; Wang, X. Crystalline Phase Formation of Poly(Vinylidene Fluoride) from Tetrahydrofuran/N,N-Dimethylformamide Mixed Solutions. *Journal of Macromolecular Science Part B-Physics* **2008**, *47* (3), 434–449. https://doi.org/10.1080/00222340801954811.

(51) Gutiérrez-Fernández, E.; Sena-Fernández, J.; Rebollar, E.; Ezquerra, T. A.; Hermoso-Pinilla, F. J.; Sanz, M.; Gálvez, O.; Nogales, A. Development of Polar Phases in Ferroelectric Poly(Vinylidene Fluoride) (PVDF) Nanoparticles. *Polymer* **2023**, *264*. https://doi.org/10.1016/j.polymer.2022.125540.

(52) Wang, T.; Wang, Y.; Dang, F.; Liu, M.; Sun, S.; Jin, K.; Cheng, P. Optimizing Solvent Dipole Moment Enables PVDF to Improve Piezoelectric Performance. *Nanotechnology* **2024**, *35* (7). https://doi.org/10.1088/1361-6528/ad0907.

(53) Nishiyama, T.; Sumihara, T.; Sasaki, Y.; Sato, E.; Yamato, M.; Horibe, H. Crystalline Structure Control of Poly(Vinylidene Fluoride) Films with the Antisolvent Addition Method. *Polym J* **2016**, *48* (10), 1035–1038. https://doi.org/10.1038/pj.2016.62.

(54) Montoya-Escobar, N.; Ospina-Acero, D.; Velásquez-Cock, J. A.; Gómez-Hoyos, C.; Serpa Guerra, A.; Gañan Rojo, P. F.; Vélez Acosta, L. M.; Escobar, J. P.; Correa-Hincapié, N.; Triana-Chávez, O.; Zuluaga Gallego, R.; Stefani, P. M. Use of Fourier Series in X-Ray Diffraction (XRD) Analysis and Fourier-Transform Infrared Spectroscopy (FTIR) for Estimation of Crystallinity in Cellulose from Different Sources. *Polymers* **2022**, *14* (23). https://doi.org/10.3390/polym14235199.

(55) Garvey, C. J.; Parker, I. H.; Simon, G. P. On the Interpretation of X-Ray Diffraction Powder Patterns in Terms of the Nanostructure of Cellulose I Fibres. *Macromol Chem Phys* **2005**, *206* (15), 1568–1575. https://doi.org/10.1002/macp.200500008.

(56) He, J.; Cui, S.; Wang, S. Y. Preparation and Crystalline Analysis of High-Grade Bamboo Dissolving Pulp for Cellulose Acetate. *J Appl Polym Sci* **2008**, *107* (2), 1029–1038. https://doi.org/10.1002/app.27061.

(57) Kobayashi, M.; Tashiro, K.; Tadokoro, H. Molecular Vibrations of Three Crystal Forms of Poly(Vinylidene Fluoride). *Macromolecules* **1975**, *8* (2), 158–171. https://doi.org/10.1021/ma60044a013.

(58) Boccaccio, T.; Bottino, A.; Capannelli, G.; Piaggio, P. Characterization of PVDF Membranes by Vibrational Spectroscopy. *J Memb Sci* **2002**, *210*, 315–329.

(59) Liang, Z.; Yan, C. F.; Rtimi, S.; Bandara, J. Piezoelectric Materials for Catalytic/Photocatalytic Removal of Pollutants: Recent Advances and Outlook. *Appl Catal B* **2019**, *241*, 256–269. https://doi.org/10.1016/j.apcatb.2018.09.028.

(60) Salimi, A.; Yousefi, A. A. FTIR Studies of β-Phase Crystal Formation in Stretched PVDF Films. *Polym Test* **2003**, *22* (6), 699–704. https://doi.org/10.1016/S0142-9418(03)00003-5.

(61) Gregorio, R.; Cestari, M. Effect of Crystallization Temperature on the Crystalline Phase Content and Morphology of Poly(Vinylidene Fluoride). *Journal of Polymer Science Part B-Polymer Physics* **1994**, *32* (5), 859–870. https://doi.org/10.1002/polb.1994.090320509.

(62) Gregorio, R.; Capitao, R. Morphology and Phase Transition of High Melt Temperature Crystallized Poly(Vinylidene Fluoride). *Journal of Material Science* **2000**, *35* (2), 299–306. https://doi.org/10.1023/A:1004737000016.

(63) Benz, M.; Euler, W. B. Determination of the Crystalline Phases of Poly(Vinylidene Fluoride) under Different Preparation Conditions Using Differential Scanning Calorimetry and Infrared Spectroscopy. *J Appl Polym Sci* **2003**, *89* (4), 1093–1100. https://doi.org/10.1002/app.12267.

(64) Zhang, G.; Weng, L.; Bao, R.; Hu, Z.; Li, W.; Qin, S.; Yang, S.; Zhang, X.; Li, M. Y.; Jiang, S. Significantly Enhanced Ferroelectric and Pyroelectric Properties in Polyvinylidene Fluoride Induced by Shear Force with Spin-Coating. *Journal of Materials Science: Materials in Electronics* **2019**, *30* (13), 12540–12544. https://doi.org/10.1007/s10854-019-01614-4.

(65) Kumar, C.; Viswanath, P. Solvent Driven Polymorphism in Langmuir and Langmuir Schaefer Film of Poly(Vinylidene Fluoride). *Eur Polym J* **2017**, *86*, 132–142. https://doi.org/10.1016/j.eurpolymj.2016.11.021.

(66) Chinaglia, D. L.; Gregorio, R.; Stefanello, J. C.; Altafim, R. A. P.; Wirges, W.; Wang, F.; Gerhard, R. Influence of the Solvent Evaporation Rate on the Crystalline Phases of Solution-Cast Poly(Vinylidene Fluoride) Films. *J Appl Polym Sci* **2010**, *116* (2), 785–791. https://doi.org/10.1002/app.31488.

(67) Zheng, J.; He, A.; Li, J.; Han, C. C. Polymorphism Control of Poly(Vinylidene Fluoride) through Electrospinning. *Macromol Rapid Commun* **2007**, *28* (22), 2159–2162. https://doi.org/10.1002/marc.200700544.

(68) He, X.; Yao, K. Crystallization Mechanism and Piezoelectric Properties of Solution-Derived Ferroelectric Poly(Vinylidene Fluoride) Thin Films. *Appl Phys Lett* **2006**, *89* (11). https://doi.org/10.1063/1.2352799.

(69) Viswanath, P.; Kumara, L. S. R.; Kesava Rao, V.; Kanishka, K.; De Silva, H.; Ryo, M.; Yoshimura, M. *GIWAXS Measurement of Ultrathin Organic Ferroelectric Polymers*; 2021.

(70) Tocci, E.; Rizzuto, C.; Macedonio, F.; Drioli, E. Effect of Green Solvents in the Production of PVDF-Specific Polymorphs. *Ind Eng Chem Res* **2020**, *59* (12), 5267–5275. https://doi.org/10.1021/acs.iecr.9b06701.

(71) Fadeeva, Y. A.; Demina, L. I.; Gorbunova, Y. G.; Shmukler, L. E.; Safonova, L. P.; Tsivadze, A. Y. Orthophosphoric Acid-N,N-Dimethylformamide System: IR Study. *Russian Journal of Coordination Chemistry* **2003**, *29* (7), 515–518. https://doi.org/10.1023/A:1024791332656.

(72) Salimi, A.; Yousefi, A. A. Conformational Changes and Phase Transformation Mechanisms in PVDF Solution-Cast Films. *Journal of Polymer Science Part B-Polymer Physics* **2004**, *42* (18), 3487–3495. https://doi.org/10.1002/polb.20223.

(73) Gutiérrez-Fernández, E.; Cui, J.; Martínez-Tong, D. E.; Nogales, A. Preparation, Physical Properties, and Applications of Water-Based Functional Polymer Inks. *Polymers* **2021**, *13* (9). https://doi.org/10.3390/polym13091419.

(74) Horibe, H.; Sasaki, Y.; Oshiro, H.; Hosokawa, Y.; Kono, A.; Takahashi, S.; Nishiyama, T. Quantification of the Solvent Evaporation Rate during the Production of Three PVDF Crystalline Structure Types by Solvent Casting. *Polym J* **2014**, *46* (2), 104–110. https://doi.org/10.1038/pj.2013.75.

(75) Li, X.; Wang, Y.; He, T.; Hu, Q.; Yang, Y. Preparation of PVDF Flexible Piezoelectric Film with High β-Phase Content by Matching Solvent Dipole Moment and Crystallization Temperature. *Journal of Materials Science: Materials in Electronics* **2019**, *30* (22), 20174–20180. https://doi.org/10.1007/s10854-019-02400-y.

Chapter 7

Photodegradation of methylene blue mediated by P3HT nanoparticles prepared by flash and miniemulsion: A comparative study and analysis of degradation products

Graphical abstract representing the main idea of Chapter 7

Universidad Complutense de Madrid

Jose Sena Fernández

Micro and Nanoparticles of Functional Polymers: From Fundamentals to Applications

As mentioned in the introduction section, the utilisation of light as an energy source in the context of organic pollutant degradation has emerged as an appealing strategy in environmental remediation. The growing incidence of water pollution, particularly that attributable to organic dyes such as textile dyes, poses a significant environmental threat due to its potential consequences for human health and the environment[1,2]. The toxicity, carcinogenicity, and resistance to biodegradation of these dyes are of particular concern[2,3]. In this context, considerable attention has been focused on the development of efficient photocatalytic materials for dye degradation under visible light.

Methylene Blue (MB) is a cationic dye extensively utilised in numerous industries and notably the textile industry[4]. MB serves as a representative model pollutant for evaluating photocatalytic performance. In this chapter, it is described the degradation of MB using NPs of P3HT. The intrinsic capacity of P3HT to induce the generation and transport of charges when excited by light, which in turn induces redox reactions, facilitates the photochemical formation of reactive oxygen species (ROS) (•OH and O_2•$^-$ radicals), including hydroxyl radicals and superoxide[5–8]. These, in turn, enable the oxidation, mineralisation, and transformation of organic compounds that are highly resistant to conventional processes[9,10].

Nevertheless, the effective implementation of semiconductor polymers in wastewater treatment is challenging. The photooxidation of the polymer itself when reactive species are formed and its limited solubility in aqueous media are critical aspects that must be addressed to ensure the efficiency and stability of the photocatalytic process[11–13]. The strategy of dispersing semiconductor polymers in the form of NPs has emerged as a promising approach to overcome the solubility issue by increasing the contact surface area with the aqueous medium and the pollutant, optimising light-harvesting and providing a means to address water pollution more efficiently[13–18]. As previously described in this thesis, the fabrication of P3HT NPs in stable dispersion within aqueous media is a facile process, thereby enabling its use in aqueous-phase applications[19,20]. In addition, it has been determined that the diverse methodologies employed for NP preparation, whether through flash nanoprecipitation or miniemulsion, exert a substantial influence on their physical and structural properties, including crystallinity, morphology, and optical characteristics. These properties are closely linked to the photocatalytic efficiency of the material, particularly due to their effects on crystallinity, exciton diffusion, and light-harvesting.

In view of these findings, the aim of this chapter is to investigate how such differences in NP preparation affect the photocatalytic performance of P3HT NPs as photocatalysts

under visible light irradiation[20–22]. The experimental setup and conditions for photodegradation are detailed in Section 2.5. In particular, as demonstrated in Chapter 3, for flash NPs, the aging effect of the precursor solutions influences the morphology, crystallinity, and optical properties of the NPs, which are determining factors for the generation of ROS[5,23,24]. In this chapter, the effect of this aging process on the efficiency of the flash NPs as a photocatalyst is investigated. In the case of miniemulsion NPs, whose physical properties have been discussed in detail in Chapter 4, the different preparation conditions, especially related to the absence or presence of sonication of the precursor emulsion, modulate the physical properties like NP size and dispersion, as well as crystallinity and properties[25]. These factors could significantly impact the efficiency of MB degradation[23,24]. To evaluate the performance of both types of P3HT NPs, the decrease in MB concentration was monitored by UV-Vis spectroscopy, and kinetic constants were calculated.

7.1. Photolysis of methylene blue in the absence of photocatalyst: A control study

The degradation of MB under conditions of darkness and light exposure using the lamp has been followed by the evolution of the UV-Vis spectra as a function of time (see Figure 7.1). For this purpose, 1 mL of Milli-Q water and 0.1 mL of the 15 mg/L MB solution are added to each experiment.

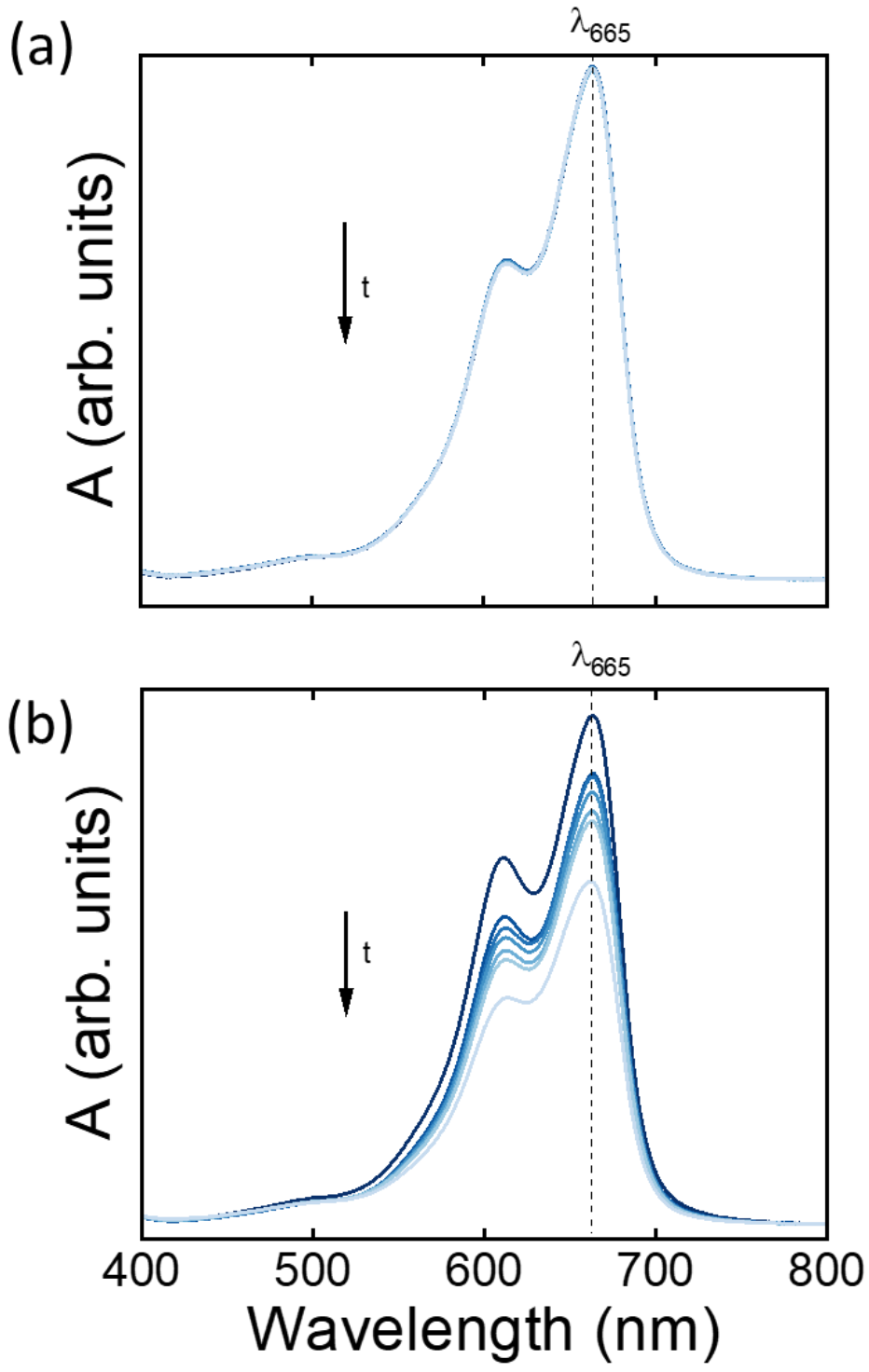

Figure 7.1. UV-Vis spectra obtained for the MB solution for 0, 30, 60, 90, 120 and 240 minutes under **(a)** darkness and **(b)** light exposure.

Figure 7.1 shows that, in the absence of light, MB does not undergo degradation. However, when irradiated, the MB exhibits degradation, as evidenced by the reduction in intensity of the UV-Vis spectrum. As previously stated in section 2.4.4.1, the concentration

of MB is calculated from the Lambert-Beer equation (Eq. 2.19) based on the extinction coefficient at 665 nm.

Figure 7.2 presents the concentration of MB as a function of time. It is possible to study the reaction kinetics by determining the initial concentration, $C_{MB}(0)$, and the concentration after a given time of exposure, $C_{MB}(t)$. It is noted that the concentration of MB exhibits negligible degradation in the dark, as demonstrated in Figure 7.1, and no reaction kinetics is observed, as evidenced by the reaction constant of the fit being equal to 0. Nevertheless, the degradation of irradiated MB follows zero-order kinetics (Eq. 7.1) with a kinetic constant of 9.20×10^{-4} mg*L^{-1}*min^{-1}.

$$\frac{C_{MB}(t)}{C_{MB}(0)} = 1\text{-}kt \qquad \text{Eq. 7.1.}$$

Where k is the zero-order rate constant and t is the time. This phenomenon can be understood by considering the fact that the only component in question is the contaminant itself, and the degradation rate is independent of the concentration of MB because the photon flux limits the reaction rate. The rate of degradation of the contaminant is solely dependent upon the rate constant and is independent of the concentration of the contaminant. Consequently, the half-life ($t_{1/2}$), defined as the time required for the concentration of MB to decrease to half of its initial value, is expressed for order zero reactions as:

$$t_{1/2} = \frac{1}{2k} \qquad \text{Eq. 7.2.}$$

For irradiated MB, with a $C_{MB}(t)/C_{MB}(0)$ of 1, its half-life was determined to be 543 minutes.

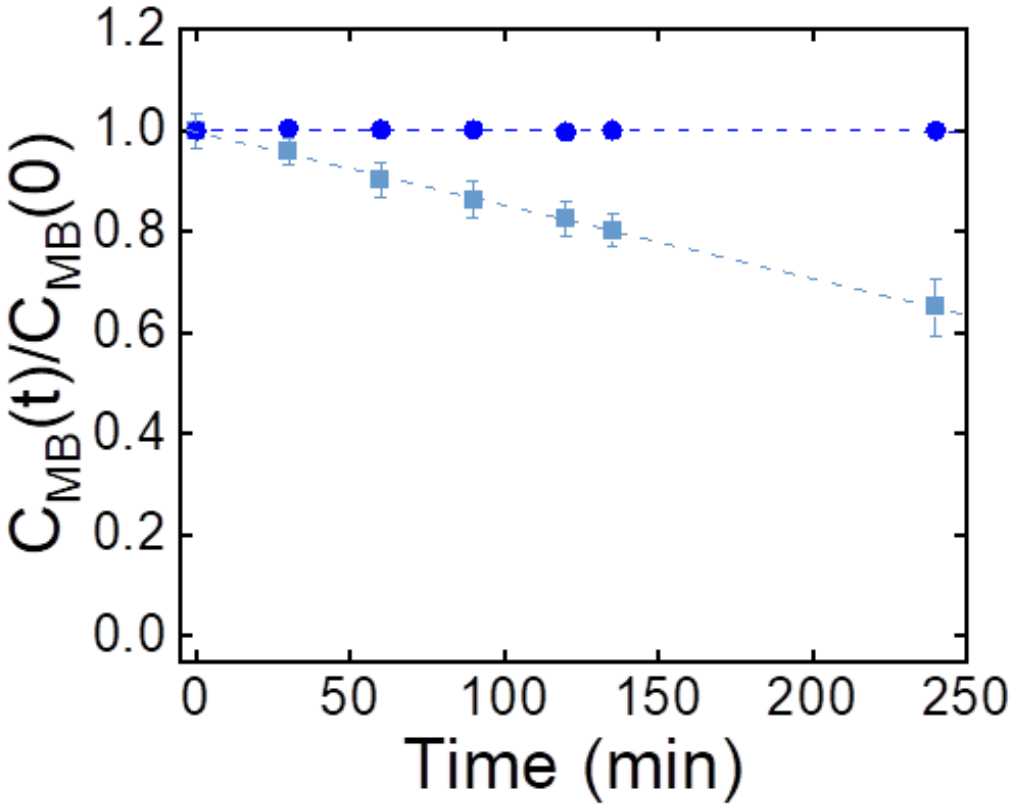

Figure 7.2. MB concentration versus time. The graph shows unirradiated MB (●) and irradiated MB (■). A fit has been performed to obtain the kinetic parameters, represented by the dotted lines. Although the relative error in the normalised concentration increases at low $C(t)/C_0$ values, this is a consequence of the intrinsic nature of the ratio and the associated propagation of uncertainty, and does not reflect a lack of reliability in the experimental trend.

Figure 7.3 illustrates the photodegradation efficiency in terms of variations of the concentration measured from UV-Vis. The photodegradation activity is defined:

$$\chi\ (\%) = \frac{c_{MB}(0) - c_{MB}(t)}{c_{MB}(0)} \times 100 \qquad \text{Eq. 7.3.}$$

As expected, Figure 7.3 illustrates that MB exhibits no degradation in darkness; however, it does demonstrate degradation in the presence of light even in the absence of a photocatalyst. The linear increase in degradation efficiency with time directly reflects the zero-order kinetics previously determined from the concentration data shown in Figure 7.2. MB is a photosensitive compound and can undergo photolysis under visible or UV light,

especially in the presence of oxygen[26,27]. The excited singlet or triplet state of MB may react with oxygen, forming ROS. These ROS have been implicated in the subsequent degradation of MB[26,27].

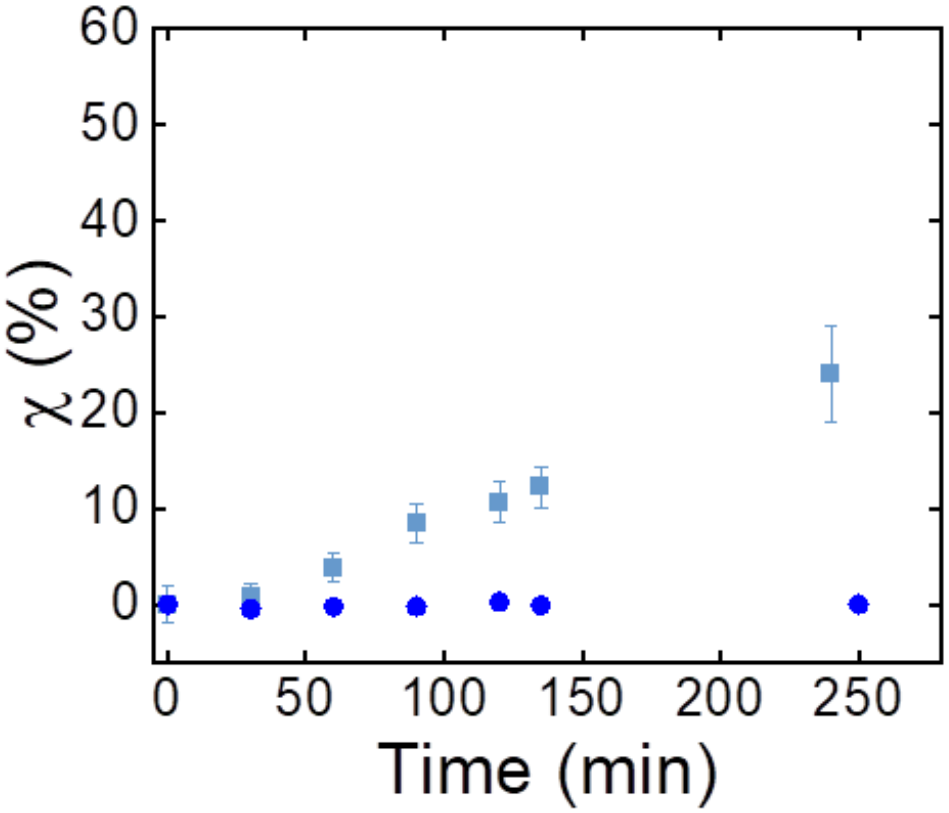

Figure 7.3. The degradation efficiency (χ, %) of MB as a function of light exposure time (min) (■). As a control, the efficiency for an unilluminated sample is presented (●).

In the following chapters, a study will be conducted on whether the degradation with P3HT NPs is more efficient.

7.2. Evaluation of the intrinsic photostability of P3HT nanoparticles under irradiation

Following the analysis of MB degradation in the absence of P3HT NPs, it was important to assess the intrinsic photostability of the P3HT NPs to ensure that any observed catalytic activity is not affected by photodegradation of the polymer NPs. Previous studies have suggested that the polymer utilised in photocatalysis may be susceptible to self-degradation[11,12,28], which could impact the rate of pollutant degradation and the number of cycles over which the photocatalyst can be employed. In the case of P3HT, degradation may be attributable to chain cleavage or oxidation of the polymer. This phenomenon can be monitored in the UV-Vis spectrum through two distinct mechanisms: firstly, a decrease in the intensity of the bands; secondly, a change in their shape or position.

Therefore, in this Section, a study of the photostability of P3HT NPs prepared by the miniemulsion method and the flash method is presented. To perform this assessment, 1 mL of Milli-Q water and 0.1 mL of the P3HT NPs dispersion have been added and irradiated. One representative preparation from each method has been selected for analysis: the NPs obtained from 168 h aged solutions in the case of flash, and the NPs sonicated in an ultrasonic bath in the case of miniemulsion.

Figure 7.4 (a) and Figure 7.4 (b) shows the UV-Vis spectra for both NPs. It can be observed that, even after 240 minutes of irradiation, only a slight decrease in absorbance is observed, indicating that MB degradation kinetics can be reliably evaluated over the irradiation period, and that multiple degradation cycles could be performed without significant catalyst loss. This phenomenon may be attributed to the fact that, in the solid state, the effects produced in the P3HT are minimised.

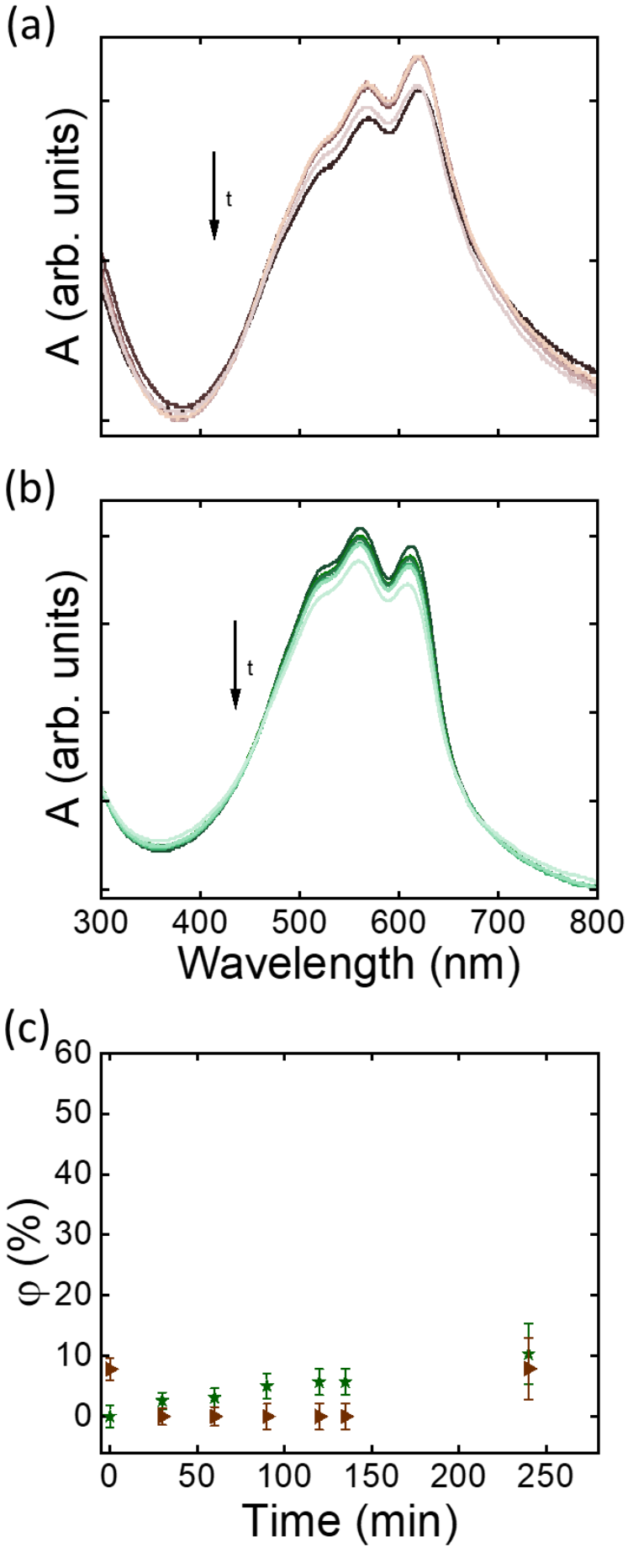
(a)
A (arb. units)
t
(b)
A (arb. units)
t
300
400
500
600
700
800
Wavelength (nm)
(c)
φ (%)
60
50
40
30
20
10
0
0
50
100
150
200
250
Time (min)

Figure 7.4. UV-Vis spectra of: **(a)** P3HT NPs prepared via flash with solutions aged for 168 hours and **(b)** P3HT NPs prepared via miniemulsion with bath sonication at different light exposure times: 0, 30, 60, 90, 120 and 240 minutes and **(c)** The degradation efficiency (φ, %) of P3HT NPs prepared by flash (▶) and miniemulsion (★).

The degradation activity of the P3HT NPs is defined as:

$$\varphi\ (\%) = \frac{A(0)-A(t)}{A(0)} \times 100 \qquad \text{Eq. 7.4.}$$

As shown in Figure 7.4 (c), analogous to that used for MB in Figure 7.3, P3HT exhibits minimal degradation under both preparation conditions, with efficiencies remaining below 11% over the experimental period. This excellent photostability confirms that the observed photocatalytic activity originates from MB degradation rather than decomposition of the P3HT catalyst.

7.3. Photocatalytic activity of P3HT flash nanoparticles prepared from fresh and aged solutions in the degradation of methylene blue

To assess the photocatalytic activity of the different types of flash NPs, those prepared with an initial concentration of 3 g/L and a solvent-antisolvent volume ratio, R = 1/6, were utilised for analysis. Therefore, the final concentration is 0.5 g/L. For the purpose of this study, NPs will be prepared from both fresh solutions and solutions that have been aged for 168 hours. Photodegradation tests were performed in aqueous MB solutions, as explained in detail in Section 2.5.

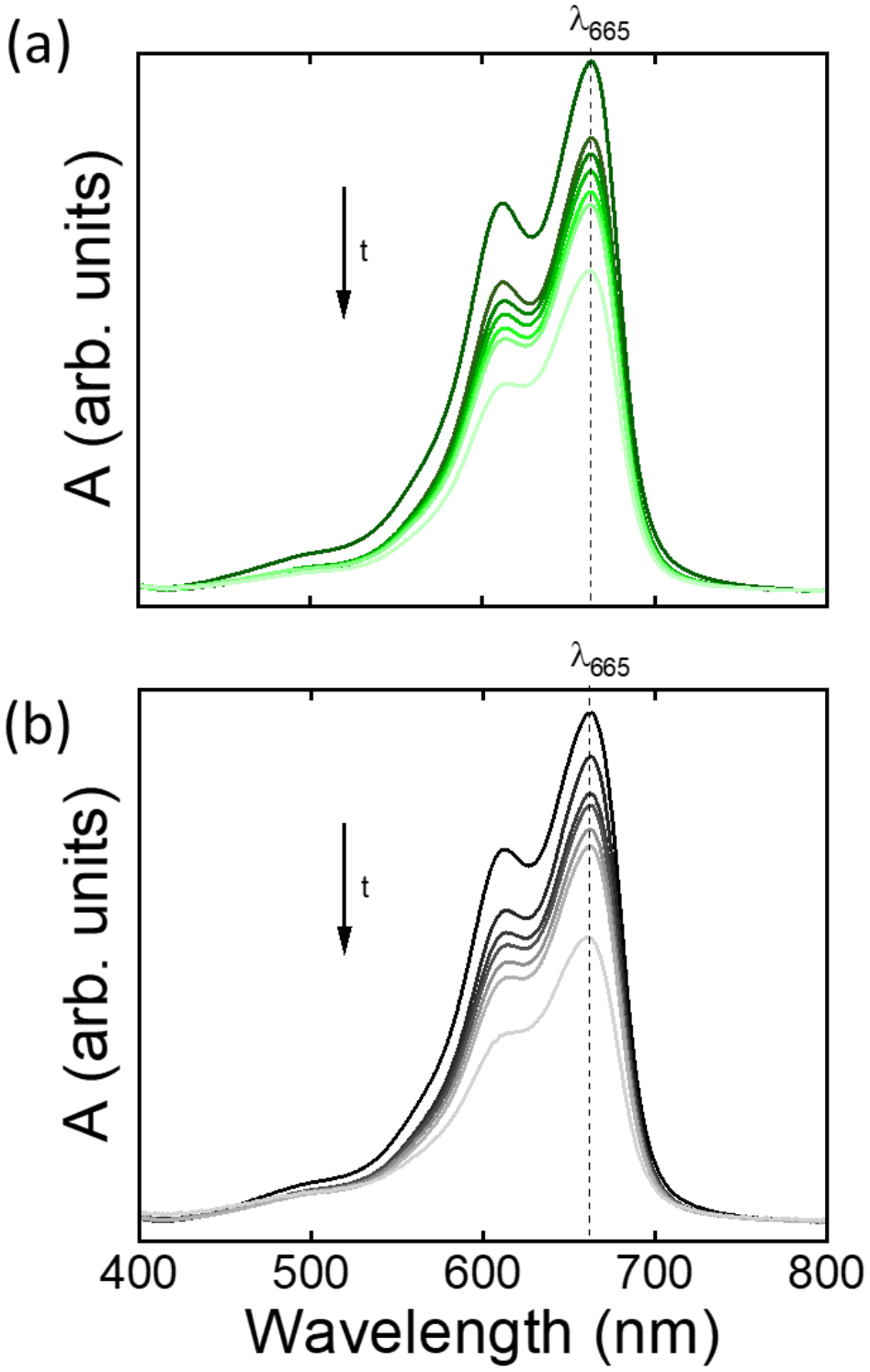

Figure 7.5. MB solution UV-VIS spectra obtained for initial mixture and after light exposure for 0, 30, 60, 90, 120 and 240 min in the presence of flash P3HT NPs prepared from **(a)** unaged solutions and **(b)** 168 h aged solutions.

Upon initial observation, a bleaching or loss of blue colouration in the sample is detected. Figure 7.5 shows the UV-Vis spectra of MB solutions exposed to lamp light for varying times in the presence of P3HT NPs prepared by flash from unaged solutions (Figure 7.5 (a)) and for the solution aged for 168 hours (Figure 7.5 (b)). The MB spectrum displays a pronounced absorption band at 665 nm (see Section 2.1.2.2), which is utilised to estimate the MB concentration of the studied solutions employing the Lambert-Beer Law (Eq. 2.19). In order to eliminate the contribution of P3HT absorption, a fit of the measured MB spectra with NPs was performed to establish the contribution of each component (see Figure 7.6).

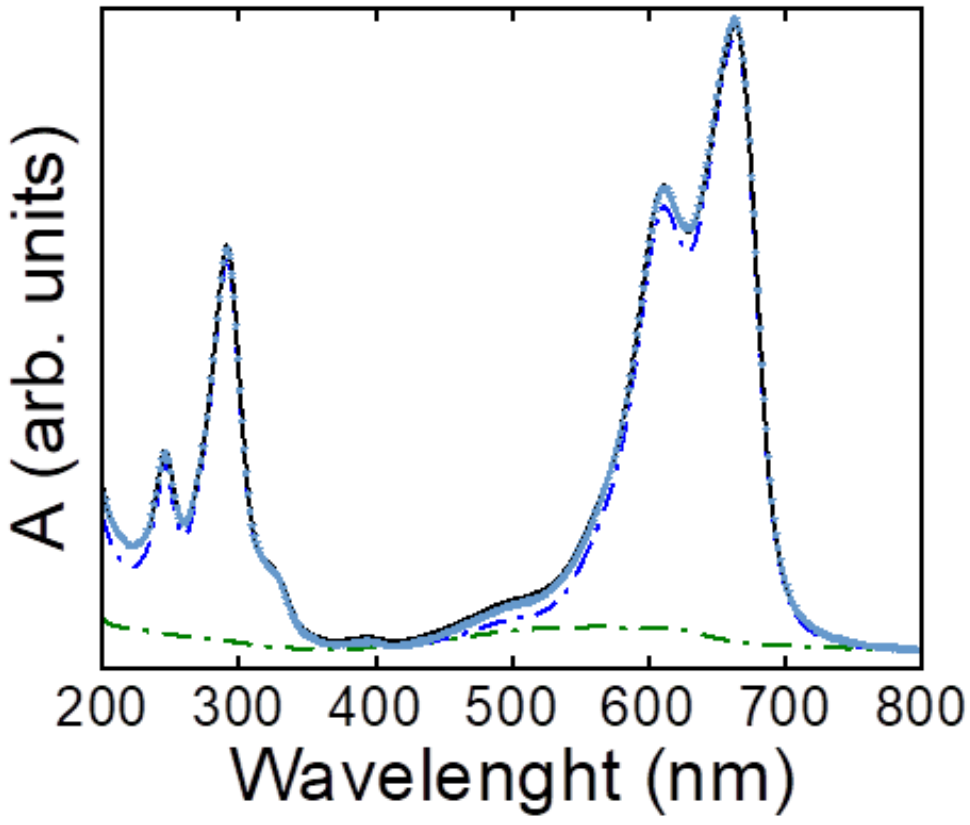

Figure 7.6. Fitting (black line) of the UV-Vis spectrum of the MB dispersion with P3HT NPs prepared for flash from fresh solutions (★), through the UV-Vis spectra of the MB solution (blue dashed dot lines) and the P3HT NP dispersion (green dashed dot lines).

The concentration of MB was then calculated from the contributions that were obtained. As demonstrated in Figure 7.5, both experiments exhibited a decrease in absorption,

suggesting a reduction in the concentration of MB. This reduction is more pronounced in NPs prepared from aged solutions. Moreover, an increase in the time of irradiation is accompanied by a shift towards lower wavelengths. To enhance comprehension of the impact of NPs on photodegradation, the kinetics of MB disappearance was analysed for the three experiments (Figure 7.7), resulting in the determination of both the MB disappearance rate constant, k, and its half-life, $t_{1/2}$. In the preceding section, both parameters were obtained for MB degradation in the absence of NPs ($k = 9.20 \times 10^{-4}$ mg*L^{-1}*min^{-1} and $t_{1/2} = 543$ min). In the case of degradation with NPs, the reaction order is pseudo-first order (Eq. 7.4) as the presence of a catalyst exerts no influence on the disappearance reaction, only on the kinetics, and the velocity only depends on the concentration of MB. This is in agreement with results from the literature[28–32].

$$\ln\left(\frac{c_{MB}(0)}{c_{MB}(t)}\right) = k_{app}t \qquad \text{Eq. 7.5.}$$

where k_{app} represents an apparent first-order rate constant. This phenomenon can be attributed to the fact that other factors influence the degradation process in addition to those that influence MB degradation in the absence of a photocatalyst. When NPs are utilised, the light is primarily absorbed by the NPs, which generates excitons that, in turn, form ROS. These ROS are responsible for the degradation of pollutants. The half-life is expressed as follows:

$$t_{1/2} = \frac{\ln 2}{k_{app}} \qquad \text{Eq. 7.6.}$$

For P3HT NPs prepared from unaged solution, the rate constant (k_{app}) is determined to be 1.54×10^{-3} min^{-1}, with a half-life ($t_{1/2}$) of 450 min, thereby reducing the time required to degrade half of the contaminant. In the case of aged NPs, $k_{app} = 2.11 \times 10^{-3}$ min^{-1} and $t_{1/2} =$ 329 min, thereby reducing the time required to degrade half of the contaminant considerably, which confirms its greater effectiveness as a photocatalyst.

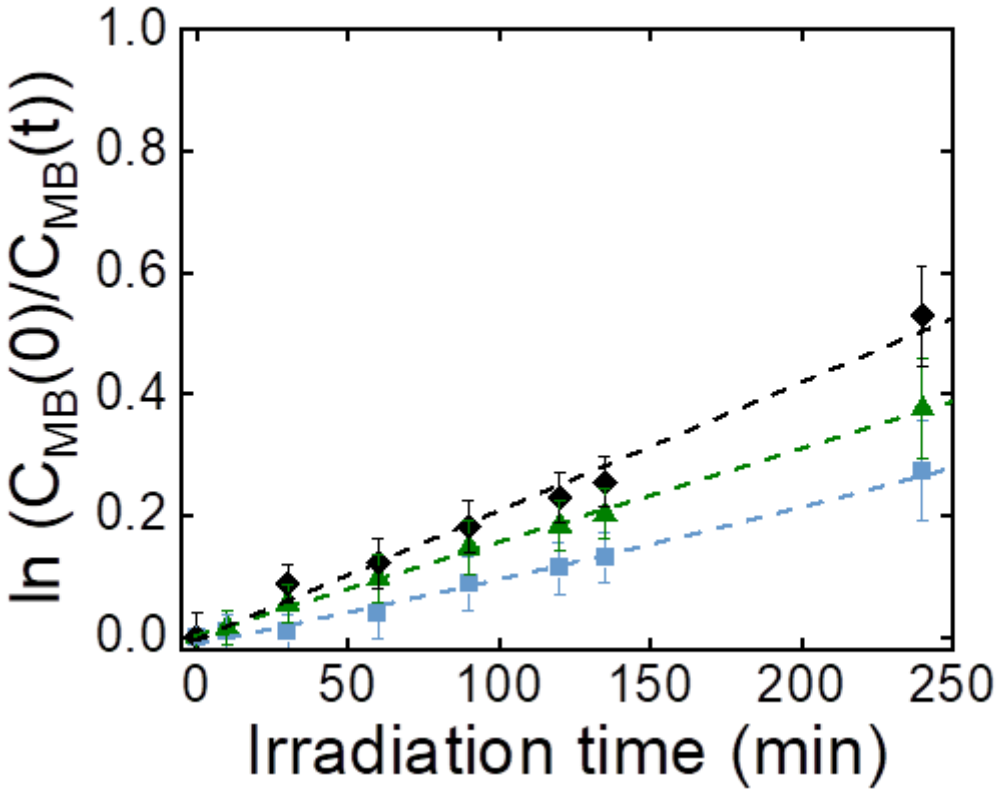

Figure 7.7. Plot showing the natural logarithm of MB concentration versus irradiation time. The blue symbols (■) represent irradiated MB, the green symbols (▲) represent irradiated MB with P3HT NPs from unaged solutions, and the black symbols (◆) represent irradiated MB with P3HT NPs from solutions aged for 168 hours. The dotted lines show the fitted model used to obtain the kinetic parameters. In the case of the MB, being a zero-order reaction, the natural logarithm of the fit has been represented.

Figure 7.8 shows the degradation efficiency versus exposure time of the MB solution without P3HT NPs and the MB solution in the presence of both types of P3HT NPs. The efficiency of MB degradation only by light exposure is also compared.

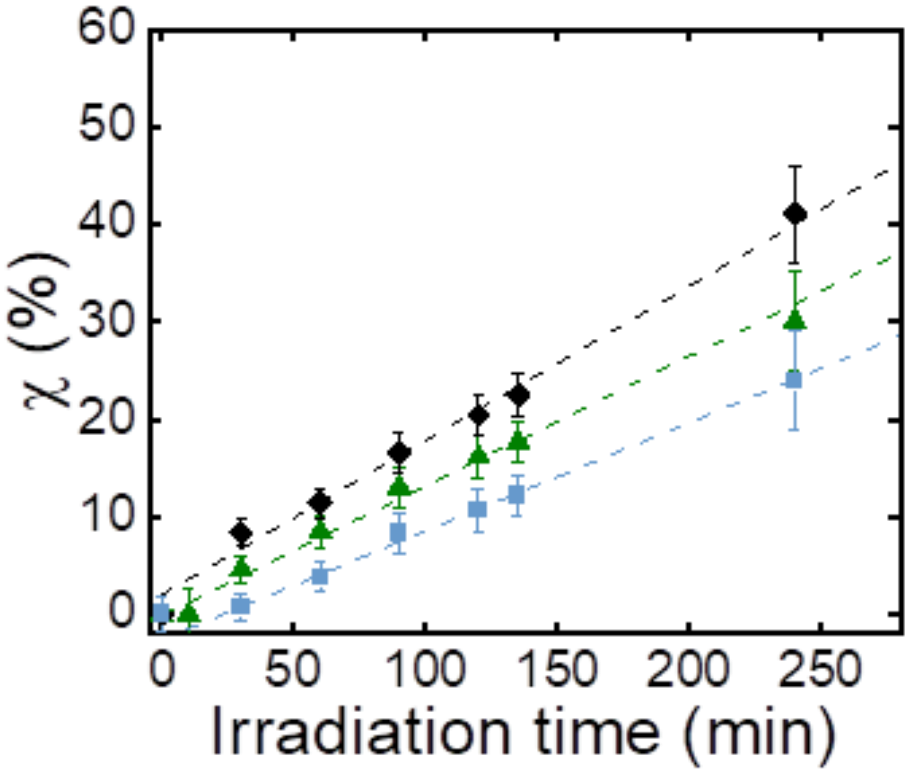

Figure 7.8. The degradation efficiency (χ(%)) is plotted as a function of irradiation time in the presence of flash NPs prepared from unaged (▲) and 168-hour (◆) solutions. For comparison, the degradation of MB by light alone is shown (■).

Figure 7.8 indicates that degradation is observable in all three experiments, with the presence of P3HT NPs enhancing this degradation, particularly when the NPs are prepared from aged solutions. It is suggested that this result may be attributable to the factors discussed in Chapter 3. Specifically, the NP diameter of NPs prepared through aged solutions exhibits a slight decrease, reducing the distance that an exciton or electron-hole pair needs to reach the surface, with a diffusion of approximately 10-20 nm. Also, Chapter 3 demonstrated that aging the solutions produces NPs with higher crystallinity, together with an increase in the coherence length, larger crystallite sizes and reduced structural defects. It has been proposed that these defects function as non-radiative recombination centres for excitons[33]. The results obtained demonstrate an enhancement in the chain ordering, thereby facilitating the diffusion of excitons within or between chains within the polymer[33]. This effect reduces the undesirable exciton recombination process, leading to an extended exciton lifetime. As a result, there is an increase in the probability of charge separation on the polymer

surface, thus enhancing the generation of ROS, which are responsible for the degradation of MB. Nevertheless, an elevated proportion of the amorphous state may impede exciton diffusion. Additionally, an increase in crystallinity in the NPs has been demonstrated to affect their optical properties significantly. For instance, the NPs prepared from the 168-h solution demonstrate a higher proportion of J-aggregates, i.e., intrachain coupling that favours charge mobility[34–38]. The enhancement in charge mobility within these J-aggregates facilitates the transport of electrons and holes to the active sites on the NP surface. Moreover, the heightened crystallinity of aged flash NPs is reflected in a narrower optical band gap (from 1.95 eV to 1.85 eV), thereby facilitating the transition of photoexcited electrons to the conduction band. This, in turn, results in an enhancement of photon absorption efficiency under the same light source, leading to the generation of a greater number of electron-hole pairs available for photocatalysis[39]. Taken together, these factors account for the superior photocatalytic efficiency observed with aged flash NPs.

7.4. The influence of sonication intensity on the photocatalytic efficiency of P3HT nanoparticles prepared by miniemulsion.

This section presents a study of P3HT NPs with an initial concentration of 3 g/L, prepared by miniemulsion using different sonication intensities. As discussed in Chapter 4, the application of different sonication intensities allows tuning of the NP characteristics. In order to later compare with the results obtained for flash NPs and presented in the previous section, the NPs dispersions prepared by miniemulsion were diluted to achieve the same theoretical concentration as the samples prepared by flash (0.5 g/L). In the experiments presented in this section, non-sonicated NPs, sonicated in an ultrasonic bath, and sonicated in a probe with an amplitude of 35% were selected for studying the impact of sonication during the NPs preparation on their photocatalytic efficiency. As is the case with the flash process, a bleaching of the mixture is observed as the irradiation time progresses. Figure 7.9 presents the UV-Vis spectra obtained during the photodegradation experiments using the three mentioned miniemulsion NPs as photocatalysts, non-sonicated NPs (Figure 7.9 (a)), bath-sonicated NPs (Figure 7.9 (b)), and probe-sonicated NPs (Figure 7.9 (c)). In all experiments, a clear reduction in the intensity of the spectra is shown as the samples are irradiated, with a more pronounced decrease in the bath-sonicated NPs. No significant

changes in the shape of the absorption spectra of the dye are observed during the irradiation process.

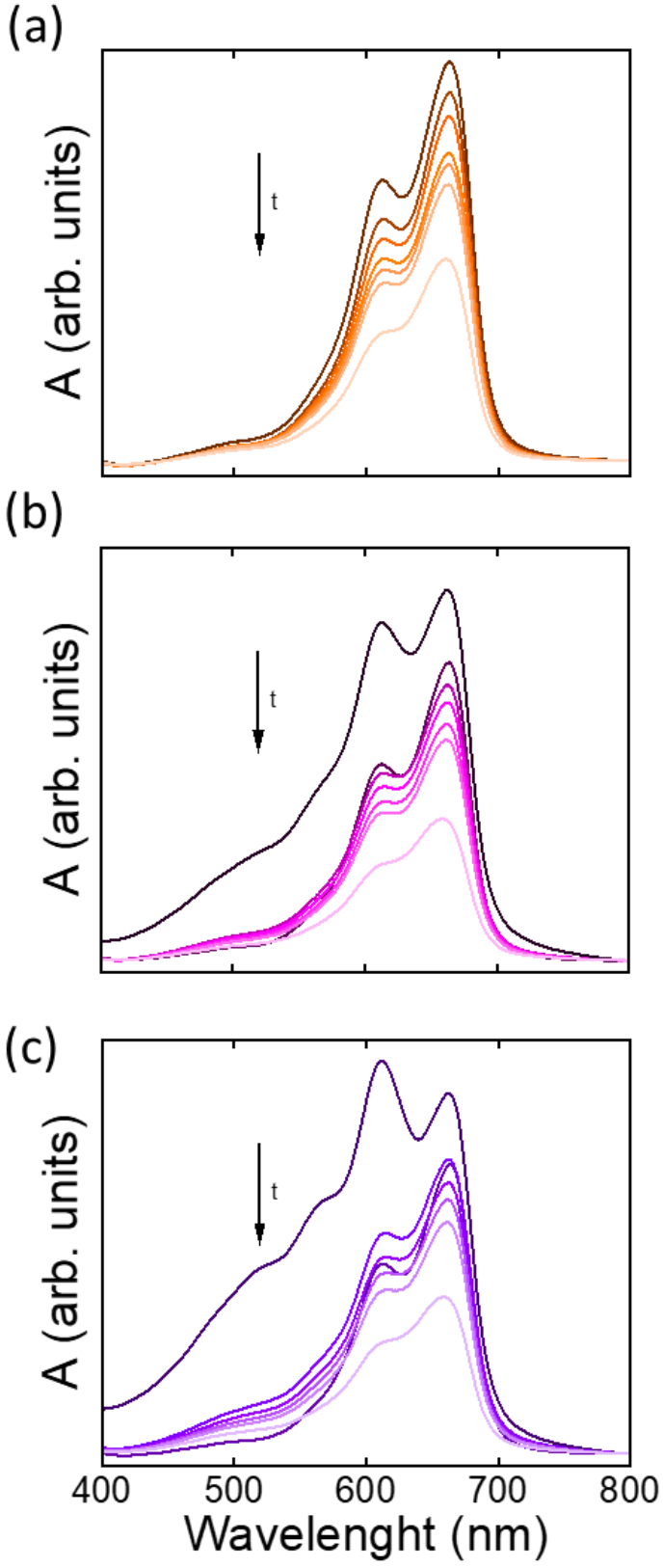

Figure 7.9. UV-Vis spectra of MB solutions recorded after 0, 30, 60, 90, 120 and 240 minutes of light exposure in the presence of P3HT nanoparticles prepared by miniemulsion: **(a)** without sonication, **(b)** sonicated using an ultrasonic bath and **(c)** sonicated using a probe at 35% amplitude.

As with the case of flash, in order to eliminate the contribution of P3HT absorption, a fit of the measured MB spectra with NPs was performed to establish the contribution of each component (see Figure 7.10).

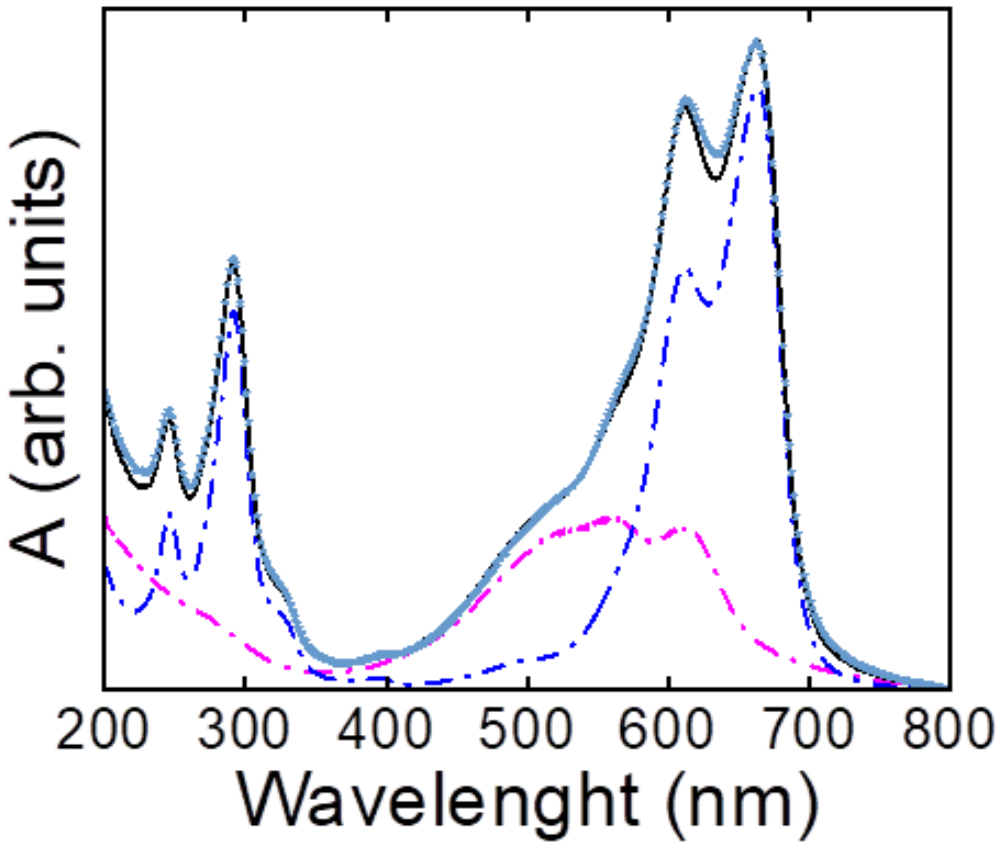

Figure 7.10. Fitting (black line) of the UV-Vis spectrum of the MB dispersion with P3HT NPs prepared via miniemulsion from solutions sonicated in a bath (★), through the UV-Vis spectra of the MB solution (blue dashed dot lines) and the P3HT NP dispersion (pink dashed dot lines).

The Lambert-Beer equation (Eq. 2.19) calculated the MB concentration after eliminating the contribution of NPs in the spectra (see Section 2.4.4.1). To determine the kinetics of MB

disappearance, the k_{app} and $t_{1/2}$ were calculated using Equations 7.5 and 7.6. Figure 7.11 shows the fit. Notably, all MB disappearance reactions with NPs follow a pseudo-first-order reaction. For all NPs, both the rate constant and the $t_{1/2}$ indicate enhanced degradation. The best values are found for the bath sonicated NPs with $k_{app} = 2.87 \times 10^{-3}$ min^{-1} and $t_{1/2} = 241$ min. The probe sonicated NPs also demonstrate degradation characteristics, exhibiting a value of $k_{app} = 2.42 \times 10^{-3}$ min^{-1} and a $t_{1/2} = 262$ minutes. However, the least effective degradation is observed in the non-sonicated NPs, with values of $k_{app} = 2.41 \times 10^{-3}$ min^{-1} and $t_{1/2} = 288$ minutes. This finding confirms the influence of the preparation conditions on the effectiveness of the photocatalyst. As demonstrated by Hoffmann et al.[40] and Kudo et al[41], the surface properties and the electronic structure of photocatalysts are critical in determining the overall efficiency of photocatalytic reactions.

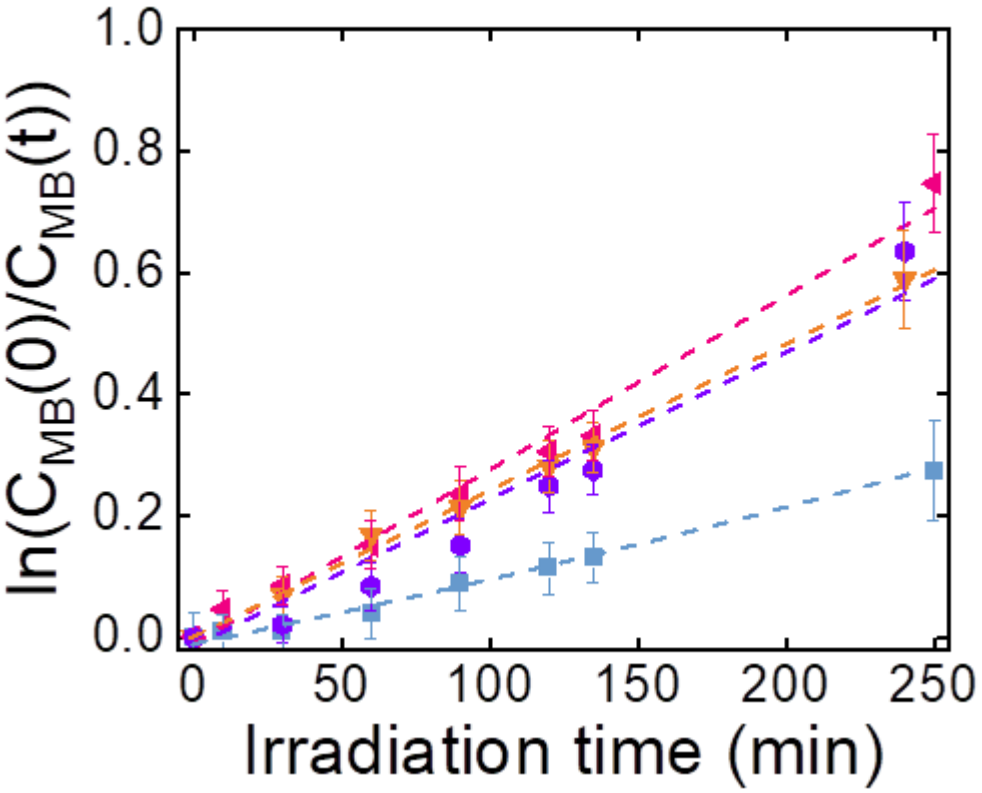

Figure 7.11. Plot of the natural logarithm of the MB concentration versus the irradiation time. Irradiated MB without NPs (■) and MB irradiated in the presence of P3HT NPs prepared by miniemulsion without sonication (▼), with bath sonication (◀), and with probe sonication at 35% amplitude (⬢) are represented. Dotted lines represent the fitted kinetic models used to calculate the

reaction parameters. In the case of MB, since it is a zero-order reaction, the natural logarithm of the adjustment has been represented.

Figure 7.12 demonstrates the degradation efficiency of the MB versus irradiation time. For all the NPs utilised, the degradation is greater than that of the MB irradiated exclusively with the lamp. However, it should be noted that the degradation efficiency of the NPs is dependent on the specific NPs employed in the process. The most effective NPs are those that were sonicated in a bath. This phenomenon can be attributed to a number of factors discussed in Chapter 4. The average particle size was found to be smaller than that of non-sonicated NPs, but similar to that of the probe-sonicated NPs. This enabled the exciton or electron-hole pair to reach the surface, limited to 10-20 nm. However, the bath sonicated NPs exhibit a reduced presence of aggregates, which is indicative of a higher surface area ratio. The aggregation of NPs, as observed in bath-sonicated NPs, is reduced, thus increasing the surface-to-volume ratio. This, in turn, results in greater exposure of the active sites and facilitates the diffusion of excitons to the surface, where they can effectively generate ROS. In addition, the bath sonicated NPs demonstrate higher crystallinity than the other NPs. Kudo et al.[41] pointed out that structure modification in inorganic photocatalysts significantly improves their electronic mobility and exciton formation efficiency. This same effect could occur in polymers such as P3HT. In conjugated polymers, a higher degree of crystallinity has been shown to favour more ordered chain packing (e.g., enhanced π–π interactions)[42–44]. This ordering reduces the density of charge traps and facilitates exciton mobility or charge transport along and between polymer chains, thereby leading to higher electron-hole pair separation efficiency and a reduction in non-radiative recombination, leading to increased charge availability for photocatalytic reactions at the surface. It should also be noted that probe-sonicated NPs present SDS crystalline domains within their structure, as revealed by XRD (Figure 4.5 (b)), exciton diffusion and thus influence their photocatalytic performance.

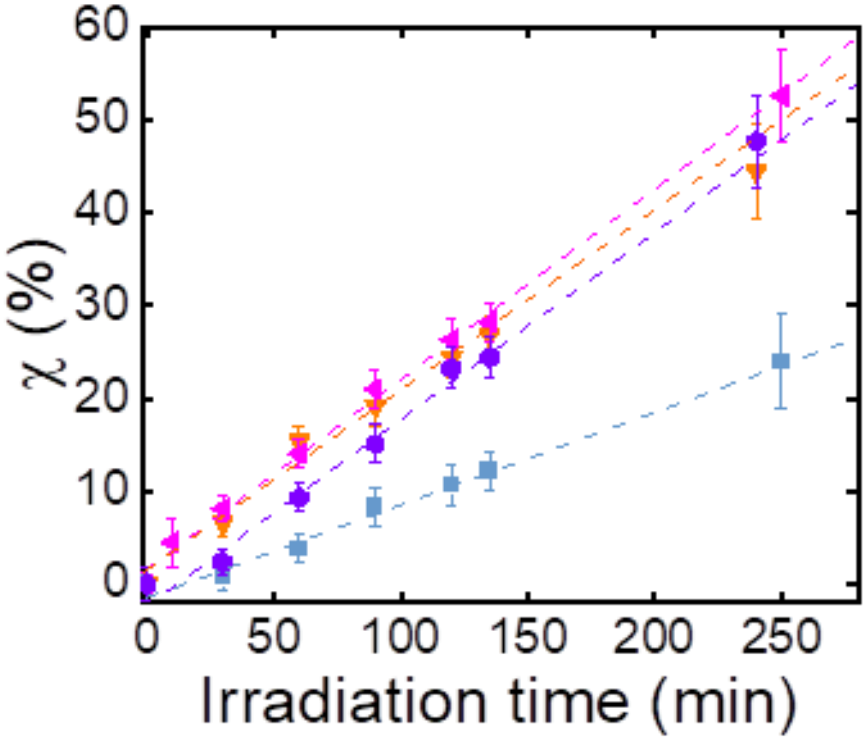

Figure 7.12. The efficiency of MB degradation (χ(%)) as a function of irradiation time. The plot compares the degradation efficiency of MB with NPs prepared using miniemulsion: non-sonicated samples (▼), bath-sonicated samples in (◀) and probe-sonicated samples in (⬢). For reference, the degradation of MB by light alone is also included (■).

7.5. Comparative photocatalytic performance of methylene blue: Nanoparticles prepared by flash vs prepared by miniemulsion

Finally, a comprehensive comparative study of photodegradation tests of MB in water was conducted using P3HT NPs prepared via flash and miniemulsion methods. These NPs exhibit distinct differences in optical absorption and excited-state lifetimes, as described in Chapter 5, which exert a direct influence on the rate of formation of ROS and, consequently, the overall photocatalytic activity[18,23,24,45].

Figures 7.5 (a) and 7.9 (b) display the UV–Vis spectra of MB solutions exposed to light for varying irradiation times in the presence of each type of P3HT NPs. In both cases, the

spectra exhibit an intense band at 665 nm, which is indicative of the MB concentration, as predicted by the Lambert–Beer equation (Section 2.4.4.1). A gradual decrease in the intensity of this peak is observed with increasing irradiation time, being particularly pronounced in the case of miniemulsion-prepared NPs.

The calculated kinetic parameters reinforce these observations. MB photolysis alone follows zero-order behaviour, limited by photon flux, whereas both flash and miniemulsion NPs mediate degradation via pseudo-first-order kinetics in line with the Langmuir–Hinshelwood model. Quantitatively, in the absence of a photocatalyst, MB exhibits a k = 9.20×10^{-4} mg*L^{-1}*min^{-1} and $t_{1/2}$ = 543 min. For the flash-prepared P3HT NPs, the pseudo-first-order rate constant improved to k_{app} = 2.11×10^{-3} min^{-1} and $t_{1/2}$ = 329 minutes. Miniemulsion-prepared NPs show an even greater enhancement, with a k_{app} = 2.87×10^{-3} min^{-1} and $t_{1/2}$ = 241 minutes.

Figure 7.13 summarises the degradation efficiency as a function of time for both NP types. The graph clearly indicates that the addition of P3HT NPs leads to a substantial enhancement in the MB degradation rate, with a notably greater effect observed for the miniemulsion-prepared NPs. This improved performance can be correlated with higher crystallinity and a shorter distance in the π–π packing direction associated with the presence of SDS. The amphiphilic nature of SDS also impacts the NP-water interface, potentially facilitating MB degradation through enhanced electron transfer. These features facilitate better charge transport and reduced exciton recombination, as previously discussed in Chapter 5. Optically, this enhanced order is manifest in more defined absorption bands and a smaller band gap for miniemulsion NPs, which promotes efficient electron excitation and subsequent exciton formation, leading to increased ROS generation. Furthermore, miniemulsion NPs exhibit a greater proportion of J-aggregates, where parallel and offset (head-to-tail) transition dipoles allow for enhanced exciton delocalisation and reduced energy dispersion[47]. Complementary fluorescence lifetime studies from Chapter 5 reveal that miniemulsion-prepared NPs show minimal fluorescence emission, indicating that absorbed photons are not re-emitted but instead drive exciton dissociation into electron-hole pairs or efficient charge transfer. This rapid exciton decay is associated with the formation of stable charge-separated states, thereby boosting the generation of ROS. In contrast, the greater structural disorder in flash-prepared NPs likely hinders efficient charge separation, leading to more exciton recombination. According to Hoffmann et al.[40], the rapid separation of

electron-hole pairs and minimisation of recombination are crucial aspects for an enhanced photocatalytic performance.

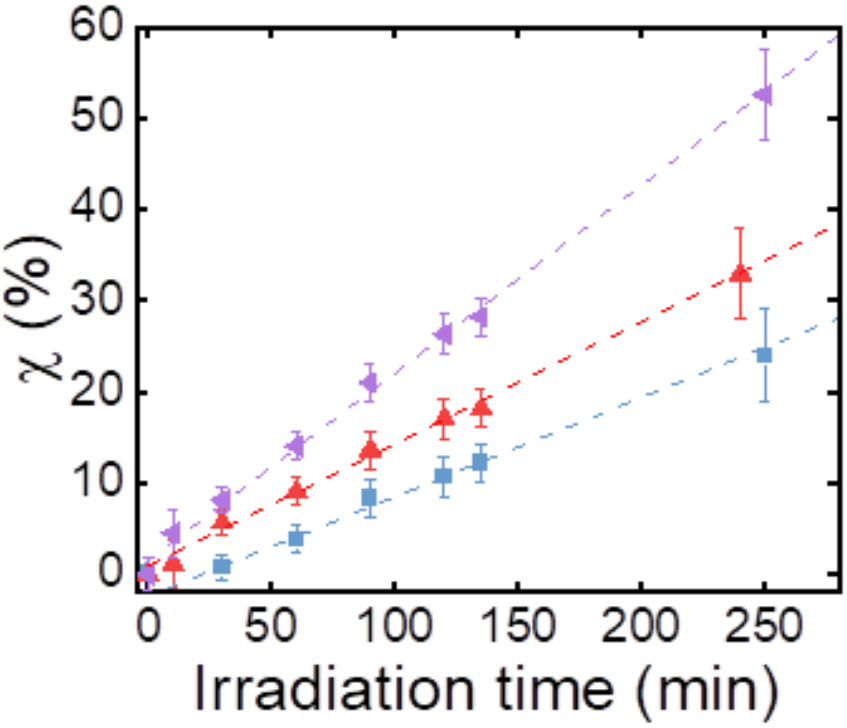

Figure 7.13. The efficiency of MB degradation (χ(%)) as a function of irradiation time. The plot compares the degradation efficiency of MB in the presence of P3HT NPs prepared by flash (▲), and P3HT NPs prepared by miniemulsion (◀). For reference, the degradation of MB by light alone is also shown (■).

A limited number of photodegradation experiments with P3HT have been documented in the extant literature for comparison with these results. For instance, Floresyona et al.[47] achieved a degradation of 15% in 240 minutes using phenol as a contaminant derived from P3HT NPs.

7.6. Adsorption of methylene blue onto P3HT nanoparticles in dark conditions

To accurately assess the photocatalytic activity of P3HT NPs, it is essential to distinguish between true degradation and the adsorption of MB onto the NP surface. Significant adsorption processes can lead to a reduction in dye concentration, which may be misattributed to photocatalytic degradation. This can compromise the accuracy of performance evaluations. Consequently, control experiments were conducted in the absence of light to determine the extent of MB adsorption on the surface of both flash-prepared and miniemulsion-prepared P3HT NPs, thereby distinguishing it from light-induced degradation effects.

For P3HT NPs prepared by the flash nanoprecipitation method using fresh solutions, suspensions were stored in conditions of darkness for two distinct time periods: 135 minutes and 360 minutes. The findings indicate that following 135 minutes of adsorption, there is an approximate decrease of 10% in MB concentration, while after 360 minutes, there is a slight increase of approximately 13%.

Similarly, experiments with P3HT NPs prepared by miniemulsion (specifically the bath-sonicated sample) were conducted under identical dark conditions. In this instance, the adsorption levels were approximately 9% at 135 minutes, rising to approximately 11% after 360 minutes. These values closely resemble those obtained for the flash-prepared NPs, indicating a comparable adsorption behaviour across preparation methods.

The adsorption levels observed for both types of P3HT NPs are relatively low and exhibit only a minor increase over prolonged periods in the dark. The findings indicate that the decrease in MB concentration observed during light-irradiated experiments is predominantly attributable to the photocatalytic degradation activity of the P3HT NPs, rather than passive adsorption phenomena.

7.7. LC-MS characterisation of methylene blue photodegradation: Demethylation and mineralisation pathways

To ensure that the action of light and NPs is degrading MB, and that the change in colour intensity is not due to only the formation of non-coloured derivatives such as leuco methylene blue or oxidised methylene blue[48–51], a comprehensive analysis of the degradation products generated during the photocatalytic process of the samples used in the experiments was performed after 240 minutes of irradiation using liquid chromatography coupled with mass spectrometry (LC-MS). LC-MS was selected due to its high sensitivity and selectivity in identifying low-concentration degradation by-products that may not absorb in the UV-Vis region[52]. This analysis will facilitate the proposal of possible degradation pathways of the contaminant and evaluate the effectiveness of P3HT NPs in the mineralisation of MB, providing valuable information for the development of efficient polymeric photocatalysts for the remediation of contaminated waters.

The results obtained are displayed in Figure 7.15 and Table 7.1. The initial MB solution shows an intense signal at a time of 12.2 min, which corresponds to an m/z ratio of 284.2. This molecular weight is associated with the intact MB molecule. Additionally, two further signals emerge at m/z 270.2 and 227.2, associated with azure B and thionin[48–51,53], respectively. These compounds are derivatives of MB, lacking methyl groups. In the case of Azure B, it has one less methyl than MB, and in the case of thionin, it has three fewer methyls. When MB is exposed to light for 240 minutes, the signal associated with MB becomes less intense, and the signal at m/z 227.2 assigned to thionin increases. This indicates that MB loses methyl groups by a demethylation cleavage, as has been previously reported in the literature[54]. The demethylation of MB is an oxidation process commonly attributed to the attack of highly reactive •OH radicals that are generated by photocatalysis. These radicals attack the methyl groups on the nitrogen atom[55], leading to the successive elimination of these groups and the formation of less methylated intermediates such as Azure B and thionin, before eventual ring cleavage[53].

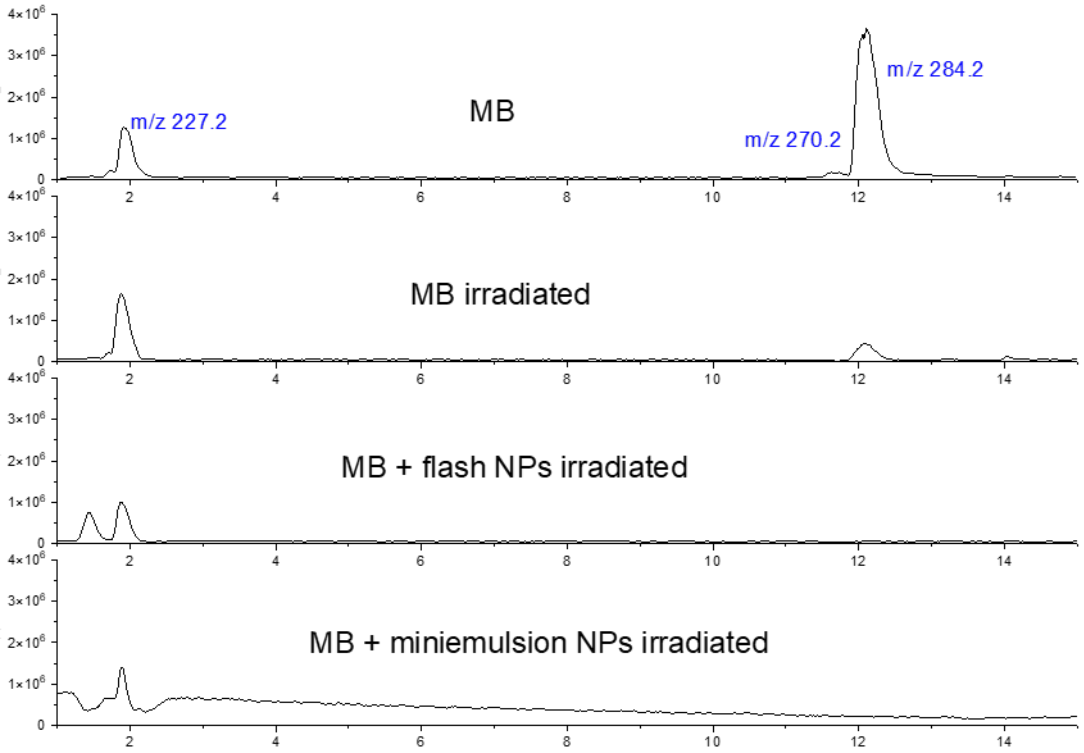

Figure 7.15. LC-MS chromatograms of the MB solution, and of MB solutions after 240 minutes of light irradiation: MB alone, MB with P3HT NPs prepared by flash nanoprecipitation, and MB with P3HT NPs prepared by miniemulsion.

When irradiation occurs in the presence of NPs, the LC-MS spectra reveal that after 240 minutes, the signal corresponding to MB disappears completely, while the signal corresponding to thionin loses intensity, indicating a more efficient and complete degradation of MB. Notably, no significant signals corresponding to leuco MB or other colourless species reported as products of adsorption or non-degradative oxidation were detected, thereby confirming that the decrease in colour intensity is primarily due to the effective degradation of MB.

Table 7.1. Summary of the LC-MS analysis of MB and its degradation products. The table presents the observed retention times, their corresponding m/z values, and their assigned chemical structures for the species identified during the degradation process.

Retention time (min)	m/z values	Structure
12.2	284.2	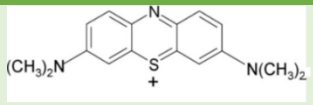

		MB
11.8	270.2	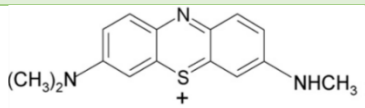 Azure B
1.90	227.2	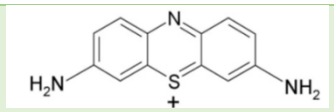 Thionin

The photocatalytic degradation of MB has been extensively investigated using a variety of semiconductor materials[32,48,54]. Although P3HT has not been as widely studied in this context, the general mechanisms reported by other authors can be extended to P3HT. Upon absorbing photons with energy exceeding than its bandgap (E_g), P3HT undergoes excitation of electrons from the HOMO to the LUMO[56,57]. This process of charge separation results in the formation of excitons, which have the potential to dissociate into free charge carriers at defect sites or interfaces[56,57]. These excitons can travel to the surface of the NP, where ionosorption of the adsorbed oxygen by the surface occurs. Photogenerated electrons can reduce the molecular oxygen and generate the formation of ROS, specifically the superoxide anion radicals ($O_2^{\bullet-}$)[56]. Concurrently, the photogenerated holes neutralise the hydroxide (OH^-) ions and oxidise water, thereby producing •OH radicals[56]. The process of neutralisation of these $O_2^{\bullet-}$ radicals is effected by H^+ ions, which, after reactions between the products and successive reductions, generate further •OH radicals that oxidise the organic reagent. The degradation of MB results in the formation of a range of final products, attributable to the presence of heteroatoms. Carbon undergoes a process of conversion into gaseous carbon dioxide (CO_2) and into inorganic ions, such as nitrate, ammonium and sulphate, respectively[32,58,59]. This process involves the presence of heteroatoms, specifically nitrogen and sulphur. Complete degradation of MB into its final products involves the cleavage of the molecular framework of the dye. The mechanism that has been proposed is based on the degradation products that have been obtained. This mechanism involves the loss of CH_3, which results in the compounds that have been detected (Azure B and thionin). Subsequent to the loss of all CH_3, the ring initiates a process of degradation through successive attacks, leading to its eventual breakdown. The succession of attacks, predominantly catalysed by the persistent action of •OH and $O_2^{\bullet-}$ radicals, results in the cleavage of bonds within the MB ring structure and the formation of lower molecular weight compounds. Complete

mineralisation of MB under photocatalytic conditions has been confirmed by the detection of CO_2, NO_3^-, $NH_4^+$and SO_4^{2-} as end products[32,58,59].

Moreover, the pH of the samples was measured both before and after the irradiation process, with the aim of determining the effect or the possible appearance of by-products. The effect of irradiation is to acidify the sample, which would be in accordance with the formation of CO_2 and inorganic salts, resulting in the mineralisation of MB and the formation of acidic species[60,61]. The present study has not revealed any evidence to suggest that the efficiency of MB degradation may be affected by the pH of the medium.

7.8. Conclusions

This chapter thoroughly investigates the photocatalytic degradation of MB using P3HT NPs prepared via flash and miniemulsion techniques, with a focus on understanding their stability, efficiency, and structure–activity relationships under visible light irradiation. The results obtained demonstrate that MB is stable in the absence of light but undergoes direct photolysis, even without the presence of a catalyst. However, this process is slow and follows zero-order kinetics due to its inherent photosensitivity and ROS formation. These results highlight the potential for enhancement via photocatalysis.

P3HT NPs, independently of their preparation method, demonstrate high photostability over prolonged irradiation, thereby ensuring their structural integrity and photocatalytic activity during degradation experiments. When employed as photocatalysts, P3HT NPs significantly enhance MB degradation, shifting the kinetics from zero-order to pseudo-first-order, and considerably lowering the half-life of the dye. The photocatalytic performance is found to be particularly enhanced in NPs derived from aged precursor solutions in the case of flash and those subjected to bath sonication in the case of miniemulsion, due to improvements in crystallinity, reduced band gap, smaller particle size, and better exciton diffusion, all of which contribute to more efficient ROS generation.

In this study, miniemulsion-prepared NPs were found to demonstrate the highest photocatalytic efficiency among the tested systems. This enhanced efficiency is indicative of their optimal structural characteristics, including reduced aggregation, smaller particle size, enhanced crystallinity, and favourable J-aggregate formation, as corroborated by

fluorescence lifetime studies indicating efficient charge separation over radiative recombination.

Finally, LC-MS analysis further confirmed that P3HT NPs mediate a more efficient and complete degradation of MB, primarily via demethylation and subsequent ring cleavage, leading to mineralisation into CO_2 and inorganic ions. This is supported by the observed acidification of the medium and the absence of non-coloured intermediates and reversibly adsorbed by-products. These findings provide validation of the degradation mechanism through •OH and O_2•$^-$ radicals, which are generated via P3HT-mediated photocatalysis.

While these findings unequivocally establish P3HT NPs as promising organic photocatalysts for environmental remediation, further optimisation is needed to match or exceed efficiencies reported for other catalysts in the literature[29,32,54,63–67]. Factors such as MB concentration and catalyst loading, which influence degradation kinetics, must be carefully considered in future studies[66]. Nevertheless, this work provides a solid foundation for the continued development of P3HT-based photocatalytic systems for environmental remediation.

7.9. Bibliography

(1) Kumari, H.; Sonia; Suman; Ranga, R.; Chahal, S.; Devi, S.; Sharma, S.; Kumar, S.; Kumar, P.; Kumar, S.; Kumar, A.; Parmar, R. A Review on Photocatalysis Used For Wastewater Treatment: Dye Degradation. *Water Air Soil Pollut* **2023**, *234* (6). https://doi.org/10.1007/s11270-023-06359-9.

(2) Khan, I.; Saeed, K.; Zekker, I.; Zhang, B.; Hendi, A. H.; Ahmad, A.; Ahmad, S.; Zada, N.; Ahmad, H.; Shah, L. A.; Shah, T.; Khan, I. Review on Methylene Blue: Its Properties, Uses, Toxicity and Photodegradation. *Water* **2022**, *14* (2). https://doi.org/10.3390/w14020242.

(3) Water, S. H. and H. (WSH). *Progress on Household Drinking Water, Sanitation and Hygiene 2000–2020: Five Years into the SDGs*; 2020.

(4) Katheresan, V.; Kansedo, J.; Lau, S. Y. Efficiency of Various Recent Wastewater Dye Removal Methods: A Review. *J Environ Chem Eng* **2018**, *6* (4), 4676–4697. https://doi.org/10.1016/j.jece.2018.06.060.

(5) Criado-Gonzalez, M.; Marzuoli, C.; Bondi, L.; Gutierrez-Fernandez, E.; Tullii, G.; Lagonegro, P.; Sanz, O.; Cramer, T.; Antognazza, M. R.; Mecerreyes, D. Porous Semiconducting Polymer Nanoparticles as Intracellular Biophotonic Mediators to Modulate the Reactive Oxygen Species Balance. *Nano Lett* **2024**, *24* (24), 7244–7251. https://doi.org/10.1021/acs.nanolett.4c01195.

(6) Zangoli, M.; Cantelli, A.; Candini, A.; Lewinska, A.; Fardella, F.; Tino, A.; Tommasini, G.; Wnuk, M.; Moschetta, M.; Perotto, S.; Lucarini, M.; Tortiglione, C.; Lanzani, G.; Di Maria, F. Photoreactivity of Thiophene-Based Core@Shell Nanoparticles: The Effect of Photoinduced Charge Separation on In

Vivo ROS Production. *J Phys Chem C* **2023**, *127* (9), 4672–4683. https://doi.org/10.1021/acs.jpcc.2c06986.

(7) Watanabe, T.; Kitamura, A.; Kojima, E.; Nakayama, C.; Hashimoto, K.; Fujishima, A. Photocatalytic Activity of TIO2 Thin-Film Under Room Light. In *Photocatalytic Purification and Treatment of Water and Air*; Ollis, D., Alekabi, H., Eds.; Elsevier Science: Amsterdam, 1993; Vol. 3, pp 747–751.

(8) Yan, H.; Deng, Y.; Shen, M.; Ye, Y. X.; Zhu, F.; Yang, X.; Ouyang, G. Regulation the Reactive Oxygen Species on Conjugated Polymers for Highly Efficient Photocatalysis. *Appl Catal B* **2022**, *314*. https://doi.org/10.1016/j.apcatb.2022.121488.

(9) Byrne, C.; Subramanian, G.; Pillai, S. C. Recent Advances in Photocatalysis for Environmental Applications. *J Environ Chem Eng* **2018**, *6* (3), 3531–3555. https://doi.org/10.1016/j.jece.2017.07.080.

(10) Oturan, M. A.; Aaron, J. J. Advanced Oxidation Processes in Water/Wastewater Treatment: Principles and Applications. A Review. *Crit Rev Environ Sci Technol* **2014**, *44* (23), 2577–2641. https://doi.org/10.1080/10643389.2013.829765.

(11) Hintz, H.; Egelhaaf, H. J.; Lüer, L.; Hauch, J.; Peisert, H.; Chassé, T. Photodegradation of P3HT - A Systematic Study of Environmental Factors. *Chemistry of Materials* **2011**, *23* (2), 145–154. https://doi.org/10.1021/cm102373k.

(12) Manceau, M.; Rivaton, A.; Gardette, J. L.; Guillerez, S.; Lemaître, N. The Mechanism of Photo- and Thermooxidation of Poly(3-Hexylthiophene) (P3HT) Reconsidered. *Polym Degrad Stab* **2009**, *94* (6), 898–907. https://doi.org/10.1016/j.polymdegradstab.2009.03.005.

(13) González-Juárez, E.; García-Hernández, E.; Arrieta-González, C. D.; Salgado-Delgado, R.; Güizado-Rodríguez, M.; Barba, V.; Espinosa-Roa, A. P3HT Colloid Stability Study and Its Application in the Degradation of Methylene Blue Dye under UV Radiation Conditions. *Polymer Bulletin* **2021**, *78* (11), 6455–6472. https://doi.org/10.1007/s00289-020-03415-w.

(14) Landfester, K.; Montenegro, R.; Scherf, U.; Güntner, R.; Asawapirom, U.; Patil, S.; Neher, D.; Kietzke, T. Semiconducting Polymer Nanospheres in Aqueous Dispersion Prepared by a Miniemulsion Process. *Advanced Materials* **2002**, *14* (9), 651–655. https://doi.org/10.1002/1521-4095(20020503)14:9<651::AID-ADMA651>3.0.CO;2-V.

(15) Nagarjuna, G.; Baghgar, M.; Labastide, J. A.; Algaier, D. D.; Barnes, M. D.; Venkataraman, D. Tuning Aggregation of Poly(3-Hexylthiophene) within Nanoparticles. *ACS Nano* **2012**, *6* (12), 10750–10758. https://doi.org/10.1021/nn305207b.

(16) Gutiérrez-Fernández, E.; Ezquerra, T. A.; Rebollar, E.; Cui, J.; Marina, S.; Martín, J.; Nogales, A. Photophysical and Structural Modulation of Poly(3-Hexylthiophene) Nanoparticles via Surfactant-Polymer Interaction. *Polymer* **2021**, *218*. https://doi.org/10.1016/j.polymer.2021.123515.

(17) Brus, L. E. Electron-Electron and Electron-Hole Interactions in Small Semiconductor Crystallites: The Size Dependence of the Lowest Excited Electronic State. *J Chem Phys* **1984**, *80* (9), 4403–4409. https://doi.org/10.1063/1.447218.

(18) Ghosh, S.; Chakraborty, S.; Ghosh, A.; Marjit, K.; Ghosh, G.; Patra, A. Ultrafast Relaxation Dynamics of Conjugated Polymer Nanoparticles by Tuning Their Interchain Interactions. *J Phys Chem C* **2022**, *126* (42), 18177–18187. https://doi.org/10.1021/acs.jpcc.2c06093.

(19) Muzammal, S.; Ahmad, A.; Sheraz, M.; Kim, J.; Ali, S.; Hanif, M. B.; Hussain, I.; Pandiaraj, S.; Alodhayb, A.; Javed, M. S.; Al-bonsrulah, H. A. Z.; Motola, M. Polymer-Supported Nanomaterials for Photodegradation: Unraveling the Methylene Blue Menace. *Energy Conversion and Management: X* **2024**, *22*. https://doi.org/10.1016/j.ecmx.2024.100547.

(20) Muktha, B.; Mahanta, D.; Patil, S.; Madras, G. Synthesis and Photocatalytic Activity of Poly(3-Hexylthiophene)/TiO2 Composites. *J Solid State Chem* **2007**, *180* (10), 2986–2989. https://doi.org/10.1016/j.jssc.2007.07.017.

(21) Ramar, P.; Aishwarya, B. V.; Samanta, D. A Photocatalytic Chip Inspired from the Photovoltaics of Polymer-Immobilized Surfaces: Self-Assembly and Other Factors. *Chemical Communications* **2021**, *57* (96), 12964–12967. https://doi.org/10.1039/d1cc04381a.

(22) Wang, X.; Maeda, K.; Thomas, A.; Takanabe, K.; Xin, G.; Carlsson, J. M.; Domen, K.; Antonietti, M. A Metal-Free Polymeric Photocatalyst for Hydrogen Production from Water under Visible Light. *Nat Mater* **2009**, *8* (1), 76–80. https://doi.org/10.1038/nmat2317.

(23) Parkinson, P.; Müler, C.; Stingelin, N.; Johnston, M. B.; Herz, L. M. Role of Ultrafast Torsional Relaxation in the Emission from Polythiophene Aggregates. *Journal of Physical Chemistry Letters* **2010**, *1* (19), 2788–2792. https://doi.org/10.1021/jz101026g.

(24) Labastide, J. A.; Baghgar, M.; Dujovne, I.; Venkatraman, B. H.; Ramsdell, D. C.; Venkataraman, D.; Barnes, M. D. Time- and Polarization-Resolved Photoluminescence of Individual Semicrystalline Polythiophene (P3HT) Nanoparticles. *J Phys Chem Lett* **2011**, *2* (17), 2089–2093. https://doi.org/10.1021/jz200958x.

(25) Satapathi, S.; Gill, H. S.; Li, L.; Samuelson, L.; Kumar, J.; Mosurkal, R. Synthesis of Nanoparticles of P3HT and PCBM for Optimizing Morphology in Polymeric Solar Cells. *Appl Surf Sci* **2014**, *323*, 13–18. https://doi.org/10.1016/j.apsusc.2014.07.175.

(26) Rauf, M. A.; Ashraf, S. S. Fundamental Principles and Application of Heterogeneous Photocatalytic Degradation of Dyes in Solution. *Chemical Engineering Journal* **2009**, *151* (1–3), 10–18. https://doi.org/10.1016/j.cej.2009.02.026.

(27) Hübner, U.; Spahr, S.; Lutze, H.; Wieland, A.; Rüting, S.; Gernjak, W.; Wenk, J. Advanced Oxidation Processes for Water and Wastewater Treatment – Guidance for Systematic Future Research. *Heliyon* **2024**, *10* (9). https://doi.org/10.1016/j.heliyon.2024.e30402.

(28) Zhu, H.; Gong, L.; Li, Z. Construction and Mechanism of a Novel Z-Scheme Photocatalyst α-Fe2O3/P3HT with O-Ti-O for Organic Pollutant Degradation under Visible Light. *Appl Surf Sci* **2020**, *505*. https://doi.org/10.1016/j.apsusc.2019.144639.

(29) Sun, C.; Karuppasamy, L.; Gurusamy, L.; Yang, H. J.; Liu, C. H.; Dong, J.; Wu, J. J. Facile Sonochemical Synthesis of CdS/COF Heterostructured Nanocomposites and Their Enhanced Photocatalytic Degradation of Bisphenol-A. *Sep Purif Technol* **2021**, *271*. https://doi.org/10.1016/j.seppur.2021.118873.

(30) Liu, F.; Nguyen, T. P.; Wang, Q.; Massuyeau, F.; Dan, Y.; Jiang, L. Construction of Z-Scheme g-C3N4/Ag/P3HT Heterojunction for Enhanced Visible-Light Photocatalytic Degradation of Tetracycline (TC) and Methyl Orange (MO). *Appl Surf Sci* **2019**, *496*. https://doi.org/10.1016/j.apsusc.2019.143653.

(31) Zhang, G.; Wo, R.; Sun, Z.; Hao, G.; Liu, G.; Zhang, Y.; Guo, H.; Jiang, W. Effective Magnetic Mofs Adsorbent for the Removal of Bisphenol a, Tetracycline, Congo Red and Methylene Blue Pollutions. *Nanomaterials* **2021**, *11* (8). https://doi.org/10.3390/nano11081917.

(32) Houas, A.; Lachheb, H.; Ksibi, M.; Elaloui, E.; Guillard, C.; Herrmann, J.-M. Photocatalytic Degradation Pathway of Methylene Blue in Water. *Appl Catal B* **2001**, *31* (2), 145–157.

(33) Brédas, J. L.; Beljonne, D.; Coropceanu, V.; Cornil, J. Charge-Transfer and Energy-Transfer Processes in π-Conjugated Oligomers and Polymers: A Molecular Picture. *Chem Rev* **2004**, *104* (11), 4971–5003. https://doi.org/10.1021/cr040084k.

(34) Rahimi, K.; Botiz, I.; Agumba, J. O.; Motamen, S.; Stingelin, N.; Reiter, G. Light Absorption of Poly(3-Hexylthiophene) Single Crystals. *RSC Adv* **2014**, *4* (22), 11121–11123. https://doi.org/10.1039/c3ra47064d.

(35) Yamagata, H.; Spano, F. C. Interplay between Intrachain and Interchain Interactions in Semiconducting Polymer Assemblies: The HJ-Aggregate Model. *J Chem Phys* **2012**, *136* (18). https://doi.org/10.1063/1.4705272.

(36) Clark, J.; Chang, J. F.; Spano, F. C.; Friend, R. H.; Silva, C. Determining Exciton Bandwidth and Film Microstructure in Polythiophene Films Using Linear Absorption Spectroscopy. *Appl Phys Lett* **2009**, *94* (16). https://doi.org/10.1063/1.3110904.

(37) Persson, N. E.; Chu, P. H.; McBride, M.; Grover, M.; Reichmanis, E. Nucleation, Growth, and Alignment of Poly(3-Hexylthiophene) Nanofibers for High-Performance OFETs. *Acc Chem Res* **2017**, *50* (4), 932–942. https://doi.org/10.1021/acs.accounts.6b00639.

(38) Bhattacharjee, U.; Elshobaki, M.; Santra, K.; Bobbitt, J. M.; Chaudhary, S.; Smith, E. A.; Petrich, J. W. Characterizing Electric Field Exposed P3HT Thin Films Using Polarized-Light Spectroscopies. *Macromol Chem Phys* **2016**, *217* (16), 1801–1809. https://doi.org/10.1002/macp.201600113.

(39) Yu, J.; Zhou, M.; Cheng, B.; Zhao, X. Preparation, Characterization and Photocatalytic Activity of in Situ N,S-Codoped TiO2 Powders. *J Mol Catal A Chem* **2006**, *246* (1–2), 176–184. https://doi.org/10.1016/j.molcata.2005.10.034.

(40) Hoffmann, M. R.; Martin, S. T.; Choi, W.; Bahnemann1', D. W.; Keck, W. M. Environmental Applications of Semiconductor Photocatalysis. *Chem. Rev* **1995**, *95* (1), 69–96.

(41) Kudo, A.; Miseki, Y. Heterogeneous Photocatalyst Materials for Water Splitting. *Chem Soc Rev* **2009**, *38* (1), 253–278. https://doi.org/10.1039/b800489g.

(42) Chen, J. H.; Li, J. Y.; Chen, L. C.; Su, C. I. Morphology and Microstructure of Aggregates and Gelation Behaviour of Poly (3-Hexylthiophene) in Xylene Solution. In *Applied Mechanics and Materials*; 2014; Vol. 479–480, pp 115–120. https://doi.org/10.4028/www.scientific.net/AMM.479-480.115.

(43) Aiyar, A. R.; Hong, J. Il; Izumi, J.; Choi, D.; Kleinhenz, N.; Reichmanis, E. Ultrasound-Induced Ordering in Poly(3-Hexylthiophene): Role of Molecular and Process Parameters on Morphology and Charge Transport. *ACS Appl Mater Interfaces* **2013**, *5* (7), 2368–2377. https://doi.org/10.1021/am3027822.

(44) Kleinhenz, N.; Persson, N.; Xue, Z.; Chu, P. H.; Wang, G.; Yuan, Z.; McBride, M. A.; Choi, D.; Grover, M. A.; Reichmanis, E. Ordering of Poly(3-Hexylthiophene) in Solutions and Films: Effects of Fiber Length and Grain Boundaries on Anisotropy and Mobility. *Chemistry of Materials* **2016**, *28* (11), 3905–3913. https://doi.org/10.1021/acs.chemmater.6b01163.

(45) Jin, Y.; Ye, F.; Zeigler, M.; Wu, C.; Chiu, D. T. Near-Infrared Fluorescent Dye-Doped Semiconducting Polymer Dots. *ACS Nano* **2011**, *5* (2), 1468–1475. https://doi.org/10.1021/nn103304m.

(46) Würthner, F.; Kaiser, T. E.; Saha-Möller, C. R. J-Aggregates: From Serendipitous Discovery to Supramolecular Engineering of Functional Dye Materials. *Angewandte Chemie - International Edition* **2011**, *50* (15), 3376–3410. https://doi.org/10.1002/anie.201002307.

(47) Floresyona, D.; Goubard, F.; Aubert, P. H.; Lampre, I.; Mathurin, J.; Dazzi, A.; Ghosh, S.; Beaunier, P.; Brisset, F.; Remita, S.; Ramos, L.; Remita, H. Highly Active Poly(3-Hexylthiophene) Nanostructures for Photocatalysis under Solar Light. *Appl Catal B* **2017**, *209*, 23–32. https://doi.org/10.1016/j.apcatb.2017.02.069.

(48) Mills, A.; Wang, J. Photobleaching of Methylene Blue Sensitised by TiO2: An Ambiguous System? *J Photochem Photobiol A Chem* **1999**, *127* (1–3), 123–134.

(49) Caram, J. A.; Suárez, J. F. M.; Gennaro, A. M.; Mirífico, M. V. Electrochemical Behaviour of Methylene Blue in Non-Aqueous Solvents. *Electrochim Acta* **2015**, *164*, 353–363. https://doi.org/10.1016/j.electacta.2015.01.196.

(50) González-Fernández, E.; Staderini, M.; Marland, J. R. K.; Gray, M. E.; Uçar, A.; Dunare, C.; Blair, E. O.; Sullivan, P.; Tsiamis, A.; Greenhalgh, S. N.; Gregson, R.; Clutton, R. E.; Smith, S.; Terry, J. G.; Argyle, D. J.; Walton, A. J.; Mount, A. R.; Bradley, M.; Murray, A. F. In Vivo Application of an Implantable Tri-Anchored Methylene Blue-Based Electrochemical PH Sensor. *Biosens Bioelectron* **2022**, *197*. https://doi.org/10.1016/j.bios.2021.113728 .

(51) Jia, P.; Tan, H.; Liu, K.; Gao, W. Synthesis, Characterization and Photocatalytic Property of Novel ZnO/Bone Char Composite. *Mater Res Bull* **2018**, *102*, 45–50. https://doi.org/10.1016/j.materresbull.2018.02.018.

(52) Richardson, S. D.; Ternes, T. A. Water Analysis: Emerging Contaminants and Current Issues. *Anal Chem* **2018**, *90* (1), 398–428. https://doi.org/10.1021/acs.analchem.7b04577.

(53) Zhang, T.; Oyama, T.; Horikoshi, S.; Hidaka, H.; Zhao, J.; Serpone, N. Photocatalyzed N-Demethylation and Degradation of Methylene Blue in Titania Dispersions Exposed to Concentrated Sunlight. *Solar Energy Materials & Solar Cells* **2002**, *73*, 287–303.

(54) Rauf, M. A.; Meetani, M. A.; Khaleel, A.; Ahmed, A. Photocatalytic Degradation of Methylene Blue Using a Mixed Catalyst and Product Analysis by LC/MS. *Chemical Engineering Journal* **2010**, *157* (2–3), 373–378. https://doi.org/10.1016/j.cej.2009.11.017.

(55) Konstantinou, I. K.; Albanis, T. A. TiO2-Assisted Photocatalytic Degradation of Azo Dyes in Aqueous Solution: Kinetic and Mechanistic Investigations: A Review. *Appl Catal B* **2004**, *49* (1), 1–14. https://doi.org/10.1016/j.apcatb.2003.11.010.

(56) Wei, S.; Chang, S.; Li, H.; Fang, Z.; Zhu, L.; Xu, Y. Polymer Photocatalysts for Photocatalytic Hydrogen Peroxide Production. *Green Chemistry* **2024**, *26* (11), 6382–6403. https://doi.org/10.1039/d4gc01321b.

(57) Salafsky, J. S. Exciton Dissociation, Charge Transport, and Recombination in Ultrathin, Conjugated Polymer-TiO2 Nanocrystal Intermixed Composites. *Phys Rev B* **1999**, *59* (16), 10885–10894. https://doi.org/10.1103/PhysRevB.59.10885.

(58) Gaya, U. I.; Abdullah, A. H. Heterogeneous Photocatalytic Degradation of Organic Contaminants over Titanium Dioxide: A Review of Fundamentals, Progress and Problems. *Journal of Photochemistry and Photobiology C: Photochemistry Reviews* **2008**, *9* (1), 1–12. https://doi.org/10.1016/j.jphotochemrev.2007.12.003.

(59) Senthilkumaar, S.; Porkodi, K.; Gomathi, R.; Geetha Maheswari, A.; Manonmani, N. Sol-Gel Derived Silver Doped Nanocrystalline Titania Catalysed Photodegradation of Methylene Blue from Aqueous Solution. *Dyes and Pigments* **2006**, *69* (1–2), 22–30. https://doi.org/10.1016/j.dyepig.2005.02.012.

(60) Krosuri, A.; Wu, S.; Bashir, M. A.; Walquist, M. Efficient Degradation and Mineralization of Methylene Blue via Continuous-Flow Electrohydraulic Plasma Discharge. *Journal of Water Process Engineering* **2021**, *40*. https://doi.org/10.1016/j.jwpe.2021.101926.

(61) Ghasemi, A. H.; Zoqi, M. J.; Zanganeh Ranjbar, P. Enhanced Photocatalytic Degradation of Methylene Blue Using a Novel Counter-Rotating Disc Reactor. *Front Chem* **2024**, *12*. https://doi.org/10.3389/fchem.2024.1335180.

(62) Mirbagheri, N. S.; Sabbaghi, S. A Ti-Doped γ-Fe2O3/SDS Nano-Photocatalyst as an Efficient Adsorbent for Removal of Methylene Blue from Aqueous Solutions. *J Environ Manage* **2018**, *213*, 56–65. https://doi.org/10.1016/j.jenvman.2018.02.035.

(63) Matthews, R. W. Photooxidative Degradation Of Coloured Organics in Water Using Supported Catalysts. TiO2 on Sand. *War. Res* **1991**, *25* (10), 1169–1176.

(64) Xu, C.; Rangaiah, G. P.; Zhao, X. S. Photocatalytic Degradation of Methylene Blue by Titanium Dioxide: Experimental and Modeling Study. *Ind Eng Chem Res* **2014**, *53* (38), 14641–14649. https://doi.org/10.1021/ie502367x.

(65) Wu, C. H.; Chern, J. M. Kinetics of Photocatalytic Decomposition of Methylene Blue. *Ind Eng Chem Res* **2006**, *45* (19), 6450–6457. https://doi.org/10.1021/ie0602759.

(66) Senthilraja, A.; Krishnakumar, B.; Nawabjan, S. A.; Sobral, A. J. F. N.; Subash, B.; Swaminathan, M.; Shanthi, M. Facile Synthesis of Y2S3/ZnO Nanocomposite and Its Catalytic Performance in the Degradation of Methylene Blue Using UV-A/Solar Illumination. *Journal of Water Process Engineering* **2016**, *12*, 32–40. https://doi.org/10.1016/j.jwpe.2016.06.002.

Conclusions

This Doctoral Thesis has explored the relationship between preparation parameters, nanoscale structure, and resulting functionality in poly(3-hexylthiophene) (P3HT) and poly(vinylidene fluoride) (PVDF) nanoparticles (NPs). The work not only explored the preparation and structure of these polymeric NPs through different preparation strategies, including flash nanoprecipitation, miniemulsion, and dialysis, but also systematically investigated how processing parameters affect their morphological, crystalline, and, in the case of P3HT, optical properties. This research analysed the correlation between the tailored properties and their performance in photocatalytic degradation processes. This advancement represents a significant step forward in comprehending the potential of controlled nanoconfinement in tailoring material properties for applications in optoelectronics and environmental remediation.

The principal conclusions derived from this research are the following:

- P3HT NPs prepared by flash nanoprecipitation and miniemulsion methods.
  - Polymer concentration, antisolvent-to-solvent ratio (R), and solution aging were found to critically affect particle size, crystallinity, and optical features of P3HT NPs prepared by flash nanoprecipitation. These results were obtained with Atomic Force Microscopy (AFM), Dynamic Light Scattering (DLS) and X-ray diffraction (XRD). Higher polymer concentrations resulted in aggregation, while intermediate R values yielded smaller and more crystalline NPs. Notably, aging of P3HT solutions promoted the formation of pre-aggregates, resulting in improved crystallinity, optimal chain alignment, enhanced chain planarization, and a reduced band gap in the formed NPs.
  - Sonication significantly impacted the particle characteristics, such as size or aggregation, crystallinity, and optical properties during miniemulsion preparation of P3HT NPs. In particular, ultrasonic bath sonication was identified as a critical factor in achieving smaller, more uniformly dispersed, and highly crystalline NPs. It was demonstrated that bath-sonicated NPs exhibited superior interchain order and J-aggregate formation in comparison to probe-sonicated or non-sonicated counterparts. Conversely, probe sonication resulted in the production of marginally larger NPs, accompanied by a decrease in crystallinity at higher amplitudes.
  - A comparison of flash and miniemulsion methods was conducted, which revealed key differences in the properties of P3HT NPs. Miniemulsion-derived

NPs exhibited more uniform size distributions, higher crystallinity, and enhanced chain planarization, as confirmed by AFM, DLS and XRD. This resulted in improved exciton dynamics and J-aggregate predominance when compared to flash-prepared NPs. Moreover, the analysis of the fluorescence lifetimes indicates that the deactivation of the excited state in miniemulsion NPs occurs predominantly through exciton transition to lower energy states and conformational planarization of the polymer backbone. Concurrently, flash NPs exhibited supplementary contributions from the decay of emissive states, attributable to exciton recombination. The observed differences are attributed to the presence of surfactant in miniemulsion NPs. The structural and optical outcomes of this process are dependent on the chosen preparation route and have a direct impact on the photocatalytic behaviour of the material.

- Role of solvent properties in the formation of different crystalline phases in deposits and PVDF NPs.
  - The study demonstrated effective control over the electroactive β and γ phases in PVDF deposits and NPs by strategically choosing processing solvents. The results concluded that solvents with high polarity promoted the electroactive phases by favouring trans conformations through strong dipole-dipole interactions. In the case of NPs prepared via dialysis or flash methods, particles in the nanometric range were observed. However, it was found that only highly polar solvents in dialysis enabled significant electroactive phase content. In the case of flash preparation, due to the boiling point of the solvents, this trend is not so clear.

    Furthermore, solvent mixtures and temperature variations during dialysis were investigated, revealing subtle effects on crystallinity and chain organisation. This research establishes that polymer dissolution and molecular interactions in solution are the determining factors dictating the final phase organisation, even in nanoconfined systems.
- P3HT NPs, prepared by both flash and miniemulsion methods, independent of preparation method, proved to be highly photostable, exhibiting effective photocatalytic effect for methylene blue (MB) degradation under visible light.
  - NPs derived from aged flash solutions and bath-sonicated miniemulsion samples exhibited the highest photocatalytic efficiency. This enhanced performance was attributed to a combination of factors, including improved crystallinity, reduced

band gap, decreased particle size, and enhanced exciton diffusion. Collectively, these factors contributed to more efficient reactive oxygen species (ROS) generation.

- Miniemulsion NPs exhibited the most optimal overall photocatalytic performance when compared to the flash-prepared system. The enhanced photodegradation efficiency of the miniemulsion NPs could be attributed to their higher crystallinity and surfactant-induced planarity. The enhanced crystallinity thus facilitates charge transfer, a non-radiative process that competes with fluorescence and is associated with the generation of free radicals, which are involved in photodegradation. Conversely, the flash-prepared NPs exhibited diminished structural organisation, leading to elevated radiative processes and diminished photodegradation efficiency.
- Liquid chromatography coupled with mass spectrometry (LC-MS) analysis confirmed a comprehensive degradation mechanism primarily via radical (demethylation and ring cleavage), leading to dye mineralisation, supported by the generation of •OH and O_2•$^-$ radicals. This established a clear structure-activity relationship for P3HT NPs, where morphological and crystalline features directly impact photocatalytic efficiency, thus validating their promise as organic photocatalysts for environmental remediation.

In summary, this work emphasises the critical importance of solvent processing conditions as fundamental tools for optimising the functional performance of polymer NPs. The investigation attempts a contribution to the advancement of the understanding of the structure-property relationships in polymer NPs, providing novel strategies for the rational design and optimisation of polymer NPs in key fields such as sustainable environmental remediation technologies. Further research is necessary to continue pursuing the ultimate goal, in which this research is framed, towards the development of scalable, sustainable, and highly efficient polymer-based photocatalytic systems.